EXPLORING THE AGGREGATION BEHAVIOURS OF SURFACE-ACTIVE MATERIALS

THESIS SUBMITTED IN FULFILLMENT OF THE REQUIREMENTS

FOR THE DEGREE OF

DOCTOR OF PHILOSOPHY (SCIENCE)

OF

JADAVPUR UNIVERSITY, INDIA

by

SUMANTA BANDYOPADHYAY, M.Sc.

2025

Department of Chemistry

Jadavpur University

Kolkata-700032

India

Prof. Soumen Ghosh, M. Sc., Ph. D.
Professor of Chemistry & Co-ordinator,
Centre for Surface Science
Department of Chemistry, **Jadavpur University**
Kolkata – 700 032, West Bengal, India
Awards of Prof. B. N. Ghosh from ICS, Dr. B. C. Deb from ISCA, Bronze Medal from CRSI, Visiting Chair Professor of St. F. X. University, Canada &
Selected as Top 2% World Ranking Scientist in Chemical Physics by Scientists of Stanford University, USA.

Phone : +91-33-2457 2503
Fax : 91-33-2414 4266
Mob - 9432 075 363
E-Mail – gsoumen17@yahoo.co.in/
soumen.ghosh@jadavpuruniversity.in

CERTIFICATE FROM THE SUPERVISOR

This is to certify that the thesis entitled **"EXPLORING THE AGGREGATION BEHAVIOURS OF SURFACE-ACTIVE MATERIALS"** submitted by **Sri. Sumanta Bandyopadhyay,** who got his name registered on 14.08.2019 for the award of **Ph.D. (Science) degree** of **Jadavpur University**, is absolutely based on his own work under the supervision of **Prof. Soumen Ghosh,** and neither this thesis nor any part of it has been submitted for any degree/diploma or any other academic award anywhere before.

Soumen Ghosh. 03.11.2025

Soumen Ghosh

Centre for Surface Science

Department of Chemistry

Jadavpur University

Kolkata- 700032

Prof. Soumen Ghosh
Department of Chemistry
Jadavpur University
Kolkata-700 032, W.B., India

"Success can only be achieved through repeated failure and introspection."

Acharya Prafulla Chandra Ray (1861 – 1944)

Dedicated To

My Beloved Parents, Pooja and little Saptaswa

DECLARATION

I hereby declare that the work incorporated in the present dissertation was carried out by me at the Centre for Surface Science, Department of Chemistry, Jadavpur University, Kolkata-700032, India. The entire work or any part of it has never been submitted before for any prize or degree anywhere.

Sumanta Bandyopadhyay 03/11/20

(Sumanta Bandyopadhyay)

ACKNOWLEDGEMENT

I am profoundly grateful to the individuals whose unwavering support and contributions have been involved in the completion of this dissertation, entitled ***"Exploring the Aggregation Behaviours of Surface-Active Materials,"*** conducted at the Centre for Surface Science, Department of Chemistry, Jadavpur University, Kolkata, India.

First and foremost, I extend my heartfelt thanks to Prof. Dr. Soumen Ghosh, Department of Chemistry, Jadavpur University, for his exceptional mentorship, scholarly guidance, and unwavering support throughout this research endeavor. His insightful advice and encouragement have been pivotal in shaping the direction and outcomes of this study.

I am deeply grateful to Prof. Dr. Shouvik Chattapadhyay for his invaluable insight, scholarly discussions, and constructive feedback that significantly enriched the research process.

Special appreciation goes to Prof. Dr. Kajal Krishna Rajak, Head of the Department of Chemistry, Jadavpur University, for facilitating access to essential research facilities and resources, which were crucial for the successful completion of this work.

I would like to thank the entire faculty of the Department of Chemistry at Jadavpur University for their academic support and guidance, as well as the university administration for their administrative assistance.

I also wish to acknowledge my colleagues, Dr Rajesh Banik, Mr. Bipin Bihari Mandal, Mr. Raju Sardar, Ms. Tanaya Saha, Mrs. Sudipta Chakraborty, Ms. Ankita Saha, Mr. Rabindranath Pal, for their collaborative spirit, technical expertise, and unwavering encouragement throughout this research journey.

Finally, I express my deepest appreciation to my parents and family members for their unwavering love, encouragement, and sacrifices throughout my academic journey.

Centre for Surface Science
Department of Chemistry
Jadavpur University
Kolkata – 700032
India

Sumanta Bandyopadhyay
03.11.25
(Sumanta Bandyopadhyay)

EXPLORING THE AGGREGATION BEHAVIOURS OF SURFACE-ACTIVE MATERIALS

Sumanta Bandyopadhyay

Jadavpur University, 2025

Index No.: 25/19/Chem./26

ABSTRACT

This comprehensive research explores the molecular interactions between diverse dyes and amphiphilic systems—comprising conventional surfactants and surface-active ionic liquids (SAILs)—in aqueous media, emphasising how variations in head group charge, hydrophobic tail structure, counterion size, and micellar polarity govern solubilization, aggregation, and spectroscopic properties. A multi-technique approach, including UV–visible and fluorescence spectroscopy, time-correlated single-photon counting (TCSPC), dynamic light scattering (DLS), zeta potential analysis, and conductometric titration, supplemented by Density Functional Theory (DFT) and Time-Dependent DFT (TDDFT) calculations, provides molecular-level insights. For the cationic dye Acridine Red (AR), the hydrophobic SAIL BMImOS exhibits superior solubilization compared to SDS and BMImBr, driven by reduced head-group repulsion and hydrophobic tail–mediated encapsulation, as supported by spectral shifts, fluorescence lifetime enhancement, and HOMO–LUMO overlap. The anionic dyes Eosin Y (EY) and Phloxine B (PhB) show maximum stabilisation and micellar incorporation with the zwitterionic surfactant C12DmCB, surpassing cationic and anionic analogues through balanced charge distribution and minimised electrostatic repulsion. In contrast, Methylene Blue (MB) interactions with CTAB, CTAT, and BMImOS reveal counterion-controlled binding, with CTAT forming the most stable ion-pair complex due to its bulky tosylate counterion. Across all systems, zwitterionic surfactants and hydrophobically tailored SAILs outperform conventional surfactants by enhancing solubilization, thermodynamic stability, and micellar efficiency while reducing toxicity. The strong agreement between experimental observations and DFT-derived electronic parameters establishes a predictive framework for rational amphiphile design. Collectively, the findings advance a generalizable strategy for tuning dye–micelle interactions through charge modulation, hydrophobic integration, and counterion engineering, with broad implications for drug delivery, photosensitization, bioimaging, solar energy harvesting, and wastewater treatment using sustainable amphiphilic materials.

Soumen Ghosh.

Signature of Supervisor

Date: 03.11.2025

Prof. Soumen Ghosh
Department of Chemistry
Jadavpur University
Kolkata-700 032, W.B., India

Sumanta Bandyopadhyay 03.11.25

Signature of the Candidate

Date:

PREFACE

This thesis presents a comprehensive investigation into the molecular interactions between diverse dyes and amphiphilic systems, including conventional surfactants and surface-active ionic liquids (SAILs), in aqueous media. By integrating advanced experimental techniques—UV-visible and fluorescence spectroscopy, time-correlated single-photon counting (TCSPC), dynamic light scattering (DLS), zeta potential measurements—with Density Functional Theory (DFT) and Time-Dependent DFT (TDDFT) calculations, the work aims to elucidate the aggregation behavior, micellization mechanisms, and spectral modifications underlying these systems.

The research spans four representative dye-amphiphile models, exploring both similarly and oppositely charged interactions, and systematically assessing the roles of surfactant head group charge, hydrophobic chain length, counterion size, and micellar polarity. The comparative analysis highlights the enhanced solubilization efficiency and structural tunability of SAILs and zwitterionic surfactants over traditional systems, alongside their reduced environmental toxicity.

By bridging experimental observation with computational insight, this study not only advances the fundamental understanding of micelle–dye interactions but also provides a predictive framework for designing optimized amphiphilic systems. The findings have broad implications for applications in drug delivery, bioimaging, photodynamic therapy, material fabrication, and wastewater treatment, thereby contributing to both scientific knowledge and sustainable technological development.

INTRODUCTION

Introduction

The study of aggregation behavior of amphiphiles in the presence of dyes is a promising area of inquiry within colloid and interface science, offering valuable insights for applications in drug delivery[1, 2], dye-sensitized solar cells[3, 4], and nanomaterials. Amphiphiles have the remarkable ability to self-assemble into micelles or other nanostructures in aqueous environments, and their interactions with dye molecules, through mechanisms such as electrostatic[5-7], hydrophobic, or π–π stacking interactions[8], can significantly enhance our understanding of these systems. By influencing key parameters like the critical micelle concentration (CMC), aggregation number, and micellar morphology, the presence of dyes can facilitate new pathways for co-aggregation or disrupt established assemblies. This dynamic interplay can improve solubilization capacity, enhance photophysical properties, and reinforce structural stability. Ultimately, exploring these interactions provides critical knowledge that can lead to more effective formulation strategies and innovative applications.

Dyes: Chemistry of Natural and Synthetic Colorants

Dyes are colorful organic compounds that can stick to materials like fabrics, papers, and plastics to add color by absorbing certain wavelengths of light[9]. Unlike pigments, which are often not soluble, dyes dissolve in water or other solvents, allowing them to be absorbed by surfaces[10]. Dyes contain two key parts: chromophores and auxochromes. Chromophores are the parts that absorb visible light, while auxochromes are groups that help to improve color and sticking ability. For instance, an azo group (–N=N–) or a carbonyl group (–C=O) acts as a chromophore, and groups like –OH or $–NH_2$ are auxochromes that enhance the color by donating electron density to the chromophore. Common chromophores include azo (–N=N–), nitro ($–NO_2$), carbonyl (C=O), and

large aromatic rings, while typical auxochromes are –OH, $–NH_2$, –COOH, and $–SO_3H$. These auxochromes can shift the color a dye absorbs and often make dyes more water-soluble.

- **Chromophore:** The part of a dye molecule (often a conjugated π-bond system or aromatic ring array) is responsible for its color. Examples include –N=N– (azo), –C=O (carbonyl), $–NO_2$ (nitro), and extended aromatic polyenes.
- **Auxochrome:** An auxochrome, such as –OH, $–NH_2$, –COOH, or $–SO_3H$, when attached to a chromophore, extends conjugation or donates electrons, causing shifts in absorption wavelength (bathochromic or hypsochromic) and enhancing dye affinity for

substrates. For example, phenol (–OH on benzene) shows stronger absorption than benzene, while –NH_2 in aniline shows red shifts and intensifies the azo dye color.

Classification of Dyes by Chemical Structure

Dyes can be classified based on their chromophoric core or ring system[11], which is fundamental to their chemical structure and application. The major structural classes of dyes include azo, anthraquinone, triarylmethane, indigoid, xanthene, heterocyclic, and phthalocyanine dyes. Each of these classes has a distinct chemical formula that contributes to its unique coloring properties and behaviors in various applications. Azo dyes, for instance, are known for their vibrant hues and are widely used in textiles, while anthraquinone dyes are recognized for their stability and rich colors. Triarylmethane dyes often exhibit bright colors and are commonly used in a variety of industries, including inks and food coloring. Indigoid dyes, renowned for their deep blue shades, have a rich history in fabric dyeing. Xanthene dyes, on the other hand, are typically fluorescent and used in biological staining. Heterocyclic dyes encompass a broad range of structures, providing versatility in color selection. Lastly, phthalocyanine dyes are valued for their intense shades and excellent lightfastness, making them ideal for commercial applications. Each of these dye classes showcases a unique blend of chemistry and artistry, leading to a wide array of options for coloring materials.

Azo Dyes

Azo dyes are a significant category of synthetic dyes, characterized by one or more –N=N– (azo) linkages between aromatic rings[12-14]. Their fundamental structure can be represented as Ar–N=N–Ar′. The extensive conjugation within these compounds contributes to a diverse range of vibrant colors, including red, orange, yellow, and brown, which vary depending on the specific substituents attached. To enhance functionality, one of the aromatic rings is typically phenyl, while the other can be naphthyl or phenyl with tailored electron-donating or electron-withdrawing groups. The incorporation of sulfonate (–SO_3^-) or carboxylate groups is common, as these modifications improve the dye's water solubility, making it more versatile in various applications. For example, tartrazine[15] ($C_{16}H_9N_4Na_3O_9S_2$) serves as a prime illustration (Figure 1A); this lemon-yellow azo dye, also known as FD&C Yellow 5, is extensively utilized as a food coloring[16] due to its appealing hue. Its structure features a pyrazolone ring linked through the –N=N– bond to a benzene sulfonate, demonstrating the thoughtful design behind azo dyes. Similarly, methyl orange ($C_{14}H_{14}N_3NaO_3S$) is employed effectively as an orange pH indicator dye[17] (Figure 1B). In the textile industry, dyes such as congo red and direct azo dyes play a

crucial role[18, 19], binding efficiently to cotton via their sulfonate groups. Overall, azo dyes are celebrated for their vibrant colors and ease of synthesis, making them invaluable in the production of fabrics, inks, plastics, and food products[20]. Their versatility and effectiveness continue to support a broad range of industries and applications.

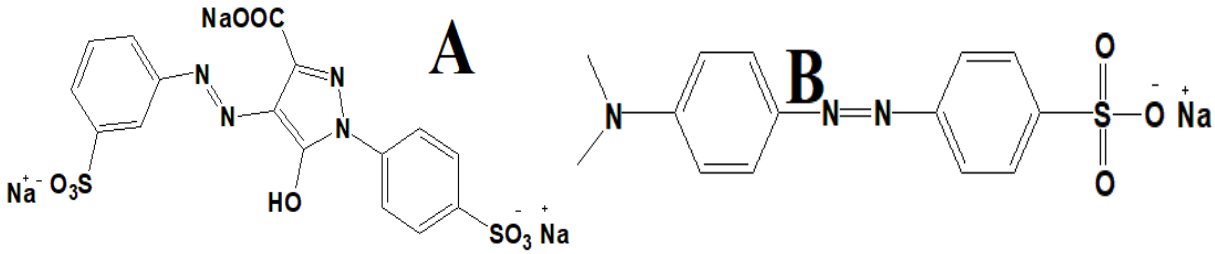

Figure 1: Chemical structure of (A) tartrazine, and (B) methyl orange.

Anthraquinone Dyes

Anthraquinone dyes are fascinating compounds built upon the anthracene-9,10-dione structure ($C_{14}H_8O_2$). By substituting various positions on this ring structure, a diverse palette of colors can be achieved, including vibrant reds, blues, and violets. A notable example is alizarin (1, 2-dihydroxyanthraquinone, $C_{14}H_8O_4$), which is a rich red dye, originally extracted from madder plants and is now predominantly produced synthetically[21, 22]. The presence of two –OH auxochromes in alizarin (Figure 2A) enhances the conjugation within the anthraquinone framework, resulting in its distinctive red hue. In the accompanying diagram, the anthraquinone core is illustrated with its three fused rings, and the red atoms indicate the oxygen substituents. Historically known as Turkey red, alizarin was widely used to dye fabrics, such as, cotton and wool. Similar to alizarin, quinizarin (1,4-dihydroxyanthraquinone) (Figure 2B) and derivatives of anthracene blue provide beautiful yellow and blue tones, respectively. Many vat dyes, particularly those that are insoluble and applied through reduction, such as, indigoid[23], are derived from anthraquinone. These dyes are highly valued for their vibrant colors and remarkable fastness, making them a staple in the textile industry.

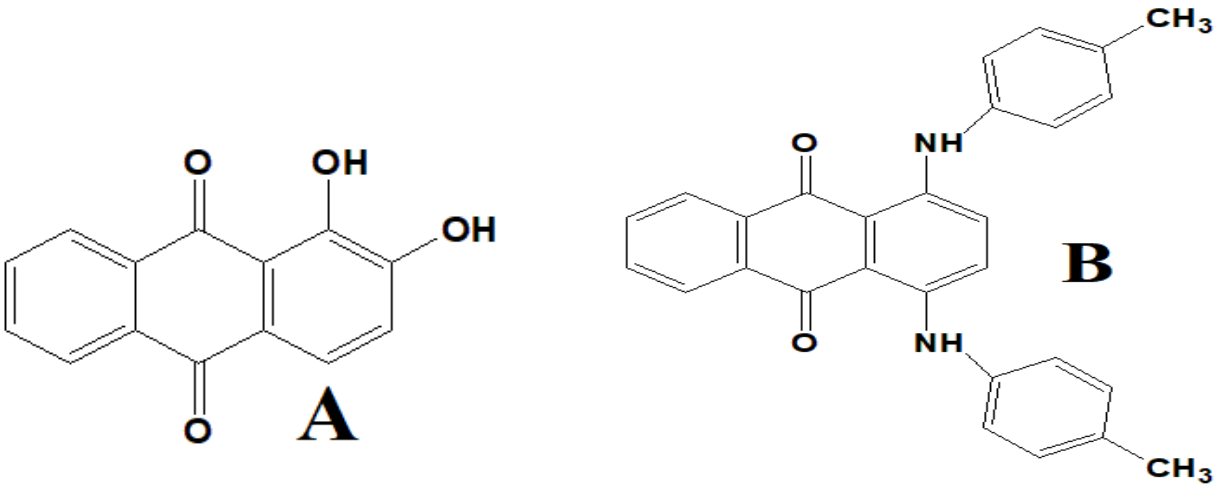

Figure 2: Chemical structure of (A) alizarin, and (B) quinizarin.

Triarylmethane Dyes

Triarylmethane dyes, also known as triphenylmethane dyes, are characterized by their unique structure, which consists of a central carbon atom that is bonded to three aromatic rings. This configuration creates a highly conjugated cationic chromophore, which is crucial for the dyes' vibrant coloration and light absorption properties. Typically classified as basic dyes or cationic salts, these dyes exhibit a range of striking hues, including vivid greens, purples, and blues. A quint essential example of a triarylmethane dye is crystal violet, with the chemical formula $C_{25}H_{30}ClN_3$ (Figure 3A). The molecular structure of crystal violet reveals a central carbon atom, C^+, which is integrally linked to three benzene rings. Each of these aromatic rings is modified by three $–N(CH_3)_2$ (dimethylamino) auxochrome groups. These auxochrome groups play an essential role by donating electrons into the conjugated system of the dye, which enhances its color intensity and saturation[24]. As a result, crystal violet is renowned for its deep violet shade. Triarylmethane dyes like crystal violet have a wide array of applications. They are extensively utilized in the textile industry for dyeing fabrics, where their ability to produce vivid and lasting colors is highly valued. Additionally, these dyes are key components in various writing instruments, such as ballpoint pens, owing to their rich pigmentation. In the field of biology, triarylmethane dyes are utilized as staining agents in microscopy[25], notably in techniques such as gram staining, which is used to differentiate bacterial species based on the characteristics of their cell walls[26]. Another noteworthy example of this class of dyes is malachite green, which is formulated as $C_{23}H_{25}ClN_2$ (Figure 3B). This dye is recognized for its green coloration and shares similar properties and applications with crystal violet, making it a staple in various industrial and biological contexts[27]. As a whole, triarylmethane dyes are integral to both

practical applications and scientific research, underscoring their importance across multiple fields.

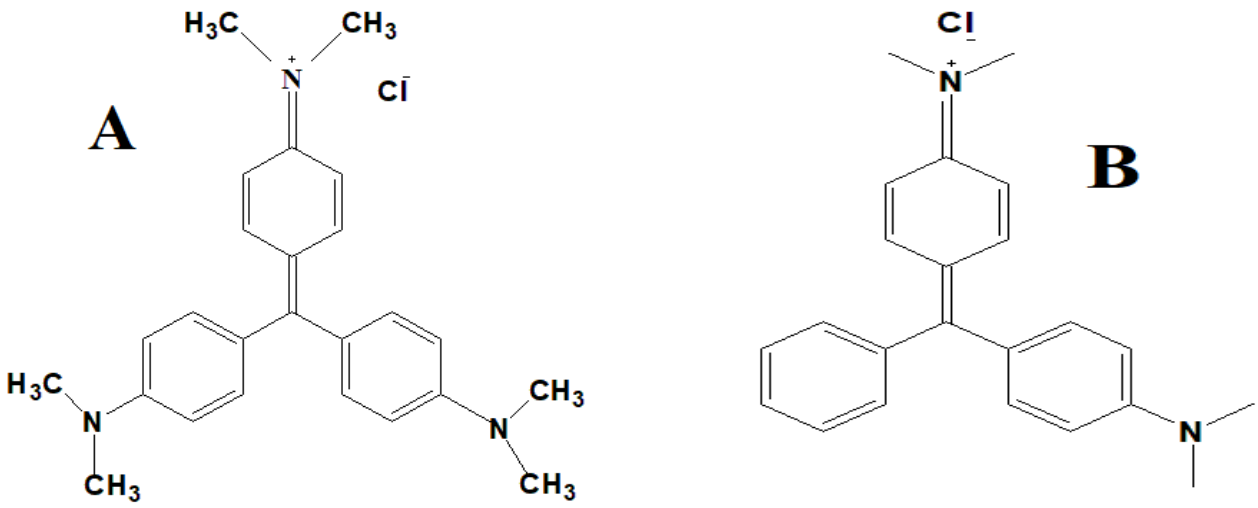

Figure 3: Chemical structure of (A) crystal violet, and (B) malachite green.

Indigoid Dyes

The indigoid class encompasses dyes that are structurally related to indigo, which are characterized by the presence of two heterocyclic or aromatic subunits connected by a double bond. The most notable example is indigo ($C_{16}H_{10}N_2O_2$), a deep blue dye that was initially derived from Indigofera plants[28, 29]. Chemically, indigo is synthesized from two indole units, which are the blue atoms in the molecular model, linked by a C=C bridge (Figure 4). The carbonyl groups, depicted as red atoms, serve as the chromophore responsible for the dye's color. The presence of auxochromatic NH groups and carbonyls imparts the distinctive blue hue to indigo. A related natural dye is tyrian purple, known scientifically as 6,6′-dibromoindigo. Indigo functions as a vat dye; it is insoluble in water and must undergo reduction to form a soluble leuco variant before application to fiber, after which it is oxidized back to its insoluble blue form. Indigoids are prominently utilized in the production of denim and in the dyeing of cotton textiles[30]. Moreover, synthetic indigo, produced via aniline, has largely supplanted the use of plant-derived sources.

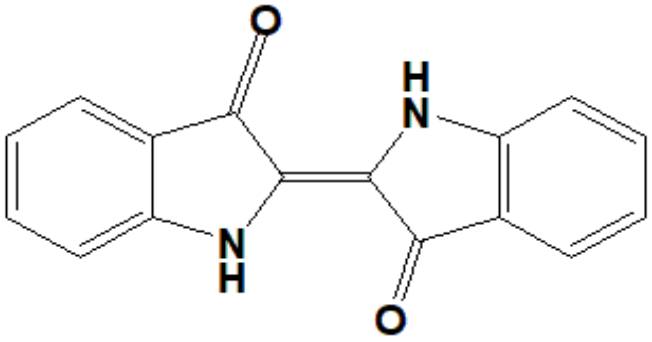

Figure 4: Chemical structure of Indigo dye.

Xanthene and Heterocyclic Dyes

Xanthene dyes are characterized by their unique tricyclic xanthene ring structure. Notable examples include fluorescein and its brominated derivative, eosin Y ($C_{20}H_6Br_4Na_2O_5$), both of which exhibit bright yellow-orange colors and are commonly used in biological staining and as fluorescent tracers[31-34]. These dyes typically feature auxochromes such as –OH and –COOR groups, enhancing their color properties (Figure 5A). Another category of dyes is the phenothiazine dyes, with methylene blue ($C_{16}H_{18}ClN_3S$) being a prominent example (Figure 5B). This thiazine-based blue dye is utilized in medical staining and as an indicator[35-37]. Both xanthene and phenothiazine dyes are highly valued for their vivid colors and fluorescence, making them significant in various applications[38].

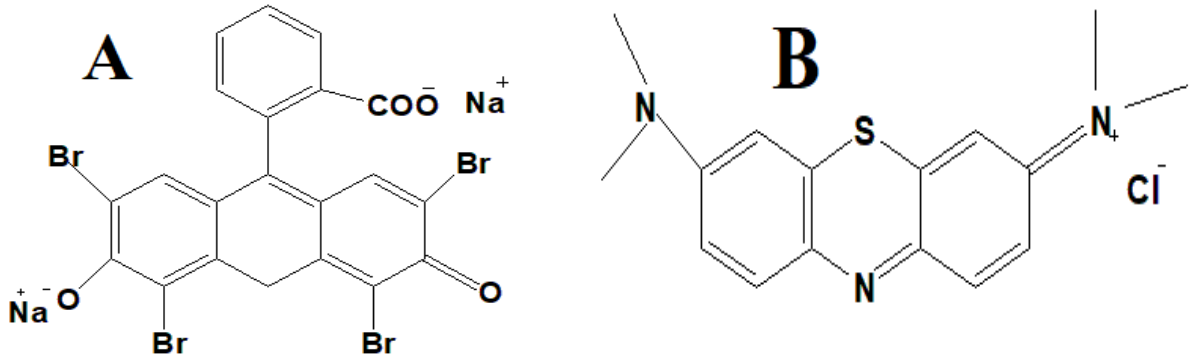

Figure 5: Chemical structure of (A) eosin yellow, and (B) methylene blue.

Other classes include phthalocyanines[39, 40], large planar macrocycles with a central metal (e.g., copper phthalocyanine, $C_{32}H_{16}CuN_8$) that are used as brilliant blue-green pigments. Cyanine dyes (polymethine chains linking nitrogen-containing rings) and carbonyl dyes (like indanthrones) also exist. In practice, dyes are often categorized by application (acid dyes, reactive dyes, vat dyes, etc.), but the chemical structure classification highlights the role of conjugated chromophores and auxochromes in the color properties.

Uses of Dyes in Industry and Science

Dyes have broad applications across textiles, foods, biological research, and more. Each field uses characteristic classes of dyes for their properties. Below are examples of dyes in textiles, food, and biological contexts.

Textile Industry

The textile industry dyes fibers like cotton, wool, silk, and synthetics[41, 42]. Indigo ($C_{16}H_{10}N_2O_2$) is commonly used for blue denim[43, 44]. Cotton fabrics are often dyed with reactive dyes, which bond covalently with cellulose, or direct dyes that adsorb through hydrogen bonding. Reactive dyes, like Remazol anthraquinone[45], contain chromophores that bond to fibers. Wool and nylon are dyed with acid dyes through ionic interactions. Acrylic fibers typically use basic (cationic) dyes, such as, triarylmethanes. In cotton printing, vat dyes like indigoid provide wash-fast colors. The choice of dye depends on fabric chemistry, with the chromophore and auxochromes determining color and solubility.

Food Industry

Food dyes, chosen for safety and brightness, include synthetic options like tartrazine (FD&C Yellow 5), a lemon-yellow azo dye used in various products, and Allura Red AC (FD&C Red 40), a red azo compound. These dyes often contain sulfonate or sodium groups for solubility and non-toxicity[46]. Natural colorants include betanin from beets[47], annatto extracts[48, 49], and spirulina phycocyanin[50]. The structures of these dyes typically feature extended conjugation for stability. Regulations ensure that they remain stable under various pH levels.

Biological applications

In biology and medicine, dyes serve functions in staining and diagnostics[51-53]. For instance, the Gram stain employs crystal violet to differentiate bacteria. Hematoxylin and eosin (H&E) are used in histology[54], with hematoxylin staining nuclei blue-black and eosin staining cytoplasm pink-orange[55]. Molecular biology uses dyes like coomassie brilliant blue G-250 for protein visualization[56] and ethidium bromide for DNA[57]. Acidic dyes bind basic proteins, while basic dyes bind acidic components. Fluorescent dyes enable fluorescence microscopy[58, 59] through their light-excitable structures.

In summary, the chemistry of dyes – their chromophores and auxochromes – underlies all their applications. Textile dyes exploit covalent or ionic attachment to fibers, food dyes require

stability and water solubility, and biological stains must bind selectively to tissues or molecules. Each example above includes chemical formulas and structures to illustrate how molecular features produce the observed colors and functions. The versatility of dyes arises from tailoring conjugated structures and substituents to achieve the desired hue and binding in natural or industrial settings.

Surfactants:

The term "surfactants" is an abbreviation for "surface active agents," referring to a category of compounds that play a crucial role in many cleaning and personal care products[60, 61]. Surfactants are the primary active ingredients found in soaps and detergents[62-64], which are widely used for laundry and various household tasks. The history of surfactants dates back to 1907 when a German company developed a groundbreaking cleaning agent known as 'PERSIL'[65]. This product was among the first commercial detergents to utilize a "self-activated" formula, revolutionizing the way laundry was done. Initially, 'PERSIL' included sodium perborate as its bleaching agent and sodium silicate as its washing agent. However, it is important to note that while these compounds contribute to the cleaning process, they do not function as typical surfactants, which are more versatile in their cleaning abilities. Surfactants possess unique molecular structures that allow them to interact effectively at various interfaces. They are designed with a hydrophilic (water-attracting) head and a hydrophobic (water-repelling) tail, enabling them to align themselves at the boundaries between different phases[66]. This alignment helps to reduce interfacial tension or free energy between different substances, such as between air and liquid, solid and liquid, or two immiscible liquids (Figure 6), enhancing the effectiveness of cleaning and emulsification processes[67, 68]. These compounds are vital across a wide range of everyday consumer products beyond just detergents. They are integral components in items such as toothpaste, shampoos, conditioners, shaving foam, facial cleansers, toilet cleaners, adhesives, hair gels, and inks. In these applications, surfactants perform varied roles, including serving as emulsifiers that help to mix oil and water[69]; dispersants that prevent the separation of ingredients[70, 71]; wetting agents that enhance the spread of liquids[72]; foaming agents that create lather, and stabilizers that maintain consistency and texture. Moreover, surfactants are known for their exceptional detergency properties, making them indispensable for achieving cleanliness and maintaining the performance of numerous products we rely on in our daily lives. Their versatility and effectiveness in reducing surface tension make them a key ingredient in both cleaning and personal care formulations.

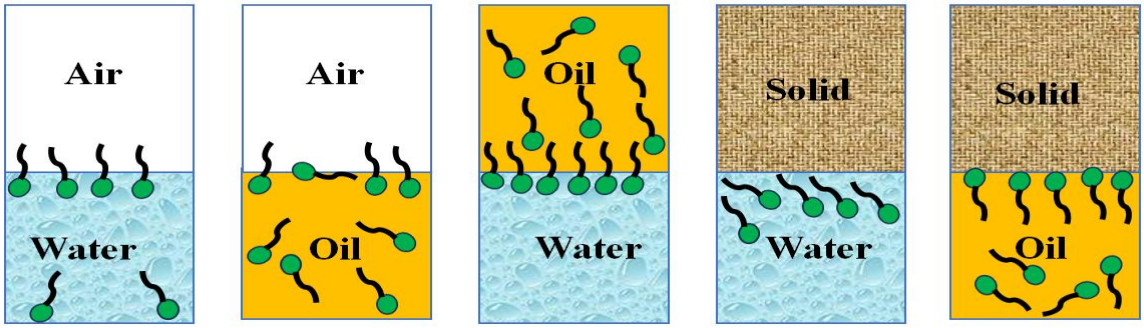

Figure. 6. Adsorption patterns of surfactants at various interfaces: (a) air-water interface, (b) air-oil interface, (c) oil-water interface, (d) solid-water interface, and (e) solid-oil interface.

Surfactants, often referred to as amphiphiles due to their remarkable ability to interact with both water and oil, possess a captivating molecular structure that includes a hydrophobic tail and a hydrophilic head. The hydrophobic tail is typically formed from lengthy chains of alkyl hydrocarbons, usually containing between 8 to 22 carbon atoms, which grants the surfactant a strong affinity for oily substances. Conversely, the hydrophilic head can adopt various forms—such as, cationic, anionic, nonionic, or zwitterionic—each imparting distinct properties that influence how the surfactant behaves in different environments. Unlike traditional soaps, which are created through the saponification of fatty acids sourced from natural materials like plants and animal fats, many surfactants are synthetically manufactured using petroleum products[73, 74]. This synthetic process offers considerable versatility, allowing for intricate adjustments to their molecular structures that enhance their effectiveness[75]. Modern detergents are complex mixtures that often consist of 10 to 20 different components, primarily composed of salts of surfactants and fatty acids[76]. These typically include sodium and potassium salts derived from long-chain alkyl groups ranging from C12 to C18. The surfactant and fatty acid salts are generally obtained from sources, such as, animal fats, palm oil, soybean oil, and coconut oil[77-82] through the saponification process. This diverse blend yields detergents that are significantly more effective than conventional soaps, allowing them to clean surfaces thoroughly even in challenging conditions, such as low temperatures or hard water. Beyond their cleaning process, surfactants play crucial roles in various biological processes[83]. In the microscopic world of living cells, phospholipids—molecules remarkably similar to amphiphiles—serve as fundamental building blocks of biological membranes known as lipid bilayers. These structures are crucial for regulating the selective movement of ions, proteins, and other essential molecules across cell membranes, thereby maintaining proper cellular function. In the digestive system, bile salts, a specific class of steroidal anionic surfactants, are vital organic solutes

present in bile juice[84]. They facilitate the absorption of dietary lipids in the intestine, ensuring efficient nutrient uptake. Additionally, in the lungs, a specialized kind of surfactant, known as pulmonary surfactant or pulmonary epithelial lining fluid (ELF), is produced by lung cells. This critical substance significantly enhances lung compliance and total lung capacity by reducing surface tension at the air-liquid interface within the alveoli. Composed mainly of lipoproteins secreted by type II alveolar epithelial cells, pulmonary surfactant plays an essential role in stabilizing the alveoli, ensuring effective gas exchange during the process of breathing.

Classification of surfactants:

In aqueous solutions, surfactants are typically organized according to the charge of their head groups. The following section lists several surfactants that are commonly used:

Cationic Surfactant: These surfactants have positively charged head groups (phosphonium salts, alkyl quaternary ammonium salts, amine salts, amine oxides, etc.)[85] along with negatively charged counterions (mainly chlorides and bromides). The preparation of these types of surfactants is expensive, limiting their use.

Example: Cetyl trimethylammonium chloride (CTAC) (Figure 7A), 1-hexadecyl triphenyl phosphonium bromide (Figure 7 B) (C_{16}TPB).

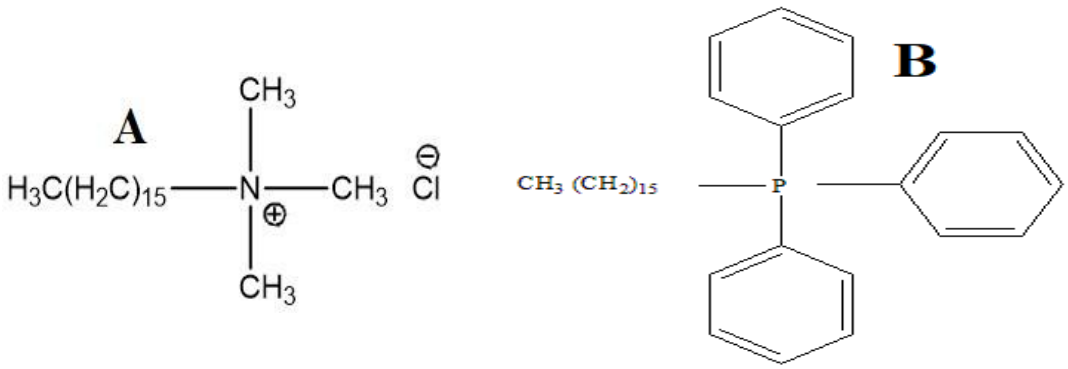

Figure 7: Chemical structure of (A) CTAC, and (B) C_{16}TPB.

Anionic Surfactant: This type of surfactant has negatively charged head groups with positively charged counterions[86]. The head groups may include sulfonates, alkyl sulfates, carboxylates, sulfosuccinates, and N-acyl amino acids. Quaternary ammonium cations and positively charged alkali metal ions (Na^+/K^+) may be present as counterions. Anionic surfactants are primarily used in daily products. Anionic surfactants are almost always used in household products.

Example: Sodium lauryl sulfate (SLS/SDS) (Figure 8A), Sodium lauryl sarcosinate (SLAS) (Figure 8B).

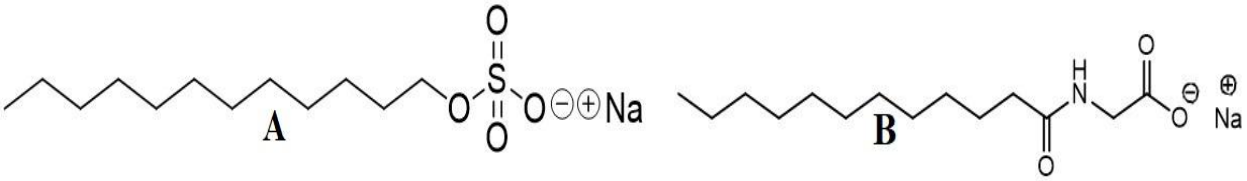

Figure 8: Chemical structure of (A) SDS and (B) SLAS.

Nonionic Surfactant: Surfactants that fall into the category of non-ionic surfactants do not carry any electrical charge, making them unique in their behavior and function[87]. These compounds are inherently miscible in water, primarily because of the polar functional groups incorporated into their molecular structures. This property allows them to interact effectively with water and is crucial for their performance in various applications. Common examples of non-ionic surfactants include alkylpolyglucosides, which are derived from renewable resources, polyoxyethylenes, which are widely used for their emulsifying properties[88], glucamine-based surfactants that offer excellent biodegradability, and polyglycidols that provide versatility in formulations. Together, these surfactants are produced on an industrial scale, amounting to large quantities, second only to anionic surfactants in terms of production volume. Their widespread use spans multiple industries, including personal care, cleaning, and pharmaceuticals, due to their effectiveness and environmental compatibility.

Example: (1,1,3,3-Tetramethylbutyl) phenyl-polyethylene glycol (Triton X-114) (Figure 9), Polyoxyethylene sorbitan monolaurate (Tween-20), N-decanoyl-N-methylglucamine (MEGA-10).

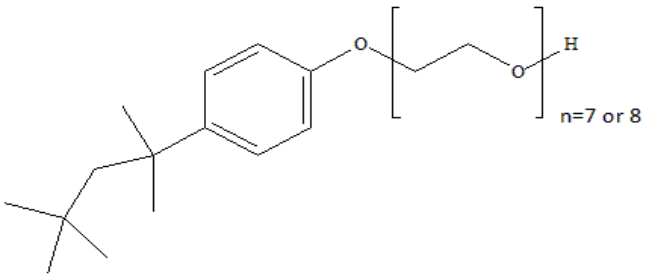

Figure 9: Chemical structure of Triton X-114.

Zwitterionic Surfactants: Zwitterionic surfactants are a unique class of compounds that possess both positively and negatively charged centers[89], which allows them to function as either anionic or cationic surfactants depending on the surrounding pH levels. Examples of

these versatile surfactants include imidazole derivatives, phosphatides, and betaines. The positive charge typically comes from ammonium ions, while the negative charge can be derived from functional groups, such as, carboxylates, sulfates, or sulfonate ions[90]. These surfactants are well-known for their exceptional dermatological properties[91], making them particularly popular in personal care formulations. Due to their high foaming ability and milder effects on the skin, zwitterionic surfactants are commonly found in a variety of cosmetic products, including shampoos, hand soaps, and dishwashing liquids. Their ability to balance both charges not only enhances their cleaning efficiency, but also minimizes irritation, making them a favorable choice for sensitive skin types[92].

Example: N-Dodecyl-N, N-dimethyl-2-ammonio-1-ethanecarbonate (C_{12}DmCB) (Figure 10).

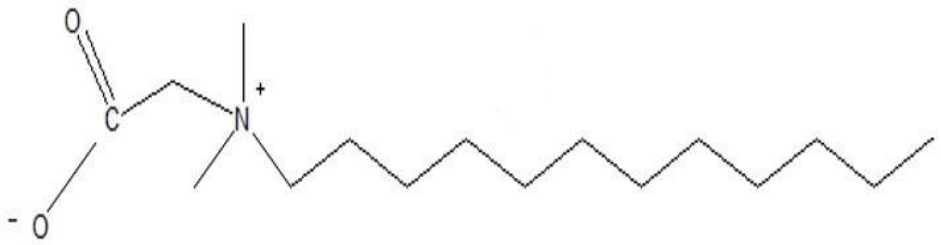

Figure 10: Chemical structure of C_{12}DmCB.

Surfactants, which play a crucial role in various applications, can be further classified into distinct categories beyond their general classification. In recent decades, particularly over the last twenty years, these specialized types of surfactants have garnered significant interest and have been the subject of extensive research efforts. Scientists and industry experts alike have explored the unique properties, mechanisms, and potential uses of these compounds, highlighting their significant contributions to fields ranging from detergents to pharmaceuticals and beyond.

Gemini Surfactant:

Gemini surfactants represent a distinctive class of surfactants (Figure 11) that exhibit enhanced surface activity compared to traditional surfactants[93]. They are composed of an extended hydrocarbon chain linked to a polar head group, accompanied by a rigid or non-rigid spacer, followed by another hydrocarbon chain that is sequentially arranged with an additional polar head group. The polar head groups can be classified as nonionic (derived from carbohydrates), negatively charged (such as sulfates and carboxylates), or positively charged (like ammonium). The lengths of the spacers can vary from two to twelve methylene groups, and they can be either stiff (as seen in stilbene) or flexible (like a saturated hydrocarbon chain). Bunton et al.

first synthesized gemini surfactants in 1971, while Menger et al. coined the term "Gemini" in 1991[94]. The spacers can connect in two ways: either at the midpoint of the elongated hydrocarbon tails or to both of the same head group.

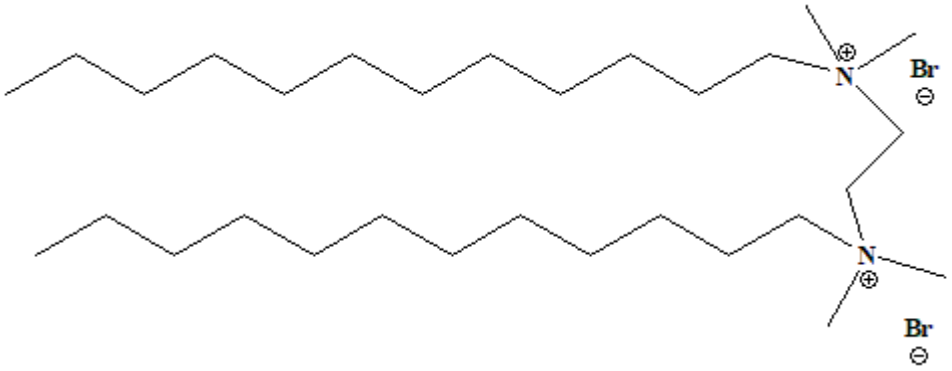

Figure 11: Chemical structure of Gemini 12-2-12 surfactant.

Fluoro surfactants:

The surfactants in question belong to a specialized category characterized by the substitution of at least one hydrogen atom in the alkyne chain with a fluorine atom (Figure 12). These fluoro surfactants are highly versatile and find extensive applications across various fields, including adhesives, cosmetics, biomedicine, and firefighting[95, 96]. The effectiveness of these surfactants is often evaluated by the number of fluorine atoms that replace the alkyne hydrogens, serving as an indicator of their surface activity. Notably, fluoro surfactants exhibit superior surface activity compared to traditional organic surfactants, making them particularly valuable in applications where enhanced performance is required.

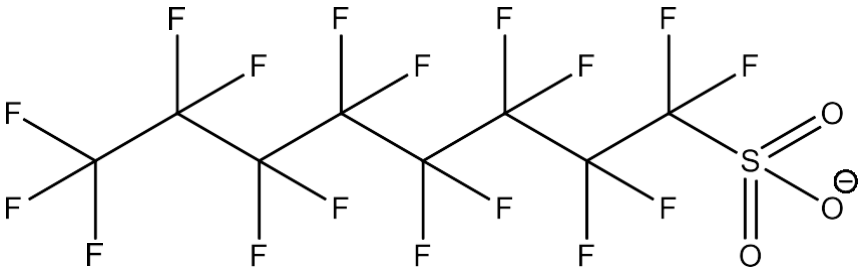

Figure 12. Perfluorooctane sulfonate (PFOS) is generally used in firefighting foam**.**

SILICONE surfactants:

Silicone surfactants, scientifically known as siloxane-polyoxyalkylene copolymers, represent a fascinating and specialized category of surfactants that possess a unique molecular

architecture[97, 98]. These compounds are characterized by the presence of one or more hydrophilic polar groups, which can take on various forms such as anionic, cationic, non-ionic, or zwitterionic. Complementing these hydrophilic elements are the permethylated siloxane hydrophobic groups, which impart distinct properties that set silicone surfactants apart from traditional hydrocarbon-based counterparts. Among the hydrophilic groups, the most prevalent types include polyoxyethylene (PEO) and polyoxypropylene (PPO), which contribute to the surfactants' ability to interact with water and oils effectively. This unique structure enables silicone surfactants to excel at reducing surface tension, achieving remarkably low values of 15-20 mN/m across both aqueous and non-aqueous environments. This level of efficacy is crucial for applications where surface activity is paramount. Owing to their exceptional spreading and wetting characteristics, silicone surfactants have become indispensable in a variety of industries. In the cosmetics industry, they play a vital role as emulsifiers in lotions and creams, facilitating the stable combination of oil and water components to achieve a smooth and luxurious texture. In textiles, these surfactants serve as effective conditioners, enhancing the softness and performance of fabrics to ensure they feel comfortable against the skin[99]. Additionally, silicone surfactants (Figure 13) are used as additives in inks, where they enhance flow and consistency, resulting in more vibrant and uniform prints. They also function as stabilizers in polyurethane foams, helping to maintain the integrity and durability of foam products. In summary, the versatility and unique properties of silicone surfactants make them a key ingredient in a wide array of formulations, spanning from personal care products to industrial applications, highlighting their significant role in enhancing product performance across diverse sectors[100, 101].

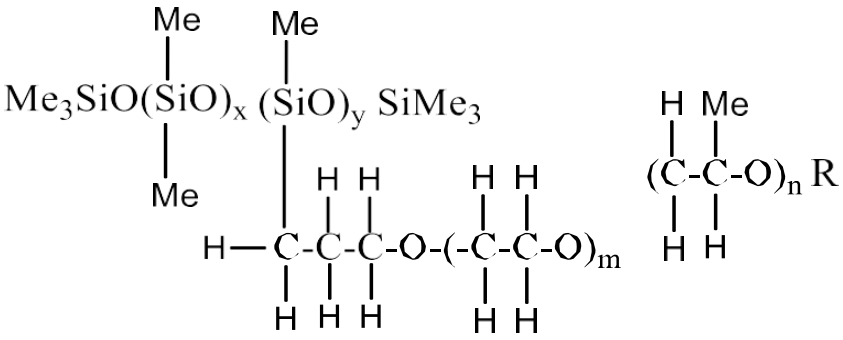

Figure 13. General structure of silicone surfactants; x = 7 to 10, y = 2 to 5, m = 5 to 15, n = 0 to 5, and R is the alkyl group which has been selected for the compatibility of surfactants in special purposes.

Amphiphilic compounds exhibit varying degrees of hydrophilicity and lipophilicity depending on their structure. The hydrophilic-lipophilic balance (HLB) is crucial for classifying surfactants as either water-soluble or oil-soluble based on their solubility.

Ionic Liquids

Ionic liquids (ILs) represent a distinctive category of organic salts that maintain a liquid form at temperatures lower than 100°C, and often even at room temperature.[102, 103] Over the last twenty years, these materials have garnered significant attention due to their remarkable characteristics, including negligible vapor pressure, high thermal stability, adjustable solvation capabilities, and excellent chemical resistance. Their customizable properties, stemming from the vast combinations of cations and anions, enable the creation of "task-specific ionic liquids" tailored for specific industrial, biochemical, and environmental uses. One of the most promising advancements in this field is the development and application of surface-active ionic liquids (SAILs)—a specific type of ILs that have amphiphilic properties akin to surfactants. These substances demonstrate notable surface activity and are utilized in various applications, including emulsification, drug delivery, micellar catalysis, and particularly in dye adsorption, solubilization, and separation.

An ionic liquid is typically composed of:

Cation: Usually a bulky, asymmetric organic ion.

Anion: Can be organic or inorganic and influences many physicochemical properties.

The identity of the cation has a dramatic effect on the IL's solubility, thermal stability, and polarity. Common cations include:

Imidazolium-based ILs

Among the various types of ionic liquids (ILs), these particular ones stand out for their remarkable chemical stability[104] and the straightforwardness with which they can be modified for specific applications.[105, 106] Their unique properties make them highly favored in a range of industries, allowing for adaptable functionalities that cater to diverse scientific and engineering needs.[107, 108]

Example: 1-Butyl-3-methylimidazolium bromide ([BMIM][Br]) (Figure 14).

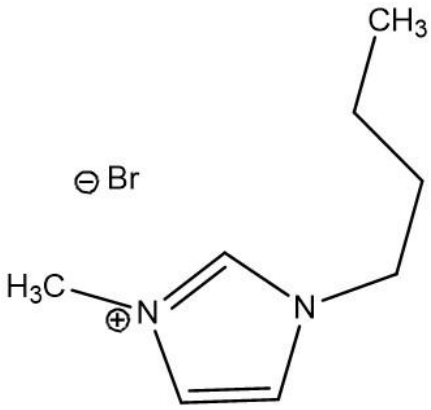

Figure 14: Chemical structures of 1-Butyl-3-methylimidazolium bromide ([BMIM][Br]).

Pyridinium-based ILs

These ionic liquids (ILs) exhibit remarkable thermal stability, making them highly suitable for various electrochemical applications[109]. Their unique properties, such as, a broad liquid range and low volatility[110] allow them to perform effectively under a range of temperatures, ensuring reliable performance in processes such as energy storage, battery technology, and electrochemical sensors[111-113].

Example: N-butylpyridinium hexafluorophosphate ([BPy][PF_6]) (Figure 15).

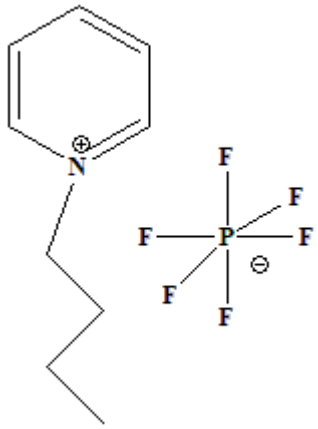

Figure 15: Chemical structures of N-butylpyridinium hexafluorophosphate ([BPy][PF_6]).

Ammonium-based ILs

These ionic liquids (ILs), which are derived from quaternary ammonium salts, are typically more cost-effective and widely utilized in various industrial applications[114]. Their unique properties make them suitable for a range of processes, contributing to their popularity in commercial settings[115].

Example: Tetra alkylammonium chloride ([N $(CH_3)_4$] [Cl]) (Figure 16).

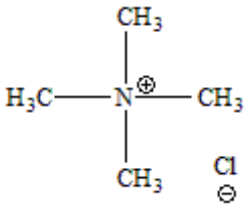

Figure 16: Chemical structures of Tetra alkylammonium chloride ([N $(CH_3)_4$] [Cl]).

Phosphonium-based ILs

Recognized for their exceptional thermal and chemical stability[116], these materials are designed to endure and perform reliably in extreme environments where high temperatures and aggressive chemicals prevail[117].

Example: Trihexyl (tetradecyl)phosphonium chloride (Figure 17).

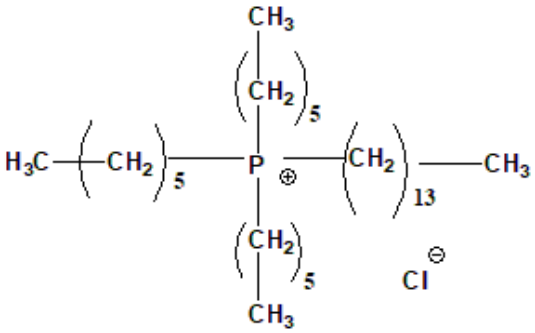

Figure 17: Chemical structures of Trihexyl (tetradecyl)phosphonium chloride.

Pyrrolidinium-based ILs

Widely utilized in battery electrolytes, these substances are favored for their excellent electrochemical stability[118], which ensures reliable performance and longevity in energy storage applications[119].

Example: N-methyl-N-propylpyrrolidinium bis(trifluoromethylsulfonyl)imide (Figure 18).

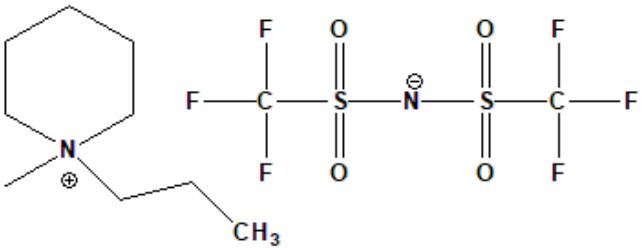

Figure 18: Chemical structures of Trihexyl (tetradecyl)phosphonium chloride.

Anions play a significant role in determining properties like hydrophilicity, viscosity, and ionic conductivity.

a. Halide Anions

Typically include Cl^-, Br^-, and I^-; often hydrophilic.

Example: 1- butyl -3- methyl imidazolium chloride [BMIM][Cl].

b. Inorganic Anions

Includes PF_6^-, BF_4^-, and NO_3^-. These confer hydrophobic properties and are used in extraction and catalysis.

Example: [BMIM][PF_6].

c. Organic Anions

Such as acetate, formate, and octyl sulfate. These ILs are often biodegradable and hydrophobic in nature and used in green chemistry.

Example: [BMIM][Os] (Octyl sulphate).

Physicochemical properties of ionic liquids

Ionic liquids (ILs), often regarded as salts in a liquid form at temperatures below 100 °C, possess a distinctive array of physicochemical properties that set them apart from traditional molecular solvents. These characteristics are vital for their use in green chemistry, electrochemistry, separation science, and materials engineering.

1. *Thermal Stability*: Ionic liquids typically demonstrate high thermal stability due to the robust electrostatic interactions among their constituent ions[120, 121]. The majority of ILs decompose at temperatures significantly exceeding 300°C, making them suitable for high-temperature applications with minimal degradation.
2. *Low Vapor Pressure*: A prominent feature of ILs is their minimal vapor pressure at ambient temperature[122]. This lack of volatility diminishes the chances of evaporation and inhalation exposure, which contributes to their designation as environmentally friendly or "green" solvents[123-125].
3. *High Ionic Conductivity*: Being composed entirely of ions, ILs inherently possess ionic conductivity[126, 127]. However, the degree of conductivity can vary based on ion mobility,

ion dimensions, and viscosity. Consequently, ILs are extensively utilized as electrolytes in batteries, supercapacitors, and fuel cells.

4. *Wide Electrochemical Window*: Ionic liquids exhibit a wide electrochemical window, often surpassing 4–6 V, which is considerably broader than that of water or many organic solvents[128]. This property enables them to act as stable electrolytes in electrochemical devices under high-voltage conditions.[129, 130]
5. *Viscosity*: The majority of ILs manifest moderate to high viscosities due to strong interactions between ions and hydrogen bonding[131]. This factor affects diffusion, solubility, and reaction kinetics in systems based on ILs. The viscosity is also responsive to temperature and the structural makeup of the ions involved.
6. *Polarity and Solvation Ability*: Ionic liquids display adjustable polarity, which is contingent on the selection of cations and anions[132, 133]. They have the capability to dissolve a diverse array of both polar and nonpolar substances, including gases, organic compounds, and metal salts. This versatility in solvation renders ILs valuable for extraction, catalysis, and drug delivery.
7. *Density*: Ionic liquids generally possess densities that range from 1.0 to 1.6 g/cm³. The density is influenced by the types of ions, their dimensions, and the efficiency of packing[134, 135]. The presence of larger atoms, such as fluorine or phosphorous-containing anions, tends to increase the overall density.
8. *Hydrophobicity/Hydrophilicity*: The hydrophobic or hydrophilic characteristics of ILs can be customized by altering the alkyl chains on the cation or by selecting certain anions. This property plays a crucial role in phase separation, biphasic catalysis, and strategies for environmental cleanup[136, 137].
9. *Melting Point*: Ionic liquids are characterized by their low melting points, which are generally below 100°C. The asymmetry and delocalization of charge in their ions diminish the lattice energy and inhibit crystallization, enabling them to remain in a liquid state across a wide temperature range[138, 139].
10. *Chemical and Thermal Tunability*: Owing to the vast array of organic cations (such as imidazolium, pyridinium, and ammonium) and various anions (including halides, PF_6^-, BF_4^-, and NTf_2^-), ILs can be specifically tailored for distinct applications, yielding optimal physicochemical properties.

These cumulative characteristics render ionic liquids versatile functional materials with a broad range of applications in both industrial and academic settings, particularly in driving sustainable and efficient chemical processes.

Significance and Uses of Ionic Liquids (ILs):

Ionic liquids (ILs), which are salts that exist in liquid form at or near room temperature, exhibit a distinctive set of physicochemical characteristics—such as minimal vapor pressure, remarkable thermal and chemical stability, adjustable solubility, and ionic conductivity—that make them essential in both scholarly research and industrial usage. Their extensive applications range from sustainable chemistry to advanced materials and biotechnology. Below is a university-level summary of their significance and uses:

1. *Eco-friendly Solvents for Sustainable Chemistry*: ILs are increasingly being utilized as environmentally friendly solvents[140] because of their non-volatile characteristics, which help to lower harmful emissions and enhance safety in processes like organic synthesis, catalysis, and separation[141, 142].
2. *Catalytic Media and Catalysts*: Numerous ILs serve as solvents and co-catalysts in various reactions, including Friedel–Crafts alkylation, Diels–Alder reactions, and hydrogenation, improving reaction rates, selectivity, and the recyclability of catalysts[143, 144].
3. *Electrolytes in Electrochemical Devices*: ILs are employed as highly stable and conductive electrolytes for batteries (like lithium-ion), fuel cells, supercapacitors, and dye-sensitized solar cells due to their broad electrochemical windows and ionic conductivity[145, 146].
4. *Extraction and Separation Processes*: ILs facilitate the selective extraction of metals (such as lanthanides and uranium), organic contaminants, and biomolecules via liquid–liquid or solid–liquid extraction, often substituting volatile organic solvents in hydrometallurgy and environmental cleanup[147, 148].
5. *Biocatalysis and Enzyme Stabilization:* Their capacity to stabilize proteins and enzymes makes ILs advantageous in non-aqueous enzymology, enhancing enzyme activity, selectivity, and lifespan in the pharmaceutical and biofuel sectors[149, 150].
6. *Gas Capture and Storage*: ILs serve as effective media for absorbing gases like CO_2, SO_2, and H_2S due to their adjustable polarity and functional groups, presenting promising applications in carbon capture and storage (CCS) technology[151, 152].

7. *Materials Synthesis and Nanotechnology*: ILs function as reaction media for the creation of nanoparticles, metal-organic frameworks (MOFs), and advanced polymers. Their ionic characteristics allow for precise control over particle size, shape, and functionalization.[153, 154]
8. *Analytical Chemistry and Chromatography*: ILs are utilized as additives in the mobile phase or as stationary phases in gas and liquid chromatography, improving separation efficiency, resolution, and consistency for complex mixtures[155, 156].
9. *Pharmaceutical Formulation and Drug Delivery*: ILs enhance drug solubility, stability, and bioavailability, and are being investigated as active pharmaceutical ingredients (API-ILs), excipients, and agents for transdermal delivery[157, 158].
10. *Lubricants and Antistatic Agents*: ILs that possess low volatility and high thermal stability are used in lubricants[159], antistatic coatings[160], and heat-transfer fluids[161], particularly in extreme conditions.
11. *Nuclear and Space Applications*: Due to their radiation stability and low flammability, ILs are being explored for applications in nuclear fuel processing and as thermal fluids in aerospace technologies[162, 163].

Interaction of ionic liquids with dyes

The relationship between dyes and ionic liquids (ILs) has gained significant interest lately due to the distinct physicochemical characteristics of ILs, including low vapor pressure, excellent thermal stability, adjustable polarity, and high ionic conductivity. These qualities render ILs remarkable solvents and media for the solubilization, stabilization, and modification of dyes[164, 165]. Several factors influence the interaction of dyes with ILs, primarily the chemical structure of the dye (particularly the types of chromophores and auxochromes), the composition of the IL's cation-anion pair, and the overall polarity and hydrogen-bonding capacity of the system. ILs can boost the solubility of hydrophobic dyes, shield them from photo-degradation, and affect their spectral behavior by changing the electronic environment surrounding the dye molecules. Surface-active ionic liquids (SAILs), a specific subclass that possesses amphiphilic properties, can create micelle-like structures[166], effectively enclosing dyes and altering their aggregation states[167], which is especially relevant for applications like dye-sensitized solar cells (DSSCs)[168], drug delivery[169], and fluorescence-based sensors[170]. For example, cationic dyes such as methylene blue[171-173] or rhodamine B[174] often show bathochromic or hypsochromic shifts in their absorption and emission spectra depending on the used IL, as the microenvironment created by the IL can affect the electronic transitions of the dye. The anion

significantly contributes to hydrogen bonding or the formation of ion pairs, while the cation affects the π-π interactions and van der Waals forces[175, 176]. Additionally, ILs facilitate the selective extraction and separation of dyes from aqueous solutions due to their affinity for specific types of dyes, making them suitable for environmental clean-up and textile wastewater treatment[177-179]. These interactions can be more than physical; ILs can occasionally form chemical bonds or engage in ion-exchange reactions with dyes, resulting in modified reactivity or photophysical characteristics. The application of ILs in dye chemistry also opens opportunities for the development of task-specific ILs that can improve dye performance in various industrial applications like printing inks, electrochemical sensors, and catalysis. Furthermore, researchers have utilized computational methods and spectroscopic techniques such as UV-Vis, FTIR, NMR, and fluorescence spectroscopy to delve into these interactions, providing insights into solvation dynamics, aggregation trends, and excited-state stabilization. Consequently, the interaction between ionic liquids and dyes offers a flexible and adjustable platform for enhancing dye applications across scientific and industrial fields, merging principles of green chemistry with functional material design.

Aggregation of Surfactants:

The primary characteristic of surfactants and the surface-active ionic liquids (SAILs) is their ability to self-aggregate in solution[180, 181]. To avoid unfavorable interactions with polar solvents, the hydrophobic regions of surfactants can create favorable interactions among themselves in the bulk phase. This leads to the establishment of structures where the hydrophobic tails (Figure 19A) come together to form an oil-like core while the hydrophilic heads remain exposed to the polar surroundings. Micelles represent a specific form of surfactant self-assembly, which can vary in size (Figure 19B). The concentration at which micelles begin to form is referred to as the Critical Micelle Concentration (CMC). In the micellization process, there is a dynamic equilibrium between free surfactant molecules and micelles[182].

Micelles fall into the category of colloidal dimensions.[183] Despite facing severe criticism from a group of scientists at a Royal Society meeting in London at the time, it was later validated by scientific research that surfactants can effectively aggregate in solution, as evidenced by their exceptional detergent properties, which enable them to dissolve dirt by reaching its hydrophobic core effortlessly. Additionally, electrostatic and van der Waals forces play crucial

roles in the formation of ionic surfactants, as they bind counterions to the oppositely charged heads of micelles, thereby neutralizing the charge and inducing repulsion between the head groups[184]. The primary driving force behind the formation of micelles is hydrophobic interactions among the tails. The micellization process is significantly affected by a positive contribution to entropy, as the increase in entropy from the free water molecules that were once "trapped" within the solvation cage around surfactant monomers due to hydrogen bonding surpasses the entropy lost from the aggregation of surfactant monomers. Essentially, the term CMC refers to a range of surfactant concentrations rather than an exact concentration, which is described as "inexact" yet "convenient." Micelles can take on various shapes that depend on the surfactant makeup and the microenvironments.

In a solution where a non-polar solvent (like alkanes, haloalkanes, aromatic solvents, etc.) predominates over polar solvents, reverse micelles can form in a manner akin to water droplets in an oil system[185]. Surfactants aid in stabilizing the components of the solution while the amphiphiles aggregate. This method has led to the creation of a type of microemulsion. In a reverse micelle (Figure 19C), the hydrophobic parts are oriented outward towards the non-polar solvents. In contrast, the polar head groups are oriented towards the inner micellar core, known as the "Water pool," surrounding the water molecules. Reverse micelles are at the nanoscale, and increasing the amount of water in a solution will lead to larger micelles. These reverse micelle water pools are utilized for solubilizing proteins and in the production of nanomaterials.

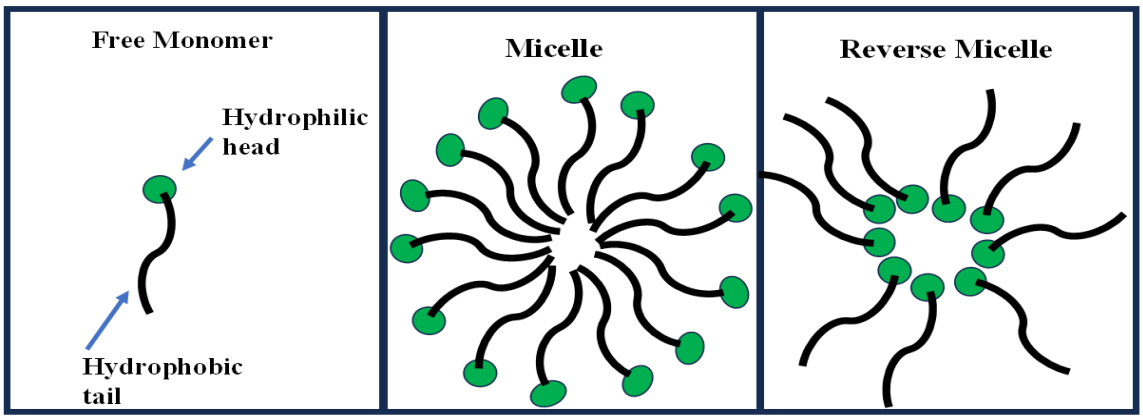

Figure 19. Aggregates of surfactants in solution: (A) free monomer, (B) normal micelle (spherical structure), (C) reverse micelle.

Determination of CMC:

The primary feature of surfactants is their CMC values. Literature provides various quantitative methods for calculating CMC. For instance, Mukerjee and Mysels identified 71 possible methods through their literature review[186] and have critically evaluated each one. The appropriate method will depend on multiple factors, including the preferences of the researcher, the available instruments, and the intended application of the methodology. Techniques such as conductometry, tensiometry, viscometry, vapor pressure osmometry, turbidimetry, light scattering, fluorimetry (including steady state, steady state anisotropy, and time-resolved fluorimetry), calorimetry, spectrophotometry, and magnetic resonance can all be utilized to determine CMC. Among these, conductometry, fluorimetry, and tensiometry are the most commonly used methods. Conductometry is restricted to ionic surfactants. Various methods are employed to assess the physical properties of surfactants in solution, and changes in surfactant concentration lead to different characteristics in the resulting plots in distinct ways.

Each physical property shows distinct breaks known as CMC, which are indicated by the dotted white line. Since CMC can vary based on the method used, it is important to note that it represents not just a single point but a narrow range, shown by a second bracket with a short bar. After the CMC, large assemblies are clearly evidenced by a notable rise in scattering radiation beyond the CMC as measured by the light scattering technique, since this scattering effect relies on the size of the scattering units present in the solution. Following an investigation into the self-diffusion of monomers, post-CMC through nuclear magnetic resonance (NMR) analysis, another important demonstration of the density of surfactant monomers within micelles has been established.

Micellar characteristics:

Structures, Shapes, Microenvironment, and properties of micelles:

In 1936, Hartley proposed the fascinating notion that micelles predominantly adopt a spherical configuration[187]. This viewpoint is consistent with the core principles introduced by McBain in 1920. Hartley suggested that these spherical micelles are composed of roughly 50 to 100 monomers, which aggregate within a relatively limited concentration range. The total diameter of these clusters of monomers is estimated to be approximately double the length of the hydrocarbon chains that make up their structure. Inside micelles, the core is mainly hydrophobic, effectively protecting water-soluble components from the surrounding aqueous environment. The hydrophilic head groups of the surfactants interact with counterions, forming

a barrier that inhibits these head groups from getting too close to each other due to their repelling like charges. This ionic surfactant system exhibits several characteristics that are well aligned with Hartley's classical micelle model[188]. Ionic micelles create an electrical double layer because of their intrinsic surface charge and zeta potential, allowing them to display electrophoresis when placed in an electric field. The head groups of ionic micelles, along with oppositely charged counterions, create a "Stern layer" through electrostatic interactions. Surrounding this stern layer is the "Gouy Chapman layer," which establishes a diffuse boundary around the stern layer. Collectively, these layers are capable of releasing free monomers, counterions, and water molecules, which further aid in the solvation of micelles through ion-dipole interactions. The expression "electrical double layer" includes both the "Stern layer" and the "Gouy Chapman layer," as shown in Figure 20. The hydrophobic core of the micelle lies within the stern layer. The kinetic characteristics of micelles comprise both the core and the stern layer.

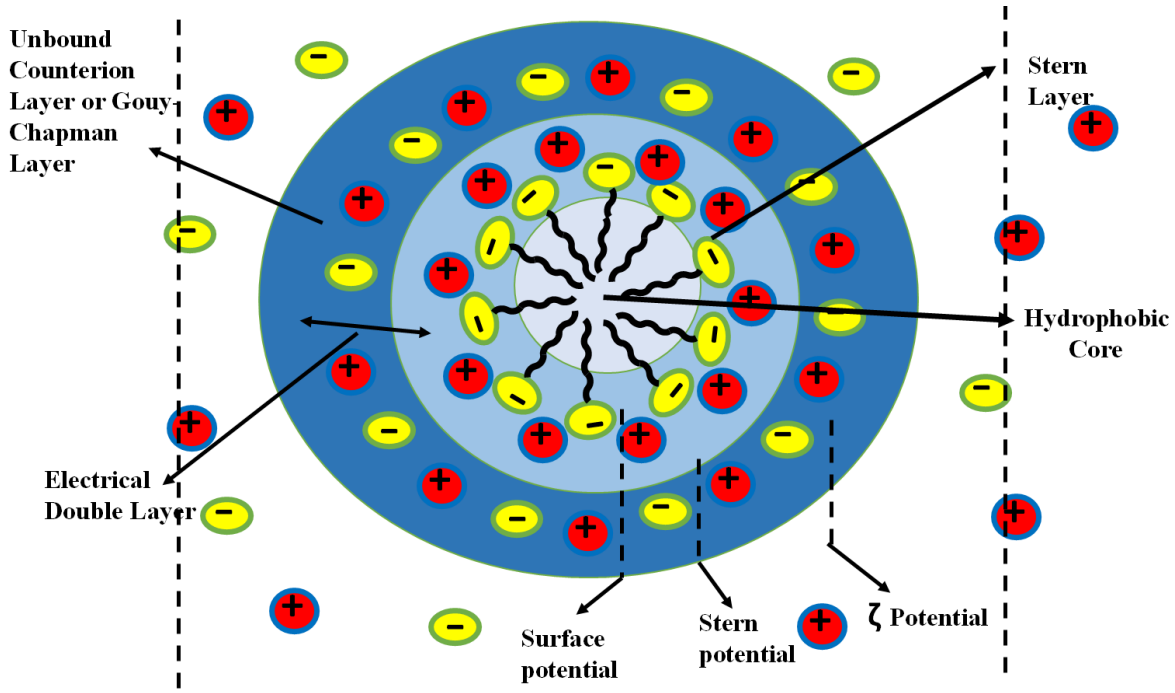

Figure 20. Schematic representation of ionic micelles demonstrating counterion binding, charge neutralization, micellar core, and electrical double layer, assuming spherical symmetry of the micelle.

The diffuse layer, commonly referred to as the Gouy Chapman layer, functions as a boundary or slipping plane that can adjust in accordance with the movement of the micelle in solution. The zeta potential (μ), a metric frequently used to assess the stability of colloidal dispersions, represents the potential at the slipping plane, as depicted in Figure 20. A micellar solution is

deemed stable when the absolute value of the zeta potential surpasses ± 30 mV[189]. For non-ionic micelles, several water molecules can infiltrate the core through hydrogen bonding interactions with polyethylene oxide groups located near the micelles' head groups, an area known as the palisade layer. Recent scientific developments have offered a more refined and complex understanding of micelles, expanding upon Hartley's original idea. Consequently, it has become evident that micelles are not static structures; instead, they are dynamic entities where molecules can rapidly shift between the solution phase and the micelle phase. When using high-resolution imaging methods, or when the molecular motion is captured in a frozen state, micelles appear as irregular molecular clusters instead of smooth, perfectly uniform shapes. Hartley's straightforward "two-state" spherical micellar model has faced criticism for its inadequacy in effectively explaining various experimental results. In investigating the solubilization of non-polar compounds within micelles, Menger presented a notably different molecular model known as the "porous cluster" model. This model indicates that water molecules can penetrate into the micelle up to a certain limit: generally about 3 to 4 methylene carbon atoms past the head group suggest that the micellar core is comparatively small and more accessible than previously thought, as demonstrated by NMR and fluorescence studies. Additional structural variations of micelles have been suggested, such as Debye's rod-like micelle[190], spherical bilayers or vesicles, worm-like formations, ellipsoidal shapes, disk-like or cylindrical structures, and the lamellar configuration described by Philippoff[191]. To distinguish among the varied supramolecular assemblies that form in solution, Israelachvili and colleagues introduced the packing parameter concept[192]. The amphiphile packing parameter (P) for micelles can be computed using a specific equation, offering insights into the micellar structure and behavior.

$$P = \frac{V}{A_{min} \times l_c} \qquad (1)$$

l_C is the maximum effective length of a hydrophobic chain of an amphiphile (nm), and v is the volume of the hydrophobic chain (nm^3), assuming it is incompressible. A_{min} is the headgroup's surface area (nm^2/molecule) at the micellar-solution interface. Tanford's formula is used to determine the effective length and volume of the hydrophobic chain in pure amphiphiles. N_c denotes the number of carbon atoms in the hydrophobic chain.

$l_c \leq l_{max} \approx (0.154 + 0.126\, n_c)$ nm and $v = (0.0274 + 0.0269 n_c)$ nm^3 (2)

where l_{max} is the maximum length of the monomer chain.

Packing parameter values for different aggregates are tabulated as follows:

Aggregates	P
Micelles	< 1/3
Non-spherical aggregates	1/3 < P < ½
Bilayers and vesicles	1/2 < P <1
Inverted aggregates	>1

Some aggregated molecular geometries are shown in Figure 21.

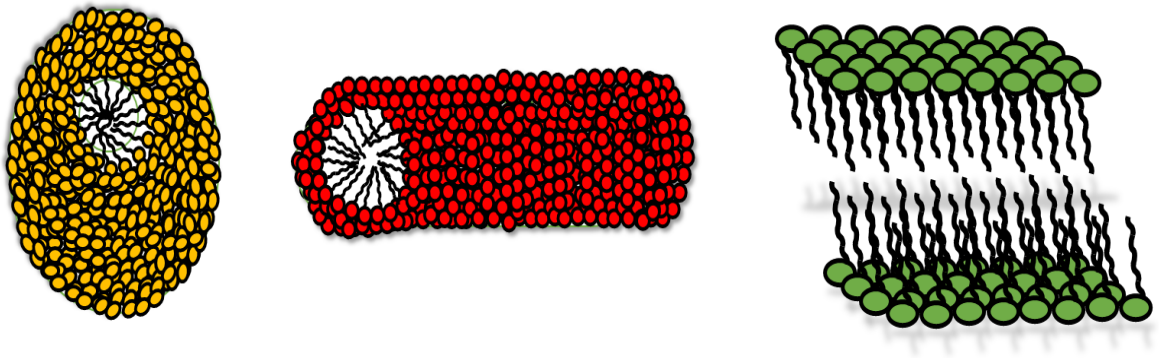

A **B** **C**

Figure 21. Schematic representation of geometrical forms of aggregates. A: spherical micelle; B: lamellar or bilayer arrangement; C: rodlike micelle.

Recent technological advancements have greatly improved our capacity to collect experimental data and visual proof concerning different types of micelles[193]. By representing micelles as spherical structures and considering their size distribution, the dynamic light scattering (DLS) method enables us to examine micellar properties such as the average hydrodynamic diameter and diffusivity. This technique provides direct insights into micelle behavior, although it does not disclose their exact structural forms. Alongside DLS, various other advanced techniques can be utilized to investigate micellar properties. Static light scattering (SLS), small angle neutron scattering (SANS), small angle X-ray scattering (SAXS), cryo-transmission electron microscopy (cryo-TEM), and atomic force microscopy (AFM) are all effective tools for estimating the dimensions and shapes of micelles. Among these methods, cryo-TEM is unique in its ability to differentiate between linear and branched micelles. Notably, the shape of micelles can undergo significant changes when exposed to different inorganic and organic salts. For example, sodium dodecyl sulfate micelles can shift from spherical to cylindrical forms when placed in concentrated sodium chloride solutions. Similarly, in case of micelles created

from sodium alkylbenzenesulfonate, transition is possible from spherical to cylindrical shapes, and at higher salt concentrations, they may further evolve into multilamellar vesicles. Additionally, micelles of cetyl trimethyl ammonium bromide and cetyl pyridinium chloride can transform into wormlike structures, illustrating the adaptable nature of micellar configurations influenced by their surroundings.

Aggregation number:

The aggregation number (n) refers to the total number of molecules that come together during the formation of micelles. Debye proposed a traditional method to determine the aggregation number that involved measuring elastic light scattering.[194] This involved assessing the intensity of scattered light at various angles, both below and above the CMC, to ascertain the average aggregation number as well as the molecular weight (MW) of the aggregates. Another method for measuring the aggregation number and hydrodynamic diameter is laser light scattering.[195] A significant technique that remains widely utilized today is the fluorescence quenching of a fluorescent probe by a hydrophobic quencher. The arrangement of the probe and quencher within micelles adheres to Poisson statistics; considering a probe located inside a micelle that is primarily quenched by a given quencher. Surfactant solutions were created above their CMC, maintaining fixed probe concentrations in both the quencher and the micellar solution. The ratios of [probe] to [micelles] and [quencher] to [micelles] were kept low enough to ensure Poisson distribution. Both the probe and the quencher should be selected to ensure that they reside either within the micellar cores or at their surfaces. The fluorescence technique employs probes to not only interact with the micellar system, yielding insights into the aggregation level, but also to assess the polarity of the micellar core, its surrounding environment, and the relationship between substrate and micelle interactions. Pyrene, anthracene sulphonate, safranine-T, fluorescein, and similar probes are commonly used to evaluate the mean aggregation number, while quenchers like cetylpyridinium chloride, dodecyl pyridinium chloride, thiourea, and inorganic complexes of Ru^{2+}, Cu^{2+}, and Ni^{2+} have been employed as well. The mean aggregation number can be calculated using both steady-state and time-resolved fluorescence methods[196], depending on whether the quenching mechanism is static or dynamic.

Static quenching:

This quenching occurs due to the formation of a non-fluorescent ground-state complex between the fluorophore and quencher. Because the complex does not absorb at the emission

wavelength, the apparent fluorescence decreases. The Stern–Volmer relation for static quenching[197] is:

$$\frac{F_0}{F} = 1 + K_a[Q] \quad (3)$$

where F_0 and F are the fluorescence intensities of the probe in the absence and in the presence of quencher molecules, respectively; K_a is the association constant between the fluorophore and the quencher complex, and [Q] is the concentration of the quencher (surfactant).

Characteristics of Static Quenching:

• Temperature dependence: The efficiency of quenching decreases with temperature as the complex dissociates.

• Lifetime change: The fluorescence lifetime remains unchanged since the complex does not fluoresce.

• Changes in the absorption spectrum occur due to new ground-state species.

The static quenching method is frequently used (in which it is presumed that an increase in quencher concentration may reduce the emission of the probe located on the micelle, without affecting its lifetime), employing the following relation.

$$ln\ \frac{F}{F_0} = \frac{n\,[Q]}{[Surfactant] - CMC} \quad (4)$$

Where F and F_0 represent the fluorescence intensities with and without the quencher. [Surfactant] denotes the total surfactant concentration, [Q] indicates the quencher concentration, and n refers to the average aggregation number at the CMC. A plot of ln (F/F_0) against [Q] easily provides the value of n from the slope.

Dynamic (Collisional) Quenching

Dynamic quenching happens when an excited fluorophore loses energy non-radiatively through interactions with a quencher molecule during its excited state. The likelihood of quenching is related to the frequency of these encounters, which in turn depends on factors such as diffusion rates, the concentration of the quencher, and temperature.

The Stern–Volmer equation for dynamic quenching is:

$$\frac{F_0}{F} = 1 + K_{sv}[Q], \text{ where } K_{SV} = K_Q\,\tau_0 \quad (5)$$

here, F_0 and F are the fluorescence intensities of the probe in the absence and presence of quencher molecules, respectively; K_{SV} is the Stern-Volmer quenching constant, K_Q is the bimolecular quenching rate constant, τ_0 indicates lifetime of the fluorophore in the absence of the quencher and [Q] is the concentration of the quencher (surfactant).

Characteristics of Dynamic Quenching:

- Temperature dependence: Quenching efficiency increases with temperature (faster diffusion).
- Lifetime change: Both fluorescence intensity and lifetime decrease proportionally.
- No change in absorption spectrum (no ground-state complex formation).

$\frac{F_0}{F}$ vs. [Q] has been plotted, and a graph showing a curved pattern with upward curvature. This leads to the inference of a simultaneous static and dynamic quenching, and the modified Stern-Volmer equation[198] has been introduced for those systems. The equation is as follows,

$$log\left(\frac{F_0-F}{F}\right) = \log K + \mathrm{n}\log[surfactant] \qquad (6)$$

where F_0 and F are the fluorescence intensities in the absence and presence of quencher, respectively, K is the binding constant, and n stands for the binding site.

However, in the plotting of $log\left(\frac{F_0-F}{F}\right)$ vs. [surfactant], a straight line is obtained. The value of the binding constant and the binding site have been calculated accordingly.

When quenching occurs in a dynamic manner, it means that the lifetime of a probe is affected by an increase in the concentration of a quencher, which coincides with a noticeable decrease in fluorescence intensity. In this context, the previously mentioned equation yields an inaccurate representation of amalgamation number values. This discrepancy is particularly evident in systems characterized by relatively high microviscosity and lower aggregation numbers. In such cases, the mean aggregation number determined through steady-state measurements is observed to be lower than predictions made using time-resolved techniques. Furthermore, the behavior of a probe that is free and not associated with the micelles contrasts sharply with that of a micelle-soluble probe when an "immobile" quencher is present. The fluorescence decay curve for the micelle-soluble probe displays a distinctly different pattern compared to the free probe. For this fluorescence decay curve in the presence of a quencher, a

specific equation can be employed, tailored to capture the unique dynamics at play in this scenario.

$$I_t = I_0\{-t/\tau_0 - R[1-\exp(-k_Q t)]\}c \quad (7)$$

I_t and I_0 are the fluorescence intensities at time t and zero, respectively. k_Q is the first-order quenching rate constant. τ_0 is the lifetime of a probe in the absence of a quencher. R can be written as,

$$R = \frac{[Q]}{[Micelle]} \quad (8)$$

[Micelle] is the concentration of micelles. R values are adjusted close to 1 and not exceeded by 2 for theoretical consideration. Taking the value of R, the average aggregation number (n) can be calculated at a particular quencher concentration $[Q]$ using the following relation:

$$n = R\,\frac{([Surf] - CMC)}{[Q]} \quad (9)$$

The light scattering experiment tends to provide an inflated estimate of the mass and, consequently, the volume of micelles due to the effects of solvation and the binding of counter-ions to the micelles themselves. To accurately assess the extent of solvation and counter-ion binding, a comparative analysis of light scattering and fluorescence studies can be quite effective. Furthermore, a variety of internal and external factors can significantly impact both the size and dispersity of micelles, contributing to the complexity of their characterization.

Internal factors:

A homologous series of surfactants characterized by longer hydrocarbon chains exhibits an increasing trend in their aggregation numbers. Recent research indicates that for each carbon atom that is transformed into an alkyl group, the micelle aggregation number increases linearly, typically by approximately 16 monomers for each micelle formed. In contrast, a decrease in the hydrophilicity of the head group—manifested through a greater degree of ion binding or a reduction in the length of the polyoxyethylene group—leads to a rise in the aggregation number (n).

Tanford's studies have projected that for spherical and ellipsoid micellar structures within a specific ellipticity range, the micellar aggregation number reaches its peak for a given alkyne chain length[193].

At a temperature of 298.15 K in an aqueous solution, it has been observed that when the spacer

length of gemini surfactants is increased from 2 to 12, the aggregation number dramatically decreases from about 48 to just 11. This indicates that increasing the effective size of the head group—particularly when head groups are relatively bulky—contributes to a reduction in the aggregation number[199].

Interestingly, bile salt micelles tend to aggregate at lower aggregation numbers, typically ranging from 4 to 10[200, 201]. Meanwhile, cationic surfactants in an aqueous environment demonstrate a broader range of aggregation numbers[202], falling between 20 and 100.

External factors:

The aggregation number of surfactant micelles tends to decrease as the salinity of the surrounding medium increases. Interestingly, however, when the concentration of salt is elevated or the pH level is increased, the micellar aggregation number becomes greater than what is observed in pure aqueous solutions[203]. This phenomenon occurs because these specific conditions help to screen the electrostatic repulsion between the head group charges of surfactant monomers, particularly those located in the stern layer. When examining the impact of temperature on ionic surfactants, we find that their aggregation numbers experience minimal reduction. In contrast, for non-ionic surfactants, an intriguing behavior known as the "cloud point" phenomenon takes place, leading to a significant rise in their aggregation numbers as temperature changes. Additionally, the size of micelles tends to increase when small amounts of poorly soluble, non-amphiphilic organic compounds are introduced into the system. However, this increase in size is likely more attributable to the process of solubilization rather than an actual rise in the number of surfactant molecules incorporated within the micelle structure.

Degree of counterion binding*:* The key constituents of micelles are counterions, which play a critical role in the structure of the micelles' stern layer[204, 205]. The behavior of the electrical double layer and the calculation of thermodynamic parameters related to the micellization process are significantly influenced by the extent of counterion binding. This degree of binding can fluctuate anywhere from 20% to 80%, depending on various factors, such as, the type of amphiphiles used, the characteristics of the solution media, and the presence of various additives[206]. To quantify counterion binding, several methods can be employed with conductometry being the most prevalent technique.

At lower concentrations of surfactants, both free surfactant monomers and counterions contribute to the overall specific conductance—a measure of how well the solution conducts

electricity. As the concentration of surfactants increases, the specific conductance also rises consistently.

However, once micellization occurs, a notable shift takes place. Some counterions begin to associate with the newly formed micelles, increasing their size and decreasing their mobility. This process results in a reduced number of free monomers and unbound counterions remaining in the solution, which is the primary factor that affects specific conductance values. Consequently, these values become offset, reflecting the presence of bound counterions in the micelles. The conductometric behavior reveals two distinct slopes (labeled S_1 and S_2) of varying magnitudes, representing different phases of the surfactant behavior in the solution. These slopes can be utilized in a straightforward mathematical relationship to effectively determine the degree of dissociation (β), offering valuable insights into the micellization process and its thermodynamics.

The degree of dissociation (β) can be calculated by using the following equation,

$$\beta = \frac{S_2}{S_1} \quad (10)$$

where S_2 and S_1 are the post-micellar and pre-micellar slopes, respectively.

The Gibbs free energy (ΔG) can be determined by using the equation[207]

$$\Delta G = (2 - \beta)\, RT\, ln\, CMC \quad (11)$$

where R and T are the universal gas constant and temperature in the Kelvin scale, the binding constant (K) has been determined by using the following formula.

$$\Delta G = - RT \ln K \quad (12)$$

Despite some assumptions, this method works quite well, and the allowable error range (about 2-3%) covers the uncertainty of the degree of counterion binding.

Thermodynamics of micellization

Micellization is a process that is significantly influenced by various thermodynamic factors. During micellization, the so-called iceberg structure formed between surfactant monomers and the surrounding aqueous environment disintegrates, leading to an increase in entropy. However, two primary models have been utilized to describe micellization: [i] the mass action model[208] and [ii] the phase separation model[209], also known as the pseudo-phase model.

In the mass action model, after reaching the CMC, the monomers and micelles behave independently with regard to any further increase in monomer concentration and vice versa, as illustrated by the following equilibrium

$$nS \leftrightarrow S \text{ or } M \quad (13)$$

For a non-ionic surfactant, S, S_n, n, and K_M denote surfactant monomers, micelles, aggregation number, and equilibrium micellization constant, respectively.

In the case of ionic surfactants, studying micellization reveals a new equilibrium that incorporates both the charges and the counterions:

$$nS^{\pm} + mZ^{\mp} KM \leftrightarrow (SnZm)^{\pm(n-m)} \text{ or } M^{\pm(n-m)} \quad (14)$$

for an ionic surfactant, where $Z^{\pm}$ and m denote counterions and the number of counterions attached to the micelle in the above equilibrium process.

Consequently, it can be expressed in the following manner for nonionic substances, while disregarding the impact of activity coefficients,

$$K_M = \frac{a_M}{a_S^n} \approx \frac{C_M}{C_S^n} \quad (15)$$

where a is the activity coefficient and C is the concentration.

For ionic surfactants,

$$K_M = \frac{a_M^{\pm(n-m)}}{a_{s\pm}^n a_{z\pm}^m} \approx \frac{C_M^{\pm(n-m)}}{C_{s\pm}^n C_{Z\pm}^m} \quad (16)$$

In the case of nonionic surfactants, we can express the standard Gibbs free energy of micellization using the following relationship:

$$\Delta G_M^0 = -RT \ln K_M = -RT \ln C_M + nRT \ln C_S \quad (17)$$

The standard Gibbs free energy change of micellization per monomeric unit (n) can be expressed as:

$$\frac{\Delta G_M^0}{n} = \Delta G_{mic}^0 = -\frac{RT}{n} \ln C_M + RT \ln C_S \quad (18)$$

At CMC, the percentage of monomers forms micelles, which are very small. Hence, the eq. 18 can be approximated as:

$$\Delta G_M^0 = RT \ln C_S = RT \ln CMC \quad (19)$$

For ionic surfactants,

$$\Delta G_M^0 = -RT \ln K_M = -RT \ln C_M^{\pm(n-m)} + nRT \ln C_S^{\pm} + mRT \ln C_Z^{\pm} \quad (20)$$

Therefore, it can be written as standard Gibbs free energy change per monomeric unit in the following form:

$$\frac{\Delta G_M^0}{n} = \Delta G_{mic}^0 = -\frac{RT}{n} \ln C_M^{\pm(n-m)} + RT \ln C_S^{\pm} + \frac{m}{n} RT \ln C_Z^{\pm} \quad (21)$$

Again, as the percentage of monomers is very small and usually n is large, the eq. 18 is transformed as

$$\Delta G_{mic}^0 = RT \ln C_S^{\pm} + \frac{m}{n} RT \ln C_Z^{\pm} \quad (22)$$

For normal ionizable surfactants, it can be written as

$$C_S^{\pm} = C_Z^{\pm} \quad (23)$$

Therefore, at CMC,

$$C_S^{\pm} = C_Z^{\pm} = CMC \quad (24)$$

So that, $\Delta G_{mic}^0 = \left(1 + \frac{m}{n}\right) RTlnCMC = (1 + g)RTlnCMC$ (25)

where g is the fraction or degree of counterion binding.

If g = 0, there is no counterion binding in the case of a non-ionic surfactant.

Therefore, the equations become,

$$\Delta G_{mic}^0 = RT \ln CMC \quad (26)$$

On the other hand, if 100% counterion binding is found, then, g= 1 and the equation becomes

$$\Delta G_{mic}^0 = 2RT \ln CMC \quad (27)$$

The previously mentioned relationship operates under the assumption of a constant aggregation number (n) along with several established approximations. The pseudophase model points that micelles, which are clusters of surfactant molecules, form a distinct phase when the concentration of surfactants reaches or exceeds the CMC. In this state, the concentration of free monomers in solution remains unchanged, even as micelles coexist.

According to the pseudophase model, we can express the following equilibrium that illustrates the phase equilibrium involved:

Monomer ↔ Micelle (pseudophase)

This equilibrium highlights the dynamic between individual surfactant molecules and the micelles they form, particularly in conditions that meet or surpass the CMC threshold.

At a constant temperature, the chemical potential of free surfactant monomers (μ_S) in solution is equal to the chemical potential of surfactant monomers in the pseudo micellar phase ($\mu_S^{micelle}$).

Thus, for a nonionic surfactant, $\mu_s = \mu_s^{Micelle}\ or\ \mu_m$ (28)

The equation can be written for a non-ionic surfactant,

$$\mu_s^0 + RT\ ln\ a_s = \mu_m^0 + RT\ ln\ a_m \quad (29)$$

Or, $$\Delta G_m^0 = \mu_m^0 - \mu_s^0 = RT\ ln\ a_s \approx RT\ ln\ CMC \quad (30)$$

Since a_m (activity of micelle, considering it as a separate pure phase or pseudo phase) = 1,

In the case of an ionic surfactant,

$$\mu_s^{\pm} + \frac{m}{n}\mu_z^{\pm} = \mu_m^{\pm} \quad (31)$$

as, $\mu_s = \mu_m$

Therefore, the equation will be transformed into

$$\mu_{s\pm}^0 + RT\ ln\ a_s^{\pm} + \frac{m}{n} RT\ ln\ a_z^{\pm} = \mu_{m\pm}^0 + RT\ ln\ a_m^{\pm} \quad (32)$$

Or, $$[\mu_{m\pm}^0 - (\mu_{s\pm}^0 + \frac{m}{n}\mu_{z\pm}^0)] = RT\ ln\ a_s^{\pm} + \frac{m}{n} RT\ ln\ a_z^{\pm} - RT\ ln\ a_m^{\pm} \quad (33)$$

Hence, $$\Delta G_m^0 = RT\ ln\ a_s^{\pm} + \frac{m}{n} RT\ ln\ a_z^{\pm} - RT\ ln\ a_m^{\pm} \quad (34)$$

Science, $a_m^{\pm} = 1$, $$\Delta G_m^0 = RT\ ln\ a_s^{\pm} + \frac{m}{n} RT\ ln\ a_z^{\pm} = (1 + \frac{m}{n})\ RT\ ln\ CMC \quad (35)$$

Or, $$\Delta G_m^0 = (1 + g)\ RT\ ln\ CMC \quad (36)$$

In the equations [33] to [35], $\mu_m^{\pm}$ is actually $\mu_m^{\pm(n-m)}$; the factor (n-m) has been neglected for simplicity.

The same equation for ΔG_m^0 is obtained from the pseudophase model like that from mass action model. μ_s^0 and μ_m^0 are the standard chemical potentials of monomer and micelle respectively, and, a_S and a_M are the activities for the same respectively. Here, it is noted that, for the above two methods, the equilibrium concentration of free monomer (C_S) is considered to be equivalent to CMC.

In the case of the mass action model, including the contribution of aggregation number (n), standard Gibbs free energy of micellization (ΔG_{mic}^0) and standard enthalpy of micellization (ΔH_{mic}^0) can be expressed by,

$$\Delta G_{mic}^0 = (1+g)\, RT\, ln\, X_{CMC} + \frac{RT}{n}\, ln\, [2n(n+m)] \quad (37)$$

$$\text{And, } \Delta H_{mic}^0 = -RT^2[(1+g)\frac{d\, ln\, X_{CMC}}{dT} + ln\, X_{CMC}\, \frac{dG}{dT} + \frac{d[(\frac{1}{n})\, ln\{2n(n+m)\}v]}{dT}] \quad (38)$$

CMC has been expressed in mole fraction (X_{CMC}) unit in the above two equations. Here, g is the number of counterions binding, and n is the aggregation number. Usually, the second and third terms of equations [37] and [38] are small. In the pseudophase model, the terms can be conceptually avoided.

Thus, for ionic micelles,

$$\Delta H_{mic}^0 = -RT^2\, [(1+g)\, \frac{d\, ln\, X_{CMC}}{dT} + ln\, X_{CMC}\, \frac{dG}{dT} \quad (39)$$

and for nonionic micelles,

$$\Delta H_{mic}^0 = RT^2\, \frac{d\, ln\, X_{CMC}}{dT} \quad (40)$$

Entropy of micellization (ΔS_{mic}^0) can be calculated from the Gibbs-Helmholtz equation,

$$\Delta S_{mic}^0 = \frac{\Delta H_{mic}^0 - \Delta G_{mic}^0}{T} \quad (41)$$

The CMC should be assessed at various temperatures to determine ΔH_{mic}^0 and ΔS_{mic}^0 using equations 38 to 41, depending on the specific system. Typically, ΔS_{mic}^0 values are positive. The negative entropy contributions from the amphiphilic association in micelles or the solvation of monomers are outweighed by the disruption of the hydration shell surrounding the monomers, causing their incorporation into micelles, which ultimately increases overall entropy.

It is important to note that for the calculation of thermodynamic parameters, CMC should be expressed in mole fraction units (as previously mentioned). The van't Hoff method is utilized

for calculating the standard enthalpy of micellization (ΔH_{mic}^{0}) by measuring CMC values at various temperatures using equation 38. With the isothermal titration calorimetry (ITC) technique, both CMC and ΔH_{mic}^{0} can be measured directly. The enthalpy values obtained through the calorimetry method provide precise measurements with a high level of accuracy. Enthalpies derived from the van't Hoff method (by measuring CMC at different temperatures) usually differ from those obtained directly, particularly for ionic surfactants. Neither the mass action model nor the pseudophase model for surfactant micellization is entirely accurate. Both models assume that the equilibrium free monomer concentration during the micellization process equals to CMC. It is also a common assumption that the aggregation number and the extent of counterion binding remain independent of temperature, or at least consistent within the 25 °C temperature range studied. Despite these limitations, these two models are the most straightforward methods for determining thermodynamic properties.

In addition to the two previously discussed models, there exists a diverse array of alternative approaches in the field of thermodynamics as applied to small systems. One notable contribution comes from Hill, who developed a comprehensive thermodynamic model specifically designed for small-scale systems[210]. This model was later adapted by Hall and Pethica for applications involving nonionized and noninteracting systems, enhancing its relevance and utility. Expanding on this foundation, Hall has provided an extensive examination of a multicomponent system characterized by interacting aggregates. This work delves into the complexities of how different components within a system interact, thereby influencing the overall thermodynamic behavior. Another significant approach was introduced by Corkill and his colleagues, who proposed a distinct thermodynamic strategy tailored specifically for non-ionic surfactant systems[211, 212]. Their work adds valuable insights into the behavior of surfactants, which play a crucial role in various industrial and biological processes. Tanford introduced a compelling concept regarding the formation of micelles, focusing on the structural aspects that govern micelle production[199, 213]. His ideas laid the groundwork for further exploration into the geometric parameters[214] influencing micellar behavior. This geometrical approach was subsequently expanded upon by the research of Israelachvili and his colleagues, who provided deeper insights into the molecular interactions at play[215, 216]. Ruckenstein and Nagarajan further built upon these findings, investigating the nuanced effects of micelle structure and behavior in greater detail[181, 217].

Despite the advancements in understanding thermodynamic parameters associated with micellization and surfactant behavior, accurately determining these parameters remains a

challenge. This difficulty arises from a variety of factors that complicate the analysis, including fluctuations in aggregation number, variations in micellar shape and size, counterion condensation effects, changes in micellar solvation driven by temperature shifts, and other environmental influences. Given the complexity and importance of these factors, it is clear that this area of study warrants further research to refine our understanding and improve the precision of thermodynamic measurements in these systems.

Scope and objective of the present work

The studies examine the complex interactions between various dyes and surfactants or surface-active ionic liquids (SAILs) in aqueous media. The aim is to understand their aggregation behavior, spectroscopic responses, micellization mechanisms, and potential applications in fields such as drug delivery, medicinal photosensitization, material fabrication, and wastewater treatment. Each study focuses on a different dye and investigates its interactions with surfactants of varying charge characteristics. A combination of experimental techniques—such as UV-visible spectroscopy, fluorescence spectroscopy, time-correlated single-photon counting (TCSPC), dynamic light scattering (DLS), zeta potential measurement, and density functional theory (DFT) calculations—is employed to provide a comprehensive molecular-level understanding of dye-surfactant or dye-SAIL interactions.

Acridine red (AR), a cationic azo dye with unique photophysical properties, is used with three amphiphilic systems: anionic sodium dodecyl sulfate (SDS), which is a conventional surfactant, and two surface-active ionic liquids (SAILs), BMImOS (an ionic liquid with an imidazolium cation and an octyl sulfate tail) and BMImBr (an imidazolium-based ionic liquid without a hydrophobic tail). The main objective is to compare the aggregation behavior and solubilization efficiency of a traditional surfactant (SDS) with those of SAILs. The study investigates how the presence or absence of hydrophobic components in these amphiphiles influences the micellization process and the encapsulation of the dye. The findings indicate that BMImOS exhibits superior solubilizing power due to its imidazolium cation and hydrophobic tail, which reduce repulsion between head groups and promote the incorporation of AR, even at concentrations below the CMC. This conclusion is supported by shifts in absorption and fluorescence spectra, increased lifetime measurements obtained from TCSPC, and changes in anisotropy values. In contrast, BMImBr, which lacks a hydrophobic chain, does not effectively solubilize AR and instead forms only salt-like ion pairs. Density functional theory (DFT) and time-dependent DFT (TDDFT) calculations further validate the observed phenomena, showing

favorable overlap between the highest occupied molecular orbital (HOMO) and the lowest unoccupied molecular orbital (LUMO) and indicating electrostatic charge transfer interactions. Overall, the study demonstrates that SAILs have enhanced capabilities compared to conventional surfactants in encapsulating dyes and altering their spectral properties, with potential applications in photosensitization, drug delivery, and advanced material fabrication.

Eosin Y (EY), an anionic dye, interacts with the four surfactants: CTAC (cationic), SLAS and NaDC (anionic), and a newly synthesized zwitterionic surfactant, C_{12}DmCB. The primary objective is to investigate how the charge of the surfactant head group influences the solubilization, spectral behavior, and stabilization of EY within micellar media. Spectroscopic analyses indicate that the zwitterionic surfactant C_{12}DmCB demonstrates the highest interaction efficiency with EY. This is evidenced by significant bathochromic shifts, an increased average fluorescence lifetime, higher anisotropy, and reduced particle size and zeta potential. The cationic surfactant CTAC also shows favorable interactions with EY, facilitated by electrostatic attraction that allows EY to incorporate into micelles. In contrast, both SLAS and NaDC, which have a similar charge to EY, exhibit poor solubilizing ability due to electrostatic repulsion, resulting in minimal spectral changes. This study highlights the unique advantages of zwitterionic surfactants in stabilizing oppositely charged dye molecules, while avoiding the environmental and toxicity issues often linked to cationic systems. The DFT-optimized structures and energy gaps further support the experimental findings, suggesting that the EY-C_{12}DmCB complex has superior thermodynamic stability. Ultimately, the study aims to demonstrate the superior role of zwitterionic surfactants in dye stabilization, which has important implications for analytical chemistry, bioimaging, dye delivery, and wastewater remediation.

Again, the interaction between Phloxine B (PhB), an anionic xanthene dye with significant biomedical and industrial applications, and three different surfactants: cationic CTAC, anionic SDS, and zwitterionic C_{12}DmCB has been investigated. Utilizing a multi-technique approach, the research demonstrates that C_{12}DmCB exhibits superior solubilization capabilities for PhB compared to CTAC and SDS. Unlike SDS, which shows minimal interaction due to electrostatic repulsion, C_{12}DmCB facilitates the intercalation of PhB into its stern layer at concentrations exceeding the CMC. This is evidenced by increased spectral shifts, longer fluorescence lifetimes and anisotropies, larger micellar sizes, and reduced zeta potentials. The zwitterionic surfactant's combination of positive and negative charge centres minimizes intramolecular repulsion, allowing more monomers to participate in micelle formation.

Conversely, CTAC demonstrates a moderate binding affinity, while SDS is the least interactive due to charge repulsion and a lack of favorable binding sites. DFT results support these findings, revealing the lowest energy gaps in the PhB-C_{12}DmCB system, which confirms its higher stability. The aim of this work is to illustrate how charge distribution and micellar size influence dye solubilization and the stability of micelle-dye interactions. This study is one of the first to report such interactions involving a zwitterionic surfactant, with significant implications for biomedical dye delivery, colorant stabilization in food and drugs, and photosensitization.

Moreover, the investigative study of methylene blue (MB), a commonly used cationic phenothiazine dye, and its interactions with two conventional cationic surfactants—CTAB and CTAT—as well as a surface-active ionic liquid (BMImOS) is performed. Even though MB and these surfactants share the same charge polarity, notable differences in solubilization behavior arise due to the effects of counterions and the properties of the micellar environment. CTAT, which contains a bulky tosylate anion, creates strong ion-pair interactions with MB. This interaction delays micellization but enhances overall binding affinity. In contrast, CTAB, which has smaller bromide ions, demonstrates a lower affinity for MB. Although BMImOS is less interactive overall, it allows MB to partially embed within its micellar stern layer due to electrostatic interactions with its octyl sulfate tail. Spectral analysis indicates no significant bathochromic shifts in the CTAB and CTAT systems, but it suggests partial encapsulation in the BMImOS micelles. This conclusion is supported by zeta potential and anisotropy studies. Observations from conductometric titration and steady-state fluorescence provide binding constants and Gibbs free energy metrics that further corroborate these findings. DFT calculations reveal that the MB-CTAT complex is the most stable configuration, with the Highest Occupied Molecular Orbital (HOMO) localized on the counterion and the Lowest Unoccupied Molecular Orbital (LUMO) on MB, indicating a potential charge transfer interaction. The objective of this research is to uncover how systems with similar charges can still exhibit favorable interactions through counterion-dye affinities, highlighting aspects, such as, micellization delay, dye partitioning, and thermodynamic stability. These insights could be valuable in designing dye delivery systems where charge matching is necessary.

Collectively, these studies systematically explore dye-surfactant and dye-surface-active ionic liquid (SAIL) interactions across various amphiphilic systems. Through detailed experimental and theoretical characterization, they demonstrate how micellar polarity, surfactant head group charge, hydrophobic chain length, and counterion size influence dye solubilization, aggregation

behavior, and spectral modifications. The findings not only enhance our fundamental understanding of micelle-dye interactions, but also pave the way for the strategic design of more efficient micellar systems for industrial and biomedical applications. Notably, SAILs and zwitterionic surfactants have emerged as superior alternatives to traditional surfactants, offering better solubilization, reduced environmental toxicity, and greater structural tunability. The incorporation of DFT and Time-Dependent DFT (TDDFT) studies into these four works provides molecular-level insights that reinforce the experimental observations, creating a predictive framework for the design of future dye-surfactant systems. The results are set to impact a wide range of fields, including drug delivery, biosensing, material science, solar energy harvesting, wastewater treatment, and photodynamic therapy. In summary, these studies significantly enhance our understanding of how amphiphilic systems interact with dyes, whether they are similarly charged or oppositely charged, and they offer a blueprint for developing intelligent, sustainable micellar systems tailored for specific applications across chemistry, biology, and materials science.

REFERENCES:

(1) Pedraza, A.; Sicilia, M. D.; Rubio, S.; Pérez-Bendito, D. Surfactant–dye binding degree method for the determination of amphiphilic drugs. *Analytica Chimica Acta* **2004**, *522* (1), 89-97.

(2) Krishna; Syeda, S.; Parshad, B.; Dhankhar, J.; Sharma, A.; Shrivastava, A.; Sharma, S. K. Stimuli-responsive azo-functionalized non-ionic amphiphiles for controlled drug delivery applications. *European Polymer Journal* **2024**, *213*, 113127.

(3) Chang, L.-Y.; Lee, C.-P.; Li, C.-T.; Yeh, M.-H.; Ho, K.-C.; Lin, J.-J. Synthesis of a novel amphiphilic polymeric ionic liquid and its application in quasi-solid-state dye-sensitized solar cells. *Journal of Materials Chemistry A* **2014**, *2* (48), 20814-20822.

(4) Patel, R.; Seo, J. A.; Koh, J. H.; Kim, J. H.; Kang, Y. S. Dye-sensitized solar cells employing amphiphilic poly(ethylene glycol) electrolytes. *Journal of Photochemistry and Photobiology A: Chemistry* **2011**, *217* (1), 169-176.

(5) Buwalda, R. T.; Jonker, J. M.; Engberts, J. B. F. N. Aggregation of azo dyes with cationic amphiphiles at low concentrations in aqueous Solution. *Langmuir* **1999**, *15* (4), 1083-1089. DOI: 10.1021/la980824i.

(6) Kutz, A.; Mariani, G.; Gröhn, F. Ionic dye–surfactant nanoassemblies: interplay of electrostatics, hydrophobic effect, and π–π stacking. *Colloid and Polymer Science* **2016**, *294* (3), 591-606. DOI: 10.1007/s00396-015-3814-2.

(7) Peyratout, C.; Donath, E.; Daehne, L. Electrostatic interactions of cationic dyes with negatively charged polyelectrolytes in aqueous solution. *Journal of Photochemistry and Photobiology A: Chemistry* **2001**, *142* (1), 51-57.

(8) Zhao, C.; Yan, Y.; Gao, J.; Yang, L.; Zhou, J.; Li, H.; Huang, K.; Wang, D. A novel surface-active monomer decorating a self-floating adsorbent with high pH adaptability for anionic dyes: π-π stacking. *Journal of Molecular Liquids* **2021**, *321*, 114864.

(9) Gürses, A.; Açıkyıldız, M.; Güneş, K.; Gürses, M. S. Dyes and pigments: their structure and properties. In *Dyes and Pigments*, Gürses, A., Açıkyıldız, M., Güneş, K., Gürses, M. S. Eds.; Springer International Publishing, **2016**; pp 13-29.

(10) Shindy, H. Basics in colors, dyes and pigments chemistry: A review. *Chem. Int* **2016**, *2* (29), 2016.

(11) Hunger, K.; Gregory, P.; Miederer, P.; Berneth, H.; Heid, C.; Mennicke, W. Important chemical chromophores of dye classes. *Industrial dyes: chemistry, properties, applications* **2002**, 13-112.

(12) Bafana, A.; Devi, S. S.; Chakrabarti, T. Azo dyes: past, present and the future. *Environmental Reviews* **2011**, *19* (NA), 350-371.

(13) Benkhaya, S.; M'rabet, S.; El Harfi, A. Classifications, properties, recent synthesis and applications of azo dyes. *Heliyon* **2020**, *6* (1).

(14) Alsantali, R. I.; Raja, Q. A.; Alzahrani, A. Y. A.; Sadiq, A.; Naeem, N.; Mughal, E. U.; Al-Rooqi, M. M.; El Guesmi, N.; Moussa, Z.; Ahmed, S. A. Miscellaneous azo dyes: a comprehensive review on recent advancements in biological and industrial applications. *Dyes and Pigments* **2022**, *199*, 110050.

(15) Leulescu, M.; Rotaru, A.; Pălărie, I.; Moanţă, A.; Cioateră, N.; Popescu, M.; Morîntale, E.; Bubulică, M. V.; Florian, G.; Hărăbor, A. Tartrazine: Physical, thermal and biophysical

properties of the most widely employed synthetic yellow food-colouring azo dye. *Journal of Thermal Analysis and Calorimetry* **2018**, *134*, 209-231.

(16) Sharma, R.; Bamola, S.; Verma, S. K. Effects of acid yellow 23 food dye on environment and its removal on various surfaces–A Mini Review. *Int Res J En g Technol* **2020**, *7*, 4550-4573.

(17) Ashok, V.; Agrawal, N.; Esteve-Romero, J.; Bose, D.; Dubey, N. P. Detection of methyl orange in saffron and other edibles using direct injection micellar liquid chromatography. *Food Analytical Methods* **2017**, *10*, 269-276.

(18) Oladoye, P. O.; Bamigboye, M. O.; Ogunbiyi, O. D.; Akano, M. T. Toxicity and decontamination strategies of Congo red dye. *Groundwater for Sustainable Development* **2022**, *19*, 100844.

(19) Sharma, J.; Janveja, B. A study on removal of congo red dye from the effluents of textile industry using rice husk carbon activated by steam. *Rasayan Journal of Chemistry* **2008**, *1* (4), 936-942.

(20) Khanum, R.; Ali, R. S.; Rangaswamy, H.; Kumar, S. S.; Prashantha, A.; Jagadisha, A. Recent review on Synthesis, spectral Studies, versatile applications of azo dyes and its metal complexes. *Results in Chemistry* **2023**, *5*, 100890.

(21) Derksen, G. C. *Red, redder, madder: analysis and isolation of anthraquinones from madder roots (Rubia tinctorum)*; Wageningen University and Research, **2001**.

(22) Derksen1, G. C.; Bechtold2, T. Natural Colorants—Quinoid, Naphthoquinoid, and Anthraquinoid Dyes. *Handbook of Natural Colorants* **2023**, 271-315.

(23) Kamboj, A.; Medha, K.; Gupta, V.; Jose, S. Ultraviolet protection of textiles with herbal dyes: A contemporary review. *Sustainable Chemistry and Pharmacy* **2024**, *41*, 101689.

(24) Jarikov, V. V.; Neckers, D. C. Photochemistry of triarylmethane dye leuconitriles. *Advances in Photochemistry* **2001**, 1-39.

(25) Mondal, S.; Verma, A.; Saha, S. Conformationally restricted triarylmethanes: synthesis, photophysical studies, and applications. *European Journal of Organic Chemistry* **2019**, *2019* (5), 864-894.

(26) Kowaltowski, A. J.; Turin, J.; Indig, G. L.; Vercesi, A. E. Mitochondrial effects of triarylmethane dyes. *Journal of Bioenergetics and Biomembranes* **1999**, *31*, 581-590.

(27) Yadav, J.; Qanungo, K. A review: on malachite green; synthesis, uses and toxic effects. In *AIP Conference Proceedings*, **2023**; AIP Publishing: Vol. 2535.

(28) Wahyuningsih, S.; Ramelan, A.; Wardani, D.; Aini, F.; Sari, P.; Tamtama, B.; Kristiawan, Y. Indigo dye derived from Indigofera tinctoria as natural food colorant. In *IOP Conference Series: Materials Science and Engineering*, **2017**; IOP Publishing: Vol. 193, p 012048.

(29) Prasad, R. Indigo—the crop that created history and then itself became history. *Indian J. Hist. Sci* **2018**, *53* (3), 296-301.

(30) Stasiak, N.; Kukula-Koch, W.; Glowniak, K. Modern industrial and pharmacological applications of indigo dye and its derivatives-a review. *Acta Pol Pharm* **2014**, *71* (71), 215-221.

(31) Derayea, S. M.; Nagy, D. M. Application of a xanthene dye, eosin Y, as spectroscopic probe in chemical and pharmaceutical analysis; a review. *Reviews in Analytical Chemistry* **2018**, *37* (3), 20170020.

(32) Rahman, H. Utilization of eosin dye as an ion pairing agent for determination of pharmaceuticals: a brief review. *Int. J. Pharm. Pharm. Sci* **2017**, *9* (1).

(33) Hari, D. P.; König, B. Synthetic applications of eosin Y in photoredox catalysis. *Chemical Communications* **2014**, *50* (51), 6688-6699.

(34) Hazebroucq, S.; Labat, F.; Lincot, D.; Adamo, C. Theoretical insights on the electronic properties of eosin Y, an organic dye for photovoltaic applications. *The Journal of Physical Chemistry A* **2008**, *112* (31), 7264-7270.

(35) Tardivo, J. P.; Del Giglio, A.; De Oliveira, C. S.; Gabrielli, D. S.; Junqueira, H. C.; Tada, D. B.; Severino, D.; de Fátima Turchiello, R.; Baptista, M. S. Methylene blue in photodynamic therapy: From basic mechanisms to clinical applications. *Photodiagnosis and photodynamic therapy* **2005**, *2* (3), 175-191.

(36) Oz, M.; Lorke, D. E.; Hasan, M.; Petroianu, G. A. Cellular and molecular actions of methylene blue in the nervous system. *Medicinal research reviews* **2011**, *31* (1), 93-117.

(37) Khan, I.; Saeed, K.; Zekker, I.; Zhang, B.; Hendi, A. H.; Ahmad, A.; Ahmad, S.; Zada, N.; Ahmad, H.; Shah, L. A. Review on methylene blue: Its properties, uses, toxicity and photodegradation. *Water* **2022**, *14* (2), 242.

(38) Valdes-Aguilera, O.; Neckers, D. Aggregation phenomena in xanthene dyes. *Accounts of Chemical Research* **1989**, *22* (5), 171-177.

(39) Claessens, C. G.; Hahn, U.; Torres, T. Phthalocyanines: From outstanding electronic properties to emerging applications. *The Chemical Record* **2008**, *8* (2), 75-97.

(40) Singh, V. K.; Kanaparthi, R. K.; Giribabu, L. Emerging molecular design strategies of unsymmetrical phthalocyanines for dye-sensitized solar cell applications. *Rsc Advances* **2014**, *4* (14), 6970-6984.

(41) El Harfi, S.; El Harfi, A. Classifications, properties and applications of textile dyes: A review. *Applied Journal of Environmental Engineering Science* **2017**, *3* (3), 00000J. Envir. Eng. Sci. 00003 N° 00003 (02017) 00311-00320.

(42) Burkinshaw, S. Application of dyes. In *The chemistry and application of dyes*, Springer, 1990; pp 237-379.

(43) Athey, S. N.; Adams, J. K.; Erdle, L. M.; Jantunen, L. M.; Helm, P. A.; Finkelstein, S. A.; Diamond, M. L. The widespread environmental footprint of indigo denim microfibers from blue jeans. *Environmental Science & Technology Letters* **2020**, *7* (11), 840-847.

(44) Wambuguh, D.; Chianelli, R. R. Indigo dye waste recovery from blue denim textile effluent: a by-product synergy approach. *New journal of chemistry* **2008**, *32* (12), 2189-2194.

(45) Suručić, L.; Andrić, D.; Jevtić, I.; Momčilović, M.; Suručić, R.; Penjišević, J. Unmodified Hemp Biowaste as a Sustainable Biosorbent for Congo Red and Remazol Brilliant Blue R. *Coatings* **2025**, *15* (5), 519.

(46) Ribeiro, J. S.; Veloso, C. M. Microencapsulation of natural dyes with biopolymers for application in food: A review. *Food hydrocolloids* **2021**, *112*, 106374.

(47) Calva-Estrada, S.; Jiménez-Fernández, M.; Lugo-Cervantes, E. Betalains and their applications in food: The current state of processing, stability and future opportunities in the industry. *Food chemistry: molecular sciences* **2022**, *4*, 100089.

(48) Rather, L. J.; Mohammad, F. Phytochemistry, biological activities and potential of annatto in natural colorant production for industrial applications–A review. *Journal of advanced research* **2016**, *7* (3), 499-514.

(49) Scotter, M. The chemistry and analysis of annatto food colouring: a review. *Food Additives and Contaminants* **2009**, *26* (8), 1123-1145.

(50) Martelli, G.; Folli, C.; Visai, L.; Daglia, M.; Ferrari, D. Thermal stability improvement of blue colorant C-Phycocyanin from Spirulina platensis for food industry applications. *Process Biochemistry* **2014**, *49* (1), 154-159.

(51) Sabnis, R. W. *Handbook of biological dyes and stains: synthesis and industrial applications*; John Wiley & Sons, **2010**.

(52) Klymchenko, A. S. Solvatochromic and fluorogenic dyes as environment-sensitive probes: design and biological applications. *Accounts of chemical research* **2017**, *50* (2), 366-375.

(53) Gurr, E. *Synthetic dyes in biology, medicine and chemistry*; Elsevier, **2012**.

(54) Chan, J. K. C. The Wonderful Colors of the Hematoxylin–Eosin Stain in Diagnostic Surgical Pathology. *International Journal of Surgical Pathology* **2014**, *22* (1), 12-32.

(55) Xue, F.; Du, W.; Chen, S.; Ma, M.; Kuang, Y.; Chen, J.; Yi, T.; Chen, H. Hypoxia-Induced photogenic radicals by Eosin Y for efficient phototherapy of hypoxic tumors. *ACS Applied Bio Materials* **2020**, *3* (12), 8962-8969.

(56) Georgiou, C. D.; Grintzalis, K.; Zervoudakis, G.; Papapostolou, I. Mechanism of Coomassie brilliant blue G-250 binding to proteins: a hydrophobic assay for nanogram quantities of proteins. *Analytical and Bioanalytical Chemistry* **2008**, *391* (1), 391-403.

(57) Galindo-Murillo, R.; Cheatham, T. E., III. Ethidium bromide interactions with DNA: an exploration of a classic DNA–ligand complex with unbiased molecular dynamics simulations. *Nucleic Acids Research* **2021**, *49* (7), 3735-3747. DOI: 10.1093/nar/gkab143 (acccessed 6/23/2025).

(58) Lichtman, J. W.; Conchello, J.-A. Fluorescence microscopy. *Nature Methods* **2005**, *2* (12), 910-919.

(59) Tian, M.; Ma, Y.; Lin, W. Fluorescent probes for the visualization of cell viability. *Accounts of Chemical Research* **2019**, *52* (8), 2147-2157.

(60) Coons, D.; Dankowski, M.; Diehl, M.; Jakobi, G.; Kuzel, P.; Sung, E.; Trabitzsch, U. Performance in detergents, cleaning agents and personal care products. In *Surfactants in Consumer Products: Theory, Technology and Application*, Falbe, J. Ed.; Springer Berlin Heidelberg, **1987**; pp 197-398.

(61) Dutta, A. K. Introductory Chapter: Surfactants in household and personal care formulations - An Overview. In *Surfactants and Detergents*, Dutta, A. K. Ed.; IntechOpen, **2019**.

(62) Achaw, O.-W.; Danso-Boateng, E. Soaps and Detergents. In *Chemical and Process Industries: With Examples of Industries in Ghana*, Achaw, O.-W., Danso-Boateng, E. Eds.; Springer International Publishing, **2021**; pp 1-37.

(63) Khan, R. A. Chapter 7 - Detergents. In *Environmental Micropollutants*, Hashmi, M. Z., Wang, S., Ahmed, Z. Eds.; Elsevier, **2022**; pp 117-130.

(64) Chenier, P. J. Surfactants, Soaps, and Detergents. In *Survey of Industrial Chemistry*, Chenier, P. J. Ed.; Springer US, **2002**; pp 461-474.

(65) Verbeek, H. Historical Review. In *Surfactants in Consumer Products: Theory, Technology and Application*, Falbe, J. Ed.; Springer Berlin Heidelberg, **1987**; pp 1-4.

(66) Halliday, H. L. Surfactants: past, present and future. *Journal of Perinatology* **2008**, *28* (1), S47-S56.

(67) Umar, A. A.; Saaid, I. B. M.; Sulaimon, A. A.; Pilus, R. B. M. A review of petroleum emulsions and recent progress on water-in-crude oil emulsions stabilized by natural surfactants and solids. *Journal of Petroleum Science and Engineering* **2018**, *165*, 673-690.

(68) Schramm, L. L.; Stasiuk, E. N.; Marangoni, D. G. Surfactants and their applications. *Annual Reports Section "C" (Physical Chemistry)* **2003**, *99* (0), 3-48, 10.1039/B208499F. DOI: 10.1039/B208499F.

(69) Ashrafizadeh, S. N.; Motaee, E.; Hoshyargar, V. Emulsification of heavy crude oil in water by natural surfactants. *Journal of Petroleum Science and Engineering* **2012**, *86-87*, 137-143.

(70) Shi, L.; Huang, J.; Zeng, G.; Zhu, L.; Gu, Y.; Shi, Y.; Yi, K.; Li, X. Roles of surfactants in pressure-driven membrane separation processes: a review. *Environmental Science and Pollution Research* **2019**, *26* (30), 30731-30754.

(71) Cheng, H.; and Sabatini, D. A. Separation of Organic Compounds from Surfactant Solutions: A Review. *Separation Science and Technology* **2007**, *42* (3), 453-475.

(72) Wu, C.; Peng, X.-l.; Wu, G.-m. Wetting agent investigation for controlling dust of lead-zinc ores. *Transactions of Nonferrous Metals Society of China* **2007**, *17* (1), 159-167.

(73) De, S.; Malik, S.; Ghosh, A.; Saha, R.; Saha, B. A review on natural surfactants. *RSC Advances* **2015**, *5* (81), 65757-65767.

(74) Foley, P.; Kermanshahi pour, A.; Beach, E. S.; Zimmerman, J. B. Derivation and synthesis of renewable surfactants. *Chemical Society Reviews* **2012**, *41* (4), 1499-1518.

(75) Nagtode, V. S.; Cardoza, C.; Yasin, H. K. A.; Mali, S. N.; Tambe, S. M.; Roy, P.; Singh, K.; Goel, A.; Amin, P. D.; Thorat, B. R.; et al. Green Surfactants (Biosurfactants): A petroleum-free substitute for sustainability─comparison, applications, market, and future prospects. *ACS Omega* **2023**, *8* (13), 11674-11699.

(76) Raffa, P.; Wever, D. A. Z.; Picchioni, F.; Broekhuis, A. A. polymeric surfactants: synthesis, properties, and links to applications. *Chemical Reviews* **2015**, *115* (16), 8504-8563.

(77) Hayes, D. G. Chapter 11 - Fatty acids–based surfactants and their uses. In *Fatty Acids*, Ahmad, M. U. Ed.; AOCS Press, **2017**; pp 355-384.

(78) Permadi, P.; Fitria, R.; Hambali, E. Palm oil based surfactant products for petroleum industry. *IOP Conference Series: Earth and Environmental Science* **2017**, *65* (1), 012034.

(79) Saxena, N.; Pal, N.; Dey, S.; Mandal, A. Characterizations of surfactant synthesized from palm oil and its application in enhanced oil recovery. *Journal of the Taiwan Institute of Chemical Engineers* **2017**, *81*, 343-355.

(80) Efendy Goon, D.; Sheikh Abdul Kadir, S. H.; Latip, N. A.; Rahim, S. A.; Mazlan, M. Palm oil in lipid-based formulations and drug delivery systems. *Biomolecules* **2019**, *9* (2), 64.

(81) Liu, Z.; Biresaw, G. Synthesis of Soybean Oil-based polymeric surfactants in supercritical carbon dioxide and investigation of their surface properties. *Journal of Agricultural and Food Chemistry* **2011**, *59* (5), 1909-1917.

(82) Zhao, F.; Clarens, A.; Murphree, A.; Hayes, K.; Skerlos, S. J. Structural aspects of surfactant selection for the design of vegetable oil semi-synthetic metalworking fluids. *Environmental Science & Technology* **2006**, *40* (24), 7930-7937.

(83) Singh, A.; Van Hamme, J. D.; Ward, O. P. Surfactants in microbiology and biotechnology: Part 2. Application aspects. *Biotechnology Advances* **2007**, *25* (1), 99-121.

(84) Malik, N. A. Solubilization and interaction studies of bile salts with surfactants and drugs: a review. *Applied Biochemistry and Biotechnology* **2016**, *179* (2), 179-201.

(85) Gonçalves, R. A.; Holmberg, K.; Lindman, B. Cationic surfactants: A review. *Journal of Molecular Liquids* **2023**, *375*, 121335.

(86) Hibbs, J. Anionic Surfactants. In *Chemistry and Technology of Surfactants*, 2006; pp 91-132.

(87) Hepworth, P. Non-ionic surfactants. In *Chemistry and Technology of Surfactants*, 2006; pp 133-152.

(88) Schott, H. Hydrophile-Lipophile balance and cloud points of nonionic surfactants. *Journal of Pharmaceutical Sciences* **1969**, *58* (12), 1443-1449.

(89) Gerola, A. P.; Costa, P. F. A.; Quina, F. H.; Fiedler, H. D.; Nome, F. Zwitterionic surfactants in ion binding and catalysis. *Current Opinion in Colloid & Interface Science* **2017**, *32*, 39-47.

(90) Gerola, A. P.; Costa, P. F. A.; Nome, F.; Quina, F. Micellization and adsorption of zwitterionic surfactants at the air/water interface. *Current Opinion in Colloid & Interface Science* **2017**, *32*, 48-56.

(91) Ridout, G.; Hinz, R. S.; Hostynek, J. J.; Reddy, A. K.; Wiersema, R. J.; Hodson, C. D.; Lorence, C. R.; Guy, R. H. The effects of zwitterionic surfactants on skin barrier function. *Fundamental and Applied Toxicology* **1991**, *16* (1), 41-50.

(92) Park, K.; Lim, J. Synthesis of phospholipid based zwitterionic surfactant from coconut oil source and characterization of their interfacial, antiseptic and antiviral properties. *Journal of Industrial and Engineering Chemistry* **2022**, *115*, 241-250.

(93) Kamal, M. S. A Review of gemini surfactants: potential application in enhanced oil recovery. *Journal of Surfactants and Detergents* **2016**, *19* (2), 223-236.

(94) Brycki, B. E.; Kowalczyk, I.; Szulc, A.; Kaczerewska, O.; Pakiet, M. Multifunctional gemini surfactants: structure, synthesis, properties and applications. In *Application and Characterization of Surfactants*, Najjar, R. Ed.; IntechOpen, **2017**.

(95) Subramaniyam, S. S.; Srilatha, R.; Avinash, L.; Kudur, J. G.; and Krishna, P. G. An insight into DFT and corrosion inhibition studies – a case of 1-ethyl-3-methyl- imidazolium tri fluro-methane sulphonate as an excellent inhibitor in acid medium. *Canadian Metallurgical Quarterly*, 1-20. DOI: 10.1080/00084433.2025.2511507.

(96) Sharma, D.; Sharma, J.; Arya, R. K.; Ahuja, S.; Agnihotri, S. Surfactant enhanced drying of waterbased poly(vinyl alcohol) coatings. *Progress in Organic Coatings* **2018**, *125*, 443-452.

(97) Petroff, L. J.; Snow, S. A. Silicone Surfactants. In *Silicone Surface Science*, Owen, M. J., Dvornic, P. R. Eds.; Springer Netherlands, **2012**; pp 243-280.

(98) Hill, R. M. Silicone surfactants—new developments. *Current Opinion in Colloid & Interface Science* **2002**, *7* (5), 255-261.

(99) Ananthapadmanabhan, K. P.; Goddard, E. D.; Chandar, P. A study of the solution, interfacial and wetting properties of silicone surfactants. *Colloids and Surfaces* **1990**, *44*, 281-297.

(100) Pukale, D. D.; Bansode, A. S.; Jadhav, N. L.; Pinjari, D. V.; Kulkarni, R. R. Review on Silicone Surfactants: Silicone-based Gemini Surfactants, Physicochemical Properties and Applications. *Tenside Surfactants Detergents* **2019**, *56* (4), 268-278. DOI: doi:10.3139/113.110617 (acccessed 2025-06-23).

(101) Cheng, Y.; Zhang, S.; Wang, J.; Zhao, Y.; Zhang, Z. Research progress in the synthesis and application of surfactants based on trisiloxane. *Journal of Molecular Liquids* **2022**, *362*, 119770.

(102) Rogers, R. D.; Voth, G. A. Ionic Liquids. *Accounts of Chemical Research* **2007**, *40* (11), 1077-1078.

(103) Introduction: Ionic Liquids. *Chemical Reviews* **2017**, *117* (10), 6633-6635.

(104) Fredlake, C. P.; Crosthwaite, J. M.; Hert, D. G.; Aki, S. N. V. K.; Brennecke, J. F. Thermophysical properties of imidazolium-based ionic liquids. *Journal of Chemical & Engineering Data* **2004**, *49* (4), 954-964.

(105) Sharma, R.; Mahajan, R. K. Influence of various additives on the physicochemical properties of imidazolium based ionic liquids: a comprehensive review. *RSC Advances* **2014**, *4* (2), 748-774, 10.1039/C3RA42228C.

(106) Gardas, R. L.; Freire, M. G.; Carvalho, P. J.; Marrucho, I. M.; Fonseca, I. M. A.; Ferreira, A. G. M.; Coutinho, J. A. P. High-pressure densities and derived thermodynamic properties of imidazolium-based ionic liquids. *Journal of Chemical & Engineering Data* **2007**, *52* (1), 80-88.

(107) Mbondo Tsamba, B. E.; Sarraute, S.; Traïkia, M.; Husson, P. Transport properties and ionic association in pure imidazolium-based ionic liquids as a function of temperature. *Journal of Chemical & Engineering Data* **2014**, *59* (6), 1747-1754.

(108) Jacquemin, J.; Husson, P.; Mayer, V.; Cibulka, I. High-pressure volumetric properties of imidazolium-based ionic liquids: effect of the anion. *Journal of Chemical & Engineering Data* **2007**, *52* (6), 2204-2211.

(109) Wu, C.; De Visscher, A.; Gates, I. D. Comparison of electronic and physicochemical properties between imidazolium-based and pyridinium-based ionic liquids. *The Journal of Physical Chemistry B* **2018**, *122* (26), 6771-6780.

(110) Cadena, C.; Zhao, Q.; Snurr, R. Q.; Maginn, E. J. Molecular modeling and experimental studies of the thermodynamic and transport properties of pyridinium-based ionic liquids. *The Journal of Physical Chemistry B* **2006**, *110* (6), 2821-2832.

(111) Bandrés, I.; Alcalde, R.; Lafuente, C.; Atilhan, M.; Aparicio, S. On the viscosity of pyridinium based ionic liquids: an experimental and computational study. *The Journal of Physical Chemistry B* **2011**, *115* (43), 12499-12513.

(112) Bandrés, I.; Montaño, D. F.; Gascón, I.; Cea, P.; Lafuente, C. Study of the conductivity behavior of pyridinium-based ionic liquids. *Electrochimica Acta* **2010**, *55* (7), 2252-2257.

(113) McCallum, R.; Barghamadi, M.; Forsyth, C.; Hollenkamp, A. F.; Oldham, G.; Mahon, P. J.; Rüther, T. Comparing the physicochemical, electrochemical, and structural properties of boronium versus pyrrolidinium cation-based ionic liquids and their performance as Li-ion battery electrolytes. *The Journal of Physical Chemistry C* **2021**, *125* (15), 8055-8067.

(114) Pernak, J.; Smiglak, M.; Griffin, S. T.; Hough, W. L.; Wilson, T. B.; Pernak, A.; Zabielska-Matejuk, J.; Fojutowski, A.; Kita, K.; Rogers, R. D. Long alkyl chain quaternary ammonium-based ionic liquids and potential applications. *Green Chemistry* **2006**, *8* (9), 798-806.

(115) Qu, J.; Truhan, J. J.; Dai, S.; Luo, H.; Blau, P. J. Ionic liquids with ammonium cations as lubricants or additives. *Tribology Letters* **2006**, *22* (3), 207-214.

(116) Khazalpour, S.; Yarie, M.; Kianpour, E.; Amani, A.; Asadabadi, S.; Seyf, J. Y.; Rezaeivala, M.; Azizian, S.; Zolfigol, M. A. Applications of phosphonium-based ionic liquids in chemical processes. *Journal of the Iranian Chemical Society* **2020**, *17* (8), 1775-1917.

(117) Kareem, M. A.; Mjalli, F. S.; Hashim, M. A.; AlNashef, I. M. Phosphonium-based ionic liquids analogues and their physical properties. *Journal of Chemical & Engineering Data* **2010**, *55* (11), 4632-4637.

(118) Anouti, M.; Caillon-Caravanier, M.; Dridi, Y.; Galiano, H.; Lemordant, D. Synthesis and characterization of new pyrrolidinium based protic ionic liquids. good and superionic liquids. *The Journal of Physical Chemistry B* **2008**, *112* (42), 13335-13343.

(119) Shimizu, Y.; Ohte, Y.; Yamamura, Y.; Tsuzuki, S.; Saito, K. Comparative study of imidazolium- and pyrrolidinium-based ionic liquids: thermodynamic properties. *The Journal of Physical Chemistry B* **2012**, *116* (18), 5406-5413.

(120) Villanueva, M.; Coronas, A.; García, J.; Salgado, J. Thermal stability of ionic liquids for their application as new absorbents. *Industrial & Engineering Chemistry Research* **2013**, *52* (45), 15718-15727.

(121) Chen, Y.; Mu, T. Thermal stability of ionic liquids. In *Encyclopedia of Ionic Liquids*, Zhang, S. Ed.; Springer Nature Singapore, 2022; pp 1288-1299.

(122) Bier, M.; and Dietrich, S. Vapour pressure of ionic liquids. *Molecular Physics* **2010**, *108* (2), 211-214.

(123) Earle, M. J.; Seddon, K. R. Ionic Liquids: Green solvents for the future. In *Clean Solvents*, ACS Symposium Series, Vol. 819; American Chemical Society, **2002**; pp 10-25.

(124) Earle, M. J.; Seddon, K. R. Ionic liquids. Green solvents for the future. *Pure and Applied Chemistry* **2000**, *72* (7), 1391-1398. DOI: doi:10.1351/pac200072071391 (acccessed 2025-06-24).

(125) Mallakpour, S.; Dinari, M. Ionic liquids as green solvents: progress and prospects. In *Green Solvents II: Properties and Applications of Ionic Liquids*, Mohammad, A., Inamuddin, D. Eds.; Springer Netherlands, **2012**; pp 1-32.

(126) Pitawala, J.; Matic, A.; Martinelli, A.; Jacobsson, P.; Koch, V.; Croce, F. Thermal Properties and ionic conductivity of imidazolium bis(trifluoromethanesulfonyl)imide dicationic ionic liquids. *The Journal of Physical Chemistry B* **2009**, *113* (31), 10607-10610.

(127) Li, M.; Yang, L.; Fang, S.; Dong, S. Novel polymeric ionic liquid membranes as solid polymer electrolytes with high ionic conductivity at moderate temperature. *Journal of Membrane Science* **2011**, *366* (1), 245-250.

(128) O'Mahony, A. M.; Silvester, D. S.; Aldous, L.; Hardacre, C.; Compton, R. G. Effect of water on the electrochemical window and potential limits of room-temperature ionic liquids. *Journal of Chemical & Engineering Data* **2008**, *53* (12), 2884-2891.

(129) Tian, Y.-H.; Goff, G. S.; Runde, W. H.; Batista, E. R. Exploring electrochemical windows of room-temperature ionic liquids: A Computational Study. *The Journal of Physical Chemistry B* **2012**, *116* (39), 11943-11952.

(130) Piatti, E.; Guglielmero, L.; Tofani, G.; Mezzetta, A.; Guazzelli, L.; D'Andrea, F.; Roddaro, S.; Pomelli, C. S. Ionic liquids for electrochemical applications: Correlation between molecular structure and electrochemical stability window. *Journal of Molecular Liquids* **2022**, *364*, 120001.

(131) Jacquemin, J.; Husson, P.; Padua, A. A. H.; Majer, V. Density and viscosity of several pure and water-saturated ionic liquids. *Green Chemistry* **2006**, *8* (2), 172-180, 10.1039/B513231B.

(132) Yalcin, D.; Drummond, C. J.; Greaves, T. L. Solvation properties of protic ionic liquids and molecular solvents. *Physical Chemistry Chemical Physics* **2020**, *22* (1), 114-128.

(133) Anderson, J. L.; Ding, J.; Welton, T.; Armstrong, D. W. Characterizing ionic liquids on the basis of multiple solvation interactions. *Journal of the American Chemical Society* **2002**, *124* (47), 14247-14254.

(134) Valderrama, J. O.; Reátegui, A.; Rojas, R. E. Density of Ionic liquids using group contribution and artificial neural networks. *Industrial & Engineering Chemistry Research* **2009**, *48* (6), 3254-3259.

(135) Mantz, R. A.; Trulove, P. C. Viscosity and density of ionic liquids. *Ionic liquids in synthesis* **2008**, *2*, 72-88.

(136) Rodrigues, R. F.; Freitas, A. A.; Canongia Lopes, J. N.; Shimizu, K. Ionic liquids and water: hydrophobicity vs. hydrophilicity. *Molecules* **2021**, *26* (23), 7159.

(137) Huddleston, J. G.; Visser, A. E.; Reichert, W. M.; Willauer, H. D.; Broker, G. A.; Rogers, R. D. Characterization and comparison of hydrophilic and hydrophobic room temperature ionic liquids incorporating the imidazolium cation. *Green chemistry* **2001**, *3* (4), 156-164.

(138) Endo, T.; Sunada, K.; Sumida, H.; Kimura, Y. Origin of low melting point of ionic liquids: dominant role of entropy. *Chemical Science* **2022**, *13* (25), 7560-7565.

(139) Dean, P. M.; Pringle, J. M.; MacFarlane, D. R. Structural analysis of low melting organic salts: perspectives on ionic liquids. *Physical Chemistry Chemical Physics* **2010**, *12* (32), 9144-9153.

(140) Zhao, H.; Xia, S.; Ma, P. Use of ionic liquids as 'green'solvents for extractions. *Journal of Chemical Technology & Biotechnology: International Research in Process, Environmental & Clean Technology* **2005**, *80* (10), 1089-1096.

(141) de Jesus, S. S.; Maciel Filho, R. Are ionic liquids eco-friendly? *Renewable and Sustainable Energy Reviews* **2022**, *157*, 112039.

(142) Alqahtani, A. S. Indisputable roles of different ionic liquids, deep eutectic solvents and nanomaterials in green chemistry for sustainable organic synthesis. *Journal of Molecular Liquids* **2024**, *399*, 124469.

(143) Gordon, C. M. New developments in catalysis using ionic liquids. *Applied Catalysis A: General* **2001**, *222* (1), 101-117.

(144) Zhao, D.; Wu, M.; Kou, Y.; Min, E. Ionic liquids: applications in catalysis. *Catalysis Today* **2002**, *74* (1), 157-189.

(145) MacFarlane, D. R.; Forsyth, M.; Howlett, P. C.; Pringle, J. M.; Sun, J.; Annat, G.; Neil, W.; Izgorodina, E. I. Ionic liquids in electrochemical devices and processes: managing interfacial electrochemistry. *Accounts of chemical research* **2007**, *40* (11), 1165-1173.

(146) Fernicola, A.; Scrosati, B.; Ohno, H. Potentialities of ionic liquids as new electrolyte media in advanced electrochemical devices. *Ionics* **2006**, *12*, 95-102.

(147) Han, D.; Row, K. H. Recent applications of ionic liquids in separation technology. *Molecules* **2010**, *15* (4), 2405-2426.

(148) Berthod, A.; Ruiz-Angel, M. J.; Carda-Broch, S. Recent advances on ionic liquid uses in separation techniques. *Journal of Chromatography A* **2018**, *1559*, 2-16.

(149) Moniruzzaman, M.; Kamiya, N.; Goto, M. Activation and stabilization of enzymes in ionic liquids. *Organic & biomolecular chemistry* **2010**, *8* (13), 2887-2899.

(150) Gao, W.-W.; Zhang, F.-X.; Zhang, G.-X.; Zhou, C.-H. Key factors affecting the activity and stability of enzymes in ionic liquids and novel applications in biocatalysis. *Biochemical engineering journal* **2015**, *99*, 67-84.

(151) Bara, J. E.; Camper, D. E.; Gin, D. L.; Noble, R. D. Room-temperature ionic liquids and composite materials: platform technologies for CO2 capture. *Accounts of Chemical Research* **2010**, *43* (1), 152-159.

(152) MacFarlane, D. R.; Tachikawa, N.; Forsyth, M.; Pringle, J. M.; Howlett, P. C.; Elliott, G. D.; Davis, J. H.; Watanabe, M.; Simon, P.; Angell, C. A. Energy applications of ionic liquids. *Energy & Environmental Science* **2014**, *7* (1), 232-250.

(153) Arumugam, V.; Redhi, G.; Gengan, R. M. The application of ionic liquids in nanotechnology. In *Fundamentals of Nanoparticles*, Elsevier, **2018**; pp 371-400.

(154) Ray, P.; Pilania, M. The application and influence of ionic liquids in nanotechnology. *Materials Today: Proceedings* **2021**, *47*, 2835-2838.

(155) Liu, J.-f.; Jiang, G.-b.; Jönsson, J. Å. Application of ionic liquids in analytical chemistry. *TrAC Trends in Analytical Chemistry* **2005**, *24* (1), 20-27.

(156) Trujillo-Rodríguez, M. J.; Nan, H.; Varona, M.; Emaus, M. N.; Souza, I. D.; Anderson, J. L. Advances of ionic liquids in analytical chemistry. *Analytical chemistry* **2018**, *91* (1), 505-531.

(157) Shamshina, J. L.; Barber, P. S.; Rogers, R. D. Ionic liquids in drug delivery. *Expert opinion on drug delivery* **2013**, *10* (10), 1367-1381.

(158) Pedro, S. N.; R. Freire, C. S.; Silvestre, A. J.; Freire, M. G. The role of ionic liquids in the pharmaceutical field: An overview of relevant applications. *International journal of molecular sciences* **2020**, *21* (21), 8298.

(159) Zhou, F.; Liang, Y.; Liu, W. Ionic liquid lubricants: designed chemistry for engineering applications. *Chemical Society Reviews* **2009**, *38* (9), 2590-2599.

(160) Roessler, A.; Schottenberger, H. Antistatic coatings for wood-floorings by imidazolium salt-based ionic liquids. *Progress in Organic Coatings* **2014**, *77* (3), 579-582.

(161) Van Valkenburg, M. E.; Vaughn, R. L.; Williams, M.; Wilkes, J. S. Thermochemistry of ionic liquid heat-transfer fluids. *Thermochimica Acta* **2005**, *425* (1-2), 181-188.

(162) Nancarrow, P.; Mohammed, H. Ionic liquids in space technology–current and future trends. *ChemBioEng Reviews* **2017**, *4* (2), 106-119.

(163) Wishart, J. F. Ionic liquid radiation chemistry. *Ionic Liquids Further Uncoiled: Critical Expert Overviews* **2014**, 259-274.

(164) Goloviznina, K.; Lepre, L. F.; Sabelle, S.; Pádua, A. A.; Gomes, M. C. Enhancement of the solubility of organic dyes in aqueous ionic solvents doped with surfactants. *Journal of Molecular Liquids* **2022**, *357*, 118958.

(165) Ferreira, A. M.; Coutinho, J. A.; Fernandes, A. M.; Freire, M. G. Complete removal of textile dyes from aqueous media using ionic-liquid-based aqueous two-phase systems. *Separation and Purification Technology* **2014**, *128*, 58-66.

(166) Buettner, C. S.; Cognigni, A.; Schröder, C.; Bica-Schröder, K. Surface-active ionic liquids: A review. *Journal of Molecular Liquids* **2022**, *347*, 118160.

(167) Jiao, J.; Dong, B.; Zhang, H.; Zhao, Y.; Wang, X.; Wang, R.; Yu, L. Aggregation behaviors of dodecyl sulfate-based anionic surface active ionic liquids in water. *The Journal of Physical Chemistry B* **2012**, *116* (3), 958-965.

(168) Mazille, F.; Fei, Z.; Kuang, D.; Zhao, D.; Zakeeruddin, S. M.; Graetzel, M.; Dyson, P. J. Influence of ionic liquids bearing functional groups in dye-sensitized solar cells. *Inorganic chemistry* **2006**, *45* (4), 1585-1590.

(169) Pal, A.; Yadav, A. Binding interactions of anesthetic drug with surface active ionic liquid. *Journal of Molecular Liquids* **2016**, *222*, 471-479.

(170) Ilyas, F.; Fazal, H.; Ahmed, M.; Iqbal, A.; Ishaq, M.; Jabeen, M.; Butt, M.; Farid, S. Advances in ionic liquids as fluorescent sensors. *Chemosphere* **2024**, 141434.

(171) Kermanioryani, M.; Mutalib, M. I. A.; Kurnia, K. A.; Lethesh, K. C.; Krishnan, S.; Leveque, J.-M. Enhancement of π–π aromatic interactions between hydrophobic Ionic Liquids and Methylene Blue for an optimum removal efficiency and assessment of toxicity by microbiological method. *Journal of Cleaner Production* **2016**, *137*, 1149-1157.

(172) Wani, H. A.; Shaikh, V. R.; More, D. H.; Patil, K. J. Applications of spectroscopic techniques to the study of monomer–dimer equilibria for methylene blue in aqueous solutions containing ionic liquid: Probing the structural interactions involving water and ionic liquids. *Spectrochimica Acta Part A: Molecular and Biomolecular Spectroscopy* **2023**, *287*, 122058.

(173) Sanan, R.; Kang, T. S.; Mahajan, R. K. Complexation, dimerisation and solubilisation of methylene blue in the presence of biamphiphilic ionic liquids: a detailed spectroscopic and electrochemical study. *Physical Chemistry Chemical Physics* **2014**, *16* (12), 5667-5677.

(174) Rather, M. A.; Bhat, S. A.; Pandit, S. A.; Bhat, F. A.; Rather, G. M.; Bhat, M. A. As catalytic as silver nanoparticles anchored to reduced graphene oxide: Fascinating activity of imidazolium based surface active ionic liquid for chemical degradation of rhodamine B. *Catalysis Letters* **2019**, *149*, 2195-2203.

(175) Matthews, R. P.; Welton, T.; Hunt, P. A. Competitive pi interactions and hydrogen bonding within imidazolium ionic liquids. *Physical Chemistry Chemical Physics* **2014**, *16* (7), 3238-3253.

(176) Matthews, R. P.; Welton, T.; Hunt, P. A. Hydrogen bonding and π–π interactions in imidazolium-chloride ionic liquid clusters. *Physical Chemistry Chemical Physics* **2015**, *17* (22), 14437-14453.

(177) Ferreira, A. M.; Coutinho, J. A. P.; Fernandes, A. M.; Freire, M. G. Complete removal of textile dyes from aqueous media using ionic-liquid-based aqueous two-phase systems. *Separation and Purification Technology* **2014**, *128*, 58-66.

(178) Thasneema, K. K.; Dipin, T.; Thayyil, M. S.; Sahu, P. K.; Messali, M.; Rosalin, T.; Elyas, K. K.; Saharuba, P. M.; Anjitha, T.; Hadda, T. B. Removal of toxic heavy metals, phenolic compounds and textile dyes from industrial waste water using phosphonium based ionic liquids. *Journal of Molecular Liquids* **2021**, *323*, 114645.

(179) Bukman, L.; Fernandes-Machado, N. R. C.; Caetano, W.; Tessaro, A. L.; Hioka, N. Treatment of wastewater contaminated with ionic dyes: Liquid-liquid extraction induced by reversed micelle followed by photodegradation. *Separation and Purification Technology* **2017**, *189*, 162-169.

(180) Svenson, S. Controlling surfactant self-assembly. *Current Opinion in Colloid & Interface Science* **2004**, *9* (3), 201-212.

(181) Nagarajan, R.; Ruckenstein, E. Theory of surfactant self-assembly: a predictive molecular thermodynamic approach. *Langmuir* **1991**, *7* (12), 2934-2969.

(182) Camesano, T. A.; Nagarajan, R. Micelle formation and CMC of gemini surfactants: a thermodynamic model. *Colloids and Surfaces A: Physicochemical and Engineering Aspects* **2000**, *167* (1-2), 165-177.

(183) Nagarajan, R. *Self-assembly: from surfactants to nanoparticles*; John Wiley & Sons, **2018**.

(184) Stigter, D. Micelle formation by ionic surfactants. II. Specificity of head groups, micelle structure. *The Journal of Physical Chemistry* **1974**, *78* (24), 2480-2485.

(185) Correa, N. M.; Silber, J. J.; Riter, R. E.; Levinger, N. E. Nonaqueous polar solvents in reverse micelle systems. *Chemical Reviews* **2012**, *112* (8), 4569-4602.

(186) Mukerjee, P.; Mysels, K. J. A Re-evaluation of the spectral change method of determining critical micelle concentration1. *Journal of the American Chemical Society* **1955**, *77* (11), 2937-2943.

(187) Eastoe, J. Surfactant aggregation and adsorption at interfaces. *Colloid Science: Principles, Methods and Applications. 2nd ed. Southern Gate: Wiley* **2010**, 61-90.

(188) Hartley, G.; Runnicles, D. The determination of the size of paraffin-chain salt micelles from diffusion measurements. *Proceedings of the Royal Society of London. Series A. Mathematical and Physical Sciences* **1938**, *168* (934), 420-440.

(189) Zadaka, D.; Radian, A.; Mishael, Y. G. Applying zeta potential measurements to characterize the adsorption on montmorillonite of organic cations as monomers, micelles, or polymers. *Journal of Colloid and Interface Science* **2010**, *352* (1), 171-177.

(190) Debye, P.; Anacker, E. Micelle shape from dissymmetry measurements. *The Journal of Physical Chemistry* **1951**, *55* (5), 644-655.

(191) Philippoff, W.; McBain, J. W. Expansion of the lamellar crystal lattice of aerosol OT upon the addition of water. *Nature* **1949**, *164* (4177), 885-885.

(192) Nagarajan, R. Molecular packing parameter and surfactant self-assembly: the neglected role of the surfactant tail. *Langmuir* **2002**, *18* (1), 31-38.

(193) Tanford, C. Micelle shape and size. *The Journal of Physical Chemistry* **1972**, *76* (21), 3020-3024.

(194) Debye, P. Molecular-weight determination by light scattering. *The Journal of Physical Chemistry* **1947**, *51* (1), 18-32.

(195) Collings, P. J.; Gibbs, E. J.; Starr, T. E.; Vafek, O.; Yee, C.; Pomerance, L. A.; Pasternack, R. F. Resonance light scattering and its application in determining the size, shape, and aggregation number for supramolecular assemblies of chromophores. *The Journal of Physical Chemistry B* **1999**, *103* (40), 8474-8481.

(196) Almgren, M.; Lo, J.-E. Determination of micelle aggregation numbers and micelle fluidities from time-resolved fluorescence quenching studies. *Journal of Colloid and Interface Science* **1981**, *81* (2), 486-499.

(197) Ciotta, E.; Prosposito, P.; Pizzoferrato, R. Positive curvature in Stern-Volmer plot described by a generalized model for static quenching. *Journal of Luminescence* **2019**, *206*, 518-522.

(198) Bandyopadhyay, S.; Banik, R.; Sardar, R.; Ghosh, S. Aggregation and characterization of the microenvironment of solvatochromic eosin yellow dye in the presence of zwitterionic, cationic, and anionic surfactants: A spectroscopic and theoretical approach. *Journal of Molecular Liquids* **2025**, 127953.

(199) Tanford, C. Theory of micelle formation in aqueous solutions. *The Journal of Physical Chemistry* **1974**, *78* (24), 2469-2479.

(200) Madenci, D.; Egelhaaf, S. Self-assembly in aqueous bile salt solutions. *Current Opinion in Colloid & Interface Science* **2010**, *15* (1-2), 109-115.

(201) Warren, D. B.; Chalmers, D. K.; Hutchison, K.; Dang, W.; Pouton, C. W. Molecular dynamics simulations of spontaneous bile salt aggregation. *Colloids and Surfaces A: Physicochemical and Engineering Aspects* **2006**, *280* (1-3), 182-193.

(202) Medoš, Ž.; Friesen, S.; Buchner, R.; Bešter-Rogač, M. Interplay between aggregation number, micelle charge and hydration of catanionic surfactants. *Physical Chemistry Chemical Physics* **2020**, *22* (18), 9998-10009.

(203) Bales, B. L. A definition of the degree of ionization of a micelle based on its aggregation number. *The Journal of Physical Chemistry B* **2001**, *105* (29), 6798-6804.

(204) Aswal, V.; Goyal, P. Role of different counterions and size of micelle in concentration dependence micellar structure of ionic surfactants. *Chemical physics letters* **2003**, *368* (1-2), 59-65.

(205) Mukerjee, P.; Mysels, K.; Kapauan, P. Counterion specificity in the formation of ionic micelles-size, hydration, and hydrophobic bonding effects. *The Journal of Physical Chemistry* **1967**, *71* (13), 4166-4175.

(206) Konop, A. J.; Colby, R. H. Role of condensed counterions in the thermodynamics of surfactant micelle formation with and without oppositely charged polyelectrolytes. *Langmuir* **1999**, *15* (1), 58-65.

(207) Muhammad, M. T.; Khan, M. N. Study of electrolytic effect on the interaction between anionic surfactant and methylene blue using spectrophotometric and conductivity methods. *Journal of Molecular Liquids* **2017**, *234*, 309-314.

(208) Desnoyers, J. E.; Caron, G.; DeLisi, R.; Roberts, D.; Roux, A.; Perron, G. Thermodynamic properties of alkyldimethylamine oxides in water. Application of a mass-action model for micellization. *The Journal of Physical Chemistry* **1983**, *87* (8), 1397-1406.

(209) Puvvada, S.; Blankschtein, D. Thermodynamic description of micellization, phase behavior, and phase separation of aqueous solutions of surfactant mixtures. *The Journal of Physical Chemistry* **1992**, *96* (13), 5567-5579.

(210) Hill, T. L. *An introduction to statistical thermodynamics*; Courier Corporation, 1986.

(211) Corkill, J.; Goodman, J.; Harrold, S.; Tate, J. Thermodynamics of comicellization of ionic detergents. *Transactions of the Faraday Society* **1966**, *62*, 994-1001.

(212) Clunie, J.; Corkill, J.; Goodman, J.; Symons, P.; Tate, J. Thermodynamics of non-ionic surface-active agent+ water systems. *Transactions of the Faraday Society* **1967**, *63*, 2839-2845.

(213) Tanford, C. Thermodynamics of micelle formation: prediction of micelle size and size distribution. *Proceedings of the National Academy of Sciences* **1974**, *71* (5), 1811-1815.

(214) Tanford, C. The hydrophobic effect and the organization of living matter. *Science* **1978**, *200* (4345), 1012-1018.

(215) Israelachvili, J. N. *Intermolecular and surface forces*; Academic press, **2011**.

(216) Meyer, E. E.; Rosenberg, K. J.; Israelachvili, J. Recent progress in understanding hydrophobic interactions. *Proceedings of the National Academy of Sciences* **2006**, *103* (43), 15739-15746.

(217) Nagarajan, R.; Ruckenstein, E. Aggregation of amphiphiles as micelles or vesicles in aqueous media. *Journal of Colloid and Interface Science* **1979**, *71* (3), 580-604.

CHAPTER- I

An inclusive comparison regarding aggregation of surface active ionic liquid and conventional surfactant with a cationic dye Acridine Red exposed in view of spectroscopic and theoretical study.

An inclusive comparison regarding aggregation of surface active ionic liquid and conventional surfactant with a cationic dye Acridine Red exposed in view of spectroscopic and theoretical study

Abstract

The investigation was conducted on the interaction of acridine red (AR) with sodium dodecyl sulfate (SDS) and 1-butyl-3-methyl imidazolium octyl sulfate (BMImOS) in both premicellar and post micellar concentrations. The interaction between AR and room temperature ionic liquid (RTIL) 1-butyl-3-methyl imidazolium bromide (BMImBr) was studied to understand the effect of imidazolium cation on micellization. Spectroscopic experiments, such as UV-visible absorption spectroscopy, steady-state fluorescence spectroscopy, time-resolved fluorescence spectroscopy, and dynamic light scattering, have been introduced. Various important parameters like spectral shifts, anisotropy, and aggregation number have been determined spectroscopically. However, a fresh insight into density functional theory calculations has also been provided. The observed results have been explained in terms of the aggregation behavior of the amphiphiles. A prominent redshift accompanied by a change in intensity is observed in the presence of surfactant and SAIL. However, in the case of BMImBr, no such spectral shift has been observed; only a decrease in spectral intensity highlights the quenching ability of the imidazolium cation. Average lifetime also provides some additional information regarding the difference in the formation of aggregates by SDS and BMImOS, which is further established from particle size density obtained from DLS. The salt like role of 1-butyl-3-methyl imidazolium cation also has been logically explained by anisotropy measurement and the determination of aggregation number. Using Gauss View 5.0 and Gaussian 09 package, the energy of optimization of each set of amphiphiles along with dye has been determined to follow

the interaction at the molecular level. TDDFT calculations have also been performed to determine the structure of HOMO and LUMO.

1. Introduction

In the past few decades, the interaction of ionic dye and ionic surfactants having the same or opposite charges generated a significant amount of coverage and discussion due to its widespread applications in various fields like textiles dying [1, 2], food [3-5], photography [6], printing ink, hair coloring [7], sustainable wastewater treatment [8, 9], etc. Moreover, besides those industrial applications, surfactant dye association is important in various analytical and pharmaceutical fields like spectrophotometric determination of metal ions [10], biological transportation [11], medicinal photosensitization [12, 13], etc. Surfactants are used in drug delivery [14-16], food processing [17, 18], petroleum industries [19, 20], and traditional household products like detergents [21]. Despite the above-mentioned usefulness, surfactants are hazardous to the environment [22, 23]. In recent eras, room temperature ionic liquids (RTILs) have had a promising future due to their unique physical properties such as low melting point, negligible vapor pressure, high viscosity, thermal stability, inclusive electrochemical window, and less toxic environmental effect [24-27]. The presence of these particular features allows these solvents to be classified as green solvents. Ionic liquids with long alkyl chains are surface active ionic liquids (SAILs), a combination of ionic liquid and a short-chain surfactant moiety. SAILs have been used extensively in fuel [28, 29], nanoparticle synthesis [30, 31], catalysis [32, 33], advanced material fabrication [34, 35], drug delivery [36, 37], polymerization [38, 39], separation, and extraction processes [40, 41]. However, SAILs containing 1-alkyl-3-methyl imidazolium cations have shown much prospect for academic and industrial purposes [42]. This work utilizes sodium dodecyl sulfate (SDS) as a surfactant and 1-butyl-3-methyl imidazolium octyl sulfate (BMImOS) as SAIL. SDS is an anionic surfactant that has been studied extensively for its interaction with cationic dyes, such as methylene blue [43],

rhodamine [44], and acridine orange [45], using spectrophotometry. It can solubilize and encapsulate dyes, altering their spectral properties and physical behavior by forming micelles. In aqueous media, BMImOS, having a polar head group is used to form micelles [46]. The photophysical properties [47] and interaction of BMImOS with coumarin [48], Safranine T, and Congo red [49] have been previously investigated. Furthermore, the literature reports the aggregation behavior of BMImOS in mixed micellar systems [50] in both aqueous and organic media. This work aims to compare conventional surfactants' aggregation behavior and similar structures of SAILs. In this study, we have opted to use acridine red (AR) as a probe. AR is a unique fluorescent, basic, cationic azo dye with distinct chemical properties that make it suitable for various applications such as photocatalysis [51], inclusion, and complexation behaviors of native and modified cyclodextrins [52, 53], and other modified supramolecular systems like 2,4,6-triaryl pyridine-modified cyclodextrin [54]. It is also utilized as a probe to improve the fluorescence intensity of nucleic acids [55]. However, the interaction of AR with surface active agents is very much less reported [55]. We aim to find out the difference in solubilization of AR in SDS and BMImOS aggregation, respectively. Moreover, BMImOS contains an imidazolium ring in many biologically important molecules, such as the amino acid histidine. To understand the role of imidazolium cation upon micellization, an RTIL, named 1-butyl-3-methyl imidazolium bromide (BMImBr) has been introduced to interact with AR. Several spectroscopic techniques like UV-visible spectroscopy, steady-state and time-resolved fluorescence spectroscopy, and anisotropy measurement have been made to explore the nature of the interaction, aggregation behaviour, and spectral changes in an aqueous medium. Moreover, a DFT study has also been conducted to understand better the molecular and non-covalent interactions at the molecular level.

2. Experimental

2.1. Materials

Acridine red (AR) (purity > 99%), pyrene (purity ≥ 98%), sodium dodecyl sulfate (purity ≥ 98%), cetylpyridinium chloride (purity ≥ 98%), 1-butyl-3-methyl imidazolium bromide (purity≥ 97%), and 1-butyl-3-methyl imidazolium octyl sulfate (purity≥ 98%) were purchased from Sigma Aldrich company. All chemicals were used without further purification. Double distilled water was used to prepare all the solutions for the experiments.

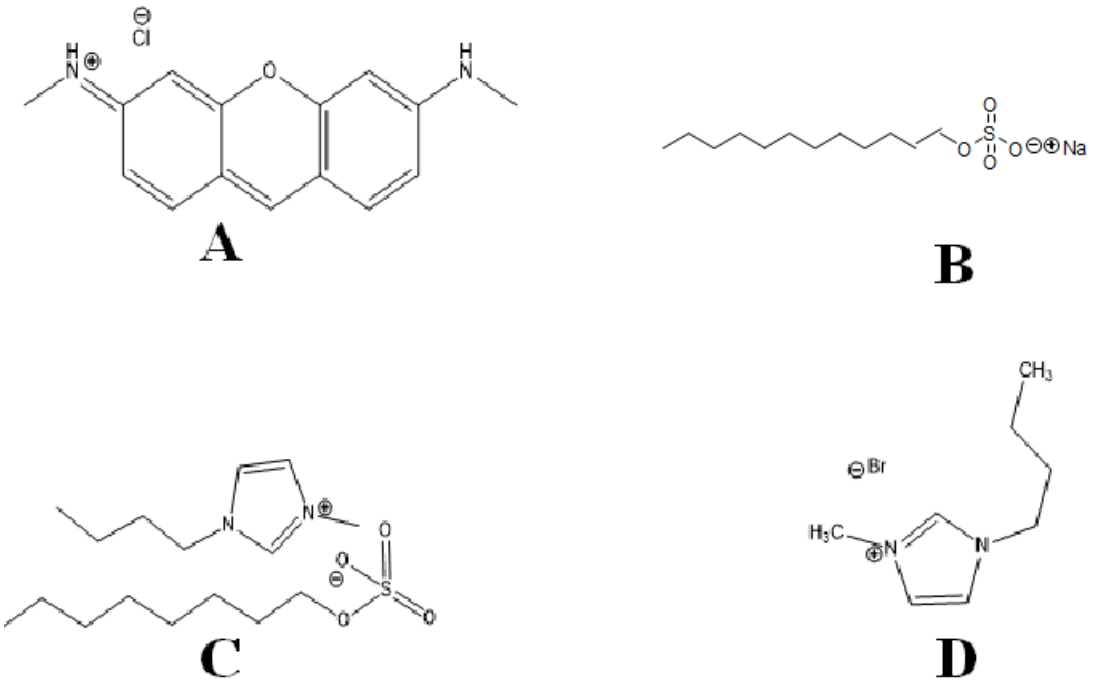

Figure 1. Structures of the materials used: (A) Acridine red, (B) Sodium dodecyl sulfate, (C) 1-butyl-3-methylimidazolium octyl sulfate and (D) 1-butyl-3-methylimidazolium bromide.

2.2. Preparation of Stock Solution

A 1.0 mM stock solution of acridine red (AR) has been prepared by taking of known weight of the respective compound in water. The required experimental concentration of dye was produced by diluting the stock solution. The concentrations of all the amphiphiles in the

aqueous solution have been kept ~ 15 times greater than their corresponding CMC. However, CMC values of SDS [56] and BMImOs [48] are available in the literature, but the CMC of BMImBr was not found there. Spectrofluorometric determination of CMC of BMImBr was carried out before making the stock solution. All the solutions were sonicated properly to get clear solutions.

2.3. UV visible spectral measurements

Absorbance was measured in a UV 1601 Shimadzu (Japan) spectrophotometer using a 10mm path-length quartz cuvette. The spectra have been measured in 200-800nm wavelength range. 5µL stock solution of acridine red was added in 2mL of water taken in a cuvette so that the concentration of dye solution became 0.0025mM. The AR concentration was deliberately kept very low to avoid self-aggregation of dye molecules and reduce the van der Waals force of attraction between the hydrophobic parts of neighbouring dye molecules. The gradual addition of SDS, BMImOs, and BMImBr has been carried out in different sets using an aqueous solution of AR to record the microenvironment's premicellar and post-micellar behaviour. The cell was kept at a constant temperature (25± 0.1) °C by circulating a water bath. All these experiments are repeated twice to minimize errors.

2.4. Steady-state fluorescence study

Fluorescence spectra, emission intensity, and anisotropy measurements were done by Perkin Elmer LS 55 fluorescence spectrophotometer attached with a Peltier facility at 298.15K with an accuracy of ±0.02K with a 10 mm path length quartz cuvette. A 5µL stock solution of AR was added to 2mL water in a cuvette to record fluorescence spectra. However, here, [AR] is also 0.0025mM. Fluorometric titrations were carried out by gradual addition of SDS (0 to ~10mM) and BMIMOS (0 to ~ 144mM) and BMImBr (0 to ~14mM) to each set of the same concentration of AR. Emission spectra were recorded from 520nm to 630nm, with excitation and emission slit widths fixed at 15.0 nm and 2.5 nm, respectively. The scan time was fixed at

250 nm/ min. Anisotropy was measured at the wavelength of excitation at 480 nm and emission at 562.5 nm for AR. The measured anisotropy value was the average of six consecutive values. All the anisotropy values were averaged over an integration time of 20 s, and temperature was fixed at 298.15K by circulating water through Peltier. The sample temperature was maintained at 298 K before each measurement. All these experiments were repeated twice to minimize errors.

2.5. Time-resolved fluorescence study:

Time-resolved fluorescence spectral analysis was carried out using the time-correlated single photon counting (TCSPC) technique in the Horiba-Jobin-Yvon Cube fluorescence lifetime system using NanoLED at 370 nm (IBH, UK) as the excitation source for AR and TBX photon detection module was used as a detector. The decaying data were fitted using IBH DAS-6 decay analysis software. The lamp profile was collected by placing a dilute micellar solution of SDS in water as a scatterer in place of the sample. The accuracy of fits was evaluated from the χ^2criterion and visual inspection of the residuals of the fitted function to the data. Mean (average) fluorescence lifetimes (τ_{avg}) for bi-exponential iterative fittings were calculated from the decay times (τ_1 and τ_2) and the pre-exponential factors (a_1 and a_2) by using the following relation.

$$\tau_{avg} = a_1\tau_1 + a_2\,\tau_2$$

However, the dye, surfactant and ionic liquid concentration were kept constant like steady state emission spectral analysis.

2.6. Dynamic Light Scattering (DLS):

DLS measurement was performed using Nano ZS Zetasizer (Malvern, UK), measuring at 900 angles with an exposure of a He-Ne laser. The temperature has been kept constant throughout the experiment at 25^0C. A set of different concentrations of solutions is taken for the measurement. The water solution of dye, premicellar, and post micellar concentration of SDS,

BMImOS, and BMImBr are added to the aqueous solutions of AR for different sets. All experiments are repeated twice for reproducibility, and the generated % of intensity *vs.* size (r nm) has been plotted.

2.7. Density functional theory calculations:

Density functional theory calculation has recently been of supreme importance to understanding covalent and non-covalent interactions at the molecular level. Structures of AR, SDS, BMImOS, and BMImBr were drawn using Avogadro software and these structures were further refined by using auto-optimization tools obtained in Avogadro software. The force field of auto optimization was MMFF94S, where steps per update were 4, and the steepest descent algorithm was used. Moreover, to determine the energy of interaction of AR with various amphiphiles in a ratio of 1:1 molecular level, energy optimization has been carried out of these pre-optimized structures using Gaussian 9 software. All calculations were carried out using b3lyp functional and 6-31g (d, p) basic set. TDDFT calculations have also been performed to know the structures of the highest occupied molecular orbital (HOMO) and lowest unoccupied molecular orbitals (LUMO) in order to illustrate the nature of interactions between dye and several added amphiphiles.

3. Results and discussion:

3.1. Absorption and emission spectra of AR:

AR in a very dilute aqueous solution shows absorption maxima at the wavelength region of ~ 543 nm (λ_{max}) along with a shoulder at the wavelength region of~505 nm. This observation is very similar to the literature [57]. The formation of this shoulder may be due to π-π stacking of the dye molecules causing H type of aggregation [58] or maybe low lying n→π* transition caused by the heterocyclic oxygen atom present in the aromatic ring. The amine group present as a substituent shows a very low tendency towards n→π* transition; rather, a lone pair of nitrogen may participate as an extended aromatic system [59], which is facilitated by the

electron-donating capability of the substituent, $-CH_3$ group present in the ammine nitrogen. As a result, $\pi \rightarrow \pi^*$ transition becomes more intense and appears in higher wavelength regions [60]. AR shows emission maxima ($\lambda_{emission}$) at the wavelength region of~ 562nm and also shows Stokes shift ~ 661.3 cm^{-1}. This small Stokes shift signifies that the energy difference between HOMO and LUMO of ground and excited states is high enough, and also, molecular geometries of the dye in the ground and excited state is very similar [61].

3.2. Absorption spectra of AR in the presence of surfactant and ionic liquids

Effect on the addition of SDS: Aqueous solution of SDS (120mM) has been added gradually from the concentration range of 0.28mM to 15.72mM to study premicellar and post micellar aggregation behavior and incorporation of dye into micelle (Figure 2A). However, at a premicellar concentration of SDS, increase in absorbance intensity without any appreciable change in λ_{max} value, indicating an electrostatic force of attraction between the cationic dye molecule and an oppositely charged polar head group of surfactants, and this results in the formation of dye-surfactant salt-like ion pair or a dye-rich dye-surfactant mixed micelle. However, when the concentration of SDS approaches its CMC, a redshift of ~ 4 nm is observed, along with an increase in absorption intensity. When [SDS] > CMC, absorption decreases with the same bathochromic shift. The addition of SDS to the cationic dye AR at premicellar concentration facilitates the formation of a special kind of micelle called dye – dye-surfactant mixed micelle or dye-surfactant salt-like ion pair. The formation of this type of complex is mainly due to the electrostatic force of attraction created between cationic dye and anionic surfactant. There will also be a chance of van der Waals's force of attraction between hydrophobic moieties of dye and surfactant, which may also be slightly responsible for the incorporation of dye into the stern layer of the micelle. However, the spectral behaviour also may be explained in terms of the change in the polarity of the medium. The addition of SDS decreases the polarity of the microenvironment in which AR becomes solubilized, and hence,

the energy gap between π and π* orbitals increases, and the probability of π→π* transition decreases to a great extent, and so absorption intensity reduces.

Effect on the addition of BMImOS and BMImBr:

BMImOS (0.5M) solution is added gradually from a concentration range of 2.94 mM to 75.04 mM. Adding BMImOS to the aqueous solution of AR causes a change in UV-visible absorption spectra (Figure 2B). According to the literature, the critical micelle concentration (CMC) of BMImOS is around 40 mM [62]. The experimental concentration of BMImOS ([BMImOS]) varies from its premicellar concentration to its post-micellar concentration. When [BMImOS] is <CMC, a prominent bathochromic shift of 3 nm occurs along with an increase in absorbance intensity. This phenomenon may be explained by the creation of a new type of interaction, especially, the electrostatic force of attraction between AR and the polar head group, octyl sulfate of BMImOS. Solubilization of AR in water produces hydrogen bonds like several weak van der Waals forces of attraction. The addition of this ionic liquid initially causes rupture of weak van der Waals force of attraction as BMImOS tends to reside on the interstitial space of AR molecules, and the formation of AR-rich AR-BMImOS mixed micelle or AR-BMImOS salt-like ion pair is possible. An increase in the concentration of BMImOS results in the formation of a new micellar environment from polar premicellar to the nonpolar micellar environment where AR is solubilized. This phenomenon can be attributed to a red shift of 4nm that appears when [BMImOS] is ≥CMC. This dehydration (replacement of water molecules by octyl sulfate chain of BMImOS) causes a decrease in the polarity of the AR-BMImOS microenvironment, and the probability of n→π* transition increases than that of π→π* [63]. This causes a reduction in absorbance intensity. However, in the case of another ionic liquid, BMImBr, no significant absorption spectral shift is observed except for an increase in absorption intensity at a very low concentration, and intensity gradually decreases with an increase in concentration (Figure 2C). This characteristic observation can be explained in terms

of the surface activity of ionic liquid moiety. As BMImBr does not have a long hydrophobic chain, it will not go to the solubilized dye molecule; rather, it will sustain itself just like an ion pair.

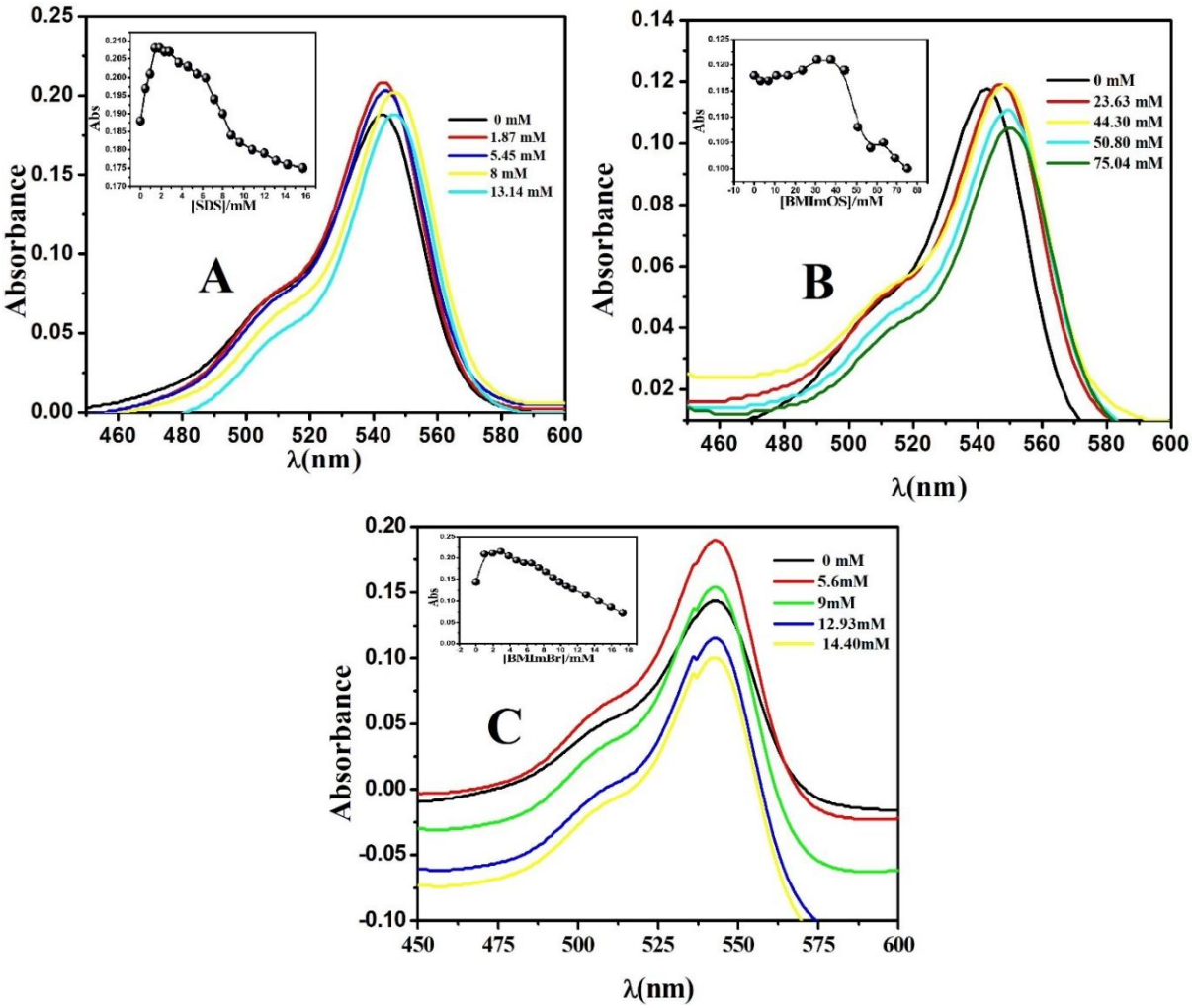

Figure 2. Absorbance of AR with varying concentrations of (A) SDS, (B) BMImOS and (C) BMImBr at different wavelengths, (Inset shows Absorbance vs. corresponding [amphiphile]).

3.3. Emission spectra of AR in the presence of surfactant and ionic liquids

Effect on the addition of SDS:

Figure 3A shows the change in emission spectra of AR in the presence of SDS. With the addition of SDS in the premicellar region, i.e., [SDS] ≤ CMC, a small red shift along with a lowering of fluorescence intensity occurs. This observation can be explained in terms of excited

state complex formation between AR and SDS. This exciplex formation causes dynamic quenching in

fluorescence intensity due to the de-excitation of exciplex. Further addition of SDS creates a micellar microenvironment where dissociation of these exciplexes is possible; AR becomes solubilized in the stern layer of the micelle, where the hydrophobic part of AR is expected to be closer to the micelle. As a result, when [SDS] is ≥ CMC, a greater bathochromic shift (5 nm) appears along with an increase in intensity.

Effect on the addition of Ionic Liquid:

Ionic liquids interact differently with AR, as they contain imidazolium cation, which acts as a charge acceptor, and this causes gradual quenching [64] in emission intensity. The addition of BMIMOS in the water solution of AR results in a bathochromic shift along with a decrease in emission intensity at constant intervals (Figure 3B). However, this bathochromic shift specifies intercalation of AR and AR-imidazolium cation exciplex to the vicinity of a stern layer of the micellar environment created by the octyl sulfate chain. This intercalation changes the microenvironment's polarity towards a more nonpolar phase following a bathochromic shift in emission spectra. Moreover, positively charged imidazolium cation is also able to reduce the mutual electrostatic repulsion among a head group of octyl sulfate chains [65] and facilitates the insertion of AR into the micellar medium. As a result, the gradual addition of BMImOS results in a quenching in fluorescence intensity (Table 1) along with redshift due to dissociation and de-excitation of exciplexes. The addition of BMImBr in the aqueous solution of AR results in no spectral shift; only a decrease in intensity is observed (Figure 3C). As BMImBr has very low surface activity and its counter ion is very small, so BMImBr shows no interaction with AR. Hence, it can be concluded that surface activity is the most important parameter for interaction with AR. As SDS and BMImOS both have surface activity and an ability to

transform from polar media to a non-polar microenvironment, so they have the ability to solubilise AR in the vicinity

of a non-polar microenvironment.

Table 1. Various spectroscopic parameters and calculation of Stokes' shift of AR and AR-amphiphiles in their pre-and post-micellar concentration.

Concentration (mM)	***λ_{max}^{abs}(nm)***	***Absorbance***	***λ_{max}^{flu}(nm)***	***Fluorescence Intensity***	***Stokes shift (Δv, cm^{-1})***
AR in water					
--	542.5	0.188	562.5	159.1	655.4
AR in SDS					
2.33	543.45	0.207	563.19	128.63	644.9
8	546.87	0.199	567.62	150.90	668.4
10.8	547.21	0.193	566	149.82	606.67
AR in BMImOs					
23.63	547.29	0.188	567.38	116.31	647
44.3	548.32	0.187	568.58	107.81	650
75.04	550.34	0.165	570.61	82.61	645.5
AR in BMImBr					
5.6	543	0.244	562.34	147.54	633.3
9	542.6	0.198	562.34	140.43	647
12.93	542.9	0.147	562.4	134.75	638.6

Formation of this kind of dye-surfactant salt like ion pair or exciplexes can be assumed as an intermediate species in electron transfer from donor to accepter, which may be further concluded by using some theoretical method with the help of calculation of the energy gap between HOMO and LUMO. Furthermore, the increase in stokes shift values follows a similar

pattern to the concentration of amphiphiles. This indicates high solvent reorganization around the fluorophore, making the dye mobile or less rigid. However, in the post-micellar region of the amphiphiles, it decreases, suggesting an incorporation phenomenon of the dye in the vicinity of the stern or palisade layer of the micellar environment.

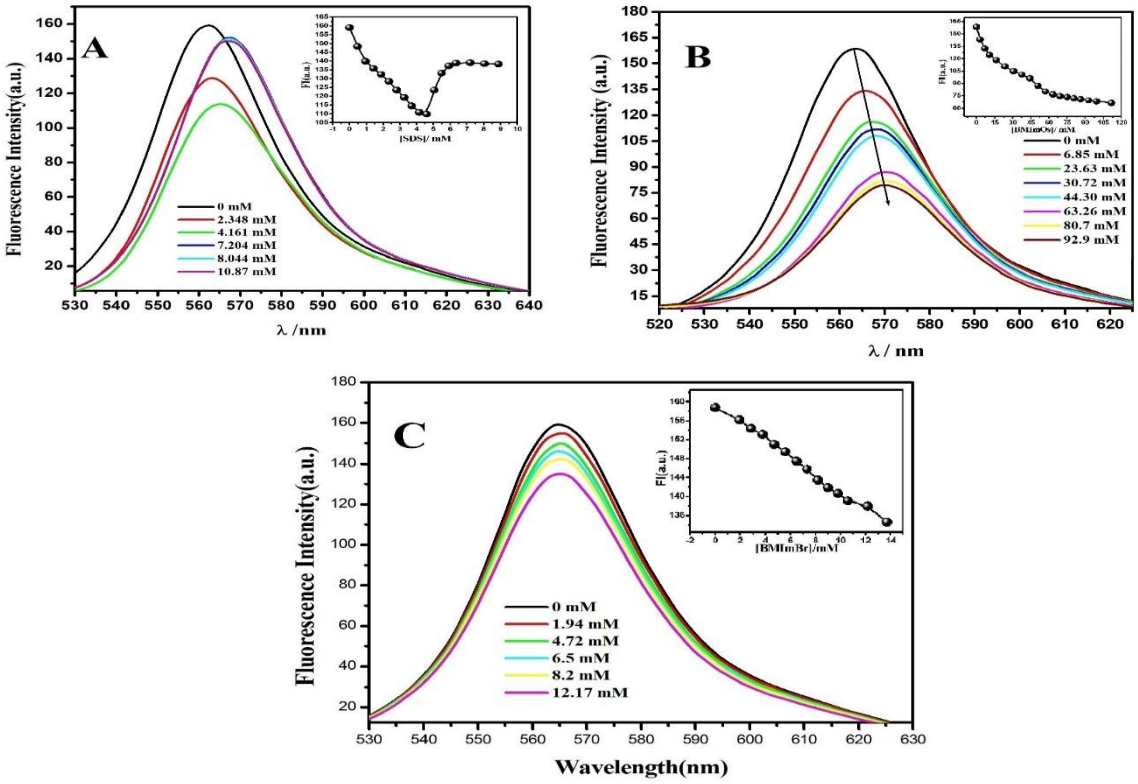

Figure 3. Variation of Fluorescence intensity of AR with varying concentrations of (A) SDS, (B) BMImOS, and (C) BMImBr (Inset shows Fluorescence Intensity vs. corresponding [Amphiphile]).

3.4. Steady-state Anisotropy study of AR with different amphiphiles

Measurement of Anisotropy can give a piece of information about rotational diffusion, molecular orientation, and rigidity of the microenvironment [66 - 68]. Anisotropy (r) can be measured by using the following equation,

$$r = \frac{I_V - GI_H}{I_V + 2GI_H} \qquad (1)$$

where I_V and I_H are the intensities of excitation light towards parallel and perpendicular directions, respectively, arising from the probe's vertically polarised excitation.

Factor G is defined as, $$G = \frac{I_V}{I_H} \quad (2)$$

In this experiment, variation of anisotropy with [SDS], [BMImOs], and [BMImBr] has been graphically represented in Figure 4. It is clearly evident that variation of anisotropy follows the same sigmoidal pattern (r = 0.99) in the case of SDS and BMImOs. However, in the case of BMImBr, no significant change in anisotropy has been observed. This observation can be illustrated in terms of rotational diffusion of AR in various amphiphilic media. SDS and BMImOs have surface activity inserted with AR in the vicinity of micellar environment, causing an increase in anisotropy because incorporation of AR in the rigid hydrophobic region of spherical amphiphile aggregate causes wobbling, as well as translational motion of dye molecule at the surface of micelle, is rendered [69]. However, as BMImBr exhibits very low surface activity, it forms an AR-BMImBr salt-like ion pair, so the motion of AR in the solution is not restricted, which causes no significant change in anisotropy (Table 2).

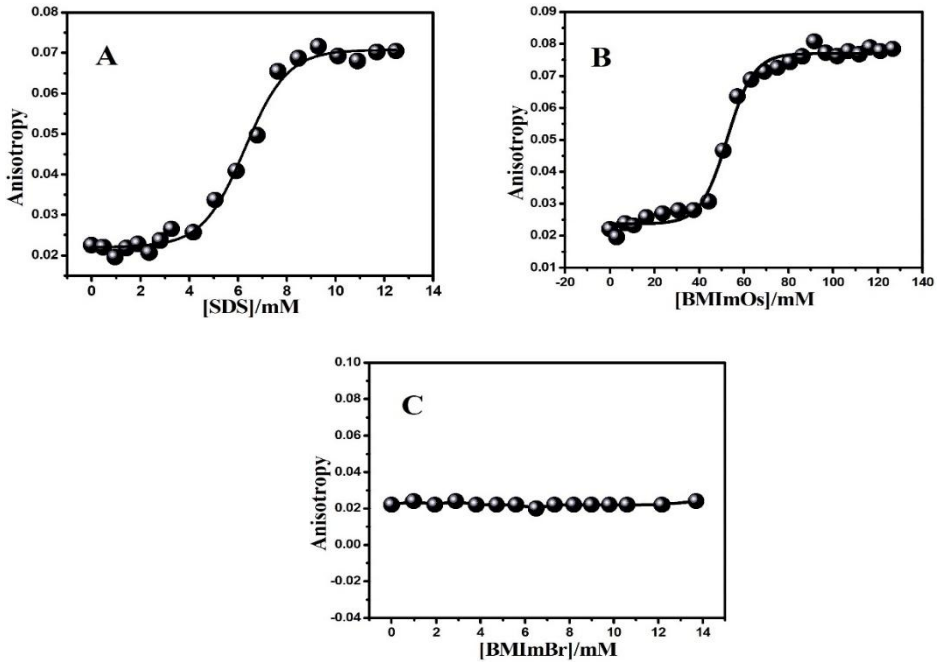

Figure 4. Variation of the anisotropy of AR with different concentrations of (A) SDS, (B) BMImOS, and (C) BMImBr.

3.5. Measurement of Aggregation Number

The aggregation number (N_{agg}) is the number of surfactant monomers accompanying CMC [70]. The determination of the aggregation number is an important parameter for understanding the accumulation behaviour of the microenvironment. In this work, aggregation numbers of dye-amphiphile binary systems have been determined by steady-state fluorescence quenching measurement. AR itself can act as a probe, and CPC can act as a quencher. In this experiment, it has been assumed that only static quenching is happening, i.e., AR and CPC are soluble in micellar pseudo-phase. All the amphiphiles were added in a concentration 15 times higher than that of their CMC values. The aggregation number was determined by the gradual addition of CPC up to 100µL to the 2mL solution of SDS, BMImOS, and BMImBr. In all solutions, 5µL of AR (10^{-3}M) has been added previously, and in aqueous solution, [SDS], [BMImOS], and [BMImBr] were 120 mM, 607 mM, and 97.5 mM, respectively. A regular pattern of fluorescence quenching is observed, supporting the Stern-Volmer equation,

$$\ln \frac{I_0}{I} = \frac{[Q]}{[Mic]} \qquad (3)$$

where I_0 and I are the fluorescence intensities in the absence and presence of the quencher, respectively, [Mic] is the concentration of the micelles, and [Q] is the total concentration of the quencher. [Mic] can also be written as

$$[Mic] = \frac{[S]-CMC}{N_{agg}} \qquad (4)$$

[S] is the concentration of various amphiphiles taken for experiments.

So, by combining equations 3 and 4, one can obtain,

$$\ln \frac{I_0}{I} = \frac{N_{agg}[Q]}{[S]-CMC} \qquad (5)$$

Equation 5 predicts a linear plot between ln (I_0/I) and [Q] with a slope equal to N_{agg}/ ([S]-CMC). So, from the slope, the aggregation number can be determined (Figure 5). The values of aggregation numbers have been depicted in Table 4. However, the exceptionally high N_{agg}

value of AR-BMImOS again supports the efficiency of the salt-like nature of the imidazolium cation. The presence of the imidazolium cation in the stern layer of the micelle favors the formation of a very large micelle by reducing the mutual electrostatic repulsion of the negatively charged head group of the octyl sulfate chain. This causes immense association of the octyl sulfate chain monomers. In the case of the AR-SDS system, small counterion Na^+ may get hydrated by surrounding water molecules. Therefore, it is not effectively engaged in reducing the mutual electrostatic repulsion of the polar head group of SDS. As a result, a smaller amount of monomers are associated, causing a lesser value of N_{agg}. The AR-BMImBr system has a meager N_{agg} value due to the surface inefficiency of the BMImBr ionic liquid.

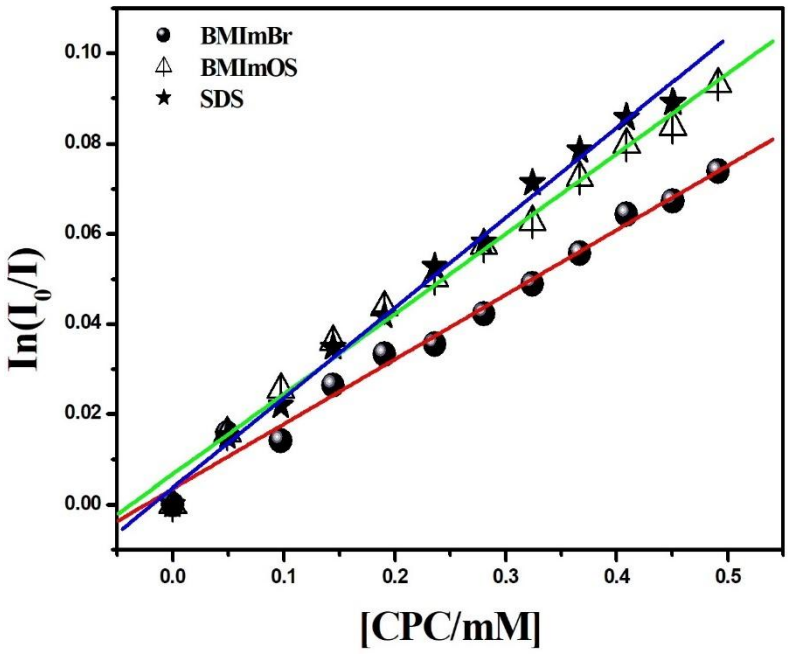

Figure 5. Plots for the determination of aggregation numbers (N_{agg}) of (a) BMImBr (b) BMImOs and (c) SDS.

3.6. Time-resolved fluorescence decay measurement

The excited state dynamics give rise to valuable information in photophysical, photochemical, and photobiological processes [71]. The stability of a probe molecule in the excited state of the micellar environment can be measured by this technique [72]. The anisotropy decay parameter of AR in water shows a double exponential decay having an average time constant of ~1.95

ns, which is very similar to what is found in the literature [57]. However, in the micellar systems, the anisotropy decays are more complex, and data can be fitted using double and single exponential decay. For double exponential decay, the anisotropy value ($r(t)$) at time t with two relaxation components, $\tau_1$and τ_2 is presented in the equation (6).

$$r(t) = r_0 \left\{ a_1 e^{-t/\tau_1} + a_2 e^{-t/\tau_2} \right\} \quad (6)$$

Here, r_0 indicates the anisotropy value at t = 0 and a_1 and a_2 are called the pre-exponential factors; in other words, a_1, a_2 are the contributing factors of each time scale component. Here, two components originate from two different environments of the probe molecules located in the water-micelle interface and penetrate into the micelle. The average value of the time scale τ_{av} is given by the equation (7) as follows:

$$\tau_{av} = a_1\tau_1 + a_2\tau_2 \quad (7)$$

In this experiment, the surfactant and both the ionic liquids have been added in their pre- and post-micellar concentrations to observe both pre- and post-micellar aggregation (Figure 6). However, in the case of [SDS] < CMC, the average lifetime of the excited state decreases (Table 2). This observation is very much compatible with observed steady-state fluorescence quenching and can be explained by diffusion-controlled collisional deactivation of the excited state of AR-SDS exciplex. Gradual increment in [SDS] results in an increase in average lifetime. However, at [SDS] ≥ CMC, micellization as well as solubilisation of AR into the vicinity of the hydrophobic core of the micelle take place, resulting in the subsequent increment of the values of fluorescence anisotropy and average lifetime. As in the micellar environment, the motion of the fluorophore has been restricted, so all types of translational, rotational, and vibrational relaxation processes are not observed.

The addition of BMImOS leads to a very interesting observation in premicellar concentration. When [BMImOS] < CMC, a single exponential decay leads to a 100% contribution of AR in a

fixed location of the microenvironment. Moreover, this observation is also commensurate with a very high aggregation number of BMImOS micelle. These two observations lead to the introduction of the role of 1-butyl-3-methyl imidazolium cation in the formation of micelle. This cation may be placed in either the stern layer or in the palisade layer of the micelle to reduce mutual electrostatic repulsions of polar head groups of octyl sulfate anion. As a result, more monomers come together to form micellar aggregates, and the increment of spacing of polar head groups facilitates the entry of AR into the hydrophobic region even at premicellar concentration. This hypothesis explains the observation of mono-exponential decay along with the highest contribution in one location of the entire microenvironment and also an increase in an average lifetime. In the case of [BMImOS] ≥ CMC, a slight increase in average lifetime is observed with double exponential decay, although the contribution of the slow component is very low. The addition of BMImBr results in no such change in a lifetime and anisotropy value in comparison with the average lifetime of an aqueous AR solution. Because this ionic liquid does not have much surface activity, there is no such hydrophobic core to stabilize the excited state of the AR-BMImBr salt-like ion pair.

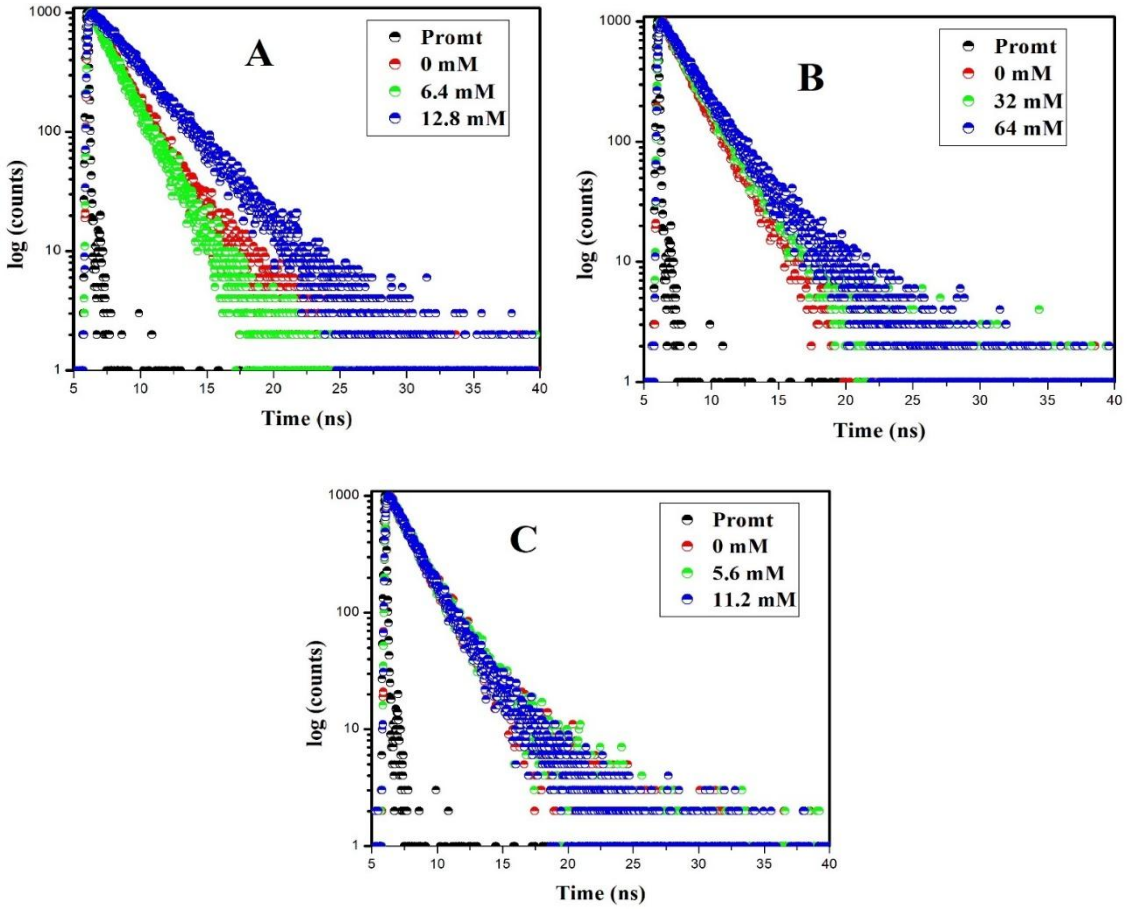

Figure 6. Time-resolved fluorescence spectra of AR along with premicellar and post-micellar concentrations of (A) SDS, (B) BMImOS, and (C) BMImBr.

Table 2. Time-resolved decay parameters and anisotropy (r) of (a) AR in water, (b) AR in SDS (pre- and post-micellar), (c) AR in BMImOS (pre- and post-micellar), and (d) AR in BMIMBr (pre- and post-micellar) media

Concentration (mM)	τ_1(ns)	a_1	τ_2(ns)	a_2	τ_{avg}(ns)	χ^2	r
AR in water							
0	1.52	0.51	2.79	0.48	1.95	1.000664	0.022
AR in SDS							
6.4	1.04	0.10	2.02	0.89	1.84	1.02522	0.049
12.8	0.41	0.02	3.20	0.98	2.83	1.030184	0.070
AR in BMImOS							
32	2.22	1.00	-	-	2.22	1.196238	0.027
64	2.04	0.73	4.16	0.26	2.36	1.085671	0.061
AR in BMImBr							
5.6	1.43	0.40	2.70	0.60	1.99	1.100046	0.022
11.2	1.53	0.52	2.79	0.48	1.96	1.042598	0.022

3.7. Dynamic Light Scattering (DLS):

DLS study has been introduced to detect the Brownian motion of particles, the size of the macromolecules and their relative existence in the dye-amphiphile aqueous mixture [73, 74]. However, this study is very much obvious to understand various types of aggregations of AR with several amphiphiles in their pre- and post-micellar concentrations. In this measurement, 5µL of an aqueous solution of AR (10-3M) is taken in a 2mL of a cuvette, and SDS, BMImOS, and BMImBr are added in each set in their pre-and post-micellar concentrations, respectively. For [SDS] < CMC, aggregate size (r) varies in the range of 43-50 nm. However, for [SDS] > CMC, r varies in the range between 91-220nm (Figure 7). The increment of this aggregate size, as well as the existence of a variety of aggregates with different sizes, is also in agreement with previous observations. In post micellar concentration, the existence of AR is not only limited to the hydrophobic core of the SDS micelle, but AR also exists in the stern layer and palisade layer and also forms either dye-rich or surfactant-rich salt-like ion pairs. In other words, in AR-SDS salt-like mixed micelle, a maximum number of aggregates (92.1%) exists in the radius range ~ 164 nm, so it can be concluded that the radius of AR-SDS micelle is the same. However, in the pre-micellar concentration of BMImOS, the value of r is much higher than that of SDS, and maximum aggregates coexist in the size range of r from 122nm to 190nm. This further leads to the fact that imidazolium cation reduces electrostatic repulsion created between octyl sulfate monomers, and a large number of octyl sulfate chains is accumulated along with AR to form a premicellar aggregate sufficiently well than SDS. Moreover, [BMImOS] > CMC, aggregate size range becomes 220nm to 342 nm, having a maximum intensity of 255 nm (38.9%) to 295.3 nm (33.6%), which further concludes the formation of bigger micelle by BMImOS than SDS. This observation is quite commensurate with the aggregation number value. In the case of both pre- and post-micellar concentrations of BMImBr, the existence of one type of particle (mean intensity 100%) is observed where r values are 32.67 and 58.77, respectively, which may further conclude its disability to form a micelle. It can only form an

AR-BMImBr salt-like ion pair. However, a relatively lower value of r can be explained in terms of charge neutralization between AR and BMImBr, which in turn decreases intramolecular repulsive interactions. This effect makes them come closer and forms a small-sized ion pair, and this causes a lessening in aggregate size. This inference is also supported by literature [75].

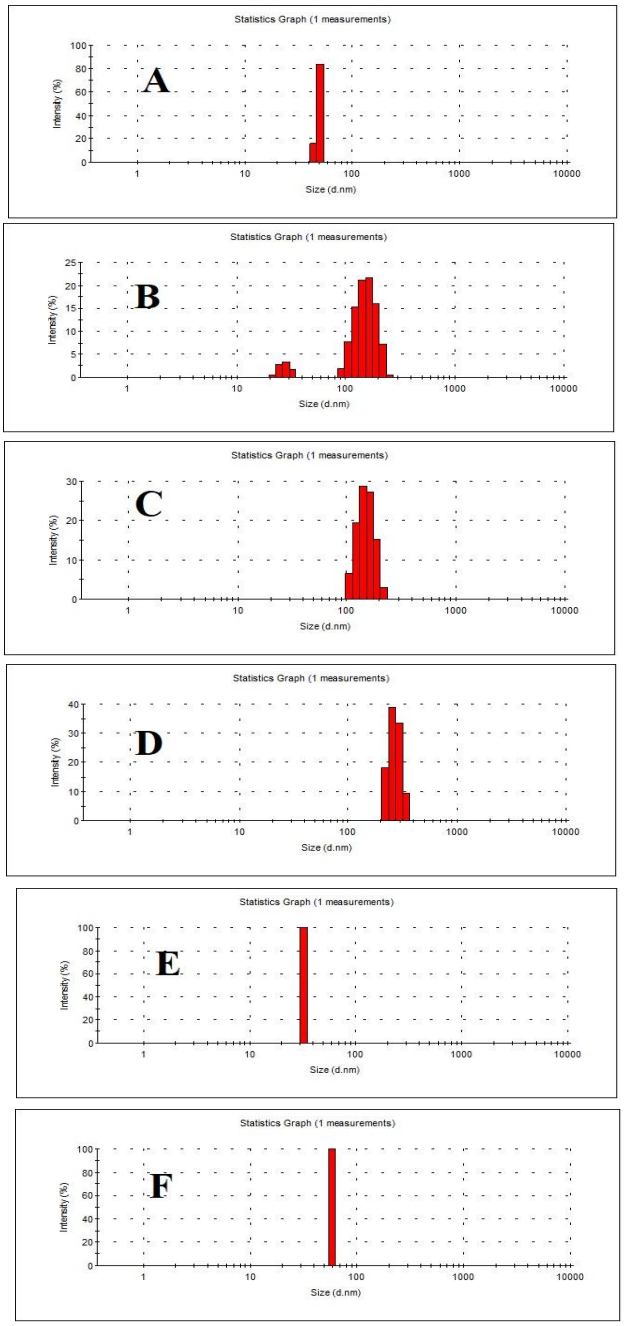

Figure 7. The size distribution of (A) SDS(5.98mM), (B) SDS (10.17mM), (C) BMImOS (24.93mM), (D) BMImOS (54.86mM), (E) BMImBr (4.98mM) and (F) BMImBr (10.97mM).

Table 3. Aggregate size range obtained from DLS measurement for (a) AR in SDS (pre- and post-micellar), (b) AR in BMImOS (pre- and post-micellar), and (c) AR in BMIMBr (pre- and post-micellar) media

Concentration (mM)	Aggregate diametre (nm)
AR in SDS	
5.98	43.82 – 50.75
10.17	91.28 – 220.2
AR in BMImOS	
24.93	122.4 – 190.1
54.86	220.2 – 342
AR in BMImBr	
4.98	32.67
10.97	58.77

3.8. Density Functional Theory Calculation:

In recent eras, the determination of molecular-level interactions by using DFT theory [76] has had a great outcome for its accuracy in predicting the position and mode of interactions at the 1:1 molecular level. In the past few years, DFT studies have become very popular in the case of dye-surfactant interactions [77, 78]. For a better understanding of the interaction of AR with various amphiphiles, DFT calculations have been made by using Gaussian 09 package to determine optimized energy (E_{opt}), energy of highest occupied molecular orbital (HOMO), lowest unoccupied molecular orbital (LUMO) and their corresponding band gap of AR, AR-SDS, AR-BMImOS, AR-BMImBr systems (Figure 8). AR, being a cationic dye, will interact with negatively charged amphiphiles primarily by electrostatic force of attraction. Hence, the optimized energy of the AR-Amphiphiles complex is much lower than AR itself due to the neutralization of charges. Among AR-Amphiphile systems, E_{opt} of AR-BMImBr is the lowest, which concludes that it forms the most stable complex salt in a 1:1 ratio due to its smallest size and being devoid of long-chain hydrophobic moiety (Table 4). However, between AR-SDS and AR-BMImOS systems, it is found that the E_{opt} of AR-BMImOS is much lower. So, it can be applicable in a 1:1 molecular ratio where the electrostatic force of attraction plays the main

role, and the AR-SDS system is the most unstable. TDDFT calculations have been made using the same functional and basic set to determine the structures of HOMO and LUMO of the same early-stated systems. However, transition contains the highest oscillator strength (f), and so the transition has been chosen for HOMO-LUMO calculations in order to get the highest transition probability. It is very interesting to observe all polar heads of amphiphiles which are potentially HOMO and π* orbitals of AR are potentially LUMO. So, it can be inferred from these observations that not only electrostatic force of attraction is created between AR-Amphiphile complexes, but the probability of intramolecular charge transfer on excitation may also be possible between AR-amphiphile complexes.

Table 4. Optimized energy, the energy of HOMO and LUMO, band gap, dipole moment, aggregation Number of (a) AR, (b) AR-SDS, (c) AR-BMImOS, and (d) AR-BMImBr systems.

System	E_{opt}(a.u)	Energy of HOMO(E_1) *(ev)*	Energy of LUMO(E_2) *(ev)*	ΔE (E_2 - E_1) *(ev)*	Dipole moment (Debye)	N_{agg}
AR	-1225.58	-0.24372	-0.10789	0.13583	16.9406	--
AR-SDS	-1936.80	-0.22328	-0.11583	0.11745	20.1961	22
AR-BMImOS	-2663.18	-0.22693	-0.11686	0.11	14.56	100
AR-BMImBr	-4220.74	-0.1835	-0.10561	0.0784	16.3413	13

From the orbital diagram, it can be observed that from Br-, the maximum electron density is shifted from the LUMO orbitals of AR (Figure 9). As Br^- has a very small size, it can reach close proximity to AR, and this causes a lowering of the energy gap between HOMO and LUMO of the AR-BMImBr complex. However, this HOMO-LUMO energy gap follows the order of AR > AR-SDS> AR-BMImOS. These observations can further conclude that AR is more stable in surfactant media than in aqueous solution. For this reason, the bathochromic

shift is observed in absorption and emission spectra, and the intensity of fluorescence lifetime also increases in both cases.

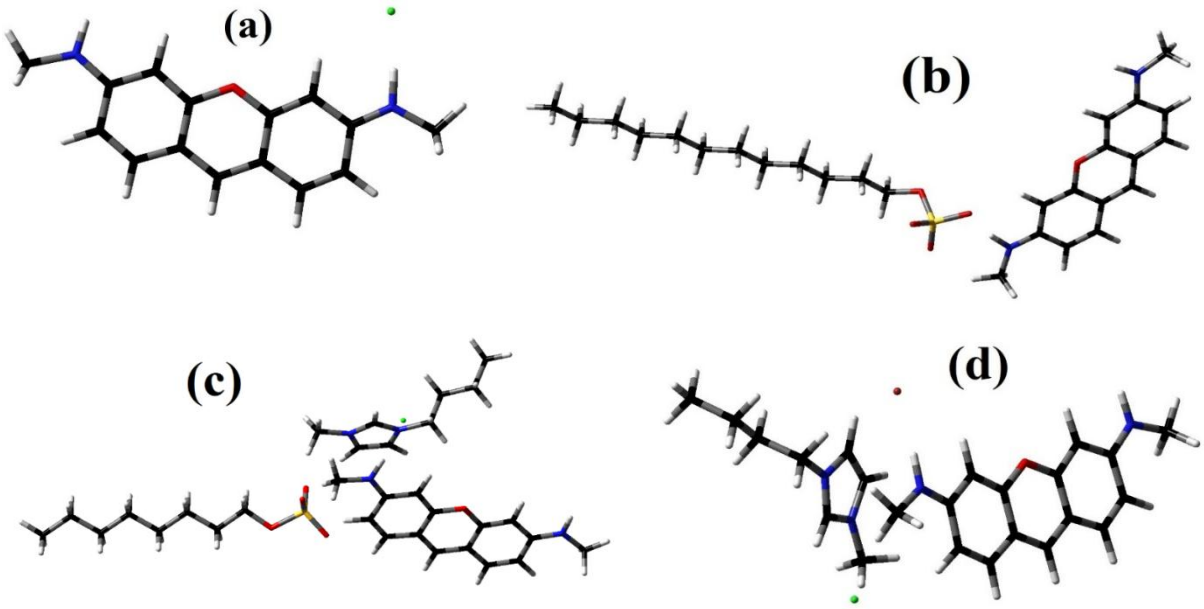

Figure 8. B3LYP/6-31g(d,p) - the optimized structure of (a) AR, (b) AR-SDS, (c) AR-BMImOS, and (d) AR-BMImBr. Color code for atoms: red, oxygen; dark grey, carbon; light grey, hydrogen; yellow, sulfur; blue, nitrogen; green, chlorine; brown, bromine.

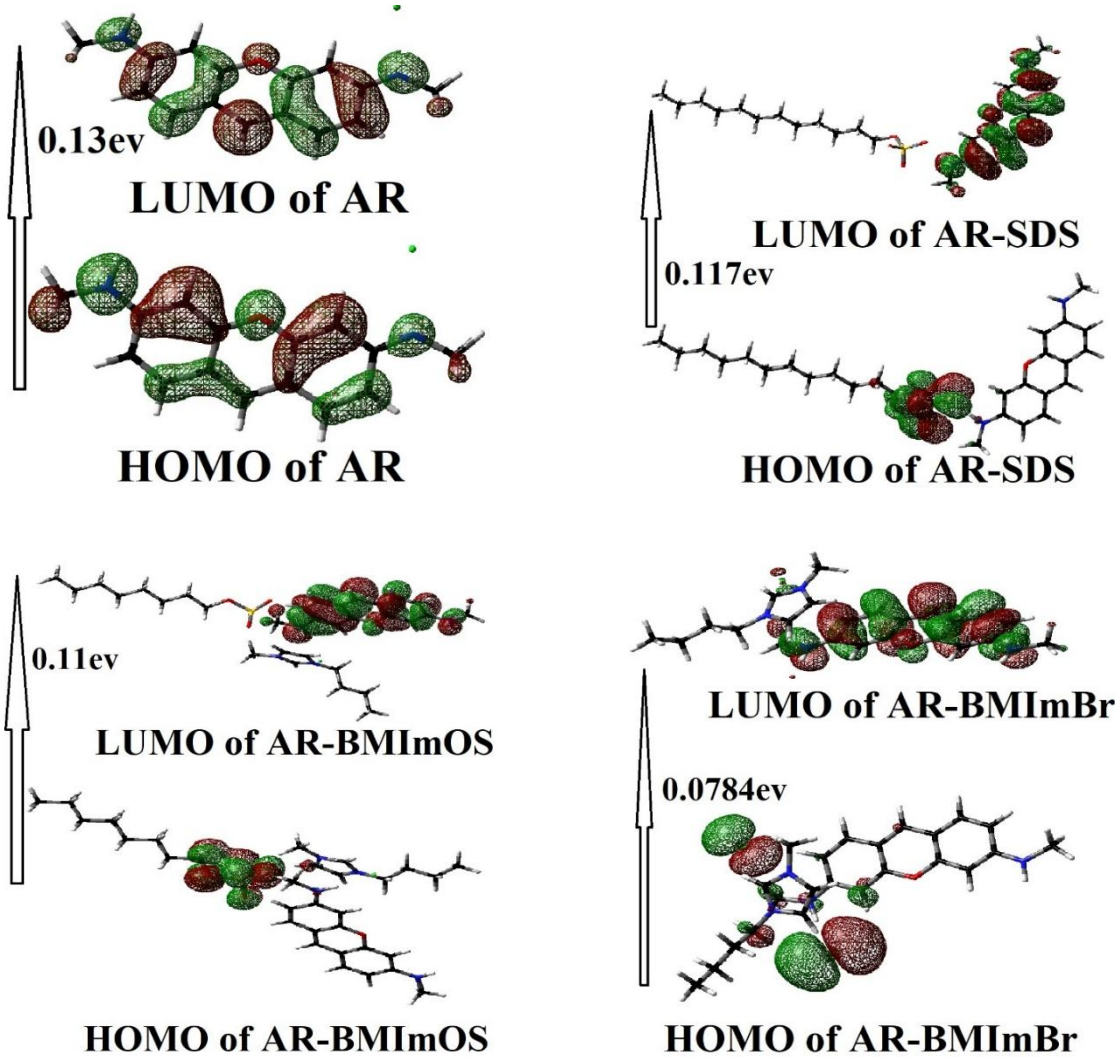

Figure 9. HOMO-LUMO diagrams of AR with various amphiphiles.

4. Conclusion

In this work, the interaction of a cationic dye with three different types of amphiphiles having opposite charges has been studied. One is a conventional anionic surfactant, SDS, and the other two are ionic liquids having different amphiphilicity. BMImOS has an octyl sulfate chain similar to SDS along with an imidazolium cation, whereas BMImBr contains only an imidazolium ring but no hydrophobic polar tail. Finally, it can be concluded that the change in polarity of the medium causes the solubilization of dye into the stern layer of the micellar environment. SDS and BMImOS both contain a hydrophobic tail, which facilitates the

formation of a micelle and solubilization of the hydrophobic portion of dye into the micelle, and the hydrophilic portion resides on the outer portion of the stern layer accompanied by water molecules, causing a bathochromic shift in both absorption and fluorescence spectra. Moreover, this phenomenon also causes an increment in the average lifetime in the TCSPC experiment. Solubilization of AR into a hydrophobic core stabilizes its excited state primarily by the formation of exciplex. Then surfactant-rich dye-surfactant mixed micelle and overall, motion-like rotational diffusion is restricted and causes an increment in anisotropy. As BMImBr does not contain long hydrophobic counter ion, it cannot solubilize AR into its micelle and exists only as an AR-BMImBr salt-like ion pair for charge neutralization. Neither absorbance and emission spectral shift, nor increment of average lifetime is evidence of this phenomenon.

However, a different mode of aggregation behaviour is also found for SDS and BMImOS. A salt-like imidazolium cation present in BMImOS facilitates the reduction of repulsive interactions of the polar head group of octyl sulfate anion. As a result, an increase in mutual spacing on a head group of octyl sulfate helps AR to enter into the stern or palisade layer in even premicellar concentration of BMImOS, whereas, in the premicellar concentration of SDS, this happening seems to be difficult. TCSPC measurement, along with the particle size obtained in DLS, can conclude this argument. Moreover, E_{opt} and diagram of HOMO and LUMO obtained from TDDFT calculation infer an electrostatic force of attraction has always been created between oppositely charged dye and amphiphiles, and an electron-rich polar head group of amphiphile moiety always resides in a state of donation into the vacant orbital of dye. Furthermore, this work is an effort to establish a more efficient solubilizing power of SAIL than conventional surfactants. We envisioned that these findings would enrich the investigation in the field of medicinal photosensitization, material fabrication, drug delivery, and so on.

REFERENCES:

[1] M. Sadeghi-Kiakhani, A.R. Tehrani-Bagha, R. Aladpoosh, E. Hashemi, Application of Different Non-ionic Surfactants on the Conventional Extraction and Dyeing Characteristics of Natural Dyes on the Wool Yarn, Progress in Color, Colorants and Coatings 17 (2024) 275-288.

[2] A.M.S. Jorge, K.K. Athira, M.B. Alves, R.L. Gardas, J.F.B. Pereira, Textile dyes effluents: A current scenario and the use of aqueous biphasic systems for the recovery of dyes, Journal of Water Process Engineering 55 (2023) 104125.

[3] V.G. Amelin, Z.A.C. Shogah, D.S. Bol'shakov, Microextraction–Colorimetric (Fluorimetric) Determination of Cationic and Anionic Surfactants in Food Products, Journal of Analytical Chemistry 76 (2021) 330-338.

[4] L. Gimadutdinova, G. Ziyatdinova, R. Davletshin, Sensors, 2024.

[5] W. Begum, B. Saha, U. Mandal, Characterization of Saponin Extracted from Acacia concinna (Shikakai or Soap Pod) and Thermodynamic Studies of Its Interaction with Organic Dye Rhodamine B, Chemistry Africa (2024).

[6] A. Srivastava, D. Elahi, M. Kumar, S. Raghav, O.G. Singh, N. Singh, Binding influence of sunset yellow dye on the sodium tetradecyl sulphate micelles in the presence of sodium carboxymethyl cellulose medium, Journal of Molecular Liquids 385 (2023) 122375.

[7] K. Yun, C. Ahn, Effect of surfactant type on the dyeability and color resistance of semi-permanent basic hair dye, Fashion and Textiles 10 (2023) 4.

[8] N. Aryanti, A. Nafiunisa, T.D. Kusworo, D.H. Wardhani, Membranes, 2020.

[9] T.U. Rashid, S.M.F. Kabir, M.C. Biswas, M.A.R. Bhuiyan, Sustainable Wastewater Treatment via Dye–Surfactant Interaction: A Critical Review, Industrial & Engineering Chemistry Research 59 (2020) 9719-9745.

[10] N.P. Milcheva, F. Genç, P.V. Racheva, V.B. Delchev, V. Andruch, K.B. Gavazov, An environmentally friendly cloud point extraction–spectrophotometric determination of trace vanadium using a novel reagent, Journal of Molecular Liquids 334 (2021) 116086.

[11] C. Peetla, V. Labhasetwar, Effect of Molecular Structure of Cationic Surfactants on Biophysical Interactions of Surfactant-Modified Nanoparticles with a Model Membrane and Cellular Uptake, Langmuir 25 (2009) 2369-2377.

[12] J. Zhao, L. Xu, H. Zhang, Y. Zhuo, Y. Weng, S. Li, D. Yu, Surfactin-methylene blue complex under LED illumination for antibacterial photodynamic therapy: Enhanced methylene blue transcellular accumulation assisted by surfactin, Colloids and Surfaces B: Biointerfaces 207 (2021) 111974.

[13] A.V. Kustov, D.B. Berezin, V.P. Zorin, P.K. Morshnev, N.y.V. Kukushkina, M.A. Krestyaninov, T.V. Kustova, A.I. Strelnikov, E.V. Lyalyakina, T.E. Zorina, O.B. Abramova, E.A. Kozlovtseva, Monocationic chlorin as a promising photosensitizer for antitumor and antimicrobial photodynamic therapy, Pharmaceutics, 15 (2023) 61.

[14] S.M. Shaban, J. Kang, D.-H. Kim, Surfactants: Recent advances and their applications, Composites Communications 22 (2020) 100537.

[15] R.J. Wilson, Y. Li, G. Yang, C.-X. Zhao, Nanoemulsions for drug delivery, Particuology 64 (2022) 85-97.

[16] Y. Liao, Z. Li, Q. Zhou, M. Sheng, Q. Qu, Y. Shi, J. Yang, L. Lv, X. Dai, X. Shi, Saponin surfactants used in drug delivery systems: A new application for natural medicine components, International Journal of Pharmaceutics 603 (2021) 120709.

[17] B.G. Ribeiro, J.M.C. Guerra, L.A. Sarubbo, Biosurfactants: Production and application prospects in the food industry, Biotechnology Progress 36 (2020) e3030.

[18] M. Zembyla, B.S. Murray, A. Sarkar, Water-in-oil emulsions stabilized by surfactants, biopolymers and/or particles: a review, Trends in Food Science & Technology 104 (2020) 49-59.

[19] O. Massarweh, A.S. Abushaikha, The use of surfactants in enhanced oil recovery: A review of recent advances, Energy Reports 6 (2020) 3150-3178.

[20] M. Mpelwa, S. Tang, L. Jin, R. Hu, C. Wang, Y. Hu, The study on the properties of the newly extended Gemini surfactants and their application potentials in the petroleum industry, Journal of Petroleum Science and Engineering 186 (2020) 106799.

[21] D. Fei, G.-W. Zhou, Z.-Q. Yu, H.-Z. Gang, J.-F. Liu, S.-Z. Yang, R.-Q. Ye, B.-Z. Mu, Low-Toxic and Nonirritant Biosurfactant Surfactin and its Performances in Detergent Formulations, Journal of Surfactants and Detergents 23 (2020) 109-118.

[22] S.O. Badmus, H.K. Amusa, T.A. Oyehan, T.A. Saleh, Environmental risks and toxicity of surfactants: overview of analysis, assessment, and remediation techniques, Environmental Science and Pollution Research 28 (2021) 62085-62104.

[23] J. Arora, A. Ranjan, A. Chauhan, R. Biswas, V.D. Rajput, S. Sushkova, S. Mandzhieva, T. Minkina, T. Jindal, Surfactant pollution, an emerging threat to ecosystem: Approaches for effective bacterial degradation, Journal of Applied Microbiology 133 (2022) 1229-1244.

[24] S. Seki, T. Kobayashi, Y. Kobayashi, K. Takei, H. Miyashiro, K. Hayamizu, S. Tsuzuki, T. Mitsugi, Y. Umebayashi, Effects of cation and anion on physical properties of room-temperature ionic liquids, Journal of Molecular Liquids 152 (2010) 9-13.

[25] H. Tokuda, K. Hayamizu, K. Ishii, M.A.B.H. Susan, M. Watanabe, Physicochemical Properties and Structures of Room Temperature Ionic Liquids. 1. Variation of Anionic Species, The Journal of Physical Chemistry B 108 (2004) 16593-16600.

[26] K.N. Marsh, J.A. Boxall, R. Lichtenthaler, Room temperature ionic liquids and their mixtures—a review, Fluid Phase Equilibria 219 (2004) 93-98.

[27] E. Kianfar, S. Mafi, Ionic liquids: properties, application, and synthesis, Fine Chemical Engineering 2 (2020) 21-29.

[28] Q. Wu, Q. Shi, J. Shang, M. Wang, H. Li, D. Shi, Y. Zhao, Q. Jiao, Synthesis of Surface-Active Heteropolyacid-Based Ionic Liquids and Their Catalytic Performance for Desulfurization of Fuel Oils, ACS Omega 5 (2020) 31171-31179.

[29] J. Ávila, D. Lozano-Martín, M. Simões Santos, Y. Zhang, H. Li, A. Pádua, R. Atkin, M. Costa Gomes, Effect of ion structure on the physicochemical properties and gas absorption of surface active ionic liquids, Physical Chemistry Chemical Physics 25 (2023) 6808-6816.

[30] K.J. Mohammed, S.K. Hadrawi, E. Kianfar, Synthesis and Modification of Nanoparticles with Ionic Liquids: a Review, BioNanoScience 13 (2023) 760-783.

[31] O. Naderi, M. Nyman, M. Amiri, R. Sadeghi, Synthesis and characterization of silver nanoparticles in aqueous solutions of surface active imidazolium-based ionic liquids and traditional surfactants SDS and DTAB, Journal of Molecular Liquids 273 (2019) 645-652.

[32] E. Szepiński, P. Smolarek, M.J. Milewska, J. Łuczak, Application of surface active amino acid ionic liquids as phase-transfer catalyst, Journal of Molecular Liquids 303 (2020) 112607.

[33] H.-P. Steinrück, P. Wasserscheid, Ionic Liquids in Catalysis, Catalysis Letters 145 (2015) 380-397.

[34] Y. Pei, Y. Zhang, J. Ma, M. Fan, S. Zhang, J. Wang, Ionic liquids for advanced materials, Materials Today Nano 17 (2022) 100159.

[35] K. Rola, A. Zając, M. Czajkowski, A. Szpecht, M. Zdończyk, M. Śmiglak, J. Cybińska, K. Komorowska, Ionic liquids for active photonics components fabrication, Optical Materials 89 (2019) 106-111.

[36] D. Zhen, M. Zhang, F. Liu, Q. Peng, Research progress of surface-active ionic liquids for drug delivery, Journal of Molecular Liquids 400 (2024) 124546.

[37] A.T. Silva, C. Teixeira, E.F. Marques, C. Prudêncio, P. Gomes, R. Ferraz, Surfing the Third Wave of Ionic Liquids: A Brief Review on the Role of Surface-Active Ionic Liquids in Drug Development and Delivery, ChemMedChem 16 (2021) 2604-2611.

[38] K. Mishra, N. Devi, S.S. Siwal, Q. Zhang, W.F. Alsanie, F. Scarpa, V.K. Thakur, Ionic Liquid-Based Polymer Nanocomposites for Sensors, Energy, Biomedicine, and Environmental Applications: Roadmap to the Future, Advanced Science 9 (2022) 2202187.

[39] P. Kubisa, Ionic liquids as solvents for polymerization processes—Progress and challenges, Progress in Polymer Science 34 (2009) 1333-1347.

[40] J. Saien, M. Kharazi, V. Pino, I. Pacheco-Fernández, Trends offered by ionic liquid-based surfactants: Applications in stabilization, separation processes, and within the petroleum industry, Separation & Purification Reviews 52 (2023) 164-192.

[41] A. Bera, J. Agarwal, M. Shah, S. Shah, R.K. Vij, Recent advances in ionic liquids as alternative to surfactants/chemicals for application in upstream oil industry, Journal of Industrial and Engineering Chemistry 82 (2020) 17-30.

[42] P.S. Kulkarni, L.C. Branco, J.G. Crespo, M.C. Nunes, A. Raymundo, C.A.M. Afonso, Comparison of Physicochemical Properties of New Ionic Liquids Based on Imidazolium, Quaternary Ammonium, and Guanidinium Cations, Chemistry – A European Journal 13 (2007) 8478-8488.

[43] P. Shah, S. Kumari Jha, A. Bhattarai, Spectrophotometric study of the sodium dodecyl sulfate in the presence of methylene blue in the methanol–water mixed solvent system, Journal of Molecular Liquids 340 (2021) 117200.

[44] S. Yamaguchi, S. Minbuta, K. Matsui, Rhodamine B adsorption on anodic porous alumina in sodium dodecyl sulfate solutions, Colloids and Surfaces A: Physicochemical and Engineering Aspects 555 (2018) 209-216.

[45] A. Dutta, R.K. Dutta, Protonation of acridine orange in dye-surfactant ion pair micelles, Journal of Molecular Liquids 178 (2013) 25-30.

[46] Z. Miskolczy, K. Sebők-Nagy, L. Biczók, S. Göktürk, Aggregation and micelle formation of ionic liquids in aqueous solution, Chemical Physics Letters 400 (2004) 296-300.

[47] S. Sarkar, S. Mandal, R. Pramanik, C. Ghatak, V.G. Rao, N. Sarkar, Photoinduced Electron Transfer in a Room Temperature Ionic Liquid 1-Butyl-3-methylimidazolium Octyl Sulfate Micelle: A Temperature Dependent Study, The Journal of Physical Chemistry B 115 (2011) 6100-6110.

[48] D. Seth, S. Sarkar, N. Sarkar, Dynamics of Solvent and Rotational Relaxation of Coumarin 153 in a Room Temperature Ionic Liquid, 1-Butyl-3-methylimidazolium Octyl Sulfate, Forming Micellar Structure, Langmuir 24 (2008) 7085-7091.

[49] N. Patra, B. Mandal, S. Ghosh, Spectroscopic Studies on the Interaction of Dye and Surface Active Ionic Liquid, Industrial & Engineering Chemistry Research 56 (2017) 10044-10052.

[50] G. Kaur, H. Kumar, M. Singla, Diverse applications of ionic liquids: A comprehensive review, Journal of Molecular Liquids 351 (2022) 118556.

[51] X. Zhu, X. Xie, P. Li, J. Guo, L. Wang, Visible-Light-Induced Direct Thiolation at α-C(sp3)–H of Ethers with Disulfides Using Acridine Red as Photocatalyst, Organic Letters 18 (2016) 1546-1549.

[52] Y. Liu, L. Jin, H.-Y. Zhang, Inclusion Complexation Thermodynamics of Acridine Red and Rhodamine B by Natural and Novel Oligo(ethylenediamine) Tethered Schiff Base β-Cyclodextrin, Journal of inclusion phenomena and macrocyclic chemistry 42 (2002) 115-120.

[53] Y. Liu, B.-H. Han, Y.-T. Chen, Inclusion complexation of acridine red dye by calixarenesulfonates and cyclodextrins: opposite fluorescent behavior, The Journal of Organic Chemistry 65 (2000) 6227-6230.

[54] Y.-M. Zhang, M. Han, H.-Z. Chen, Y. Zhang, Y. Liu, Reversible Molecular Switch of Acridine Red by Triarylpyridine-Modified Cyclodextrin, Organic Letters 15 (2013) 124-127.

[55] M. Wang, J. Yang, X. Wu, F. Huang, Study of the interaction of nucleic acids with acridine red and CTMAB by a resonance light scattering technique and determination of nucleic acids at nanogram levels, Analytica Chimica Acta 422 (2000) 151-158.

[56] S. Ghosh, S. P. Moulik, Interfacial and micellization behaviors of binary and ternary mixtures of amphiphiles (Tween-20, Brij-35 and SDS) in aqueous medium, J. Colloid and Interface Science 208 (1998) 357-366.

[57] X.-F. Zhang, J. Zhang, X. Lu, The Fluorescence Properties of Three Rhodamine Dye Analogues: Acridine Red, Pyronin Y and Pyronin B, Journal of Fluorescence 25 (2015) 1151-1158.

[58] E. Jiménez-Millán, J.J. Giner-Casares, E. Muñoz, M.T. Martín-Romero, L. Camacho, Self-Assembly of Acridine Orange into H-Aggregates at the Air/Water Interface: Tuning of Orientation of Headgroup, Langmuir 27 (2011) 14888-14899.

[59] Fluorescence, Molecular. "Principles and Applications." Bernard Valeur 2001.

[60] S. Chatterjee, G.S. Kumar, Binding of fluorescent acridine dyes acridine orange and 9-aminoacridine to hemoglobin: Elucidation of their molecular recognition by spectroscopy, calorimetry and molecular modeling techniques, Journal of Photochemistry and Photobiology B: Biology 159 (2016) 169-178.

[61] A. Safavi, H. Abdollahi, N. Maleki, S. Zeinali, Interaction of anionic dyes and cationic surfactants with ionic liquid character, Journal of Colloid and Interface Science 322 (2008) 274-280.

[62] Z. Barhoumi, M. Saini, N. Amdouni, A. Pal, Interaction between amphiphilic ionic liquid 1-butyl-3-methylimidazolium octyl sulfate and anionic polymer of sodium polystyrene sulfonate in aqueous medium, Chemical Physics Letters 661 (2016) 173-178.

[63] A. Asadzadeh Shahir, S. Javadian, B.B.M. Razavizadeh, H. Gharibi, Comprehensive Study of Tartrazine/Cationic Surfactant Interaction, The Journal of Physical Chemistry B 115 (2011) 14435-14444.

[64] K. Rawat, H.B. Bohidar, Universal Charge Quenching and Stability of Proteins in 1-Methyl-3-alkyl (Hexyl/Octyl) Imidazolium Chloride Ionic Liquid Solutions, The Journal of Physical Chemistry B 116 (2012) 11065-11074.

[65] K. Thakkar, B. Bharatiya, V.K. Aswal, P. Bahadur, Aggregation of 1-alkyl-3-methylimidazolium octylsulphate ionic liquids and their interaction with Triton X-100 micelles, RSC Advances 6 (2016) 80585-80594.

[66] S. Mondal, S. Ghosh, Spectroscopic study on the interaction of curcumin with single chain and gemini surfactants, Chemical Physics Letters 762 (2021) 138144.

[67] S. Mondal, S. Ghosh, Spectroscopic Study on the Interaction of Medicinal Pigment, Curcumin with Various Surfactants: An Overview, Journal of Surface Science and Technology 28 (2012) 179.

[68] S. Rakshit, S. Das, P. Poonia, R. Maini, A. Kumar, A. Datta, White Light Generation from a Self-Assembled Fluorogen–Surfactant Composite Light Harvesting Platform, The Journal of Physical Chemistry B 124 (2020) 7484-7493.

[69] K.M. Sachin, S.A. Karpe, D. Kumar, M. Singh, H. Dominguez, M. Ríos-López, A. Bhattarai, A simulation study of self-assembly behaviors and micellization properties of mixed ionic surfactants, Journal of Molecular Liquids 336 (2021) 116003.

[70] R.V. Pereira, M.H. Gehlen, Fluorescence of acridinic dyes in anionic surfactant solution, Spectrochimica Acta Part A: Molecular and Biomolecular Spectroscopy 61 (2005) 2926-2932.

[71] P.K. Singh, M. Kumbhakar, H. Pal, S. Nath, Modulation in the Solute Location in Block Copolymer−Surfactant Supramolecular Assembly: A Time-resolved Fluorescence Study, The Journal of Physical Chemistry B 113 (2009) 1353-1359.

[72] I.N. Kurniasih, H. Liang, P.C. Mohr, G. Khot, J.P. Rabe, A. Mohr, Nile Red Dye in Aqueous Surfactant and Micellar Solution, Langmuir 31 (2015) 2639-2648.

[73] P. Karunanithi, V. R, E. Paul Raj, P. Rajesh, S. Krishnamoorthy, S. Dash, Pluronic based neutral-ionic binary micellar surfactant systems for solubilizing the cationic methylene blue dye, Chemical Physics Impact 5 (2022) 100092.

[74] S. Das, S. Ghosh, A detailed assessment on the interaction of sodium alginate with a surface-active ionic liquid and a conventional surfactant: a multitechnique approach, Physical Chemistry Chemical Physics 24 (2022) 13738-13762.

[75] J. Antony, S. Grimme, Density functional theory including dispersion corrections for intermolecular interactions in a large benchmark set of biologically relevant molecules, Physical Chemistry Chemical Physics 8 (2006) 5287-5293.

[76] A. Dutta, B. Boruah, P.M. Saikia, R.K. Dutta, Stabilization of diketo tautomer of curcumin by premicellar cationic surfactants: A spectroscopic, tensiometric and TD-DFT study, Journal of Molecular Liquids 187 (2013) 350-358.

[77] F. Warsi, M.R. Islam, M.A. Khan, M. Osama, M. Ali, Delineating molecular interactions within surface active ionic liquids + tartrazine dye solutions: A comparative study with conventional surfactant-DTAC, Journal of Molecular Structure 1260 (2022) 132798.

[78] H. Hajjaoui, M. Khnifira, A. Soufi, M. Abdennouri, S. Kaya, R. Akkaya, N. Barka, Experimental, DFT and MD simulation studies of Mordant Black 11 dye adsorption onto polyaniline in aqueous solution, Journal of Molecular Liquids 364 (2022) 120045.

CHAPTER – II

Aggregation and characterization of the microenvironment of solvatochromic eosin yellow dye in the presence of zwitterionic, cationic, and anionic surfactants: a spectroscopic and theoretical approach.

Aggregation and characterization of the microenvironment of solvatochromic eosin yellow dye in the presence of zwitterionic, cationic, and anionic surfactants: a spectroscopic and theoretical approach

Abstract

This study explores the interactions between the anionic dye eosin yellow (EY) and various amphiphiles, specifically focusing on a newly synthesized zwitterionic surfactant called N-dodecyl-N, N-dimethyl-2-ammonio-1-ethanecarbonate (C_{12}DmCB), along with sodium lauryl sarcosinate (SLAS), sodium deoxycholate (NaDC), and cetyl trimethyl ammonium chloride (CTAC). The investigation encompasses both premicellar and postmicellar concentrations. By utilizing advanced techniques such as conductometric titration, UV-visible absorption spectroscopy, steady-state fluorescence spectroscopy, time-resolved fluorescence spectroscopy, and dynamic light scattering (DLS) measurements, this research aims to provide a comprehensive understanding of the behavior and properties of these interactions. We have effectively determined several vital parameters through spectroscopic analysis, including spectral shift, Stokes shift, and anisotropy. This contributes significantly to our understanding of the underlying phenomena. Recent findings from density functional theory calculations have effectively integrated into this work. Moreover, particle size and zeta potential of the studied system have been determined regarding the colloidal stability of each EY-surfactant system. The observed results can be thoughtfully interpreted in light of the differing aggregation behaviours of amphiphiles, which contributes to a nuanced understanding of their interactions. By utilizing Gauss View 5.0 and Gaussian 09, we have effectively optimized the energy of each amphiphile-dye combination, allowing us to uncover critical insights into their molecular interactions. Furthermore, the implementation of TDDFT calculations has provided us with a comprehensive analysis of the HOMOs and LUMOs, enhancing our understanding of these

complex systems. C_{12}DmCB, a zwitterionic surfactant, stabilizes EY most effectively by creating a more protective microenvironment than all other amphiphiles. CTAC, being an oppositely charged surfactant concerning EY, provides extra stability to the EY-CTAC system. However, a very prominent spectral shift in UV-visible absorption and steady-state fluorescence spectroscopy denoting an increment in the average lifetime of EY-C_{12}DmCB establish the stable system.

1. Introduction:

Since the beginning of the 20th century, the surfactant-dye association has had a supreme increasing interest due to its vast applications in the fields of textiles [1, 2], cosmetics [3, 4], food [5-7], and the photographic industry[8]. Surfactants are a special class of amphiphiles with a hydrophilic polar head group and a hydrophobic non-polar tail group consisting of mainly long-chain alkyl groups. Considering the charge of the hydrophilic group, classification of surfactants are into four types: cationic, anionic, non-ionic, and zwitterionic. It also has a self-association property when its concentration is on or above its critical micellar concentration (CMC)[9]. However, the interaction of the dyes with surfactants also serves a valuable contribution in various analytical and pharmaceutical fields, such as spectrophotometric determination of metal ions[10-12], biological transportation[13-15], characterization of drug delivery[16, 17], medicinal photosensitization[18], etc. Moreover, from an environmental point of view, the dye-surfactant association also has an important use in wastewater treatment [19, 20]. The association mechanism of oppositely charged dye-surfactants assembly depends on some parameters, especially, the electrostatic force of attraction created between two oppositely charged species[21, 22], the van der Waals force of attraction generated between the hydrophobic portions of each moiety[23], and the change in solvent polarity[24] to affect the microenvironment of dye-surfactant association.

Eosin yellow [EY], a member of triaryl methane dyes, has several biological applications, such as, histology[25, 26], pap stain[27, 28], solar energy conversion[29], photoreduction of water[30-32], characterization of superconductors[33], and is widely used as a photosensitizer in organic synthesis[32, 34]. Depending on the polarity and nature of the solvent, it can form aggregates of either (H type or J type)[35]. Chakraborty and Panda[36]investigated the interactions of EY with cationic surfactants in different solvent polarity and concluded that dimerization happened more in the ground state and in the presence of a protic solvent where Mahajan et al. [37] studied the interaction of EY in gemini pyridinium surfactants and observed charge transfer complexation between EY and surfactants. Previtali et al.[38] studied photophysics of EY in the reverse micellar environment; Rebery and Acharya[39] studied interactions of EY with several cationic, anionic and nonionic surfactants; Jerca et al.[23] investigated solubilization of EY in non-ionic surfactant ($C_{12}E_6$) medium in the presence of hydrophobically modified poly acrylic acid. In the present work, interaction between EY and a synthesized zwitterionic surfactant named N-Dodecyl-N,N-dimethyl-2-ammonio-1-ethanecarbonate (C_{12}DmCB), cetyl trimethyl ammonium chloride (CTAC), sodium lauryl sarcosinate(SLAS), and sodium deoxycholate (NaDC) separately have been investigated in aqueous medium using conductometry, UV-visible spectroscopy, steady-state and time-resolved fluorescence spectroscopy, anisotropy measurement, DLS and zeta potential methods. Such studies explore the nature of the interaction, aggregation behaviour and the spectral changes. Moreover, a DFT study has also been made for optimization of molecular structure and to get the energy gap between HOMOs and LUMOs of several EY-surfactant systems, such as, in zwitterionic surfactant, nitrogen is positive, and oxygen is negative. The same pattern has been followed for other chosen surfactants, i.e., in CTAB, nitrogen is positive; in NaDC, oxygen is negative; and in SLAS, nitrogen is neutral, but oxygen contains a negative charge. This work aims to study the association property of various surfactants containing different

polar head groups in the presence of EY in the ground and excited states and the extent of EY-surfactant moiety stabilization. To the best of our knowledge, this is the first investigation report on the interaction of EY with zwitterionic surfactant.

2. Experimental

2.1 Materials

Eosin Yellow (purity ≥90 %), CTAC (purity ≥98%), SLAS (purity ≥97%), NaDC (purity ≥97%) and C_{12}DmCB were the primary chemicals for all the experiments. All substances except C_{12}DmCB were purchased from Sigma Aldrich (see table 1). C_{12}DmCB has been synthesized in our laboratory [40] (yield: 10.04g, 93%). All chemicals were used without further purification. Double-distilled water was used to prepare all experiment solutions. The structures of all the chemicals have been drawn in Figure 1.

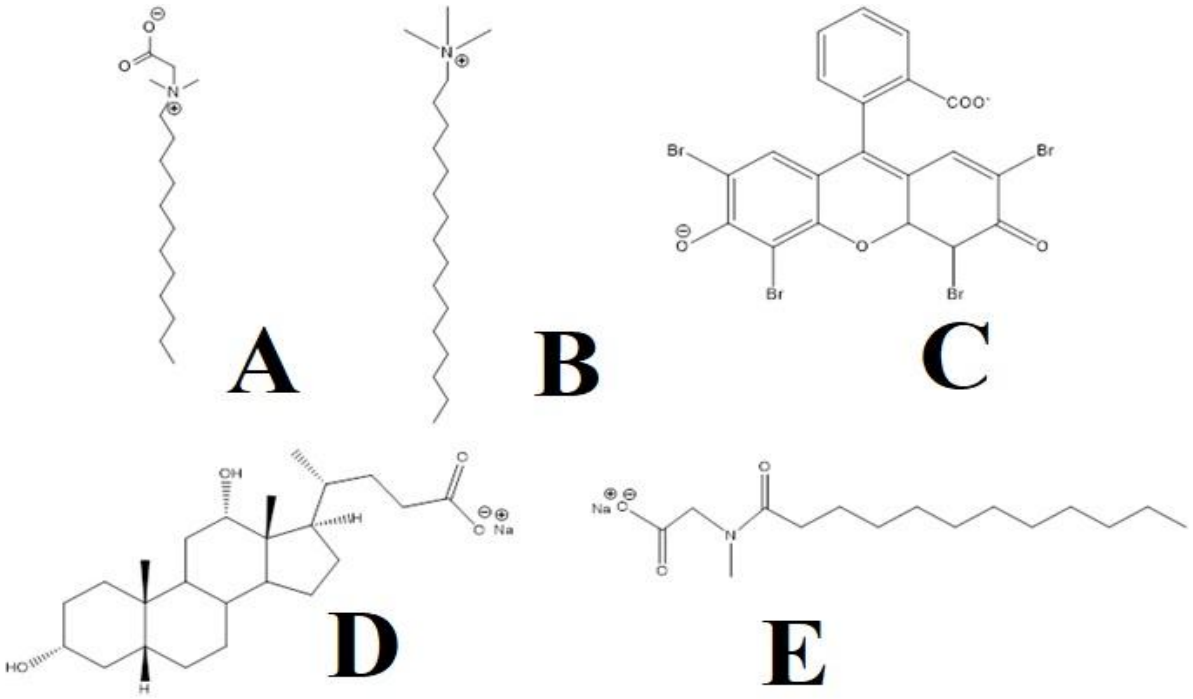

Figure 1: (A) C_{12}DmCB, (B) CTAC, (C) EY, (D) NaDC and (E) SLAS.

Table 1. Chemical compounds and models used in the Study

materials	chemical formula	CAS	supplier	purity
Eosin Yellow	$C_{20}H_6Br_4Na_2O_5$	302-95-4	Sigma Aldrich	≥ 90%
cetyl trimethyl ammonium chloride	$C_{19}H_{42}ClN$	112-02-7	Sigma Aldrich	≥ 98%
sodium lauryl sarcosinate	$C_{15}H_{28}NNaO_3$	137-16-6	Sigma Aldrich	≥ 97%
sodium deoxycholate	$C_{24}H_{39}NaO_4$	302-95-4	Sigma Aldrich	≥ 97%
N-Dodecyl-N, N-dimethyl-2-ammonio-1-ethanecarbonate	C_{12}DmCB	-	Synthesized	-

2.2 Preparation of stock solution

A 1.0 mM stock solution of Eosin Yellow (EY) was prepared by dissolving the compound of known weight in water. The desired experimental concentration of the dye was achieved by diluting the stock solution. The concentration of all surfactants in the aqueous solution was maintained at approximately 15 times greater than their respective CMCs. The CMC of C_{12}DmCB has been previously determined[40], and a solution has been prepared accordingly. Proper sonication was performed on all solutions to ensure clarity.

2.3 Electrical conductivity measurements

In this experiment, electrical conductivity measurements were conducted using an Eutech (Singapore) conductivity meter, which was calibrated with a cell constant value of 1 cm^{-1}. To ensure accurate readings, the temperature of the solution was maintained at a steady 298 K, utilizing a water bath with a precision of ±0.1 K. A stock solution was prepared in aqueous medium at approximately 15 times the critical micelle concentration (CMC), and was gradually introduced into a container holding 6 mL of the water, using a Hamilton microsyringe. After each addition of the stock solution, the mixture was thoroughly agitated to ensure uniformity

before recording the specific conductance (k). Each measurement was repeated three times to ensure reliability, and the average value was calculated along with an error assessment of 2 standard deviations. The CMC values were determined by analyzing the breakpoints in the graphs of specific conductance (k) plotted against surfactant concentration, providing valuable insights into the behavior of the surfactant in solution.

2.4 UV visible spectral measurements

Absorbance was measured using a UV-1601 Shimadzu spectrophotometer from Japan, employing a quartz cuvette with a 10 mm path length. The spectra were recorded over a wavelength range of 200 to 800 nm. To create the dye solution, 5 µL of EY stock solution was combined with 2 mL of water in the cuvette, resulting in a concentration of 0.0025 mM. This low concentration of EY was selected to prevent self-aggregation of the dye molecules and to reduce the van der Waals forces of attraction between the neighbouring hydrophobic regions of the molecules. Incremental additions of C_{12}DmCB, CTAC, NaDC, and SLAS were made to the aqueous EY solution to study the premicellar and post-micellar behavior of the microenvironment. The temperature was carefully maintained at a constant 25 ± 0.1 °C using a water bath. Each experiment was replicated twice to minimize any potential errors.

2.5 Steady-state fluorescence study:

The Perkin Elmer LS 55 fluorescence spectrophotometer, equipped with a Peltier system, was employed to measure the fluorescence spectra, emission intensity, and anisotropy of various surfactant-dye systems at a controlled temperature of 298.15 K, with an accuracy of ±0.02 K. A 10 mm path-length quartz cuvette was used for all measurements. For the fluorescence spectra recordings, a 10 µL stock solution of EY was introduced into 2 mL of water within the cuvette, ensuring an EY concentration of approximately 0.0025 mM. Fluorometric titrations were carried out by gradually adding C_{12}DmCB (from 0 to ~6 mM), CTAC (from 0 to ~3 mM),

SLAS (from 0 to ~31 mM), and NaDC (from 0 to ~12 mM) to each sample, all maintaining the same concentration of EY. Emission spectra were documented across the wavelength range of 520 nm to 650 nm, with fixed excitation and emission slit widths set at 15.0 nm and 2.5 nm, respectively. The scan speed was adjusted to 250 nm / min. Anisotropy measurements were taken with an excitation wavelength of 515 nm and an emission wavelength of 539 nm for EY. The average anisotropy value is determined from six consecutive readings. All anisotropy values were computed over an integration time of 20 seconds. The temperature was consistently maintained at 298.15 K using the Peltier system and circulating water, and the sample temperature was stabilized at 298 K prior to each measurement. Each experiment was performed twice to minimize potential errors

2.6 Time-resolved fluorescence study

This study executed time-resolved fluorescence spectral analysis using the time-correlated single photon counting (TCSPC) technique, utilizing the Horiba-Jobin-Yvon Cube fluorescence lifetime system. The excitation source for the EY and TBX photon detection module was a NanoLED operating at 370 nm (IBH, UK), and the TBX photon detection module served as the detector. The decay data were analyzed with the IBH DAS-6 decay analysis software. To capture the lamp profile, a dilute micellar solution of sodium dodecyl sulfate in water was employed as a scatterer instead of the sample. The accuracy of the fits was assessed through the χ^2 criterion as well as visual inspection of the residuals of the fitted function compared to the data. Mean (average) fluorescence lifetimes (τ_{avg}) for bi-exponential iterative fittings were calculated using the decay times (τ_1 and τ_2) and the pre-exponential factors (a_1 and a_2) according to the following equation:

$$\tau_{avg} = a_1\tau_1 + a_2\tau_2 \qquad (1)$$

It is important to highlight that the concentrations of both the dye and surfactants remained constant throughout the steady-state emission spectral analysis.

2.7 Dynamic Light Scattering (DLS): DLS (Dynamic Light Scattering) and zeta potential measurements were carried out using the Nano ZS Zetasizer (Malvern, UK) at an angle of 90° with exposure to a He-Ne laser. The temperature was maintained consistently at 25°C throughout the experiment. Measurements were conducted using a range of solution concentrations. A dye solution was prepared, to which premicellar and post-micellar concentrations of C_{12}DmCB, CTAC, SLAS, and NaDC were added separately. To ensure reproducibility, all experiments were repeated twice, and the percentage of intensity versus size (in nanometers) was plotted.

2.8 Density functional theory calculations: Recent advancements in density functional theory calculations have significantly enhanced our understanding of covalent and non-covalent interactions at the molecular level. This progress is paving the way for new insights and applications in various fields of chemistry and materials science. Structures of EY, C_{12}DmCB, CTAC, SLAS, and NaDC were generated using Avogadro software and subsequently refined through an auto-optimization tool within the same platform. The auto-optimization utilized the MMFF94S force field, with four steps per update, and employed the steepest descent algorithm for improved accuracy. Furthermore, to evaluate the interaction energy between EY and various amphiphiles at a 1:1 ratio on a molecular level, energy optimization was performed on these pre-optimized structures using Gaussian 09 software. All data were collected using the B3LYP functional and the 6-21G (d, p) basis set to balance accuracy and computational efficiency. To investigate the structures of the highest occupied molecular orbital (HOMO) and the lowest unoccupied molecular orbital (LUMO), time-dependent density functional theory (TDDFT) calculations were executed by using those optimized structures, thereby elucidating the nature of the interactions between the dye and different surfactants.

3. Results and Discussion

3.1 Conductivity measurements

Specific conductance measurements were conducted to investigate the aggregation behavior of C_{12}DmCB, CTAC, SLAS, and NaDC in the presence and absence of EY. The results of these experiments are illustrated in Figure 2. Figure 2 shows a noticeable increase in specific conductivity when surfactants are introduced into the aqueous medium, both with and without the presence of dye molecules. The addition of surfactants contributes more charged ions to the solution, leading to a rapid increase in conductance. However, up to a specific concentration of the surfactants, the rate of growth in conductivity values diminishes, and the slope of the conductivity graph shows a sharp decline, resulting in an intersection point. The concentration at which this breakpoint occurs is referred to as the critical micellar concentration (CMC) of the respective surfactants. Figure 2 illustrates a decrease in CMC values for C_{12}DmCB and CTAC in the presence of EY, indicating that these surfactants achieve micellization at lower concentrations when EY is present. This behavior can be attributed to the electrostatic and hydrophobic forces of attraction between EY and the surfactants. Specifically, CTAC exhibits a CMC value of 1.17 mM without EY and 1.03 mM with EY. As a cationic surfactant, CTAC is consistently influenced by the electrostatic attraction between its positively charged head group and the negatively charged EY. This interaction facilitates the positioning of EY near the polar head group of CTAC. Within sub-micellar aggregates, the inclusion of EY into the stern layer of CTAC diminishes the mutual electrostatic repulsion among the polar head groups of the CTAC surfactant. Consequently, this phenomenon enables more CTAC monomers to form micelles at lower CTAC concentrations. C_{12}DmCB, being a zwitterionic surfactant, has its anionic component [COO^-] already engaged in mitigating the mutual electrostatic repulsion of the NR_2^+ group, which also serves as a potential binding site for EY. This interaction enhances the intercalation of EY into the premicellar aggregation of C_{12}DmCB, leading to a reduction in

critical micelle concentration (CMC) values. Pure C_{12}DmCB exhibits a CMC of 1.74 mM, whereas the presence of EY lowers the CMC to 1.40 mM. Additionally, hydrophobic interactions may contribute to the decreased CMC values. Given that both surfactants and dyes are predominantly hydrophobic, introducing the surfactant into an aqueous EY solution reduces the polarity of the microenvironment. This reduction, combined with the hydrophobic interactions between the dye and surfactant, facilitates the self-aggregation of surfactant monomers at lower concentrations to form micelles. The interaction between SLAS and NaDC in the presence of EY reveals a complex and delayed micellization process. When assessed individually, the critical micelle concentration (CMC) values for pure SLAS and NaDC were recorded at 11.54 mM and 3.85 mM, respectively. However, upon the introduction of EY, the CMC values for SLAS and NaDC increased to 12.57 mM and 4.23 mM, respectively. This increase in CMC indicates a stronger mutual electrostatic repulsion between the similarly charged dye and the surfactants. The presence of the dye in the water-surfactant binary system enhances the repulsive interactions among the polar head groups of the surfactants. Consequently, the surfactant monomers experience greater difficulty coming together, resulting in a delayed micellization process. This intricate interplay of electrostatic forces underscores the significant influence that such interactions have on surfactant behavior [41].

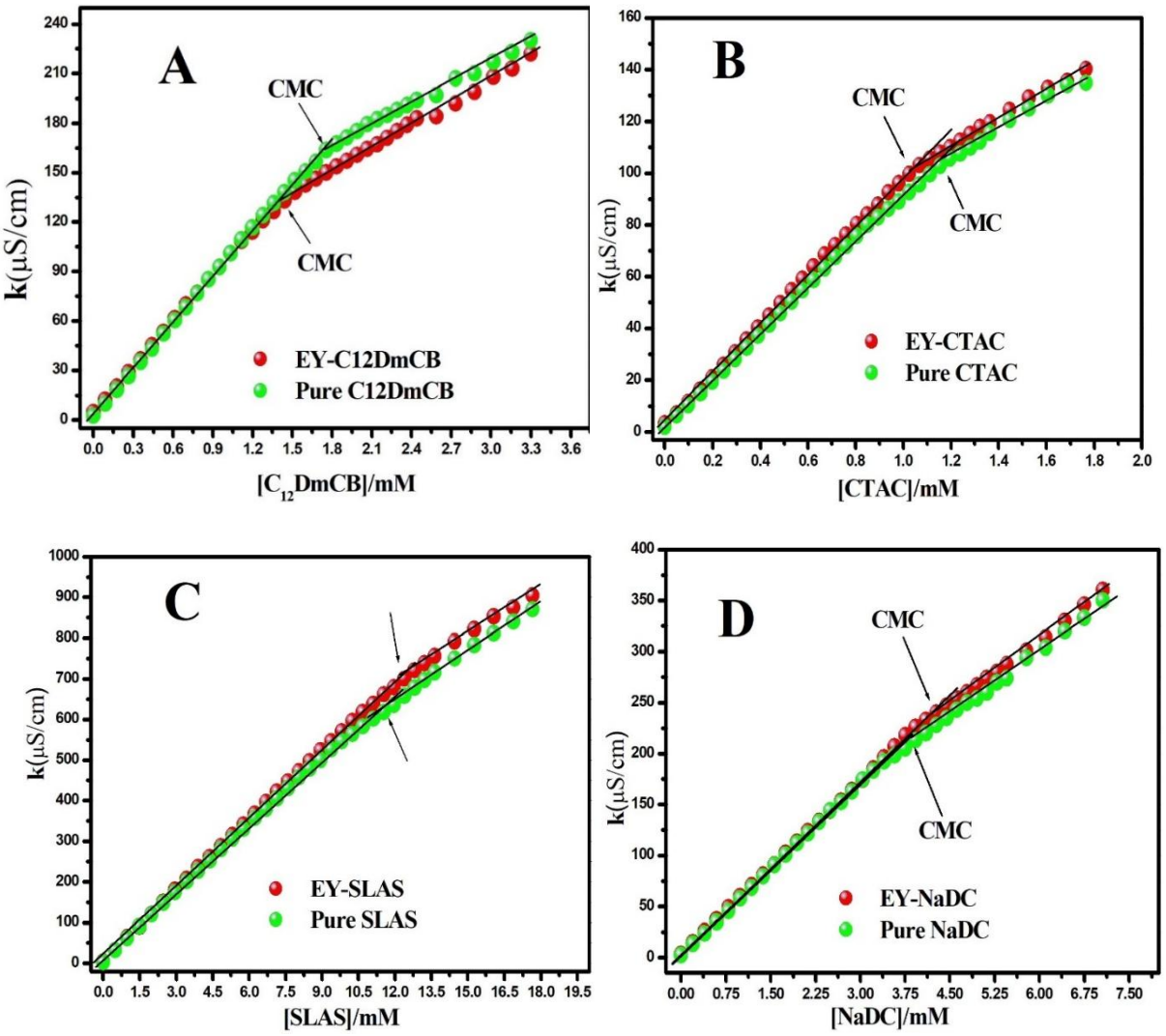

Figure 2: Plot of specific conductivity *vs.* concentration of (A) C_{12}DmCB, (B) CTAC, (C) SLAS, and (D) NaDC in the presence and absence of EY.

3.2 Spectroscopic investigation

Spectroscopic investigation always helps to elucidate a fluorophore's physical properties in the presence of various surface-active media. Here, the UV-visible and fluorescence techniques are applied. The reacting surfactants do not show any absorbance and emission in the wavelength region in which the absorbance and emission of EY are studied.

3.2.1 UV-visible spectroscopy:

UV-visible spectral data of EY in aqueous solution has been recorded where [EY]~ 10^{-5}(M). The absorption spectrum shows absorption maxima (λ_{max}) in the wavelength region 517nm

along with a shoulder peak at 491nm. This observed data resembles data found in the literature[42]. The band's appearance at 517nm corresponds to the monomeric form of EY, and the shoulder peak corresponds to the aggregated form of EY[36]. [EY] is very low in this work to avoid any self-aggregation of EY. However, in the presence of various surfactants, EY shows characteristic spectral shifts, which suggest different types of interactions of EY with various amphiphiles. All the λ_{max} values at different concentrations of the corresponding surfactants and the corresponding absorbance have been depicted in Table 2. The addition of C_{12}DmCB in an aqueous solution of AR provides a prominent spectral change, which suggests a significant interaction between EY and C_{12}DmCB (Figure 3A). Initially, [C_{12}DmCB] <CMC, a gradual decrease in absorbance clearly indicates the creation of an electrostatic force of attraction between dye and surfactant and the formation of EY- C_{12}DmCB salt-like ion pair or dye surfactant mixed micelle[43]. However, with the increase in the concentration of C_{12}DmCB in the range of 1× CMC to 2.2 × CMC, i.e., in the post micellar region, a sharp rise in absorbance along with a prominent bathochromic shift (~ 17 nm) has been observed. This observation is quite different from the interaction of conventional cationic surfactants with EY, which was reported earlier regarding absorbance. As C_{12}DmCB is a zwitterionic surfactant, the anionic part, i.e., the carboxyl group, COO- may help to reduce the mutual repulsive interaction of the cationic part of the surfactant (-NH^{3+}), which is also the binding site of EY. As a result, intercalation of EY into the stern layer of the micelle becomes easier, and EY is trapped into the hydrophobic portion of C_{12}DmCB immediately after the formation of oppositely charged EY-C_{12}DmCB salt-like ion pair, causing a gradual increase in absorbance. Moreover, due to an increase in van der Waals force of attraction between hydrophobic portion, i.e., aromatic rings of EY moiety (π-π) stacking may cause self-association of EY, i.e., formation of J-aggregate (head to tail) which may cause a prominent bathochromic shift in the absorbance spectra[44]. Gradually, CTAC was added to the aqueous solution of EY. However, spectral changes show a

significant difference concerning the spectral change of C_{12}DmCB. From Figure 3B, it is evident that adding CTAC to the concentration range of the solution of 0.1 × CMC to 2.2 ×CMC increases absorbance continuously, and a gradual red shift of 10 nm appears. This bathochromic shift may be attributed to the change in the microenvironment of the chromophore from more polar to less polar, i.e., pre-micellar aggregation between EY-CTAC forming a salt-like ion pair[45]. Moreover, [CTAC] >CMC indicates greater solubilization of EY-CTAC mixed micelle taking place due to the adhesion of ion pairs to the micelle surface, causing an increase in absorbance. As SLAS and NaDC are both anionic in nature, the addition of both of them to the aqueous solution of EY in the concentration range 0.1 × CMC to 2.2 × CMC causes only an increase in absorbance (Figure 3C and 3D). Still, unlike C_{12}DmCB and CTAC, no bathochromic shift has been observed. This phenomenon may be explained in terms of the position of the dye in the microenvironment. As both dye and surfactants contain the same charges, their polar part has created a repulsive interaction. However, a weak attractive force in the hydrophobic portion between dye and amphiphiles facilitates dye entering the surfactants' stern layer[46] to a lesser extent. The insights of Figure 3 show the variation of absorbance with the concentration of the corresponding surfactants at λ_{max} of EY.

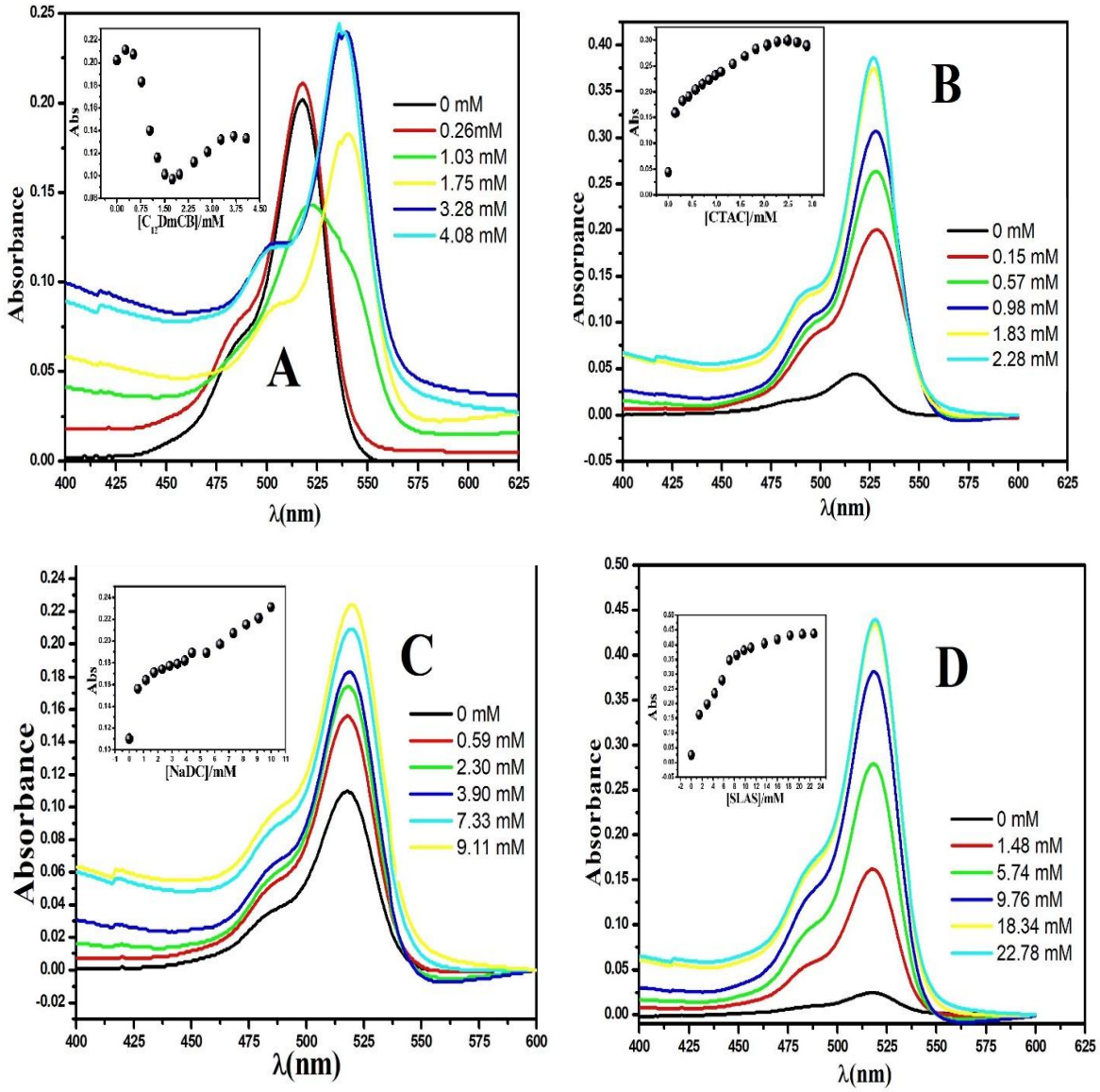

Figure 3: Absorbance of EY with varying concentrations of (A) C_{12}DmCB, (B) CTAC, (C) NaDC, and (D) SLAS (Inset shows absorbance recorded at 517nm vs. corresponding [Amphiphile]).

3.2.2 Steady-state fluorescence measurement

In order to understand more accurately the interaction phenomenon of EY with various amphiphiles, the fluorescence spectroscopic technique has been introduced as emission spectroscopy, which is very sensitive to the microenvironment where fluorophore resides[47]. Emission spectra of EY in an aqueous solution have been recorded at 540 nm (i.e., $\lambda_{emission}$),

which is very similar to literature values[48]. However, emission spectra of EY with various amphiphiles have been recorded in their pre-micellar and post-micellar concentrations (Figure 4). Like absorption spectroscopy, a similar trend has also been followed. Interaction of EY with CTAB and C_{12}DmCB causes a very prominent redshift, indicating a variation in the microenvironment from polar water to non-polar amphiphilic media. Moreover, in both cases, emission intensity has decreased markedly (Insight of Figure 4A and 4B) when [surfactant]<< CMC. This phenomenon can be attributed to forming an exciplex, i.e., EY-surfactant salt-like ion pair, due to the electrostatic force of attraction between EY and oppositely charged surfactants. This type of dye-surfactant mixed micelle is a lesser absorbing species than EY alone; so, fluorescence intensity decreases rapidly[49]. However, both CTAC and C_{12}DmCB interact differently with EY in their respective higher concentration, and this difference has been depicted in their respective spectral pattern. In the case of CTAC, when [CTAC] ≥ CMC, a sharp increase in emission intensity along with a bathochromic shift of 10nm has been observed. This observation can be explained in terms of the solubilization of EY into the hydrophobic environment of the micelle, which may stabilize the excited state of EY, resulting in a red shift in the spectra[50]. As C_{12}DmCB is a zwitterionic surfactant, its anionic part may play a role in reducing the mutual repulsive interactions of the positively charged heads, which may more efficiently bind with EY. When [C_{12}DmCB] ≥ CMC, a sharp increase in fluorescence intensity has been observed along with a prominent bathochromic shift of 20 nm. This observation can be attributed to the better solubilization of EY into the stern layer of the micellar environment. EY, being a polar probe, may undergo intramolecular charge transfer upon excitation. Therefore, in the EY-C_{12}DmCB intercalated micelle, EY may undergo a reorganization phenomenon leading to a relaxed, excited state of minimum free energy, and this leads to reduced hydrophobic repulsive interaction of the nonpolar part of EY and C_{12}DmCB as well so that they can come closer to each other[51]. However, being anionic

surfactants, SLAS, and NaDC do not show any characteristic spectral shifts in their pre and post-micellar concentration. Still, emission intensity increases (Insight of Figure 4C and 4D) due to the adhesion created between the hydrophobic part of EY and amphiphiles. Though they have the same charges, mutual electrostatic repulsion may be overcome by the van der Waals force of attraction created between the hydrophobic part of EY and surfactants. When [surfactants] ≥ CMC, EY may approach the vicinity of the micelle's stern layer and cause emission intensity enhancement. Stokes' shift is a physical parameter of a fluorophore, and it happens due to the dissipation of energy of excited state electron and can be measured following the equation,

$$\text{Stokes' shift} = 10^7 \left[\frac{1}{\lambda ex} - \frac{1}{\lambda em}\right] \quad (2)$$

where λ_{ex} and λ_{em} are the excitation and emission maxima, respectively, expressed in nanometers, stokes' shift values of EY along with EY-surfactants in their specific concentrations have been depicted in Table 2. However, Stokes' shift values of EY-surfactants do not change significantly concerning Stokes' shift value of aqueous solution of EY. Moreover, the decrease in Stokes' shift is due to a decrease in the polarity of the microenvironment surrounded by a fluorophore, and this phenomenon is clearly visible in the EY-C_{12}DmCB system.

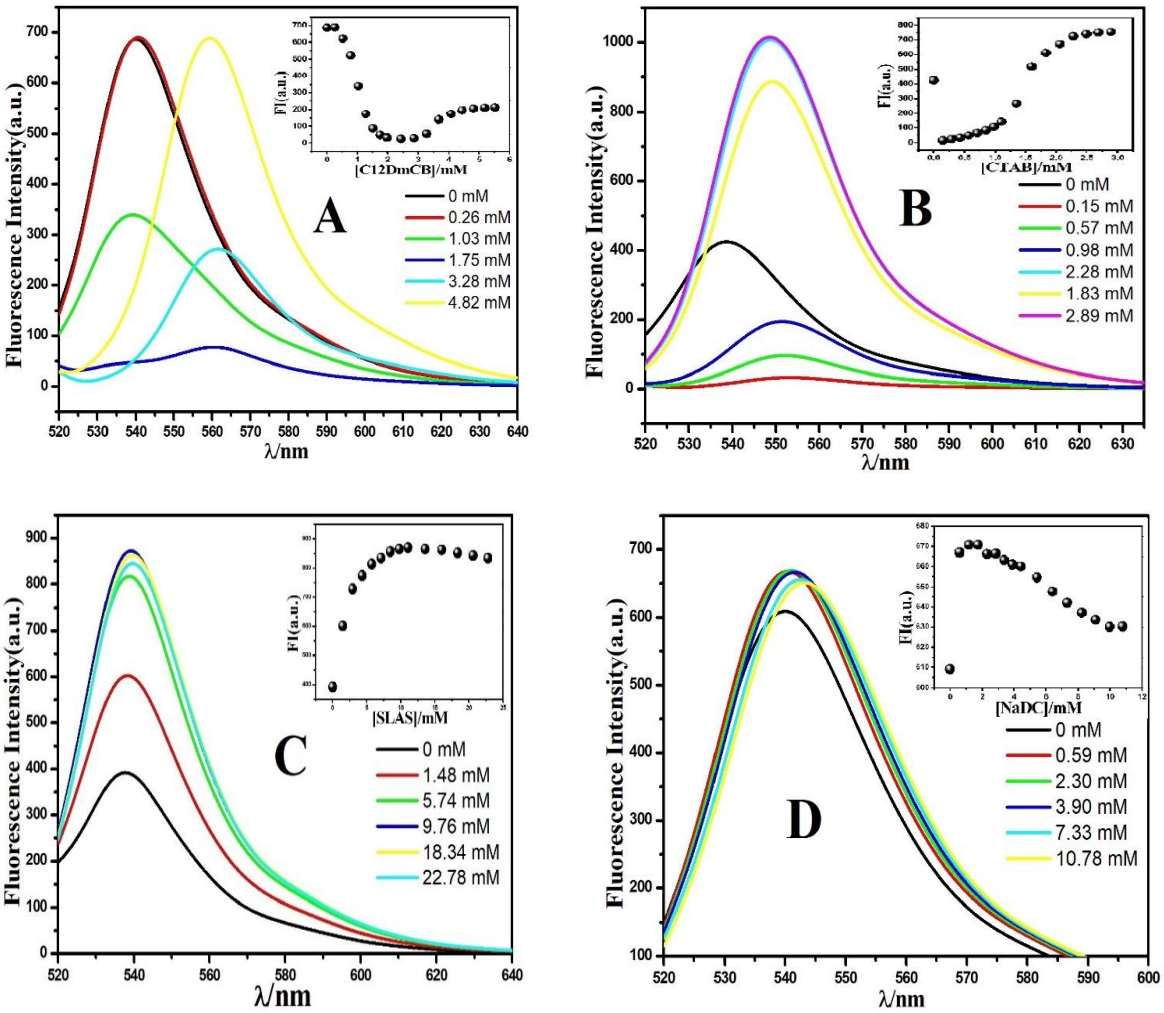

Figure 4: Variation of Fluorescence intensity of EY with varying concentration of (A) C_{12}DmCB, (B) CTAC, (C) SLAS and (D) NaDC. (The inset shows fluorescence intensity recorded at 540nm, compared to the corresponding [Amphiphile]).

Table 2: Various spectroscopic parameters and calculation of Stokes shift of EY and EY-amphiphiles in their pre- and post-micellar concentration.

Concentration [mM]	λ^{Abs}_{max} (nm)	Abs	λ_{max}^{Flu} (nm)	F. I.	Stokes' shift
EY in water					
10^{-5}	518	0.045	540	686	786.5
EY in C_{12}DmCB					
0.26	518	0.211	540	684	786.5
1.03	521	0.143	539	337	640.9
1.75	540	0.181	561	78	693.2
3.28	540	0.239	562	270	724.9
4.82	540	0.240	560	691	661.3
EY in CTAC					
0.15	529	0.20	551	34.41	754.7
0.57	528	0.26	551	97.41	790.5
0.98	528	0.305	552	195.4	823.4
1.83	527	0.373	550	886.4	793.5
2.28	527	0.386	548	1002	727.15
EY in SLAS					
1.48	518	0.161	539	242	752.14
5.74	518	0.28	539	327	752.14
9.76	518	0.38	539	348	752.14
18.34	518	0.43	539	344	752.14
22.78	518	0.44	539	338	752.14
EY in NaDC					
0.59	517	0.156	539	666	789.5
2.30	518	0.173	540	668	786.5
3.90	518	0.184	541	667	820.73
7.33	519	0.208	542	653	817.63
10.78	520	0.22	543	646	814.6

3.2.3 Determination of binding constants of EY with various surfactants

To enhance our understanding of the interaction between EY and various surfactants, we aimed to determine the binding constants that reflect EY's binding capacity in a surface-active microenvironment. In the EY-C_{12}DmCB system, we observed a pronounced quenching of fluorescence intensity at C_{12}DmCB concentrations of up to 2.43 mM. The Stern-Volmer

equation has been introduced to determine the nature of quenching, i.e., whether the quenching is static or dynamic in nature, and the equation is as follows.

$$\frac{F_0}{F} = 1 + K_s[Q] \quad (3)$$

Here, F_0 and F are the fluorescence intensities of the of probe in the presence and absence of quencher molecules. K_s is the binding constant or Stern-Volmer constant and [Q] is the concentration of the quencher. If F_0/F changes linearly with [Q] there can be one form of quenching present in the microenvironment. But in case of the EY-C_{12}DmCB system plotting of F_0/F vs [Q] give rise to a curved graph having a upward curvature (Inset of Figure 5A). This observation strongly signifies the occurring of both static and dynamic quenching in the microenvironment. So, we employed a modified Stern-Volmer equation [52, 53] to analyze these findings effectively, facilitating a more accurate assessment of the interactions involved and the equation is as follows.

$$\log\left(\frac{F_0-F}{F}\right) = \log K + n \log[\text{surfactant}] \quad (4)$$

Where F_0 and F are the fluorescence intensities of the fluorophore in the absence and presence of different concentrations of surfactants, respectively, K represents the binding constant. At the same time, n denotes the number of binding sites. If $\log\left(\frac{F_0-F}{F}\right)$ *vs.* $\log[\text{surfactant}]$ is plotted in a linear fitting, then the equilibrium binding constant (K) can be obtained from the intercept. In the EY-NaDC system, the fluorescence intensity exhibits a consistent decrease as the concentration of NaDC ranges from 0.59 mM to 9.96 mM. Consequently, Stern-Volmer equation has been introduced and a curved graph pointing in a upward direction (Inset of Figure 5B) arises by plotting F_0/F vs [NaDC] indicate the presence of simultaneous static and dynamic quenching. So, here also the modified Stern-Volmer equation also has been employed to calculate the binding constants, using the fluorescence intensity obtained at NaDC

concentration of 0.59 mM as F_0. C_{12}DmCB being a zwitterionic surfactant most effectively binds with EY and this results in very good commensurate with the other spectroscopic and conductometric findings. K for EY -C_{12}DmCB system is 1.14×10^{-3} M^{-1} and the same for EY-NaDC system is 0.0014×10^{-3} M^{-1}. NaDC, a negatively charged surfactant, shows a very weak binding affinity with EY due to electrostatic repulsion created between same charged species. In the EY-CTAC system, fluorescence intensity steadily increases when the concentration of CTAC is increased from 0.15 mM to 2.89 mM. So, the Benesi-Hildebrand equation [54] has been introduced to determine the binding constants, and the equation is as follows

$$\frac{1}{F-F_0} = \frac{1}{(F_\infty - F_0)\, K_b\, [\text{Surfactant}]^n} + \frac{1}{(F_\infty - F_0)} \qquad (5)$$

Where F_0, F and F_∞ are the fluorescence intensities at the absence of surfactant, the intermediate surfactant concentration, and the final surfactant concentration, respectively. K_b is the binding constant and can be determined by plotting of $\frac{1}{F-F_0}$ *vs.* $\frac{1}{[\text{Surfactant}]^n}$. Here, we have assumed the fluorescence intensity recorded at 0.15 mM concentration of CTAC as F_0 and the calculations have been done accordingly. CTAC, being a negatively charged surfactant, effectively binds with EY by electrostatic force of attraction and K_b obtained for CTAC-EY binding is 0.79×10^{-3} M^{-1}. The EY-SLAS system will undoubtedly adhere to this equation, as we have observed that FI consistently increases with the addition of SLAS, and the EY-SLAS system shows a very weak binding ($K_b = 0.0413\times10^{-3}$ M^{-1}) as both dye and surfactant contain the same charge. All the binding constant values have been depicted in Table 3.

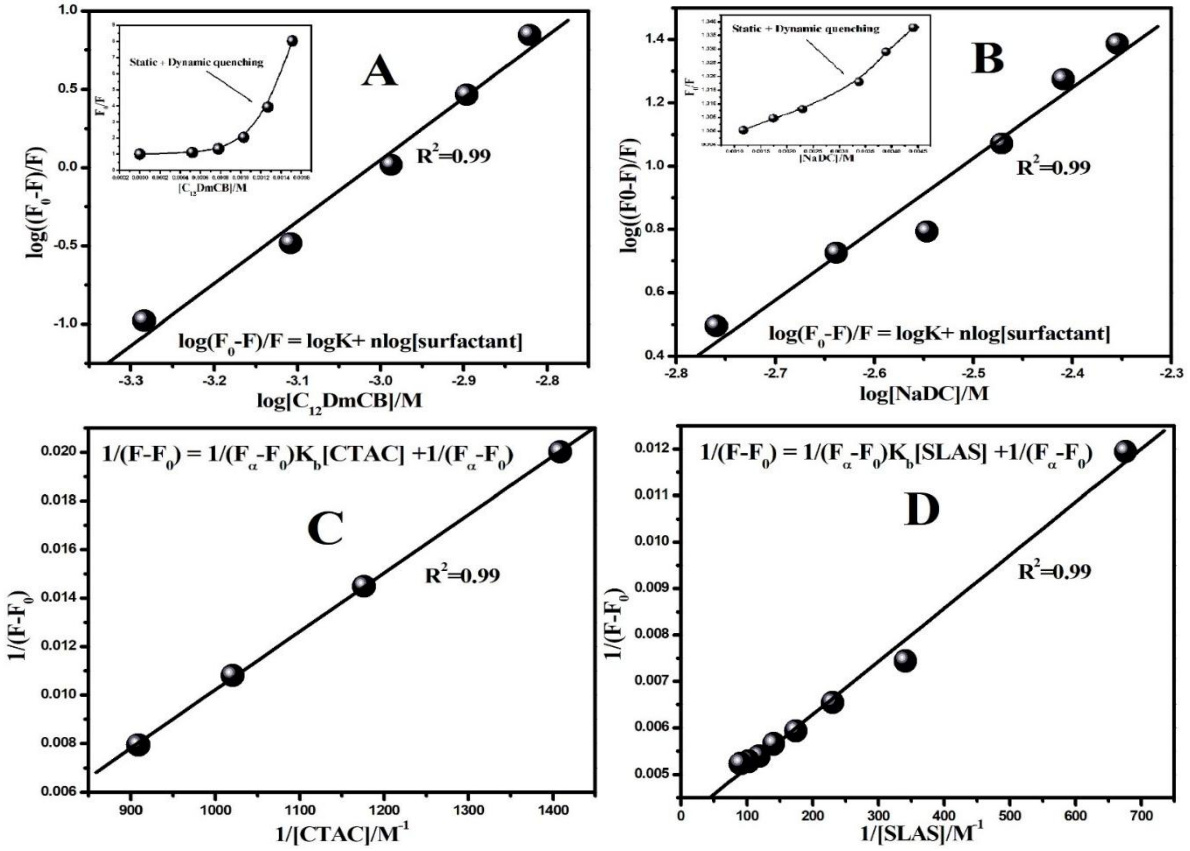

Figure 5: A and B are the modified Stern Volmer plot for the system EY-C_{12}DmCB and EY-NaDC and C and D are Benesi-Hildebrand plot for the system EY-CTAC and EY-SLAS. Inset of A and B are the Stern-Volmer plots of EY-C_{12}DmCB and EY-NaDC system respectively.

Table 3. The binding constants of different systems.

System	Binding constant (M^{-1})	Number of binding sites (n)
EY-C_{12}DmCB	7.94×10^7	4
EY-NaDC	0.39×10^1	1
EY-CTAC	5.76×10^4	1
EY-SLAS	3.55×10^1	1

3.2.4 Steady-state anisotropy study of EY with different amphiphiles:

Measurement of anisotropy can give information about rotational diffusion molecular orientation, and rigidity of the microenvironment[55]. Anisotropy can be measured by using the following equation,

$$r = \frac{I_V - GI_H}{I_V + 2GI_H} \quad (6)$$

Here, I_V and I_H are the intensities of excitation light towards parallel and perpendicular directions, respectively, arising from the probe's vertically polarised excitation.

Factor G defines

$$G = \frac{I_V}{I_H} \quad (7)$$

Measurement of anisotropy with varying concentrations of surfactants in an aqueous solution of EY provides a piece of important information regarding the microenvironment. The addition of C_{12}DmCB and CTAC in an aqueous solution of EY gives rise to a decrease in anisotropy of the medium when [surfactants]<< CMC (Figure 6A and 6B). This lowering in anisotropy explains the rupturing of hydrogen bonding between EY and water, i.e., EY becomes relatively free to bind with surfactants, or EY moves towards the polar end of the oppositely charged surfactants by breaking the H bond between EY and water. However, by adding more surfactants in the aqueous solution of EY, when the concentration of CTAC and C_{12}DmCB has reached their respective CMC values, a sharp increase in anisotropy happens in both cases. These results can be attributed in terms of varying the nature of the microenvironment, i.e., incorporation of EY into the micellar environment, where the motion of the fluorophore has been restricted, resulting in an enhancement in anisotropy[56]. These observations are also supported by absorption and emission spectroscopy. Moreover, the addition of SLAS and NaDC to the aqueous solution of EY also executes, and a small enhancement in anisotropy has been recorded in their respective pre-micellar and post-micellar concentrations (Figure 6C and 6D). These observations also provide a good agreement with respect to absorbance and

emission spectrum. A weak hydrophobic interaction between EY and those surfactants facilitates approach of EY to the stern layer of the micelle to a lesser extent. As a result, the motion of EY has not been restricted so much, i.e., a slight change in anisotropy is recorded.

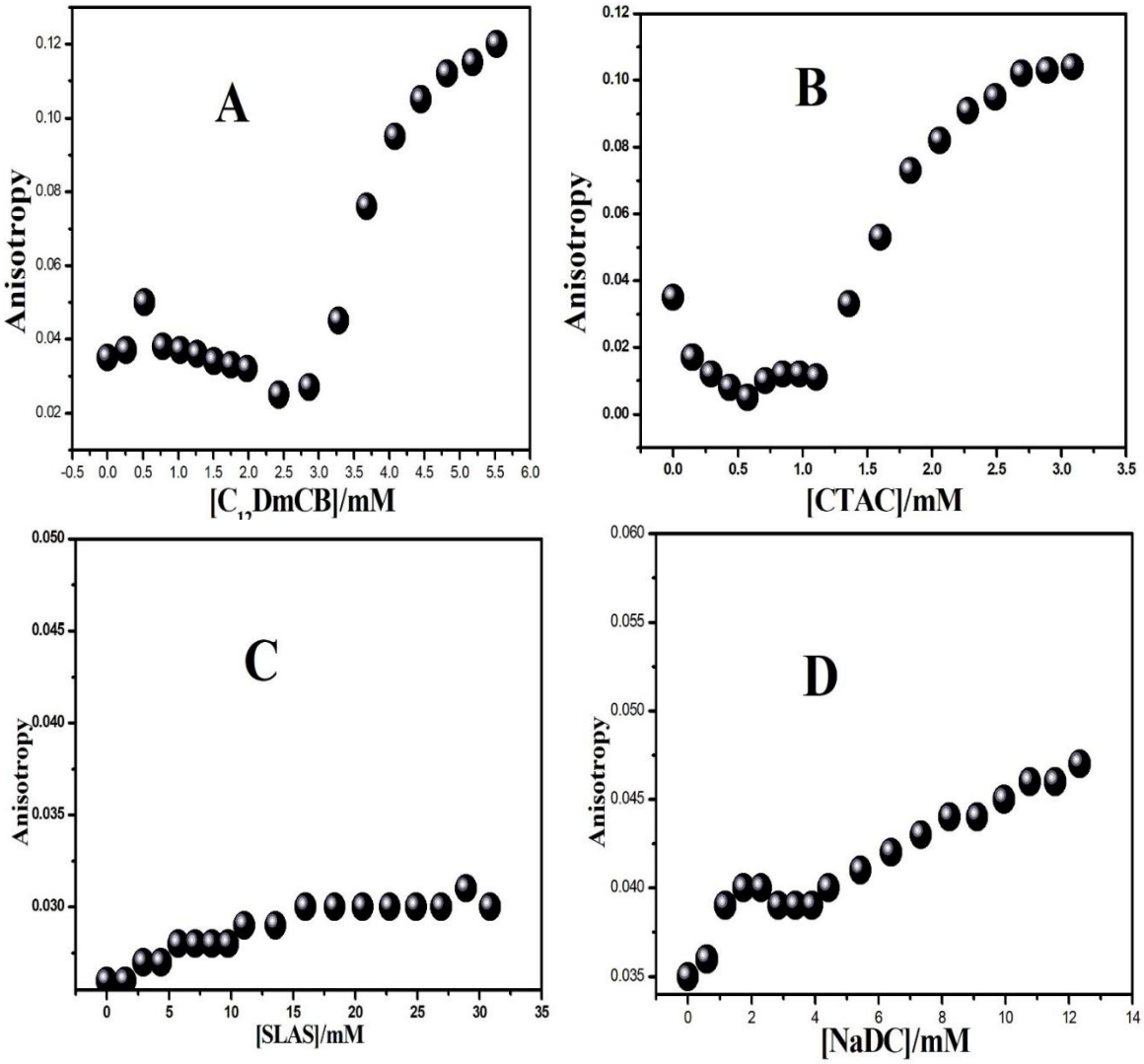

Figure 6: Variation of anisotropy of EY with varying concentrations of (A) C_{12}DmCB, (B) CTAC, (C) SLAS, and (D) NaDC.

3.2.5 Dynamic light scattering and zeta potential measurement.

Dynamic light scattering also provides critical information regarding the solution's particle size, which helps to infer various types of aggregation behavior of dye with various amphiphiles. The DLS method enables the measurement of the particle size of an aqueous

solution of EY and various surfactants in their pre-micellar and post-micellar concentrations. In this experiment, 10μL stock solution of EY was taken in 2mL water placed in a cuvette, and all four surfactants were added separately in the solution of the same volume to measure the changes in aggregate size (r) (Figure 7). However, an aqueous solution of EY exhibits two types of aggregates, one in a size range of 7.5-11.3 nm, which corresponds to the monomeric form of EY, and the other in a size range of 105-160 nm, which corresponds to the aggregated form of dye molecules. The hydrodynamic diameter of the monomeric form of EY obtained in this study more or less aligns well with values reported in the literature [57]. The aggregated form of EY arises due to π-π stacking of the dye molecules or due to hydrogen bonding with water, which makes a larger hydrodynamic radius. The addition of C_{12}DmCB to the aqueous solution of EY initially causes enhancement of particle size (400-450 nm). This observation relates very well to other spectroscopic experiments. As C_{12}DmCB is zwitterionic in nature, its cationic part is attracted by the anionic part of EY, and this electrostatic attraction causes the formation of an EY- C_{12}DmCB salt-like ion pair and results in enhancement in particle size, but when [C_{12}DmCB] ≥CMC, aggregate size decreases. This observation also supports the intercalation of EY into the stern layer or the palisade layer of the micelle of C_{12}DmCB very effectively and supports the bathochromic shift found from absorbance as well as emission spectra. The addition of CTAC also provides the same result in the premicellar concentration of CTAC. However, when [CTAC] ≥CMC, the particle size of CTAC decreases approximately 1.5 times compared to the previous one. CTAC is a cationic surfactant whose polar part attracts negatively charged EY in its premicellar concentration, forming a dye-rich dye-surfactant mixed micelle. Then, with an increase in the concentration of CTAC, EY gets solubilized into the stern layer of the micelle due to the micelle's adhesion effect, causing a decrease in particle size[58]. Moreover, the addition of SLAS and NaDC to the aqueous solution of EY results in a huge increment, approximately 4 times, in their respective aggregation size. The formation

of such huge aggregates by these surfactants with EY can be explained by the repulsive electrostatic force created between them as they contain the same charge[59]. However, the van der Waals force of attraction between the hydrophobic moiety of EY and surfactants also plays an attractive effect. These dual effects cause EY-surfactant aggregate when [surfactant] ≥ CMC and cause an increment in aggregation size.

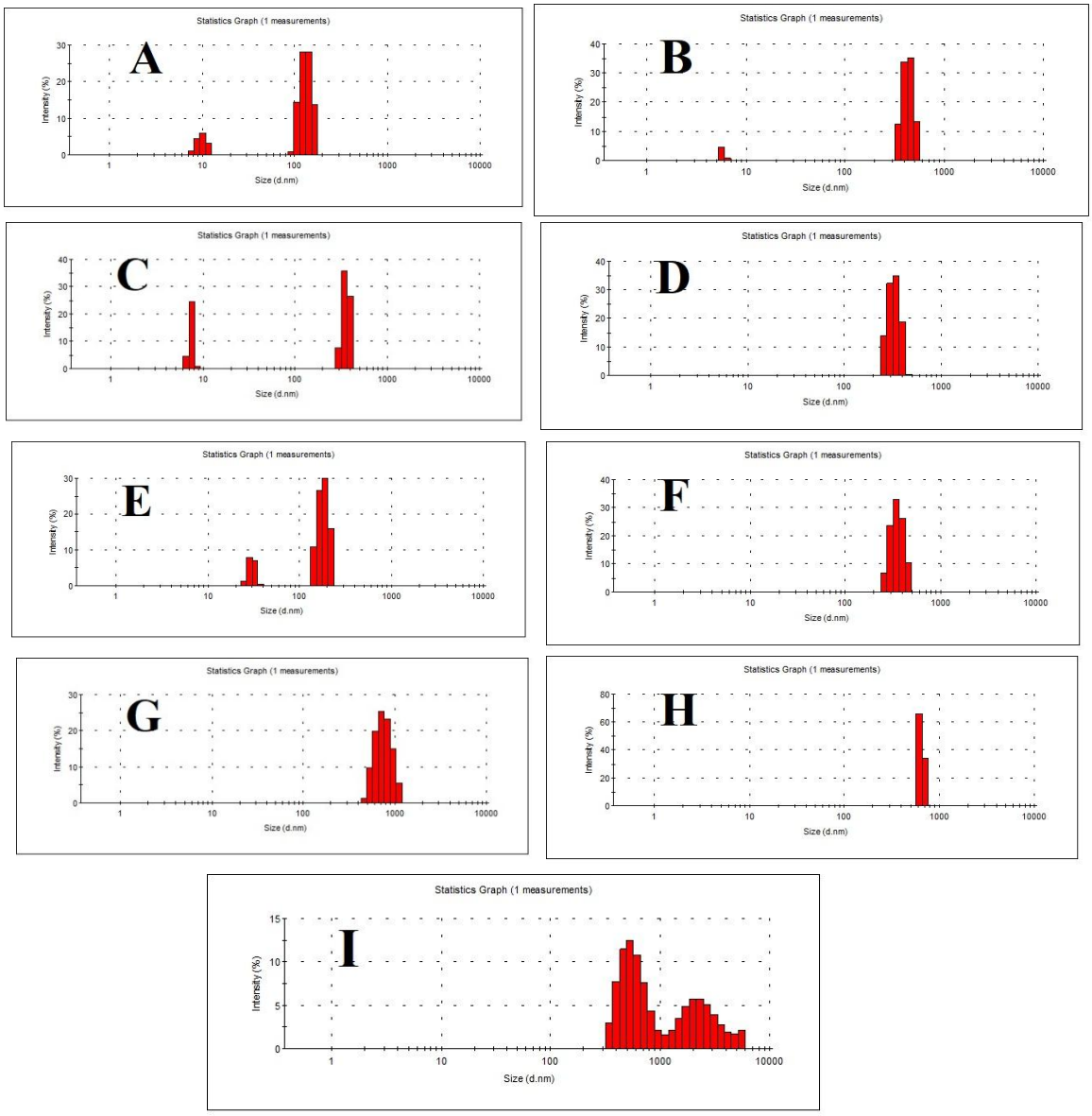

Figure 7: DLS profile of (A) EY, (B) EY-C_{12}DmCB (< CMC), (C) EY-C_{12}DmCB (> CMC), (D) EY-CTAC (< CMC) (E) EY-CTAC (> CMC) (F) EY- SLAS (< CMC), (G) EY- SLAS (> CMC) (H) EY- NaDC (< CMC) (I) EY- NaDC (> CMC).

3.2.6 Measurement of Zeta potential

Zeta potential or electrokinetic potential develops in the interfacial double layer of the colloidal system. It is a very useful tool for measuring the stability of colloids[60]. The Zeta potential of the 10^{-5} M solution of EY was measured, and the same experiment was carried out with various surfactants in their premicellar and post-micellar concentrations. All the zeta potential values are depicted in Table 4. The Zeta potential of the aqueous EY solution is 5.11 mV. However, the addition of C_{12}DmCB reduces the zeta potential of the system. More reduction of zeta potential has been observed in the post-micellar concentration of C_{12}DmCB. These observations infer the reduction of charges in the micelle-water interface[61] by virtue of the proximity of EY and C_{12}DmCB. When [C_{12}DmCB] ≥ CMC, the best intercalation of EY facilitates the residing EY into the stern layer of the C_{12}DmCB micelle; here, it binds with the cationic part of C_{12}DmCB. However, the anionic counterpart of the surfactant may now be engaged in bonding with the water molecules, the counter ion of EY, and reducing the mutual electrostatic repulsion of the cationic micelle-forming head group. This reduction of charges may cause coagulation of the micellar system[62], leading to a relatively sizeable aggregate in DLS measurement. Again, in the case of the EY-CTAC system, when [CTAC] < CMC, higher zeta potential indicates the formation of an electrical double layer between two oppositely charged dye-surfactants. However, with an increase in the concentration of CTAC, the positive zeta potential value increases due to the enhancement of the positive charge in the micelle water interface, leading to higher colloidal stability. This observation also supports the localization of the hydrophilic portion of the dye into the stern layer of micelle [63]. Negative zeta potential values were observed in the case of anionic surfactants like SLAS and NaDC. Those values were also sharply incremented when [surfactants] ≥ CMC. A negative zeta potential value results from negatively charged surfactants and dye. The higher negative values in the post-micellar concentration of the surfactants are a good indication of the potential stability of the

colloidal system[64]. In both cases, negatively charged dye and surfactants tend to repel each other electrostatically. Still, due to hydrophobic interactions, the hydrophobic part of EY has been placed into the stern layer of the micelle, and these may stabilize the colloidal system by enhancement in zeta potential values.

Table 4. Aggregate size, zeta potential, and anisotropy values of aqueous EY and EY-surfactants in their respective premicellar and post micellar concentrations.

Concentration(mM)	Aggregate size (nm)	Zeta potential (mV)	Anisotropy
EY in water			
0	~140	5.11	0.033
EY in C_{12}DmCB			
0.78	~458	4.52	0.038
3.68	~342	1.96	0.076
EY in CTAC			
0.43	~342	29.9	0.006
2.06	~190.1	39.5	0.082
EY in SLAS			
4.34	~342	-2.98	0.026
20.6	~712	-26.7	0.030
EY in NaDC			
1.74	~615	-17.8	0.038
8.24	~615	-47.3	0.042

3.2.7 Time-resolved fluorescence study.

Time-correlated single photon counting (TCSPC) is a very sophisticated technique used to measure the lifetime of a fluorophore. The fluorescence lifetime of a dye depends on its chemical structure, shape, and, very importantly, on its external microenvironment[65]. So, the difference in the lifetime of the same fluorophore in various microenvironments provides valuable information regarding the interaction of the dye with these microenvironments and their relative stability in the excited state. In this work, the TCSPC technique was applied to an aqueous solution of EY along with various surfactants in their respective premicellar and post-micellar concentrations. The corresponding lifetimes of EY with varying concentrations of

different surfactants with their respective pre-exponential factor have been depicted in Table 5. Moreover, the average lifetime has also been determined to establish the stability of the excited state. 10^{-5}(M) aqueous solution EY exhibited an average lifetime (τ_{avg}) of 1.03 ns with a single exponential decay. This value is consistent with the findings in the literature[66]. However, the average fluorescence lifetime has been increased markedly during CTAC and C_{12}DmCB addition when [surfactant] > CMC (Figures 8A and 8B). Between CTAC and C_{12}DmCB, C_{12}DmCB is found to form a more protective and stable microenvironment with higher microviscosity[67], leading to the enhancement of τ_{avg} by shielding the excited state from non-radiative decay than CTAC. The value of τ_{avg} of EY-CTAC complex is 2.32ns when [CTAC]>CMC whereas τ_{avg} of EY-C_{12}DmCB complex is found to be 3.74ns when [C_{12}DmCB] >CMC. From lifetime measurements, it is evident that in post micellar concentration, C_{12}DmCB stabilized excited state more than CTAC. These observations lead to an excellent agreement with previous spectroscopic data and give rise to a prominent explanation regarding the bathochromic shift in post micellar concentration of C12DmCB in an aqueous solution of EY in absorption and emission spectral studies. CTAC, being an oppositely charged surfactant, binds obviously with EY electrostatically, and with an increase in the concentration of CTAC, placing EY in the vicinity of the micellar environment of CTAC is a prophecy. However, during this experiment, a new synthesized zwitterionic surfactant named C_{12}DmCB is more capable of stabilizing negatively charged EY. Moreover, in their premicellar concentration, τ_{avg} of C_{12}DmCB and CTAC shows no significant change. These observations infer that quenching in fluorescence intensity is a static quenching, i.e., EY-surfactants complexation forms in the ground state before excitation occurs. The addition of SLAS in the aqueous solution of EY does not affect τ_{avg} significantly (Figures 8C and 8D). This observation also leads to the limited interaction between the same charged dye and surfactant. However, when [SLAS] >CMC, a slight increase in observed average lifetime may be due to hydrophobic interactions. NaDC, a

negatively charged surfactant, does not show any significant change in average lifetime when added to an aqueous solution of EY; however, when [NaDC]>CMC, a slight increment in the value of τ_{avg} with a single exponential decay may be due to the attraction of the hydrophobic part of EY and NaDC in the post-micellar concentration of NaDC.

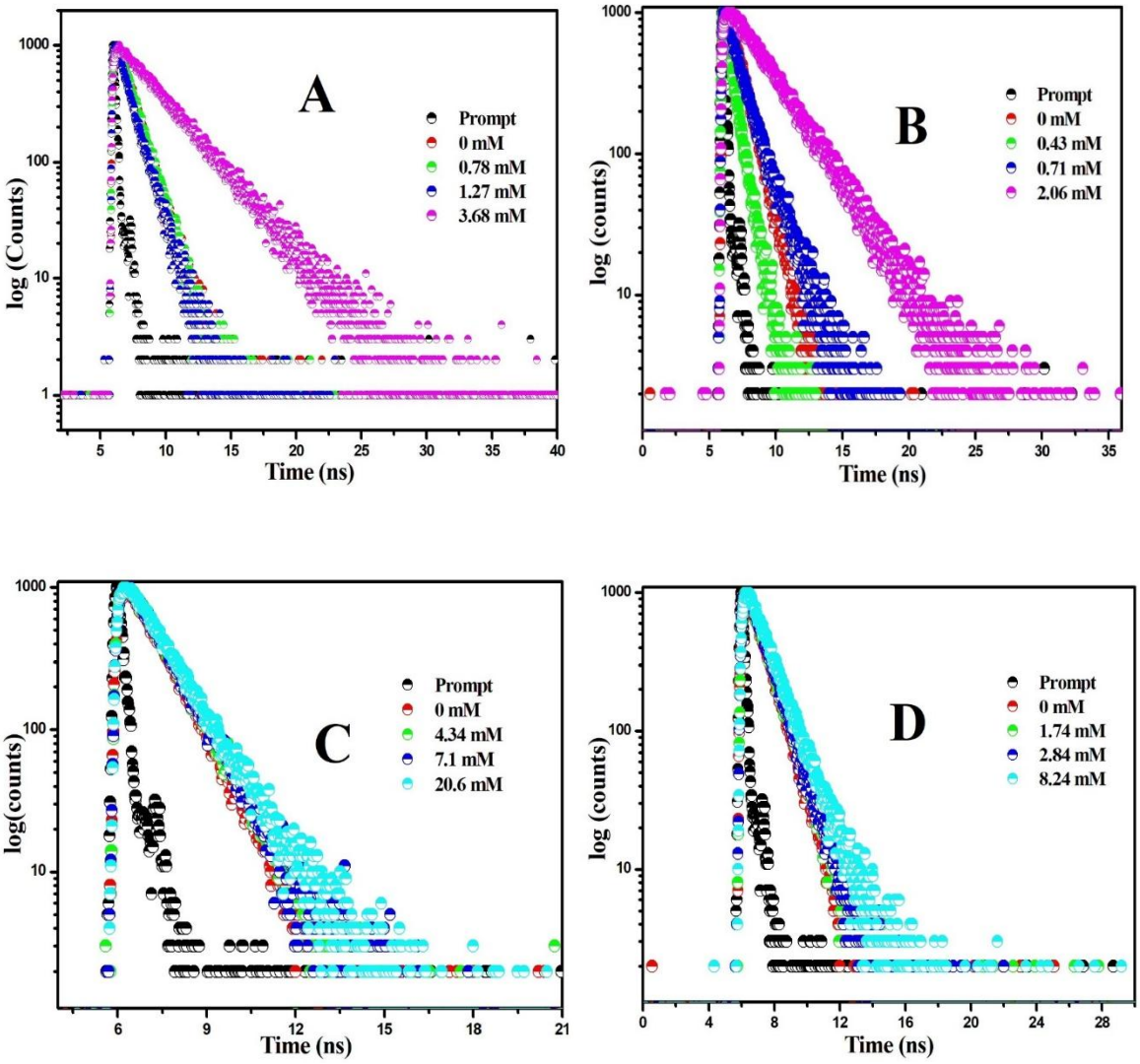

Figure 8: Time-resolved fluorescence spectra of EY along with premicellar and post-micellar concentrations of (A) C_{12}DmCB, (B) CTAC, (C) SLAS, and (D) NaDC.

Table 5. Time-resolved decay parameters of EY in (a) water, (b) C_{12}DmCB (pre- and post-micellar), (c) CTAC (pre- and post-micellar), (d) SLAS (pre- and post-micellar) and (e) NaDC (pre- and post-micellar) media.

Concentration (mM)	τ_1 (ns)	a_1	τ_2(ns)	a_2	τ_{avg}(ns)	χ^2
EY in water						
-	1.03	1	-	-	1.03	0.97
EY in C_{12}DmCB						
0.78	1.03	1	-	-	1.03	1.08
1.27	0.38	0.2	1.07	0.8	0.78	1.18
3.68	11.93	0.06	3.31	0.94	3.47	1.08
EY in CTAC						
0.43	0.31	0.52	0.80	0.48	0.44	1.16
0.71	0.42	0.2	1.40	0.8	0.95	1.09
2.06	2.30	0.49	2.33	0.51	2.32	1.00
EY in SLAS						
4.34	0.94	0.35	0.99	0.65	0.98	1.13
7.1	1.07	1	-	-	1.07	1.16
20.6	0.67	0.08	1.19	0.92	1.12	1.09
EY in NaDC						
1.74	1.09	1	-	-	1.09	0.99
2.84	1.09	1	-	-	1.09	1.04
8.24	1.24	1	-	-	1.24	1.07

3.3 Density functional theory calculations.

A theoretical aspect in terms of density functional theory (DFT) introduced a better understanding of EY-surfactant interactions at the 1:1 molecular level. All DFT calculations are performed in this experiment using the gaussian-09 package. Energy optimization of EY, EY- C_{12}DmCB, EY-CTAB, EY-SLAS, and EY-NaDC systems has been performed using b3lyp functional and 6-31g (d,p) basic set. Moreover, TDDFT calculations have been introduced to find out the nature of both the Frontier molecular orbitals (FMOs), i.e., HOMOs and LUMOs of each system and their corresponding energy. The HOMO-LUMO energy gap has a crucial

impact on a molecule's chemical and optical properties, like spectroscopic behavior, optical polarizability, kinetic stability, etc[68]. Optimized energy structures and structures of HOMOs and LUMOs of each system have been shown in Figures 9 and 10, respectively. All optimized energy values and energies of HOMOs and LUMOs of each system have been depicted in Table 6. The optimized energy value data clearly indicates that the EY-C_{12}DmCB system is the most stable as it contains minimum optimization energy. Moreover, the energy gap between HOMO and LUMO is also least for this system. So, it can be said that C_{12}DmCB effectively solubilizes EY by lowering the energy of π^* excited state [33]. EY-CTAB system also has less optimized energy and lesser energy gap between HOMO and LUMO in comparison with EY alone. CTAC, being a positively charged surfactant, also effectively solubilizes EY into its micellar core and stabilizes the system by reducing the HOMO-LUMO energy gap. However, in the case of SLAS and NaDC, higher energy optimization values, as well as a greater energy gap between respective HOMOs and LUMOs, indicate instability and poor interaction of EY with surfactants. However, the HOMOs and LUMOs of each system have been located over EY. HOMO-LUMO structures evidently indicate intramolecular charge transfer of polar probe EY. It can be assumed that EY is solubilized into the micellar microenvironments and also reorganized its π electron density, leading to a relaxed state of minimum free energy[69]. This process happens most effectively in the micellar environment ofC_{12}DmCB. As a result, the value of HOMO-LUMO energy gap (ΔE) of the EY-C_{12}DmCB system is minimal. Zwitterionic surfactant solubilizes EY more effectively than other conventional cationic and anionic surfactants.

Table 6. Optimized energy, the energy of HOMO and LUMO, band gap and dipole moments of (a) EY, (b) EY-C_{12}DmCB (c) EY-CTAC (d) EY- SLAS and (E) EY- NaDC systems.

System	E_{OPT} (a.u)	Energy of HOMO (E_1) (ev)	Energy of LUMO (E_2) (ev)	$\Delta E(E_2-E_1)$ (ev)	Dipole moment (Debye)
EY	-11705.5	-0.22	-0.08	0.140	16.8935
EY-C_{12}DmCB	-12174.02	0.02	0.136	0.116	22.0564
EY-CTAC	-12104.40	-0.097	0.031	0.128	26.6487
EY- SLAS	-12047.01	0.02	0.177	0.157	27.4204
EY- NaDC	-11540.23	0.0093	0.152	0.142	33.8485

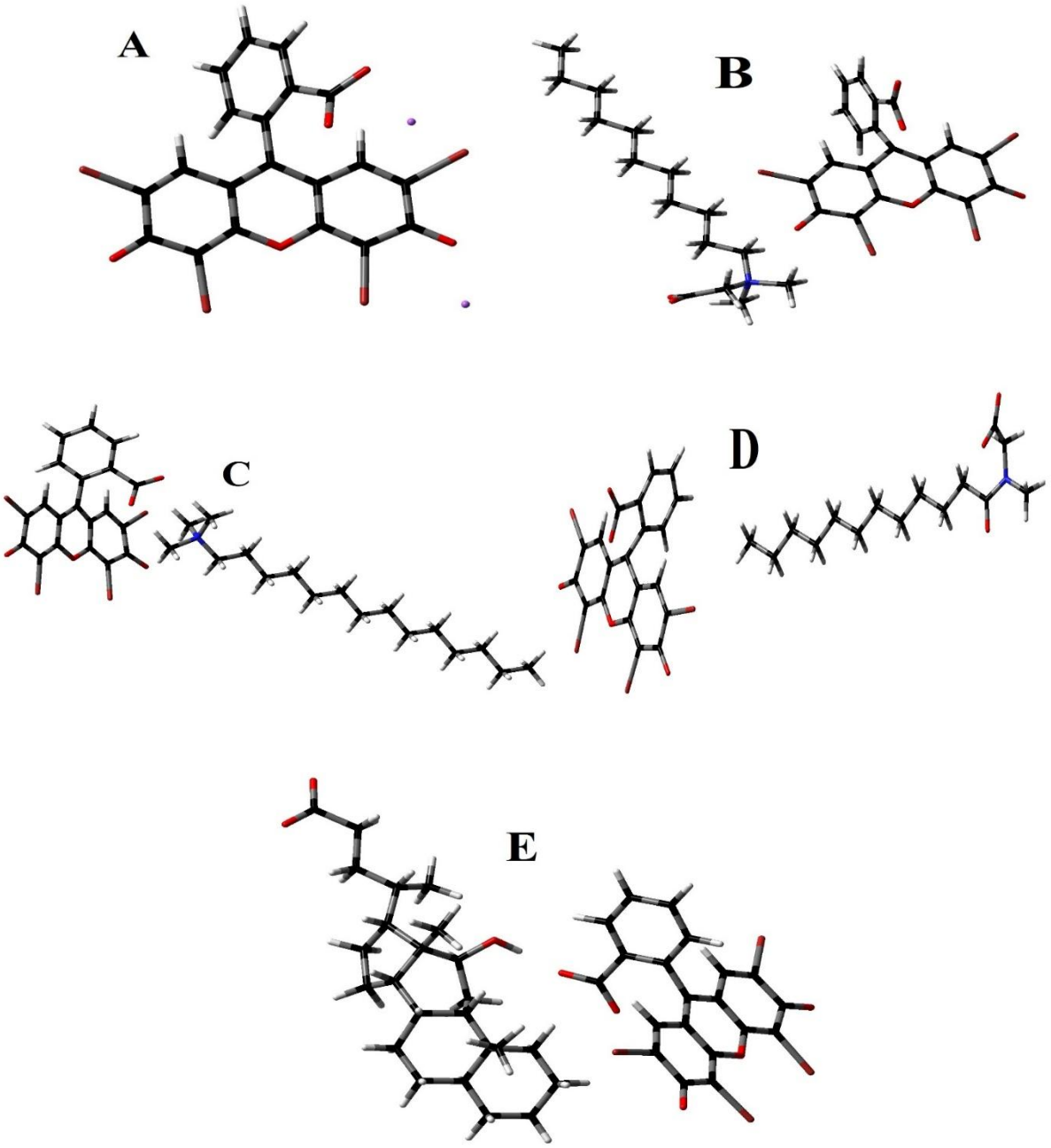

Figure 9. b3lyp/6-31g (d,p)- the optimized structure of (A) EY, (B) EY-C_{12}DmCB, (C) EY-CTAC, (D) EY- SLAS and (E) EY-NaDC. Color code for atoms: red, oxygen; dark gray, carbon; light gray, hydrogen; blue, nitrogen.

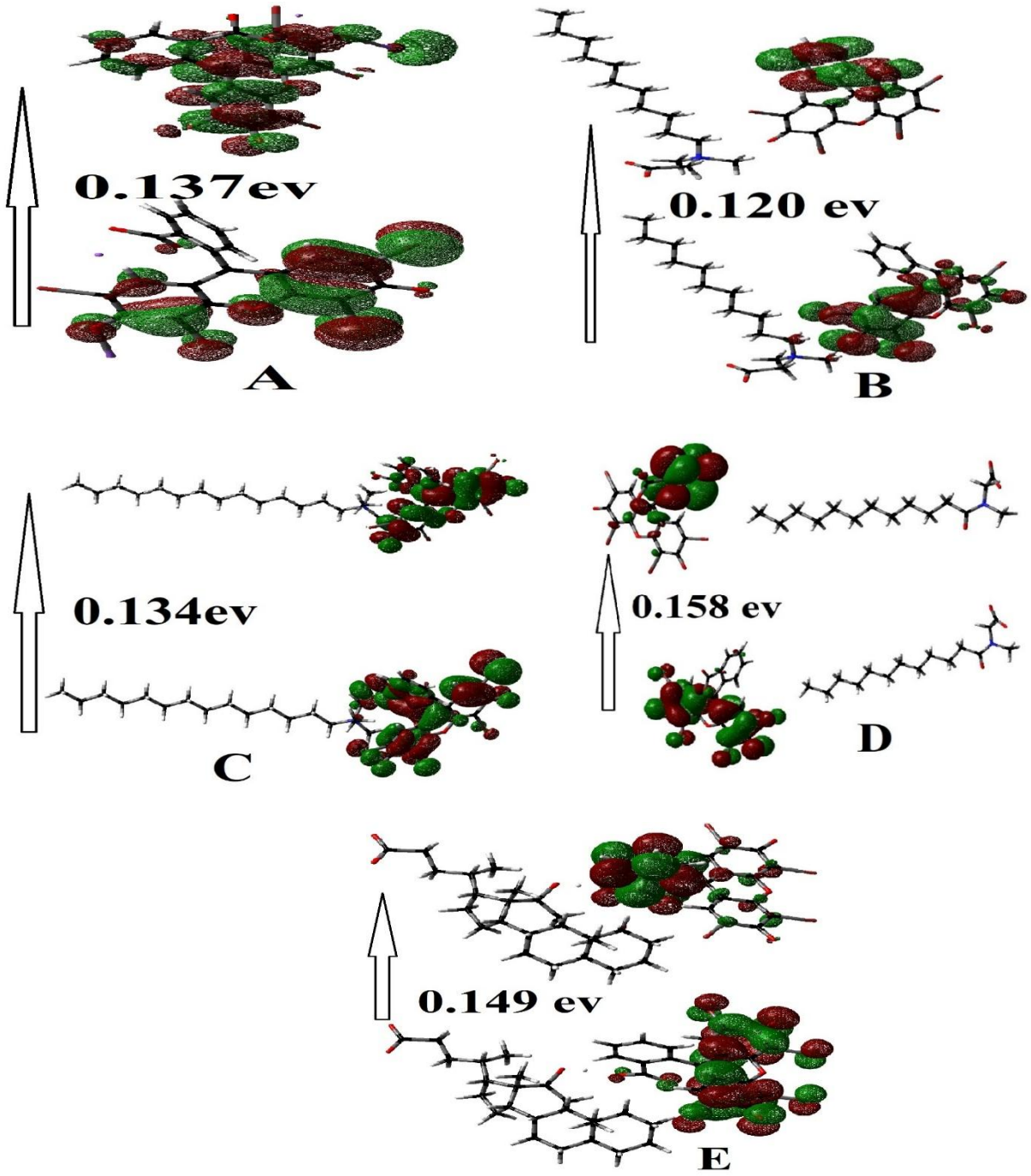

Figure 10. HOMO-LUMO diagrams of (A) EY, (B) EY-C_{12}DmCB (C) EY-CTAC (D) EY-SLAS, and (E) EY- NaDC systems.

4. Conclusion

This study comprehensively examines the interactions between an anionic dye, known as EY, and four distinct surfactants. The aim is to elucidate the nature of these interactions and to understand how varying concentrations influence the behavior of the dye in the presence of the

surfactants, thereby providing insights into their potential applications in various chemical and industrial processes. As SLAS and NaDC contain the same charge concerning EY, it predicts that neither surfactant can solubilize EY properly into the micellar environment. Adding both surfactants results in a minimum spectral shift in absorption and emission with no such increment in an average lifetime. However, due to hydrophobic attraction, EY and surfactants may approach each other mutually. This inference is a support by an increment in particle size and very high negative values in the zeta potential as well as the colloidal stability of EY-SLAS and EY-NaDC systems. Moreover, optimized energy and energy gap between HOMOs and LUMOs also support the instability of these systems concerning an aqueous solution of EY itself. An oppositely charged surfactant, CTAC provides extra stability in the EY-CTAC system by producing a protective microenvironment. Incorporation of EY into the stern layer of the micelle is a support by prominent bathochromic shift in absorption and emission spectra, increment in anisotropy and average lifetime and decrease in particle size and energy gap between HOMOs and LUMOs concerning aqueous solution of EY itself. However, C_{12}DmCB stabilizes EY mostly and the interaction of C_{12}DmCB with EY has been found to be most prominent among the four surfactants. The addition of C_{12}DmCB to the aqueous solution of EY results in the most considerable bathochromic shift in both absorption and emission spectra; average lifetime and anisotropy have been increased markedly, and a decrease in particle size and zeta potential supports the incorporation of EY into the vicinity of the micellar microenvironment. Moreover, the lowest optimized energy and lowest energy gap between HOMOs and LUMOs also establish that EY- C_{12}DmCB system is the most stable. In this work, a new synthesized zwitterionic surfactant is introduced, and it interacts effectively with EY. We are optimistic that these findings will significantly enhance advancements in various branches of analytical chemistry, material fabrication, medicinal photosensitization, drug delivery, wastewater treatment, and other related fields.

REFERENCES:

[1] S. Baliarsingh, J. Jena, T. Das, N.B. Das, Role of cationic and anionic surfactants in textile dyeing with natural dyes extracted from waste plant materials and their potential antimicrobial properties, Industrial Crops and Products 50 (2013) 618, https://doi.org/10.1016/j.indcrop.2013.08.037.

[2] A.G. Hassabo, F. Saad, B.M. Hegazy, A. Sediek, H. Ghazal, The use of cationic surfactants in the textiles industry, Journal of Textiles, Coloration and Polymer Science 20 (2023) 227, 10.21608/jtcps.2023.216820.1189.

[3] D. Venkataramani, A. Tsulaia, S. Amin, Fundamentals and applications of particle stabilized emulsions in cosmetic formulations, Advances in Colloid and Interface Science 283 (2020) 102234, https://doi.org/10.1016/j.cis.2020.102234.

[4] L. Zhang, X. Liu, M. Zhang, T. Wang, H. Tang, Y. Jia, The effect of pH/PAC on the coagulation of anionic surfactant wastewater generated in the cosmetic production, Journal of Environmental Chemical Engineering 11 (2023) 109312, https://doi.org/10.1016/j.jece.2023.109312.

[5] A.S. Murali, Sreelekshmi, B. Saraswathyamma, in: J.G. Manjunatha, C.M. Hussain (Eds.), Surfactant Based Electrochemical Sensors and Biosensors, Elsevier, 2024, p. 363-385.

[6] S.V. Smirnova, V.V. Apyari, Aqueous Two-Phase Systems Based on Cationic and Anionic Surfactants Mixture for Rapid Extraction and Colorimetric Determination of Synthetic Food Dyes, Sensors 23 (**2023**), 10.3390/s23073519.

[7] I. Kralova, J. Sjöblom, Surfactants Used in Food Industry: A Review, Journal of Dispersion Science and Technology 30 (2009) 1363, 10.1080/01932690902735561.

[8] G.M. Nabil, N.M. El-Mallah, M.E. Mahmoud, Enhanced decolorization of reactive black 5 dye by active carbon sorbent-immobilized-cationic surfactant (AC-CS), Journal of Industrial and Engineering Chemistry 20 (2014) 994, https://doi.org/10.1016/j.jiec.2013.06.034.

[9] T. Chakraborty, S. Ghosh, A Unified Survey of Applicability of Theories of Mixed Adsorbed Film and Mixed Micellization, Journal of Surfactants and Detergents 11 (2008) 323, https://doi.org/10.1007/s11743-008-1095-1.

[10] S.S. Taha, D.S. Ali, R.O. Hassan, H. Omar Othman, S. Smaoui, Colorimetric and fluorescent dual mode detection of Fe (III) ion in blood samples in combination with

cloud point extraction, Microchemical Journal 195 (2023) 109390, https://doi.org/10.1016/j.microc.2023.109390.

[11] W.I. Mortada, H.E. Zedan, M.E. Khalifa, Spectrophotometric determination of trace vanadium in fresh fruit juice samples by ion pair-based surfactant-assisted microextraction procedure with solidification of floating organic drop, Spectrochimica Acta Part A: Molecular and Biomolecular Spectroscopy 302 (2023) 123107, https://doi.org/10.1016/j.saa.2023.123107.

[12] S. Mondal, M. Karar, N. Dey, Dye-surfactant co-assembly as the chromogenic indicator for nanomolar level detection of Cu(i) ions via a color-changing response, Journal of Materials Chemistry B 11 (2023) 4111, 10.1039/D3TB00115F.

[13] G. Singh, M. Kaur, V.K. Aswal, T.S. Kang, Aqueous colloidal systems of bovine serum albumin and functionalized surface active ionic liquids for material transport, RSC Advances 10 (2020) 7073, 10.1039/C9RA05549E.

[14] S. Das, P. Roy, P.S. Sardar, S. Ghosh, Addressing the interaction of stem bromelain with different anionic surfactants, below, at and above the critical micelle concentration (cmc) in phosphate buffer at pH 7: Physicochemical, spectroscopic, & molecular docking study, International Journal of Biological Macromolecules 271 (2024) 132368, https://doi.org/10.1016/j.ijbiomac.2024.132368.

[15] M.R. Bittermann, T.I. Morozova, S.F. Velandia, E. Mirzahossein, A. Deblais, S. Woutersen, D. Bonn, Surface-Mediated Molecular Transport of a Lipophilic Fluorescent Probe in Polydisperse Oil-in-Water Emulsions, Langmuir 39 (2023) 4207, 10.1021/acs.langmuir.2c02597.

[16] N.A. Atiyah, T.M. Albayati, M.A. Atiya, Interaction behavior of curcumin encapsulated onto functionalized SBA-15 as an efficient carrier and release in drug delivery, Journal of Molecular Structure 1260 (2022) 132879, https://doi.org/10.1016/j.molstruc.2022.132879.

[17] M.T.R. Joy, S. Mahbub, M.A. Rub, M.A.A. Hossain, M.D. Hossain, M.J. Khatun, S.C. Mohanta, M.F. Hossain, Y.G. Alghamdi, M.A. Hoque, Interaction of crystal violet dye with dodecyltrimethylammonium bromide in aqueous and electrolyte medium at different temperatures, Journal of Molecular Liquids 343 (2021) 117592, https://doi.org/10.1016/j.molliq.2021.117592.

[18] H. You, H. Spaeth, V.N.L. Linhard, A.J. Steckl, Role of Surfactants in the Interaction of Dye Molecules in Natural DNA Polymers, Langmuir 25 (2009) 11698, 10.1021/la901646d.

[19] L.-L. Zhang, A. Zaoui, W. Sekkal, Y.-Y. Zheng, Interlayer adsorption of cationic dye on cationic surfactant-modified and unmodified montmorillonite, Journal of Hazardous Materials 442 (2023) 130107, https://doi.org/10.1016/j.jhazmat.2022.130107.

[20] T.U. Rashid, S.M.F. Kabir, M.C. Biswas, M.A.R. Bhuiyan, Sustainable Wastewater Treatment via Dye–Surfactant Interaction: A Critical Review, Industrial & Engineering Chemistry Research 59 (2020) 9719, 10.1021/acs.iecr.0c00676.

[21] T.D. Pham, T.T. Pham, M.N. Phan, T.M.V. Ngo, V.D. Dang, C.M. Vu, Adsorption characteristics of anionic surfactant onto laterite soil with differently charged surfaces and application for cationic dye removal, Journal of Molecular Liquids 301 (2020) 112456, https://doi.org/10.1016/j.molliq.2020.112456.

[22] G. Chakraborty, A. Bhattarai, R. De, Polyelectrolyte–Dye Interactions: An Overview, Polymers 14 (**2022**), 10.3390/polym14030598.

[23] A. Băran, L. Aricov, G. Stîngă, A. Iovescu, A.-R. Leontieş, V.V. Jerca, The effect of $C_{12}E_6$ nonionic surfactant on the solubilization of Eosin Y in unmodified- and hydrophobically modified poly(Acrylic acid) solutions, Journal of Molecular Liquids 346 (2022) 117103, https://doi.org/10.1016/j.molliq.2021.117103.

[24] S. Noor, M.B. Taj, S. M, I. Naz, Comparative solubilization of reactive dyes in single and mixed surfactants, Journal of Dispersion Science and Technology 43 (2022) 2058, 10.1080/01932691.2021.1956528.

[25] K.N. Elfer, A.B. Sholl, M. Wang, D.B. Tulman, S.H. Mandava, B.R. Lee, J.Q. Brown, DRAQ5 and Eosin (‘D&E’) as an Analog to Hematoxylin and Eosin for Rapid Fluorescence Histology of Fresh Tissues, PLOS ONE 11 (2016) e0165530, 10.1371/journal.pone.0165530.

[26] P. Dey, in: P. Dey (Ed.) Basic and Advanced Laboratory Techniques in Histopathology and Cytology, Springer Nature Singapore, Singapore, **2023**, p. 71-82.

[27] R. Permatasari, P. Fuji Verdian, M. Silvia, Potensi Buah Delima Merah (Punica Granatum L.) Sebagai Pewarnaan Alternatif Pengganti Eosin pada Pewarnaan Papanicolaou, SEHATMAS: Jurnal Ilmiah Kesehatan Masyarakat 2 (2023) 288, 10.55123/sehatmas.v2i1.1204.

[28] K. Raju, Evolution of Pap Stain, Biomedical Research and Therapy 3 (2016) 6, 10.7603/s40730-016-0006-8.

[29] S.P. Singh, V. Srivastava, P.K. Singh, P.P. Singh, Visible-light induced eosin Y catalysed C(sp2)-H alkylation of carbonyl substrates via direct HAT, Tetrahedron 132 (2023) 133245, https://doi.org/10.1016/j.tet.2023.133245.

[30] A. Lewandowska-Andrałojć, D. Larowska, E. Gacka, T. Pedzinski, B. Marciniak, How Eosin Y/Graphene Oxide-Based Materials Can Improve Efficiency of Light-Driven Hydrogen Generation: Mechanistic Aspects, The Journal of Physical Chemistry C 124 (2020) 2747, 10.1021/acs.jpcc.9b09573.

[31] P. Wang, Z. Guan, Q. Li, J. Yang, Efficient visible-light-driven photocatalytic hydrogen production from water by using Eosin Y-sensitized novel g-C3N4/Pt/GO composites, Journal of Materials Science 53 (2018) 774, 10.1007/s10853-017-1540-5.

[32] J.-H. Wu, T.-H. Yang, F. Chen, F. Zhang, J.-J. Chen, H.-Q. Yu, Quantifying nitroaromatics via terminating their photoreduction catalyzed by Eosin Y, Applied Catalysis B: Environmental 325 (2023) 122363, https://doi.org/10.1016/j.apcatb.2023.122363.

[33] E. Edwards, Bionic algae for solar hydrogen, Joule 7 (2023) 863, https://doi.org/10.1016/j.joule.2023.04.013.

[34] B. Fan, W. Peng, Y. Zhang, P. Liu, J. Shen, ROS conversion promotes the bactericidal efficiency of Eosin Y based photodynamic therapy, Biomaterials Science 11 (2023) 4930,

[35] C. Anselmi, D. Capitani, A. Tintaru, B. Doherty, A. Sgamellotti, C. Miliani, Beyond the color: A structural insight to eosin-based lakes, Dyes and Pigments 140 (2017) 297, https://doi.org/10.1016/j.dyepig.2017.01.046.

[36] M. Chakraborty, A.K. Panda, Spectral behaviour of eosin Y in different solvents and aqueous surfactant media, Spectrochimica Acta Part A: Molecular and Biomolecular Spectroscopy 81 (2011) 458, https://doi.org/10.1016/j.saa.2011.06.038.

[37] R. Sharma, A. Kamal, R.K. Mahajan, Detailed study of interactions between eosin yellow and gemini pyridinium surfactants, RSC advances 6 (2016) 71692,

[38] E.M. Arbeloa, G.V. Porcal, S.G. Bertolotti, C.M. Previtali, Effect of the interface on the photophysics of eosin-Y in reverse miceles, Journal of Photochemistry and Photobiology A: Chemistry 252 (2013) 31, https://doi.org/10.1016/j.jphotochem.2012.11.003.

[39] S. Acharya, B. Rebery, Fluorescence spectrometric study of eosin yellow dye–surfactant interactions, Arabian Journal of Chemistry 2 (2009) 7, https://doi.org/10.1016/j.arabjc.2009.07.010.

[40] R. Banik, S. Das, A. Ghosh, S. Ghosh, Comparative studies on the aggregate formation of synthesized zwitterionic gemini and monomeric surfactants in the presence of the amphiphilic antipsychotic drug chlorpromazine hydrochloride in aqueous solution: an experimental and theoretical approach, Soft Matter 19 (2023) 7995,

[41] R. Sardar, S. Das, R. Banik, S. Bhunia, S. Ghosh, Exploration of the impact of graphene oxide, acetylenic gemini, and CTAT on the photophysical and aggregation properties of

dipolar coumarin 153, Physical Chemistry Chemical Physics 26 (2024) 8900, 10.1039/D3CP05361J.

[42] V.J. Mayani, S.V. Mayani, S.W. Kim, A Sustainable Nanocomposite Au(Salen)@CC for Catalytic Degradation of Eosin Y and Chromotrope 2R Dyes, Scientific Reports 7 (2017) 7239, 10.1038/s41598-017-07707-6.

[43] P. Garg, B. Kaur, G. Kaur, S. Saini, G.R. Chaudhary, A study of the spectral behaviour of Eosin dye in three states of metallosurfactants: Monomeric, micelles and metallosomes, Colloids and Surfaces A: Physicochemical and Engineering Aspects 610 (2021) 125697, https://doi.org/10.1016/j.colsurfa.2020.125697.

[44] M. Bielska, A. Sobczyńska, K. Prochaska, Dye–surfactant interaction in aqueous solutions, Dyes and Pigments 80 (2009) 201, https://doi.org/10.1016/j.dyepig.2008.05.009.

[45] C. Mall, P.P. Solanki, Spectrophotometric and conductometric studies of molecular interaction of brilliant cresyl blue with cationic, anionic and non-ionic surfactant in aqueous medium for application in photogalvanic cells for solar energy conversion and storage, Energy Reports 4 (2018) 23, https://doi.org/10.1016/j.egyr.2017.09.001.

[46] A.R. Tehrani-Bagha, K. Holmberg, Solubilization of Hydrophobic Dyes in Surfactant Solutions, Materials 6 (**2013**) 580, 10.3390/ma6020580.

[47] N. Patra, B. Mandal, S. Ghosh, Spectroscopic Studies on the Interaction of Dye and Surface Active Ionic Liquid, Industrial & Engineering Chemistry Research 56 (2017) 10044, 10.1021/acs.iecr.7b02052.

[48] M. Koegl, C. Weiß, L. Zigan, Fluorescence Spectroscopy for Studying Evaporating Droplets Using the Dye Eosin-Y, Sensors 20 (**2020**) 5985, 10.3390/s20215985.

[49] D.S. Pellosi, B.M. Estevão, J. Semensato, D. Severino, M.S. Baptista, M.J. Politi, N. Hioka, W. Caetano, Photophysical properties and interactions of xanthene dyes in aqueous micelles, Journal of Photochemistry and Photobiology A: Chemistry 247 (2012) 8, https://doi.org/10.1016/j.jphotochem.2012.07.009.

[50] S. Mallick, A.S. Arathi, A.L. Koner, Customized tuning of aggregation-induced emission of a napthalimide dye by surfactants and cyclodextrin, Journal of Colloid and Interface Science 499 (2017) 46, https://doi.org/10.1016/j.jcis.2017.03.097.

[51] A. Manna, S. Chakravorti, Effect of micellar environment on charge transfer dye photophysics, Journal of Molecular Liquids 168 (2012) 94, https://doi.org/10.1016/j.molliq.2012.01.007.

[52] E. Maltas, Binding interactions of niclosamide with serum proteins, Journal of Food and Drug Analysis 22 (2014) 549, https://doi.org/10.1016/j.jfda.2014.03.004.

[53] D. Sahoo, P. Bhattacharya, S. Chakravorti, Quest for Mode of Binding of 2-(4-(Dimethylamino)styryl)-1-methylpyridinium Iodide with Calf Thymus DNA, The Journal of Physical Chemistry B 114 (2010) 2044, 10.1021/jp910766q.

[54] H.M. Marwani, A.M. Asiri, S.A. Khan, Spectral, stoichiometric ratio, physicochemical, polarity and photostability studies of newly synthesized chalcone dye in organized media, Journal of Luminescence 136 (2013) 296, https://doi.org/10.1016/j.jlumin.2012.12.021.

[55] P.J.G. Coutinho, E.M.S. Castanheira, M. Céu Rei, M.E.C.D. Real Oliveira, Nile Red and DCM Fluorescence Anisotropy Studies in C12E7/DPPC Mixed Systems, The Journal of Physical Chemistry B 106 (2002) 12841, 10.1021/jp026479u.

[56] S. Ghosh, S. Mondal, Spectroscopic study on the interaction of medicinal pigment, curcumin with various surfactants: an overview, J. Surf. Sci. Technol 28 (2012) 179,

[57] M. Secu, C.E. Secu, M. Sima, R.F. Negrea, C. Bartha, M. Dinescu, V. Damian, Luminescent Eosin Y–SiO2 hybrid nano and microrods prepared by sol–gel template method, Journal of Luminescence 143 (2013) 89, https://doi.org/10.1016/j.jlumin.2013.04.043.

[58] P. Karunanithi, V. R, E. Paul Raj, P. Rajesh, S. Krishnamoorthy, S. Dash, Pluronic based neutral-ionic binary micellar surfactant systems for solubilizing the cationic methylene blue dye, Chemical Physics Impact 5 (2022) 100092, https://doi.org/10.1016/j.chphi.2022.100092.

[59] S. Das, S. Ghosh, A detailed assessment on the interaction of sodium alginate with a surface-active ionic liquid and a conventional surfactant: a multitechnique approach, Physical Chemistry Chemical Physics 24 (2022) 13738,

[60] D.J. Pochapski, C. Carvalho dos Santos, G.W. Leite, S.H. Pulcinelli, C.V. Santilli, Zeta Potential and Colloidal Stability Predictions for Inorganic Nanoparticle Dispersions: Effects of Experimental Conditions and Electrokinetic Models on the Interpretation of Results, Langmuir 37 (2021) 13379, 10.1021/acs.langmuir.1c02056.

[61] A. Asadzadeh Shahir, S. Javadian, B.B.M. Razavizadeh, H. Gharibi, Comprehensive Study of Tartrazine/Cationic Surfactant Interaction, The Journal of Physical Chemistry B 115 (2011) 14435, 10.1021/jp2051323.

[62] P. Bajpai, Chapter 10—Papermaking Chemistry, Biermann's Handbook of Pulp and Paper, 3rd ed.; Elsevier: Amsterdam, The Netherlands 2 (2018) 207,

[63] S. Fazeli, B. Sohrabi, A.R. Tehrani-Bagha, The study of Sunset Yellow anionic dye interaction with gemini and conventional cationic surfactants in aqueous solution, Dyes and Pigments 95 (2012) 768, https://doi.org/10.1016/j.dyepig.2012.03.022.

[64] R. Sharma, A. Kamal, R.K. Mahajan, A quantitative appraisal of the binding interactions between an anionic dye, Alizarin Red S, and alkyloxypyridinium surfactants: a detailed micellization, spectroscopic and electrochemical study, Soft Matter 12 (2016) 1736,

[65] S. Joshi, D.D. Pant, Steady state and time-resolved fluorescence spectroscopy of quinine sulfate dication bound to sodium dodecylsulfate micelles: Fluorescent complex formation, Journal of Luminescence 145 (2014) 224, https://doi.org/10.1016/j.jlumin.2013.07.060.

[66] E.A. Slyusareva, M.A. Gerasimova, pH-Dependence of the Absorption and Fluorescent Properties of Fluorone Dyes in Aqueous Solutions, Russian Physics Journal 56 (2014) 1370, 10.1007/s11182-014-0188-8.

[67] A. Mishra, G.B. Behera, M.M.G. Krishna, N. Periasamy, Time-resolved fluorescence studies of aminostyryl pyridinium dyes in organic solvents and surfactant solutions, Journal of Luminescence 92 (2001) 175, https://doi.org/10.1016/S0022-2313(00)00255-6.

[68] M. Bergaoui, V. Deimede, M. Khalfaoui, A computational and experimental investigation of anionic dyes adsorption onto hydrophilic macroporous polymers: Insights from morphological characterization and molecular simulations, Journal of Environmental Chemical Engineering 10 (2022) 107583, https://doi.org/10.1016/j.jece.2022.107583.

[69] A.K. Vats, A. Pradhan, S. Hayase, S.S. Pandey, Synthesis, photophysical characterization and dye adsorption behavior in unsymmetrical squaraine dyes with varying anchoring groups, Journal of Photochemistry and Photobiology A: Chemistry 394 (2020) 112467, https://doi.org/10.1016/j.jphotochem.2020.112467.

CHAPTER – III

A thorough investigation into the interactions of Phloxine b with surfactants of varying charges, employing advanced spectroscopic techniques and robust theoretical analyses to deliver compelling insights.

A thorough investigation into the interactions of Phloxine B with surfactants of varying charges, employing advanced spectroscopic techniques and robust theoretical analyses to deliver compelling insights.

Abstract:

This study effectively explores the property of the microenvironment and the aggregation behavior of different surfactants, namely a synthesized zwitterionic surfactant called N-dodecyl-N, N-dimethyl-2-ammonio-1-ethanecarbonate (C_{12}DmCB), the cationic surfactant CTAC, and the anionic surfactant SDS in their respective pre- and post-micellar concentrations using a novel fluorophore known as Phloxine B (PhB). Several advanced techniques were utilized, including UV-visible absorption spectroscopy, steady-state and time-resolved fluorescence spectroscopy, and dynamic light scattering (DLS) measurements. A theoretical approach was also conducted using density functional theory (DFT) calculations. Various spectroscopic parameters, such as spectral shifts, Stokes shift formation, and the creation of exciplexes, were analyzed by altering the polarity of the microenvironment. Additionally, by varying fluorescence intensity, the nature of the interaction between PhB and the different surfactants was predicted in terms of static and dynamic quenching, as well as by calculating the binding constant and the number of binding sites. Anisotropy measurements were performed to assess the rigidity of the microenvironment provided by the surfactants. Time-correlated single photon counting (TCSPC) experiments helped to determine the probe's location in the excited state in both pre- and post-micellar concentrations of the surfactants. DLS measurements were conducted to assess aggregate size and the intercalation of the probe within various micellar environments, and zeta potential calculations were performed to predict the stability of the colloidal system. DFT calculations were employed to investigate the nature of interactions at a 1:1 molecular ratio, while time-dependent DFT (TDDFT) calculations provided insights into the location of frontier molecular orbitals (FMOs). Generally, the

interaction between the dye and surfactant is governed by electrostatic attraction when they carry opposite charges. The anionic dye PhB interacts readily with CTAC, resulting in a significant bathochromic shift and an increase in average lifetime values. Conversely, C_{12}DmCB, the zwitterionic surfactant, proved to be the most effective in solubilizing PhB, resulting in a greater bathochromic shift and a more pronounced increase in average lifetime. In contrast, a hydrophobic stacking mechanism was observed in the PhB-SDS system, resulting in effective static quenching.

1. Introduction:

In the past few decades, surfactant dye interactions in dilute aqueous solutions have drawn widespread attention due to their vast industrial applications in various fields, including textile dying [1, 2], food [3, 4], photography [5], printing ink [6, 7], and hair coloring [8, 9]. Moreover, besides its industrial applications, surfactant dye association is of significant practical importance in various analytical and pharmaceutical fields, such as the spectrophotometric determination of metal ions [10, 11], biological transport [12, 13], and medicinal photosensitization [14, 15], among others. Surfactants, a special class of amphiphiles characterized by a polar head group and a non-polar, long hydrophobic tail, have been utilized in drug delivery[16, 17], in addition to the fields above. Considering the charge of the hydrophilic group, surfactants can be classified into four types: cationic, anionic, non-ionic, and zwitterionic. It also exhibits a self-association property, forming micelles when its concentration exceeds its respective critical micellar concentration (CMC) [18, 19]. Dyes are unsaturated organic compounds with various biological and industrial applications. Based on their solubility and chemical properties, the nature of chromophore dyes can be classified into several groups. Xanthene dyes are found to be one of the most important classes of compounds for their wide variety, several biological applications, and remarkable photophysical properties[20]. Karaman et al. utilized xanthene dyes for cancer imaging and treatment [21]. Sekar et al. made Xanthene-based fluorophores for NIR emission[22, 23]. The

interaction of several xanthene dyes with surfactants has been reported earlier[24-26]. Ganguly et al. studied several photophysical properties of erythrosine B, rose bengal, and eosin in the presence of cationic, anionic, and nonionic surfactants[27, 28]. P Garg et al. studied the interaction behavior of several xanthene dyes with chromium-based metallosurfactants [29]. Phloxine B, commonly known as phloxine [PhB], a derivative of xanthene dye fluorescein, has several biological and industrial uses. It is a water-soluble red dye and has been used as a color additive in food [26, 27], drugs [28], and cosmetics [30]. Moreover, the various bactericidal and antimicrobial activities of phloxine have also been reported [31-33]. It is also used as a potential bacterial stain as well as a staining material for dead cells [34]. Although phloxine B has potential applications in various fields of chemistry, the interaction between phloxine and surfactants is very low. Genwa et al. studied the photocurrent response of phloxine with cationic surfactant CTAB[35], and Teja et al. used phloxine as a filler in the composite of octadecyl trimethylammonium cations with saponite [36]. However, in this work interaction of phloxine B has been studied with cationic surfactant cetyl trimethyl ammonium bromide [CTAB], anionic surfactant [SDS], and synthesized zwitterionic surfactant N-Dodecyl-N, N-dimethyl-2-ammonio-1-ethanecarbonate (C_{12}DmCB), by using UV-visible spectroscopy, steady state and time resolve fluorescence spectroscopy, anisotropy measurement, DLS and zeta potential measurements to explore the nature of interaction, aggregation behaviour and spectral changes in aqueous medium. Moreover, a DFT study has also been made for the optimisation of molecular structure and to get the energy gap between HOMOs and LUMOs of several PB-surfactant systems. The primary objective of this work is to investigate the nature and strength of interaction between PB and differently charged surfactants. Dye surfactant interaction is commonly attributed to the electrostatic force of attraction [37, 38], forming a salt-like ion pair between the dye and oppositely charged surfactants [39]. Various other factors, such as hydrogen bonding, van der Waals forces of attraction, π-π stacking [40-42], and the formation of H and J

aggregates [43, 44], may also significantly impact the spectral behavior. However, in this work, the association property of PB in various charged micellar media has been studied spectrophotometrically and theoretically. To the best of our knowledge, this is the first report on the investigation of the interaction between PB and a zwitterionic surfactant.

2. Experimental:

2.1. Materials:

Phloxine B (Dye content ≥ 80%), CTAC (purity ≥ 98%), SDS (purity ≥ 98.5%), and C_{12}DmCB were the primary chemicals used in all experiments. All substances except C_{12}DmCB were purchased from Sigma Aldrich (see Table 1). C_{12}DmCB has been synthesized in our laboratory[45], (yield: 10.04g, 93%). All chemicals were used without further purification. Double-distilled water was used to prepare all experimental solutions. The structures of all the chemicals are depicted in Figure 1.

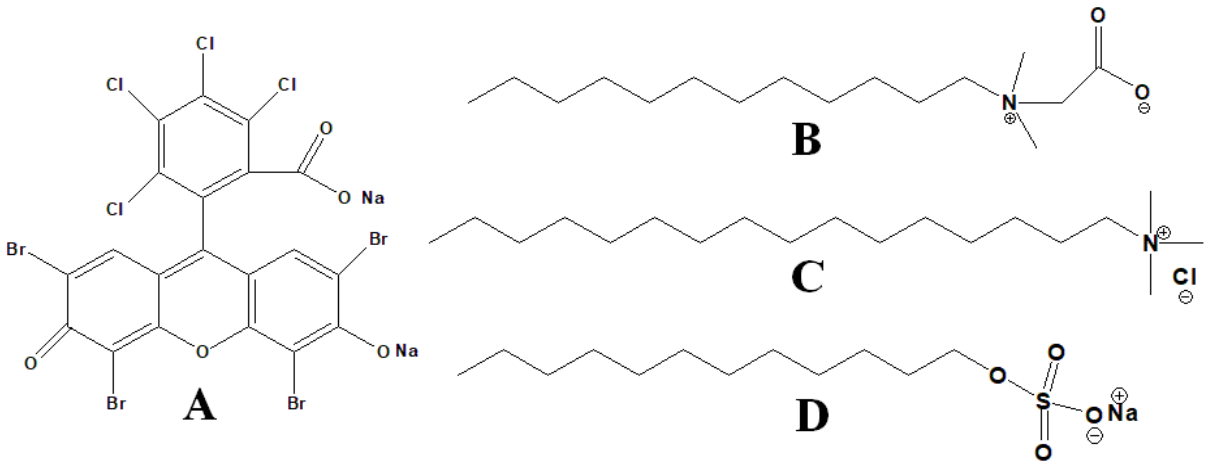

Figure 1: Chemical Structures of (A) PhB (B) C_{12}DmCB, (C) CTAC, (D) SDS.

Table 1. Specifications of chemical compounds used in the Study

Materials	Chemical formula	CAS	Supplier	Purity
Phloxine B	$C_{20}H_2Br_4Cl_4Na_2O_5$	18472-87-2	Sigma Aldrich	≥ 80%
Sodium dodecyl sulphate	$C_{12}H_{25}O_4SNa$	151-21-3	Sigma Aldrich	≥ 98%
cetyl trimethyl ammonium chloride	$C_{19}H_{42}ClN$	112-02-7	Sigma Aldrich	≥ 98%
N-Dodecyl-N, N-dimethyl-2-ammonio-1-ethanecarbonate	C_{12}DmCB	-	Synthesized	-

2.2. Preparation of Stock Solution:

A 1.0 mM stock solution of phloxine B (PhB) was carefully prepared by dissolving a precise amount of the vibrant dye in distilled water, ensuring complete dissolution for accurate concentration. To achieve the desired experimental concentrations, this stock solution was systematically diluted with additional water. In the aqueous solutions containing surfactants, the concentrations were meticulously maintained at approximately 15 times their respective critical micelle concentrations (CMCs), which is essential for the intended interaction of the surfactants. The critical micelle concentration (CMC) for C_{12}DmCB has been successfully established [41], and we've prepared the solution accordingly to ensure optimal results. To enhance the clarity and homogeneity of all solutions, they were thoroughly sonicated, facilitating uniform dispersion of the dye and surfactants.

2.3. UV-Visible spectral measurements:

Absorbance was recorded using a Shimadzu UV-1601 spectrophotometer (Japan) with a 10 mm path-length quartz cuvette. The spectra were acquired in the wavelength range of 200-800nm. A 5 µL stock solution of PhB was mixed with 2 mL of water in a cuvette to achieve a dye solution concentration of 0.0025 mM. The concentration of PhB was intentionally kept

low to prevent self-aggregation of dye molecules and to diminish the van der Waals forces between the hydrophobic regions of adjacent dye molecules. Different sets were prepared by gradually adding C_{12}DmCB, CTAC, and SDS to an aqueous solution of PhB to observe the premicellar and post-micellar behavior of the microenvironment. The cell's temperature was maintained at a constant 25 °C ± 0.1 °C through the use of a circulating water bath. All experiments were conducted twice to reduce errors.

2.4. Steady-state fluorescence study:

Fluorescence spectra, emission intensity, and anisotropy measurements were conducted using a PerkinElmer LS 55 fluorescence spectrophotometer equipped with a Peltier system at 298.15 K, with an accuracy of ±0.02 K, utilizing a 10 mm path length quartz cuvette. To capture the fluorescence spectra, 5 µL of a PhB stock solution was added to 2 mL of water in a cuvette, resulting in a concentration of [PhB] of 0.0025 mM. Fluorometric titrations involved the gradual introduction of C_{12}DmCB (ranging from 0 to approximately 5.18 mM), CTAC (from 0 to around 2.90 mM), and SDS (from 0 to about 24.04 mM) to each set of PhB at the same concentration. Emission spectra were recorded over a range of 540nm to 600nm, with excitation and emission slit widths fixed at 15.0 nm and 2.5 nm, respectively. The scanning rate was set to 250 nm/min. Anisotropy was assessed at an excitation wavelength of 525 nm and an emission wavelength of 557.9 nm for PhB. The anisotropy value recorded was the average of six consecutive measurements. All anisotropy calculations were averaged over a 20-second integration time, and the temperature was stabilized at 298.15K by circulating water through the Peltier system. Prior to each measurement, the sample temperature was maintained at 298 K. All experiments were repeated twice to reduce any potential errors.

2.5. Time-resolved fluorescence study:

Fluorescence spectral analysis with time resolution was performed using the advanced technique of time-correlated single photon counting (TCSPC). This was executed in the

Horiba-Jobin-Yvon Cube fluorescence lifetime system, which utilized a NanoLED emitting at 370 nm (supplied by IBH, UK) as the excitation source. For the detection of photons from both PhB and TBX, a specialized photon detection module was employed. To analyze the decay of fluorescence signals, the collected data were fitted using the IBH DAS-6 decay analysis software, which allows for rigorous modeling of the decay kinetics. To establish a baseline for the analyses, the lamp profile was recorded by substituting the sample with a dilute micellar solution of sodium dodecyl sulfate (SDS) in water, acting as a scatterer. The accuracy of the fitting process was assessed using the χ^2 criterion, alongside a thorough visual inspection of the residuals from the fitted functions compared to the experimental data. The mean (average) fluorescence lifetimes (τavg) for the bi-exponential iterative fittings were derived from the individual decay times (τ1 and τ2) and the corresponding pre-exponential factors (a1 and a2) using a specific mathematical relation, which helps in accurately characterizing the fluorescence decay behavior of the samples.

$$\tau_{avg} = a_1\tau_1 + a_2\,\tau_2 \qquad (1)$$

The concentration of the dye and surfactants was maintained at a constant level throughout the experiment, resembling a steady-state condition for emission spectral analysis. This approach ensured that the results were reliable and comparable, allowing for a clearer understanding of the spectral emissions observed.

2.6. Dynamic Light Scattering (DLS) and zeta potential measurement:

Dynamic Light Scattering (DLS) and the Zeta potential measurements were conducted using a Nano ZS Zetasizer from Malvern, UK, employing a He-Ne laser at an angle of 90 degrees for optimal sensitivity. Throughout the experiment, the temperature was meticulously maintained at 25°C to ensure consistency in the results. A series of various concentrations of solutions was prepared for measurement, specifically focusing on water solutions of dye, along with premicellar and postmicellar concentrations of C_{12}DmCB, CTAC, and SDS. These were

systematically blended with aqueous solutions of PhB across different experimental sets. To ensure reliability and accuracy, each set of experiments was repeated twice, allowing for a thorough assessment of reproducibility. The resultant data was plotted to illustrate the percentage of intensity versus particle size (in nm), providing valuable insights into the characteristics of the samples analyzed.

2.7. Density functional theory calculations:

The calculation of density functional theory has recently been crucial for comprehending both covalent and non-covalent interactions at the molecular scale. Structures of PhB, C_{12}DmCB, CTAC, and SDS were created using Avogadro software, and these structures underwent further refinement through the auto-optimization tools available in the same software. The force field employed for auto optimization was MMFF94S, with 4 steps per update, utilizing the steepest descent algorithm. Additionally, to assess the interaction energy of PhB with various surfactants at a 1:1 molecular ratio, energy optimization was performed on these preoptimized structures using Gaussian 9 software. All calculations utilized the B3LYP functional along with a 6-31g(d,p) basis set. TDDFT calculations were also conducted to analyze the structures of the highest occupied molecular orbital (HOMO) and the lowest unoccupied molecular orbital (LUMO) to illustrate the nature of interactions between the dye and different amphiphiles added.

3. Results and discussion

3.1 UV-Visible Spectral Study: The UV-Visible spectral study is a preliminary yet critical experiment for predicting how the dye interacts in micellar media. In aqueous media, PhB shows a maximum absorption wavelength (λmax) at 539 nm and a shoulder peak at 512 nm (Fig. 2). These findings are consistent with the reported literature[30, 46]. The shoulder peak may arise from the aggregation of dye molecules in the bulk aqueous phase. However, the absorbance and spectral patterns of PhB vary across different micellar environments.

When C_{12}DmCB and CTAC are added to an aqueous solution of PhB in their premicellar concentrations, a reduction in absorbance is observed (Fig. 2A, 2B). This change is attributed to the formation of colloidal dye-surfactant submicellar aggregates (mixed micelles) or insoluble dye-surfactant salts[47], resulting from the electrostatic attraction between oppositely charged molecules. Notably, as the concentration of C_{12}DmCB increases from 0.15 CMC to 2.70 CMC, a significant bathochromic shift of 15 nm occurs, accompanied by a marked increase in absorbance. This behavior can be explained by a change in the polarity of the microenvironment from a more polar (water) to a less polar (C_{12}DmCB micelle) one, indicating that PhB is being solubilized in the stern or palisade layer of the micellar core.

Additionally, when CTAC is added up to 2.62 CMC, a notable redshift of 13 nm is observed. Since CTAC is an oppositely charged surfactant, PhB is intercalated into the Stern layer of the micelle. However, the degree of the bathochromic shift is greater with C_{12}DmCB than with CTAC, indicating better incorporation of PhB in the former.

The addition of SDS at premicellar concentrations initially leads to an increase in absorbance (Fig. 2C) due to repulsive interactions between the similarly charged dye and surfactant. PhB tends to remain in the aqueous bulk phase. However, increasing the SDS concentration from 1 CMC to 2.5 CMC may result in weak hydrophobic interactions between the hydrophobic moiety of PhB and SDS. The subsequent decrease in absorbance can be interpreted as π-π stacking between the aromatic rings of the dye, leading to the formation of dye J aggregates, ground-state complexes, or associations between the hydrophobic part of PhB and SDS [48].

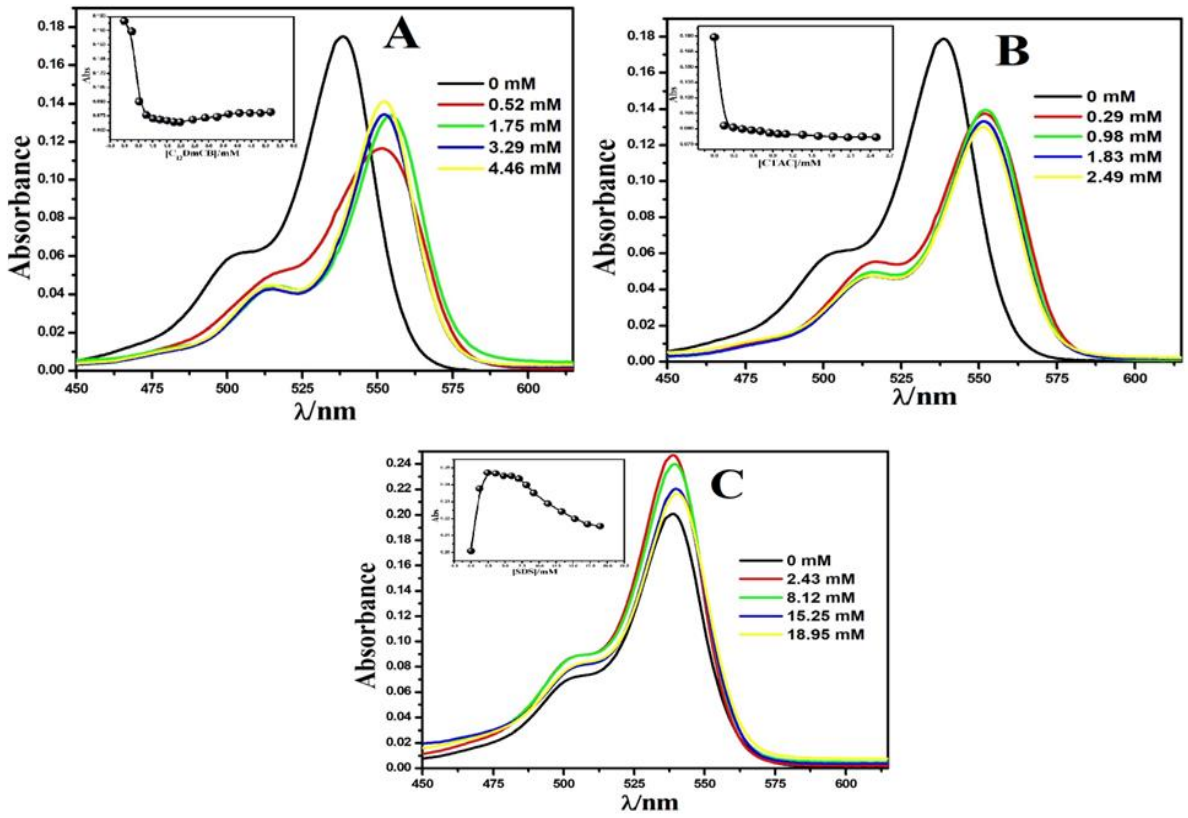

Figure 2. Absorbance of Ph B with varying concentration of (A) C_{12}DmCB, (B) CTAC, and (C) SDS, (Inset shows Absorbance vs corresponding [Amphiphile]).

3.2 Steady-state fluorescence spectra analysis: Like absorption spectroscopy, emission spectra provide important insights into the position and nature of the interaction between a fluorophore and its sub-micellar and micellar microenvironments. The emission wavelength (λemission) of aqueous PhB has been recorded at 558 nm, which aligns well with values found in the literature[49]. Initially, the addition of C_{12}DmCB and CTAC to the aqueous solution of PhB results in a quenching of fluorescence intensity (Fig. 3A, 3B). This observation can be explained by the oppositely charged head groups of the surfactants relative to PhB, leading to the initial formation of exciplexes at submicellar concentrations [50], i.e., when [surfactant] is less than the critical micelle concentration (CMC). However, as the concentrations of C_{12}DmCB and CTAC increase to levels where [surfactant] is equal to or greater than CMC, the

spectral patterns and the extent of bathochromic shift also change. C_{12}DmCB is a zwitterionic surfactant, which contains both COO- and NR4+ groups attached to the same carbon atom. In the presence of the anionic PhB, the NR4+ group of C_{12}DmCB is predicted to serve as a potential binding site. This interaction allows the COO- group to engage in reducing the electrostatic repulsion between the NR4+ head groups. As these repulsive interactions diminish, it is expected that more surfactant monomers will cluster together to form larger micelles, enhancing the solubilization of PhB [51]. This micelle-rich environment results in an increase in fluorescence intensity, accompanied by a significant bathochromic shift of 12 nm.

In the CTAC micellar system, when [CTAC] is greater than or equal to CMC, a prominent red shift of 10 nm is observed, but there is no significant increase in the corresponding fluorescence intensity. Since CTAC is anionic, the incorporation of PhB-CTAC ion pairs occurs within the Stern layer of the CTAC micelles at these concentrations.

In the C_{12}DmCB micellar system, it appears that the solubilization of PhB takes place more efficiently. This efficiency creates a predominantly nonpolar microenvironment, which significantly influences the behavior of polar PhB molecules. Within this environment, the PhB can rearrange itself into a more relaxed, excited state that minimizes its free energy. As a result of this reorganization, there is a noticeable increase in fluorescence intensity, indicating a favorable interaction between the micellar system and the solubilized compound. Conversely, the gradual addition of SDS to the aqueous solution of PhB results in a steady decrease in fluorescence intensity, accompanied by no significant spectral shift. This phenomenon arises from repulsive interactions between the similarly charged dye and surfactant, preventing PhB from entering the micellar phase. However, hydrophobic interactions may still occur between the non-polar regions of both the dye and surfactant, allowing PhB and SDS to approach each other, which slightly quenches the fluorescence intensity (Fig. 3C). All the absorption and emission spectral findings have been depicted in Table 2.

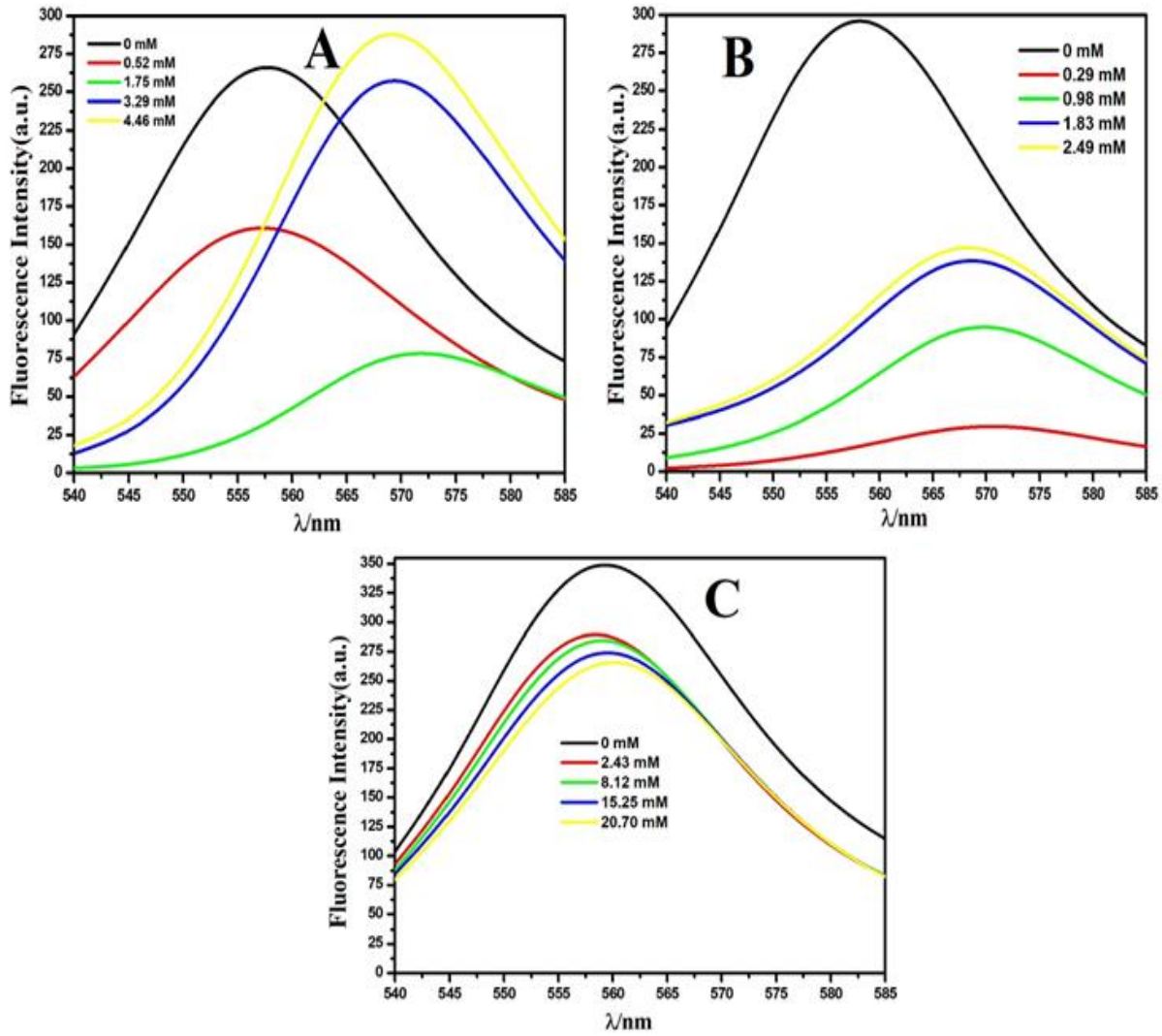

Figure 3. Variation of Fluorescence intensity of Ph B with varying concentration of (A) C_{12}DmCB, (B) CTAC, and (C) SDS

Table 2: Various spectroscopic parameters and calculation of Stokes shift of PhB and PhB-surfactants in their pre- and post-micellar concentration.

Concentration (mM)	λ_{max}^{abs}(nm)	Absorbance	λ_{max}^{flu}(nm)	Fluorescence Intensity (F.I.)	Stokes shift ($\Delta\nu$, cm^{-1})
PhB in water					
10^{-5}	538.75	0.175	557.69	266.73	630.37
PhB in C_{12}DmCB					
0.52	551.62	0.116	557.19	160.52	181.22
1.75	554.45	0.132	572.21	78.24	559.78
3.29	552.41	0.134	569.47	257.97	542.30
4.46	552.14	0.141	569.39	287.45	548.69
PhB in CTAC					
0.29	552.13	0.137	571.29	29.89	607.43
0.98	552.41	0.139	570.52	93.99	574.62
1.83	552.13	0.132	568.70	139.21	527.71
2.49	551.62	0.129	568.34	147.39	533.32
PhB in SDS					
2.43	538.75	0.247	558.65	290.41	661.18
8.12	539.00	0.239	558.73	285.13	655.14
15.25	539.79	0.220	559.01	272.47	636.95
18.95	539.79	0.216	559.64	265.80	657.10

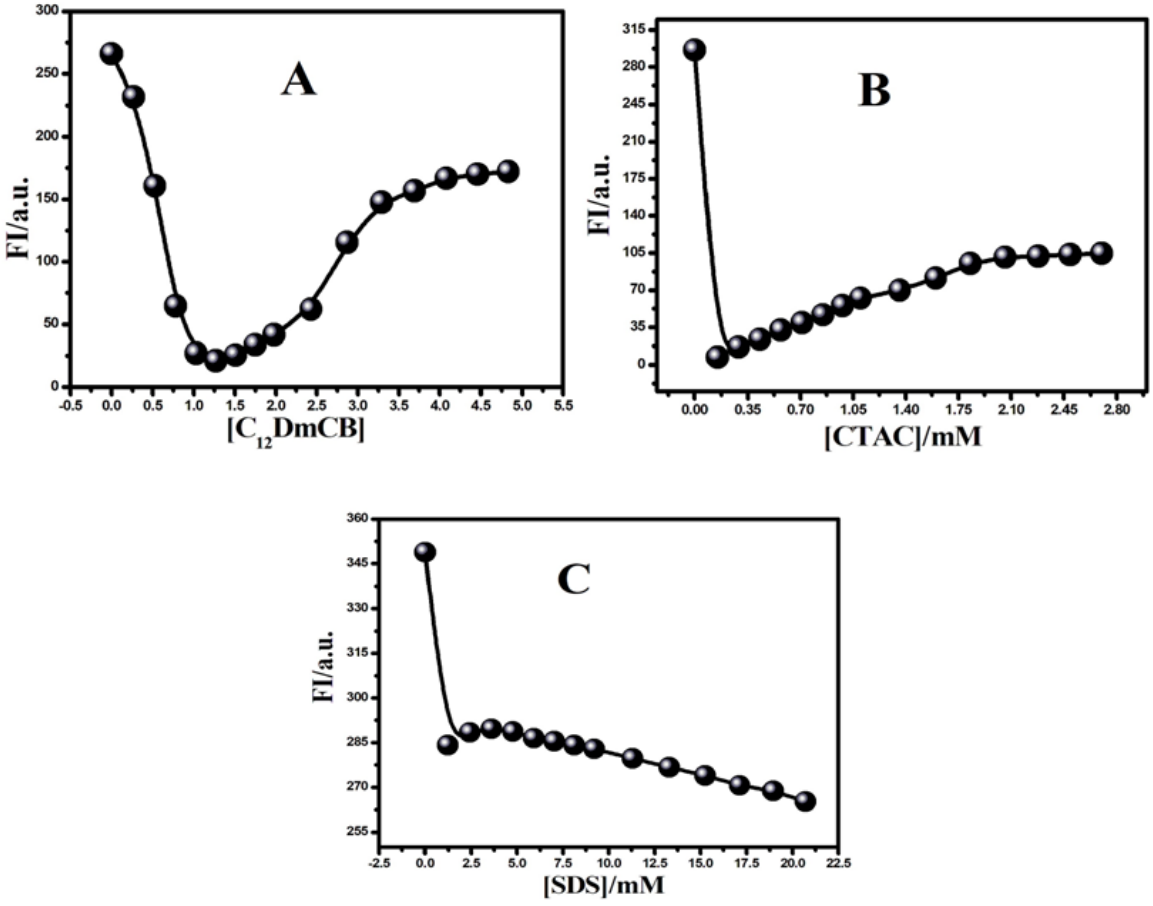

Figure 4: Variation of Fluorescence Intensity of PhB vs concentration (A) C_{12}DmCB, (B) CTAC, and (C) SDS

3.2.1 Determination of binding parameters of PhB with various surfactants

Varying the fluorescence intensity of PhB with the concentration of added surfactant reveals important parameters, including the binding constant, binding site, and the nature of interaction between the fluorophore and surfactant in their pre- and post-micellar microenvironments. In the PhB-C_{12}DmCB system, fluorescence intensity exhibits steady quenching (Fig. 4A) with varying concentrations of C_{12}DmCB, ranging from 0 mM to 1.27 mM. Therefore, the Stern-Volmer equation [52] has been applied to the system.

$$\frac{F_0}{F} = 1 + K_{sv}[Q] \qquad (2)$$

Where F_0 and F are the fluorescence intensities of the probe in the absence and in the presence of quencher molecules, respectively, K_{SV} is the Stern-Volmer quenching constant, and [Q] is the concentration of the quencher (surfactant).

$\frac{F_0}{F}$ vs. [Q] has been plotted, and a graph showing a curved pattern with upward curvature (Fig. 5A). This leads to the inference of a simultaneous static and dynamic quenching [53] in the pre-micellar concentration of C_{12}DmCB, so instead of Ksv, the apparent quenching constant (Kapp) has been introduced in the Stern-Volmer equation (Fig. 5A).

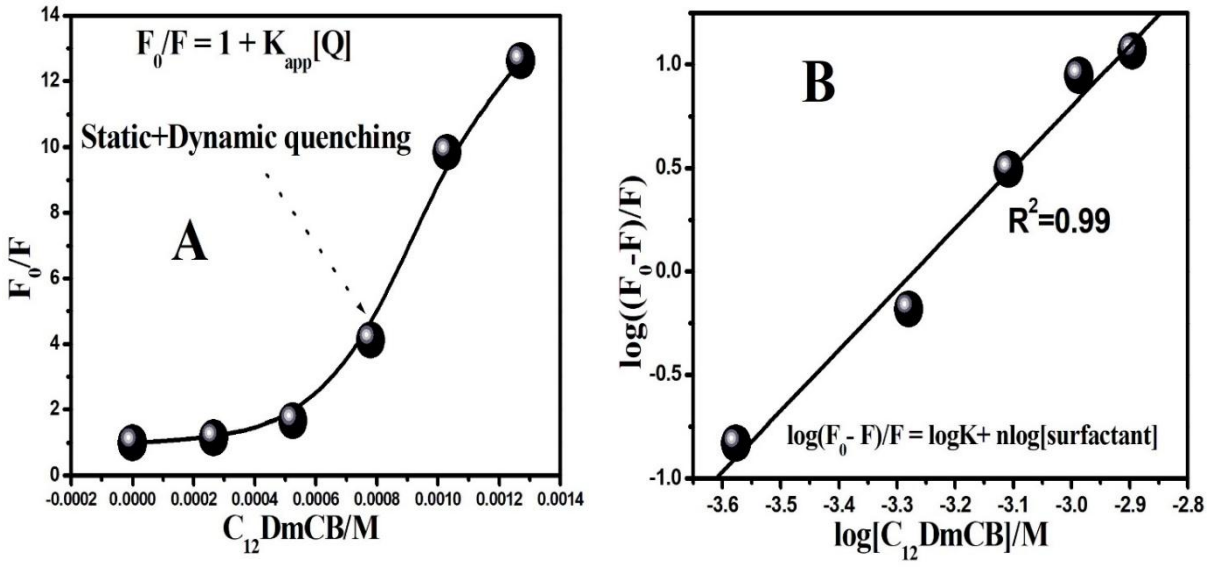

Figure 5: Stern-Volmer plot (A) and modified Stern-Volmer plot(B) of the PhB-C_{12}DmCB system.

Again, the modified Stern-Volmer equation [53] has been introduced for the PhB-C_{12}DmCB system to determine the binding constant and the binding site. The equation is as follows,

$$log\left(\frac{F_0-F}{F}\right) = \log K + \mathrm{n}\log[surfactant] \qquad (3)$$

Where F_0 and F are the fluorescence intensities in the absence and the presence of quencher, respectively, K is the binding constant, and n stands for the binding site.

However, plotting of $log\left(\frac{F_0-F}{F}\right)$ vs. [surfactant], a straight line has been obtained (Fig. 5B) with a slope of 1.97. The value of the binding constant and the binding site have been depicted in Table 3.

In the case of the PhB-CTAC system, fluorescence intensity shows a steady increase with varying concentrations of CTAC from 0.15 mM to 2.70 mM (Fig. 4B). Therefore, Beneshi Hildebrand's equation [54] has been introduced to determine the binding constant. The equation is as follows,

$$\frac{1}{F-F_0} = \frac{1}{(F_\infty - F_0)\, K_b\, [Surfactant]^n} + \frac{1}{(F_\infty - F_0)} \qquad (4)$$

Where F, F_0, and F_∞ The fluorescence intensities are in the presence of surfactant, in the absence of surfactant, and in the final addition of the surfactant, respectively. In this case, [CTAC] = 0.15 mM has been assumed as F_0. However, plotting of $\frac{1}{F-F_0}$ vs. $\frac{1}{[Surfactant]^n}$ A straight line has been obtained (Fig. 6A). Assuming a 1:1 interaction ratio between Phb and CTAC, the linear pattern of the curve supports this ratio. The binding constant obtained from this equation is also depicted in Table 3.

Table 3. The binding constants of different systems.

System	**Binding constant (M^{-1})**	**Number of binding sites (n)**
PhB - C_{12}DmCB	4.1×10^7	2
PhB - CTAC	1×10^2	1
PhB - SDS	0.5×10^1	------

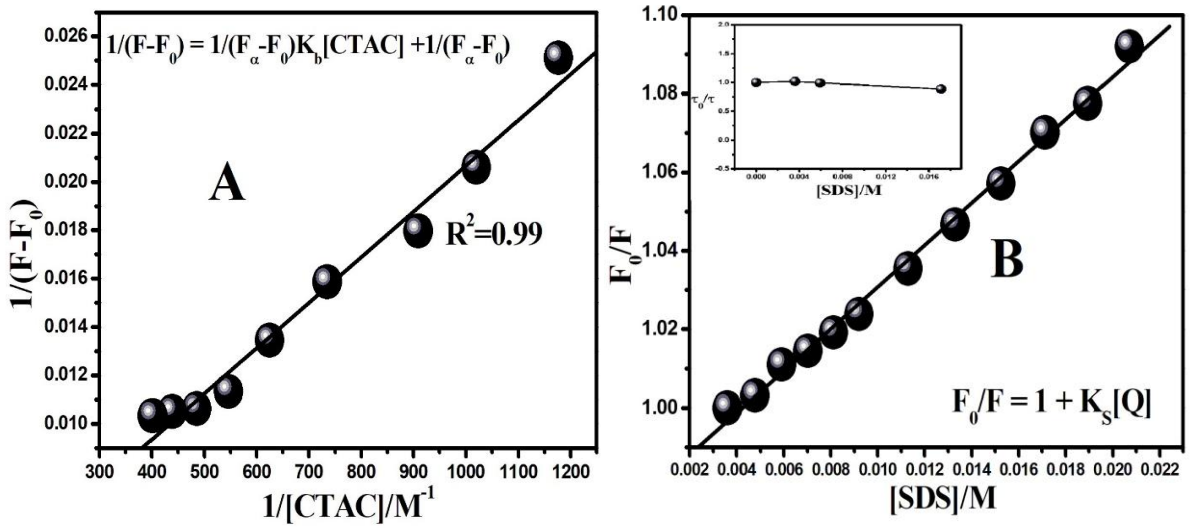

Figure 6: (A) Beneshi Hildebrand plot of PhB-CTAC system and (B) Stern Volmer plot of PhB-SDS system (6B inset shows Stern Volmer plot by lifetime data of PhB-SDS system).

Moreover, in the case of the PhB SDS system, fluorescence intensity shows a steady decrease with varying concentrations of SDS from 0 mM to 20.70 mM (Fig. 4C); therefore, the Stern-Volmer equation (equation 2) has also been introduced here. Here, the plotting of $\frac{F_0}{F}$ vs. [Q] gives rise to a linear fitting curve indicating either solo dynamic or solo static quenching. To determine whether the quenching is static or dynamic, the Stern-Volmer equation has been applied to fluorescence lifetime data as,

$$\frac{\tau_0}{\tau} = 1 + K_{sv}\,[Q] \qquad (4)$$

Where, τ_0 and τ The fluorescence lifetime in the absence and in the presence of quencher, respectively, K_{SV} is the Stern-Volmer quenching constant, and [Q] is the concentration of SDS.

However, plotting of $\frac{\tau_0}{\tau}$ vs. [Q] gives rise to a linear plot parallel to the x-axis (inset of Fig. 6B). So, it can be concluded that quenching of fluorescence intensity of PhB in the presence of SDS is static in nature; there may be creation of a Van der Waals force of attraction between the hydrophobic portion of PhB and SDS. In Figure 6B, the Stern-Volmer quenching constant

is denoted as K_S, representing the static quenching constant, also known as the association constant or binding constant [55]. The values of binding constants obtained from Table 3 indicate the highest binding affinity of C_{12}DmCB with PhB. The zwitterionic nature of C_{12}DmCB may facilitate PhB by allowing for closer proximity, as it masks the repulsive interaction created by polar head groups. This causes a greater intercalation of PhB into the micellar environment of C_{12}DmCB. Moreover, in the PhB-SDS system, a weak association has been created between the hydrophobic portion of PhB and SDS, resulting in a low binding constant value.

3.2.2 Stokes shift

The Stokes shift is a key characteristic of a fluorophore that arises from the energy loss occurring when excited-state electrons relax. This phenomenon can be quantitatively evaluated using an equation that relates the emission and absorption spectra of the fluorophore.

$$\text{Stokes' shift} = 10^7 \left[\frac{1}{\lambda ex} - \frac{1}{\lambda em}\right] \quad (6)$$

Where λ_{ex} and λ_{em} indicate the peaks of excitation and emission, respectively, measured in nanometers. The absorbance, fluorescence intensity, and Stokes shift are summarized in Table 2. In the PhB-C_{12}DmCB and PhB-CTAC systems, the values of the Stokes shift decrease. This observation can be attributed to a reduction in the polarity of the microenvironment surrounding the fluorophore[56]. These decreased values also support the idea that PhB is incorporated into the micellar interface of C_{12}DmCB and CTAC. In contrast, for the PhB-SDS system, a slight increase in Stokes shift values suggests an increase in solvent polarity, indicating that PhB resides in the aqueous bulk phase within the SDS micellar environment.

3.3 Time-resolved fluorescence spectral analysis: The TCSPC experiment is the most sophisticated technique for gaining advanced knowledge about the nature of the microenvironment and the location of the fluorophore in both aqueous and micellar media [57,

[58]. In this work, lifetime measurement of PhB has been carried out in both aqueous and micellar media in their respective pre- and post-micellar concentrations. An aqueous solution of PhB exhibits a single exponential decay with τ_{avg} = 1.16 ns (Table 4). The initial addition of C_{12}DmCB, i.e., [C_{12}DmCB] << CMC, to the aqueous solution of PhB doesn't provide any noticeable change in the value of τ_{avg} as well as in the decay pattern (Fig. 7A). So, it can be concluded that in this concentration of the surfactant, PhB likes to stay in the aqueous bulk phase. However, the premicellar concentration of C_{12}DmCB results in a bi-exponential decay curve and also a drastic decrease in the value of τ_{avg}. This observation can certainly infer the two different positions of PhB; Some portion of PhB is present in the aqueous bulk phase, and some portion is with sub micellar aggregation of C_{12}DmCB, in this concentration, electrostatic force of attraction created between anionic PhB and NR_4^+ group of C_{12}DmCB results to exist as PhB-C_{12}DmCB mixed micelle or salt like ion pair. This observation resembles the quenching in emission spectra. However, when [C_{12}DmCB] ≥ CMC, a three times incremented value of τ_{avg} compared to the τ_{avg} value of PhB in the aqueous bulk phase has been observed with a single exponential decay (Table 4). This observation strongly suggests that at this specific concentration of surfactant, 100% of PhB is completely incorporated within the Stern layer of the C_{12}DmCB micelle. This indicates that the total intercalation of PhB into the micellar environment has been successfully achieved. In contrast, when examining the CTAC-PhB system, we notice an initial decrease in the average relaxation time (τ_{avg}) with increasing micellar concentrations of CTAC (Fig. 7B). This decrease can be attributed to the electrostatic attraction generated between the oppositely charged dyes and surfactants, highlighting the interplay of their charges in this dynamic system. However, when [CTAC] ≥ CMC, τ_{avg} becomes double that of an aqueous solution of PhB. This experimental observation once again reinforces the concept that PhB is effectively integrated into the micellar structure of CTAC. However, the bi-exponential decay curve suggests that, at the post-micellar concentration of

CTAC, PhB does not occupy a fixed position within the micelle. This finding emphasizes the intricate behavior of PhB, indicating that salt-like ion pairs of PhB and CTAC tend to intercalate within the Stern layer of the CTAC micelle. Such dynamics suggest a more complex interaction, where PhB exhibits a level of mobility rather than being confined to a singular location. Notably, the average lifetime (τ_{avg}) of PhB in the post-micellar concentration of the C_{12}DmCB system exceeds that of the corresponding system utilizing CTAC. This difference suggests that C_{12}DmCB creates a more favorable and protective microenvironment for PhB compared to the traditional cationic surfactant CTAC. Within this enhanced environment, the stability and interaction of PhB are likely improved, reflecting the unique properties of C_{12}DmCB in surfactant chemistry. In the case of the PhB-SDS system, when [SDS]< CMC, no observable change in the value of τ_{avg} has been observed (Fig. 7C). This fact can be attributed to the lack of interaction between the same charged dye and surfactant. However, a slight increment in the value of τ_{avg} along with a biexponential decay curve is observed when [SDS] ≥ CMC. This observation again supports the hydrophobic interaction created between the hydrophobic portion of the dye and the micellar core of SDS after micelle formation, as well as the biexponential decay, which also explains the two locations of PhB. One position is in the aqueous bulk phase, and another is weakly attached to the micellar core of the SDS micelle.

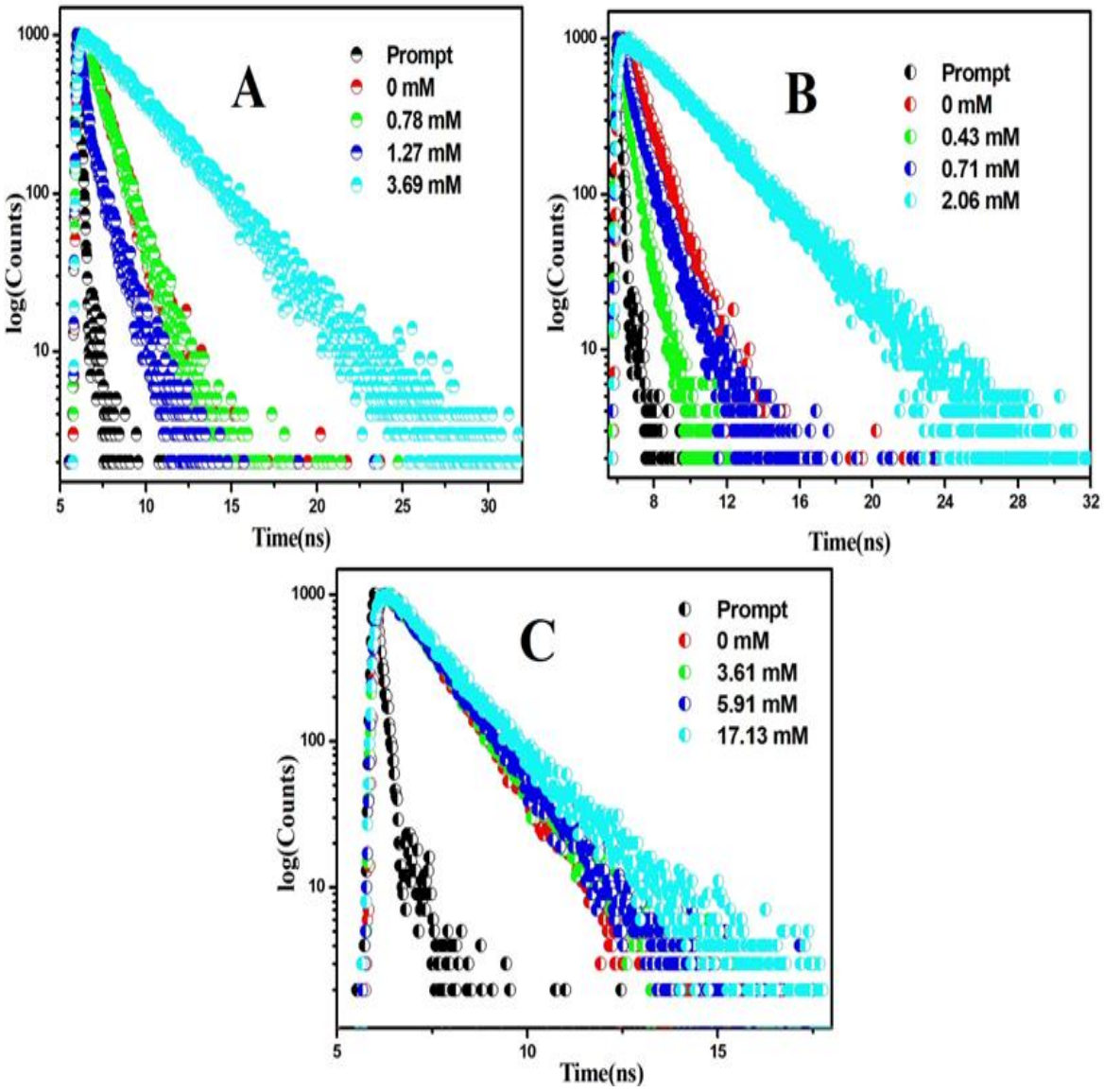

Figure 7: Time-resolved fluorescence spectra of PhB along with premicellar and post-micellar concentration of (A) C_{12}DmCB, (B) CTAC, and (C) SDS

Table 4: Time-resolved decay parameters of PhB in (a) water, (b) C_{12}DmCB (pre- and post-micellar), (c) CTAC (pre- and post-micellar), and (d) SDS (pre- and post-micellar)

Concentration (mM)	τ_1 (ns)	a_1	τ_2 (ns)	a_2	τ_{avg} (ns)	χ^2
PhB in water						
10^{-5}	1.16	1	--	--	1.16	1.005
PhB in C_{12}DmCB						
0.78	1.15	1	--	--	1.15	0.99
1.27	0.21	0.53	1.12	0.47	0.34	0.96
3.69	3.39	1	--	--	3.39	1.086
PhB in CTAC						
0.43	0.47	1	--	--	0.47	1.02
0.71	0.38	0.39	1.19	0.61	0.65	0.99
2.06	2.12	0.24	2.97	0.76	2.71	0.99
PhB in SDS						
3.61	1.14	1	--	--	1.14	0.97
5.91	1.17	1	--	--	1.17	0.96
17.13	1.09	0.56	1.77	0.44	1.31	1.07

3.4 Steady-state anisotropy study of PhB with different surfactants:

Anisotropy measurement offers valuable insights into several important factors such as rotational diffusion, molecular orientation, and the rigidity of the surrounding microenvironment [59, 60] . By analyzing anisotropy, one can assess how molecules move and orient themselves in space, which in turn reflects the structural characteristics and behavior of their environment. The quantification of anisotropy can be accomplished through a specific equation[61] that details the relationship between these variables.

$$r = \frac{I_V - GI_H}{I_V + 2GI_H} \quad (5)$$

where I_V and I_H The emission intensities to the electric vector of the plane-polarised excitation, towards parallel and perpendicular directions, respectively, arise from the probe's vertically polarised excitation.

Factor G is defined as

$$G = \frac{I_V}{I_H} \quad (6)$$

An aqueous solution of PhB exhibits a non-zero anisotropy due to its asymmetric structure and hydrogen bonding with water molecules. This expected hydrogen bonding restricts the rotational motion of the probe. However, when both C_{12}DmCB and CTAC are added to the aqueous solution of PhB, the anisotropy value decreases (Table 5). This phenomenon can be explained by the electrostatic attraction between the polar probe and the oppositely charged head groups of the surfactants. This attraction may disrupt existing hydrogen bonds, allowing for a relatively free rotational motion of the probe and resulting in a decrease in anisotropy.

Furthermore, the gradual addition of the surfactants leads to the formation of dye-surfactant salt-like ion pairs at submicellar concentrations of the surfactants. However, when [surfactant]>CMC, a gradual increase in the value of anisotropy leads (Table 5) to the incorporation of PhB into the micellar environment of C_{12}DmCB and CTAC, respectively. In a stern layer of the micellar system or within a dehydrated micellar environment, PhB exhibits restricted rotational motion, which leads to an increase in its anisotropy value [62]. Notably, in the case of the C_{12}DmCB micellar system, the anisotropy value increases threefold compared to that in the PhB aqueous system (Fig. 8A). In contrast, within the CTAC/water binary system (Fig. 8B), the anisotropy value doubles compared to the value observed in the aqueous system of PhB. These findings suggest that, in the C_{12}DmCB/water binary system, PhB experiences greater constraints on its rotational motion than in the CTAB/water binary system. This restriction is attributed to a higher degree of intercalation into the Stern layer of the micellar microenvironment [63]. Conversely, when SDS is added to the aqueous solution of PhB, there is

no significant change in the anisotropy value within the sub-micellar region of the SDS system. However, with an increase in concentration of SDS, i.e., [SDS] > CMC, a slight increase in the value of anisotropy is observed (Fig. 8C) due to the Van der Waals force of attraction created between the hydrophobic portion of PhB and SDS. This hydrophobic stacking imposes a minor restriction on the rotational motion of PhB.

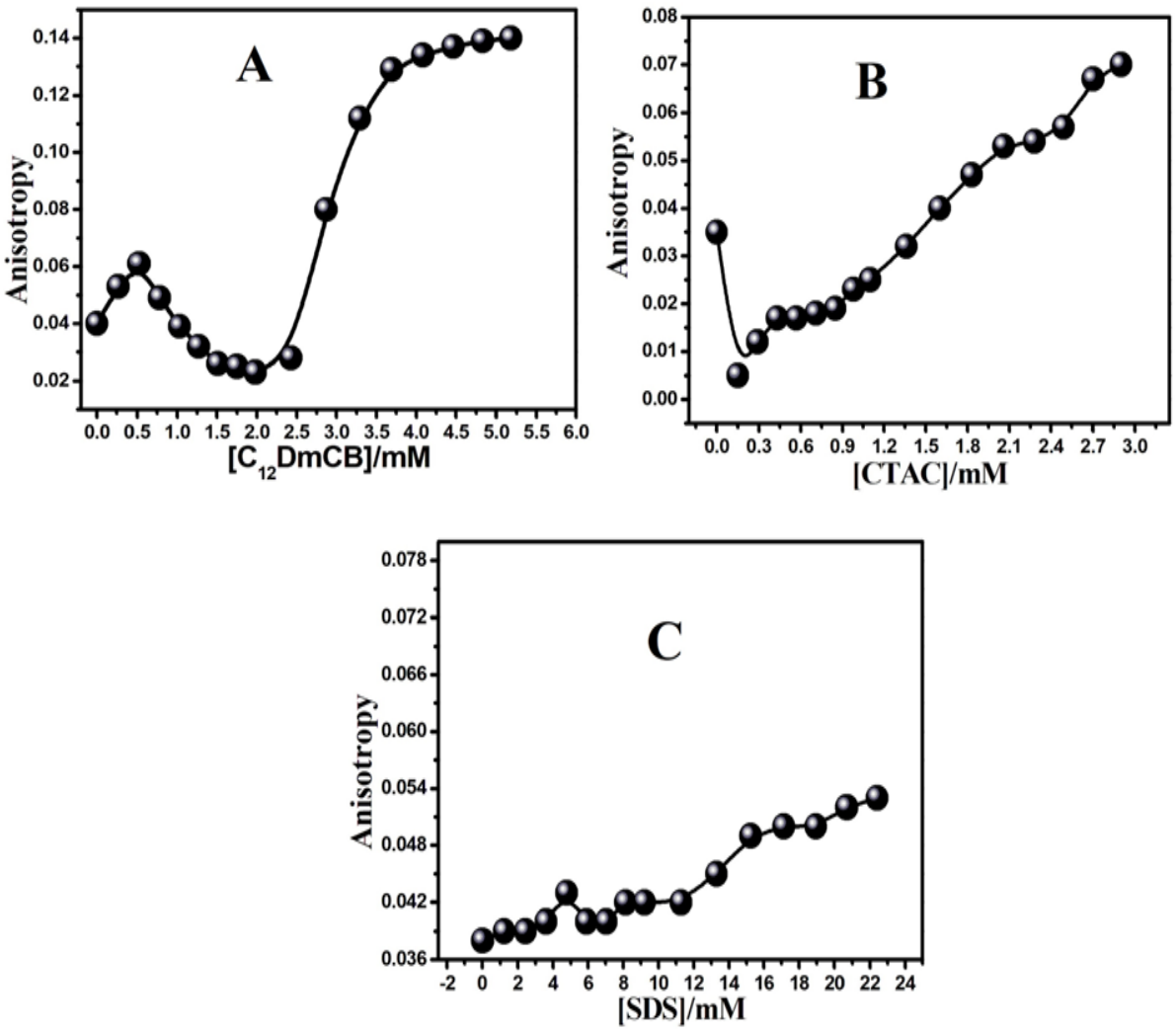

Figure 8. Variation of Anisotropy of Ph B with varying concentration of (A) C_{12}DmCB, (B) CTAC and (C) SDS

3.5 Dynamic light scattering and measurement of zeta potential: Dynamic light scattering (DLS) offers important insights into the particle size within the microenvironment [64], allowing predictions about aggregation characteristics in aqueous or water/surfactant binary systems. DLS measurements were conducted using an aqueous solution of PhB combined with various surfactants at their respective pre- and post-micellar concentrations. In this study, 10 μL of the stock solution of PhB was added to 2 mL of water in the cuvette, and each surfactant was introduced separately and gradually into the aqueous PhB solution to assess the hydrodynamic radius (R_H) at both pre- and post-micellar concentrations. An aqueous solution of PhB exhibits two types of aggregates (Fig. 9A), one in a size range of $44 \leq R_H \leq 68$ nm, which corresponds to the monomeric form of PhB, and another size range is $396 \leq R_H \leq 712$ nm, which corresponds to the aggregated form of dye molecules (Table 5). The aggregated form of PhB arises due to π-π stacking of the dye molecules or due to hydrogen bonding with water, which makes a larger hydrodynamic radius [65]. Addition of a small amount of C_{12}DmCB, i.e., [C_{12}DmCB] << CMC, coexisting with two different aggregates (Fig. 9B), has also been observed, one in a size range $164 \leq R_H \leq 220$ nm and the other in a size range $396 \leq R_H \leq 712$ nm. This observation can infer the initial formation of salt-like ion pairs between the monomeric form of PhB and the positively charged binding site of zwitterionic C_{12}DmCB. This binding results in an increment in the size of the aggregate that corresponds to the monomeric form of PhB [66]. Furthermore, the aggregated form of PhB doesn't show any effect at this concentration range of C_{12}DmCB. However, when [C_{12}DmCB] ≥ CMC, the formation of one type of aggregates with hydrodynamic radius $122 \leq R_H \leq 141$ has been observed (Fig. 9C, 9D). This observation satisfactorily concludes the formation of micelles and the absolute intercalation of PhB into the Stern layer of the micellar system of C_{12}DmCB. The incorporation of PhB into the micellar system results in a decrease in the hydrodynamic radius of the aggregates, and further addition of C_{12}DmCB leads to the formation of larger micelles (220 ≤

$R_H \leq 255$); consequently, an increase in aggregation has also been observed. CTAC, being a cationic surfactant, addition of CTAC to its submicellar concentration results in a decrease in aggregate size due to the prominent electrostatic force of attraction created between PhB and the oppositely charged polar head group of the surfactant (Fig. 9E). This CTAC-PhB mixed micelle prevents PhB from forming self-aggregation and also reduces the tendency of PhB to be exposed in water, thereby facilitating the formation of hydrogen bonds. As a result, there is a considerable decrease in hydrodynamic radius ($255 \leq R_H \leq 342$ nm) in the microenvironment (Table 5). Furthermore, when [CTAC] ≥ CMC, the formation of one type of aggregate, i.e., R_H = 190 nm, indicates a good agreement that the encampment of PhB into the micellar stern layer of CTAC [67] and the microenvironment surrounding PhB has shifted from a more polar to a less polar environment (Fig. 9F, 9G). These observations are very well commensurate with the absorption and emission spectra of PhB with C_{12}DmCB and CTAC. Moreover, as the PhB-C_{12}DmCB system exhibits a bigger aggregate size compared to the PhB-CTAC system, it can be evidently concluded that C_{12}DmCB forms a bigger micelle due to the reduction of mutual force of repulsion by the COO-group of the polar NH4+ group, which is also the potential binding site of PhB.

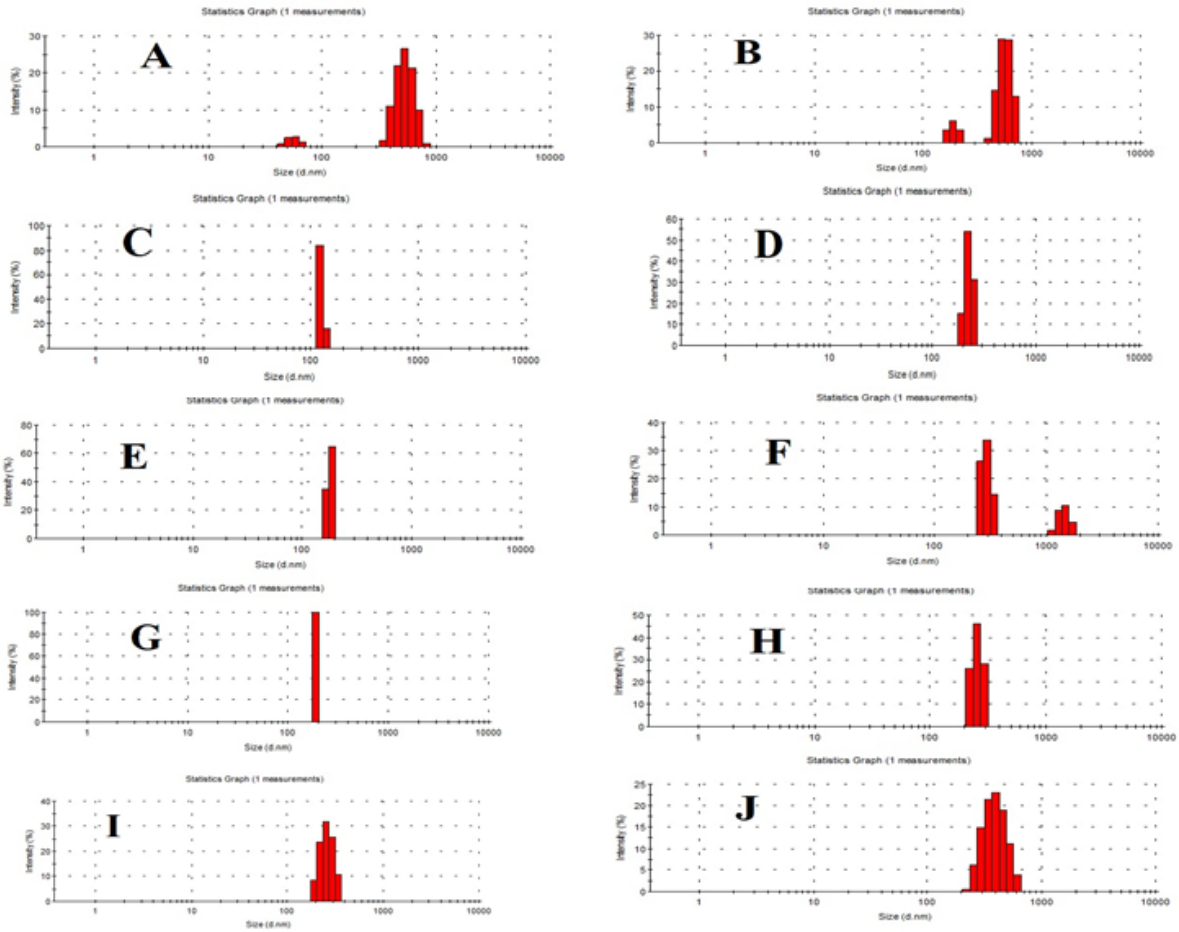

Figure 9. The size distribution of (A) PhB, (B) PhB in C_{12}DmCB (0.78 mM), (C) PhB in C_{12}DmCB (1.27 mM), (D) PhB in C_{12}DmCB (3.69 mM), (E) PhB in CTAC (0.43 mM), (F) PhB in CTAC (0.71 mM), (G) PhB in CTAC (2.06 mM), (H) PhB in SDS (3.61mM), (I) PhB in SDS (5.91 mM), (J) PhB in SDS (17.13 mM).

On the other hand, the addition of SDS to its submicellar concentration (Fig. 9H) results in a decrease in aggregate size, i.e., $220 \leq R_H \leq 300$. This observation can be attributed to the hydrophobic interaction between the non-polar part of PhB and SDS. Moreover, when [SDS] $\geq$ CMC, there is also an increment in particle size due to the formation of SDS micelles and the stacking of PhB into the hydrophobic part of the SDS micelle (Fig. 9I, 9J).

3.5.1 Measurement of Zeta potential: Zeta potential measures the surface charge of a colloidal system and can predict its stability. In this experiment, the zeta potential of an aqueous solution of PhB was measured alongside various surfactants, both at their pre-micellar and post-micellar concentrations. We began by adding 10 µL of the PhB stock solution to a 2 mL cuvette, followed by the addition of different surfactants separately. The results of the various surfactant concentrations are summarized in Table 4. The zeta potential of the aqueous PhB was found to be -15.3 mV. Notably, the addition of C_{12}DmCB resulted in an increase in zeta potential values (Table 5), indicating improved stability of the microenvironment [68]. Moreover, [C_{12}DmCB]> CMC, the observed zeta potential becomes -32.1 mV. The enhancement of zeta potential values can be attributed to the incorporation of PhB into the micellar system of C_{12}DmCB. As PhB also consists of negatively charged polar groups, it will never reside in the hydrophobic part of the micellar system; rather, it will prefer to reside at the Stern layer of the micellar microenvironment, where it can effectively bind with the NR_4^+ group of zwitterionic C_{12}DmCB. As a result, the COO^- group of the surfactant is expected to be exposed in the aqueous phase and cause a negative zeta potential. The addition of CTAC results in an enhancement of zeta potential values. CTAC, being a cationic surfactant, will form a very stable colloidal system [69] with PhB, resulting in more enhanced positive zeta potential values when [CTAC] ≥ CMC; zeta potential values were found to be +48.7 mV. This value indicates encampment of PhB into the stern layer of the micellar CTAC, resulting in a very stable colloidal system. Furthermore, as zeta

potential values in post-micellar concentration of CTAC are found to be more than that of C_{12}DmCB, it can be inferred that the PhB-CTAC micellar system is more stable. As a large number of C_{12}DmCB monomers are being associated to form micelles due to the reduction of repulsive interaction of polar NR4+ head group by polar COO- group, it has a lesser stability than CTAC micelle, which is smaller in size. SDS also forms a very stable micellar system,

and when [SDS] > CMC, the zeta potential value is found to be highest (-55.5 mV). This observation clearly indicates the repulsive interaction between PhB and SDS, which causes a highly stable colloidal system.

Table 5: Aggregate size, zeta potential, and anisotropy values of aqueous PhB and PhB-surfactants in their respective premicellar and post-micellar concentrations.

Concentration (mM)	Aggregate size (nm)	Zeta potential (mV)	Anisotropy
PhB in water			
10^{-5}	458-615	-15.3	0.040
PhB in C_{12}DmCB			
0.78	458-712	-22.5	0.049
1.27	122-141	-31.2	0.032
3.69	220-255	-32.1	0.129
PhB in CTAC			
0.43	164-190	+37.6	0.017
0.71	255-342	+48.7	0.018
2.06	190.1	+44.3	0.053
PhB in SDS			
3.61	220-295	-10.9	0.040
5.91	220-300	-35.3	0.040
17.13	295-531	-55.5	0.050

3.6 Density functional theory calculations: To enhance our understanding of interactions at the 1:1 molecular level, we conducted Density Functional Theory (DFT) calculations [70]. Utilizing the B3LYP functional along with the 6-31G(d,p) basis set, we carried out both DFT and Time-Dependent DFT (TDDFT) calculations. Our findings reveal that the PhB-C_{12}DmCB system exhibits the lowest optimized energy, suggesting it is the most stable configuration among those evaluated [71]. The optimized energies for PhB, PhB-C_{12}DmCB, PhB-CTAC, and PhB-SDS are summarized in Table 5, and the optimized structures are illustrated in Figure 10.

Interestingly, the dipole moment of the PhB-C_{12}DmCB system is the lowest, a consequence of the zwitterionic nature of C_{12}DmCB. To further dissect the system, we carried out TDDFT calculations to explore the structure and characteristics of the frontier molecular orbitals (FMOs) [72], specifically the highest occupied molecular orbital (HOMO) and the lowest unoccupied molecular orbital (LUMO), as well as their related energies. The energy gap between the FMOs is crucial, as it contributes significantly to the spectroscopic behavior, optical polarizability, and kinetic stability of these systems. Our analysis indicates that the FMOs are primarily localized on PhB (Fig. 11), which eliminates the likelihood of charge transfer from the surfactants' polar head group. As a polar probe, PhB is capable of transitioning to a more relaxed, lower-energy excited state through structural reorganization or by entering the micellar microenvironment [73], where the energy gap between the π and π^* orbitals decreases. In the presence of C_{12}DmCB, we observed that the energy gap between the HOMO and LUMO of PhB is minimized, highlighting the effectiveness of C_{12}DmCB in solubilizing PhB compared to other micellar or aqueous media. Furthermore, CTAC, as a cationic surfactant, also demonstrates effective solubilization of PhB. However, the least solubilization occurs with SDS, an anionic surfactant, which results in the largest energy gap between the FMOs in the PhB-SDS system (Table 6). These findings are well-aligned with the observed spectral behavior of PhB when interacting with these surfactants, paving the way for future studies to investigate further and optimize these interactions.

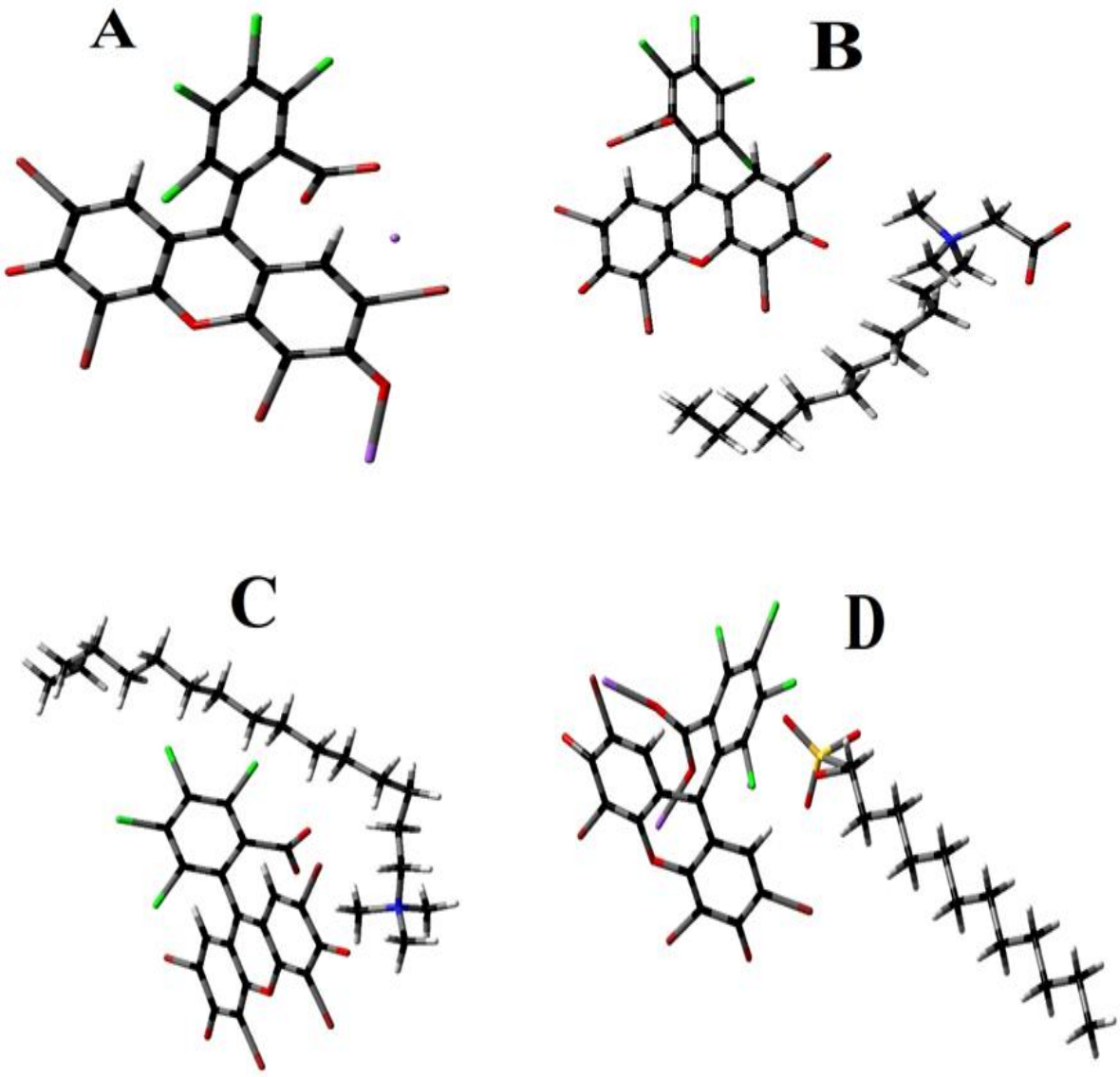

Figure 10. B3LYP/621G- optimised structure of (a) PhB, (b) PhB-C_{12}DmCB, (c) PhB-CTAC, (d) PhB-SDS. Colour code for atoms: red, oxygen; dark grey, carbon; light grey, hydrogen; yellow, sulphur; blue, nitrogen; green, chlorine; brown, bromine.

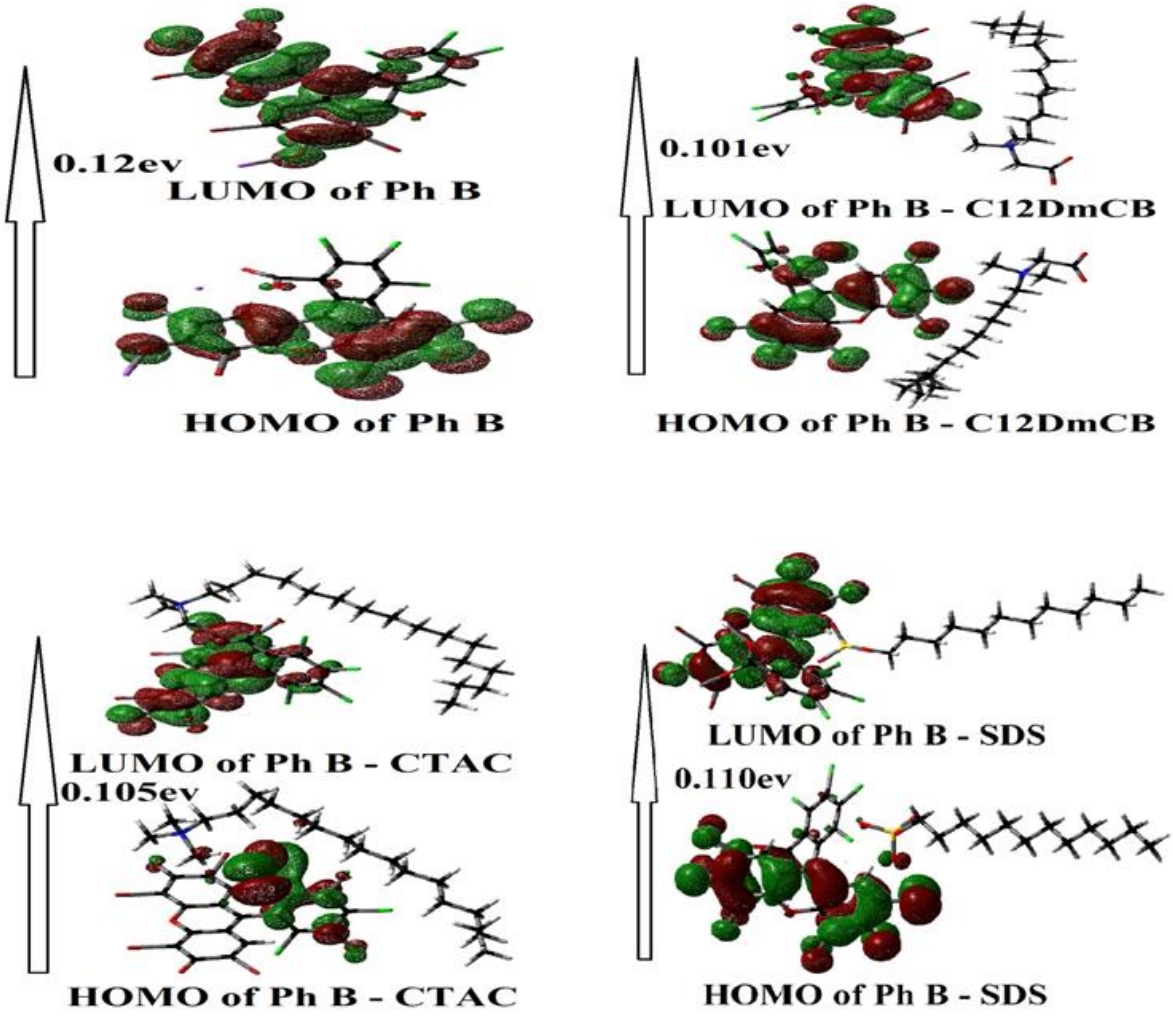

Figure 11: HOMO-LUMO diagram of PhB with various surfactants.

Table 6: Optimized energy, energy of HOMO and LUMO, band gap, and dipole moments of (a) PhB, (b) PhB-C12DmCB, (c) PhB-CTAC, and (d) PhB-SDS systems.

System	E_{OPT} (a.u)	Energy of HOMO (E_1) (ev)	Energy of LUMO (E_2) (ev)	ΔE (E_2-E_1) (ev)	Dipole moment (Debye)
PhB	-13591.76	-0.11470	0.01075	0.125	19.20
PhB-C_{12}DmCB	-14101.23	-0.02792	0.07345	0.10137	9.99
PhB-CTAC	-14071.40	-0.20094	-0.09573	0.10521	21.09
PhB- SDS	-14861.01	0.24705	-0.13060	0.11015	10.43

4. Conclusions:

In this experiment, we explored the interactive behavior of anionic PhB with three different types of surfactants: zwitterionic, cationic, and anionic, through a combination of spectroscopic and theoretical methods. Our findings indicate that by changing the polarity of the microenvironment, we can effectively enhance the solubility of PhB. This insight could prove valuable for further research and applications involving PhB in various settings. C_{12}DmCB, a zwitterionic surfactant, demonstrates superior effectiveness in solubilizing PhB compared to the cationic surfactant CTAC. This superiority is evidenced by the observed bathochromic shifts in both absorption and emission spectra, along with an increase in average lifetime (τavg). Furthermore, comparisons of anisotropy values and the enhanced particle sizes observed in the post-micellar concentration of C_{12}DmCB, as measured by dynamic light scattering (DLS), further reinforce this conclusion. In time-correlated single photon counting (TCSPC) experiments, when the concentration of C_{12}DmCB exceeds the critical micelle

concentration (CMC), a single exponential decay indicates that PhB occupies a distinct position within the Stern layer of the micellar interface. The observed increase in anisotropy values when [C_{12}DmCB] surpasses CMC can be explained by the enhanced intercalation of PhB into this Stern layer. Moreover, the PhB-C_{12}DmCB complex exists at an optimized energy state, characterized by a minimized energy gap between frontier molecular orbitals (FMOs) as indicated by density functional theory (DFT) calculations. In the case of the surfactant C_{12}DmCB, there is a noteworthy reduction in electrostatic repulsion between the positively charged NR4+ group and the negatively charged COO- group adjacent to it. This reduction in repulsive forces facilitates the incorporation of a greater number of monomers into the micellar structure. Consequently, C_{12}DmCB is able to form larger micelles compared to traditional cationic surfactants such as cetyltrimethylammonium chloride (CTAC). The ability to create larger micelles is significant because it enhances the intercalation of PhB into the micellar environment. This means that PhB can be more effectively integrated within the micelles formed by C_{12}DmCB, potentially improving its solubility and bioavailability in various applications. Thus, the unique interactions within the micellar structure of C_{12}DmCB play a crucial role in optimizing the delivery of PhB in comparison to other surfactants. SDS, an anionic surfactant, is established as the least interactive with PhB. The spectral behavior observed is convincingly attributed to hydrophobic interactions and π-π stacking. Notably, SDS demonstrates the highest zeta potential value in its post-micellar aggregation with PhB, due to the strong electrostatic force of repulsion that ensures a stable colloidal microenvironment. Furthermore, there are no significant spectral shifts or notable increases in τavg observed. PhB is a highly valuable dye known for its versatile applications. This study is groundbreaking as it is the first to report on the solubilization of PhB within a micellar environment that features different charge characteristics. Utilizing various micellar systems can enhance the stability and effectiveness of the dye in different settings. We believe that the results of our research will

have significant implications in several industries, including food, pharmaceuticals, and cosmetics. Furthermore, the findings may also contribute to advancements in other related fields such as dye recovery processes, the solubilization techniques for pharmaceuticals, the enhancement of medicinal photosensitization, improved drug delivery systems, and innovative approaches to wastewater treatment. By exploring the potential of PhB in these areas, we aim to open new avenues for research and practical applications.

REFERENCES:

1. K.-M. Chen, L.-H. Lin, C. F. Wang and M.-C. Hwang, *Colloids and Surfaces A: Physicochemical and Engineering Aspects*, 2010, **356**, 46-50.
2. A. R. T. Bagha, H. Bahrami, B. Movassagh, M. Arami and F. M. Menger, *Dyes and Pigments*, 2007, **72**, 331-338.
3. S. V. Smirnova and V. V. Apyari, *Sensors*, 2023, **23**, 3519.
4. M. Nitschke and S. S. e. Silva, *Critical reviews in food science and nutrition*, 2018, **58**, 631-638.
5. R. Hofmann, *Nanotechnology Perceptions*, 2015, **11**, 5-19.
6. J.-Y. Park, Y. Hirata and K. Hamada, *Journal of Oleo Science*, 2011, **60**, 627-637.
7. B. Zhmud and F. Tiberg, in *Surfactants in polymers, coatings, inks, and adhesives*, Blackwell2020, pp. 211-244.
8. K. Yun and C. Ahn, *Fashion and Textiles*, 2023, **10**, 4.
9. R. Hefford, in *Handbook of textile and industrial dyeing*, Elsevier2011, pp. 175-203.
10. D. Zhang, G. Zeng, J. Huang, W. Bi and G. Xie, *Journal of Environmental Sciences*, 2012, **24**, 2068-2074.
11. H. Akbaş and Ç. Kartal, *Spectrochimica Acta Part A: Molecular and Biomolecular Spectroscopy*, 2005, **61**, 961-966.
12. H. You, H. Spaeth, V. Linhard and A. Steckl, *Langmuir*, 2009, **25**, 11698-11702.
13. K. Bogman, F. Erne-Brand, J. Alsenz and J. Drewe, *Journal of pharmaceutical sciences*, 2003, **92**, 1250-1261.
14. A. Khdair, B. Gerard, H. Handa, G. Mao, M. P. Shekhar and J. Panyam, *Molecular pharmaceutics*, 2008, **5**, 795-807.
15. B. Sharma, M. Samperi, A. Jain, G. R. Chaudhary, G. Kaur and L. Pérez-García, *ACS Biomaterials Science & Engineering*, 2022, **8**, 1878-1891.
16. V. P. Torchilin, *Journal of controlled release*, 2001, **73**, 137-172.
17. M. J. Lawrence, *Chemical Society Reviews*, 1994, **23**, 417-424.
18. S.-Y. Lin, Y.-Y. Lin, E.-M. Chen, C.-T. Hsu and C.-C. Kwan, *Langmuir*, 1999, **15**, 4370-4376.
19. A. P. Santos and A. Z. Panagiotopoulos, *The Journal of chemical physics*, 2016, **144**.
20. F. Brøndsted and C. I. Stains, *Chemistry–A European Journal*, 2024, **30**, e202400598.
21. O. Karaman, G. A. Alkan, C. Kizilenis, C. C. Akgul and G. Gunbas, *Coordination Chemistry Reviews*, 2023, **475**, 214841.

22. X.-Y. Ran, Y.-F. Wei, Y.-L. Wu, L.-R. Dai, W.-L. Xia, P.-Z. Zhou and K. Li, *Journal of Materials Chemistry B*, 2025.
23. I. Rajapaksha, H. Chang, Y. Xiong, S. Marder, S. R. Gwaltney and C. N. Scott, *The Journal of Organic Chemistry*, 2020, **85**, 12108-12116.
24. L. Espinar-Barranco, P. Luque-Navarro, M. A. Strnad, P. Herrero-Foncubierta, L. Crovetto, D. Miguel, M. D. Giron, A. Orte, J. M. Cuerva and R. Salto, *Dyes and Pigments*, 2019, **168**, 264-272.
25. A. S. Burange, K. G. Gadam, P. S. Tugaonkar, S. D. Thakur, R. K. Soni, R. R. Khan, M. S. Tai and C. S. Gopinath, *Environmental Chemistry Letters*, 2021, **19**, 3283-3314.
26. R. Manivannan, S. H. Park, H. Oh and Y.-A. Son, *Dyes and Pigments*, 2022, **205**, 110480.
27. B. Ganguly, R. Nath and A. Panda, *Journal of dispersion science and technology*, 2012, **33**, 307-315.
28. B. Ganguly and R. Nath, *Journal of Surfaces and Interfaces of Materials*, 2013, **1**, 87-92.
29. P. Garg, G. Kaur and G. R. Chaudhary, *New Journal of Chemistry*, 2018, **42**, 1141-1150.
30. A. F. Alghamdi, *Journal of Applied Spectroscopy*, 2025, **91**, 1394-1403.
31. K. O. Willeford, T. A. Parker and S. V. Diehl, *Journal of Agricultural and Food Chemistry*, 1998, **46**, 1637-1641.
32. K. Bilská, J. Bujdák and H. Bujdáková, *Heliyon*, 2024, **10**.
33. E. Skoura, P. Boháč, M. Barlog, H. Pálková, A. Mautner, L. Bugyna, H. Bujdáková and J. Bujdák, *Applied Clay Science*, 2023, **242**, 107037.
34. R. Rasooly, *FEMS Immunology & Medical Microbiology*, 2007, **49**, 261-265.
35. K. Genwa, *Materials Science Poland*, 2015, **33**, 612-619.
36. N. C. T. Dadi, J. Bujdák, V. Medvecká, H. Pálková, M. Barlog and H. Bujdáková, *Materials*, 2021, **14**, 7583.
37. B. Simončič and J. Špan, *Dyes and Pigments*, 1998, **36**, 1-14.
38. M. T. Muhammad and M. N. Khan, *Journal of Molecular Liquids*, 2018, **266**, 591-596.
39. S. Streubel, F. Schulze-Zachau, E. Weißenborn and B. r. Braunschweig, *The Journal of Physical Chemistry C*, 2017, **121**, 27992-28000.
40. N. Gospodinova and E. Tomšík, *Progress in Polymer Science*, 2015, **43**, 33-47.
41. R. S. Paton and J. M. Goodman, *Journal of Chemical Information and Modeling*, 2009, **49**, 944-955.
42. M. Goel and M. Jayakannan, *The Journal of Physical Chemistry B*, 2010, **114**, 12508-12519.

43. N. C. Maiti, S. Mazumdar and N. Periasamy, *The Journal of Physical Chemistry B*, 1998, **102**, 1528-1538.
44. S. Dutta Choudhury, A. C. Bhasikuttan, H. Pal and J. Mohanty, *Langmuir*, 2011, **27**, 12312-12321.
45. R. Banik, S. Das, A. Ghosh and S. Ghosh, *Soft Matter*, 2023, **19**, 7995-8010.
46. E. Skoura, P. Boháč, M. Barlog, H. Pálková, A. Mautner, L. Bugyna, H. Bujdáková and J. Bujdák, *Applied Clay Science*, 2023, **242**, 107037.
47. P. Garg, B. Kaur, G. Kaur, S. Saini and G. R. Chaudhary, *Colloids and Surfaces A: Physicochemical and Engineering Aspects*, 2021, **610**, 125697.
48. M. Bielska, A. Sobczyńska and K. Prochaska, *Dyes and Pigments*, 2009, **80**, 201-205.
49. P. Duarte, D. P. Ferreira, I. Ferreira Machado, L. F. Vieira Ferreira, H. B. Rodríguez and E. San Román, *Molecules*, 2012, **17**, 1602-1616.
50. R. Sharma, A. Kamal and R. K. Mahajan, *Soft Matter*, 2016, **12**, 1736-1749.
51. S. Bandyopadhyay, R. Banik, R. Sardar and S. Ghosh, *Journal of Molecular Liquids*, 2025, **433**, 127953.
52. M. H. Gehlen, *Journal of Photochemistry and Photobiology C: Photochemistry Reviews*, 2020, **42**, 100338.
53. T. Kohlmann and M. Goez, *Physical Chemistry Chemical Physics*, 2019, **21**, 10075-10085.
54. I. D. Kuntz, Jr., F. P. Gasparro, M. D. Johnston, Jr. and R. P. Taylor, *Journal of the American Chemical Society*, 1968, **90**, 4778-4781.
55. E. Ciotta, P. Prosposito and R. Pizzoferrato, *Journal of Luminescence*, 2019, **206**, 518-522.
56. N. Pandey, N. Tewari, S. Pant and M. S. Mehata, *Spectrochimica Acta Part A: Molecular and Biomolecular Spectroscopy*, 2022, **267**, 120498.
57. V. B. Gawandi, S. N. Guha, K. I. Priyadarsini and H. Mohan, *Journal of Colloid and Interface Science*, 2001, **242**, 220-229.
58. A. I. Skilitsi, Université de Strasbourg, 2017.
59. A. Pal and N. Dey, *Soft Matter*, 2024, **20**, 3044-3052.
60. M. A. Haidekker, M. Nipper, A. Mustafic, D. Lichlyter, M. Dakanali and E. A. Theodorakis, in *Advanced Fluorescence Reporters in Chemistry and Biology I: Fundamentals and Molecular Design*, ed. A. P. Demchenko, Springer Berlin Heidelberg, Berlin, Heidelberg2010, pp. 267-308.

61. P. Quagliotto, N. Barbero, C. Barolo, K. Costabello, L. Marchese, S. Coluccia, K. Kalyanasundaram and G. Viscardi, *Dyes and Pigments*, 2009, **82**, 124-129.
62. N. C. Maiti, M. M. G. Krishna, P. J. Britto and N. Periasamy, *The Journal of Physical Chemistry B*, 1997, **101**, 11051-11060.
63. R. Ranganathan, J. Franklin, T. Oh and M. Peric, *Journal of Photochemistry and Photobiology A: Chemistry*, 2025, **466**, 116401.
64. A. Saxena, T. Antony and H. B. Bohidar, *The Journal of Physical Chemistry B*, 1998, **102**, 5063-5068.
65. Z. Chen, A. Lohr, C. R. Saha-Möller and F. Würthner, *Chemical Society Reviews*, 2009, **38**, 564-584.
66. G. Mariani, R. Schweins and F. Gröhn, *Macromolecules*, 2016, **49**, 8661-8671.
67. S. Das and S. Ghosh, *Physical Chemistry Chemical Physics*, 2022, **24**, 13738-13762.
68. G. Midekessa, K. Godakumara, J. Ord, J. Viil, F. Lättekivi, K. Dissanayake, S. Kopanchuk, A. Rinken, A. Andronowska, S. Bhattacharjee, T. Rinken and A. Fazeli, *ACS Omega*, 2020, **5**, 16701-16710.
69. K. Cacua, F. Ordoñez, C. Zapata, B. Herrera, E. Pabón and R. Buitrago-Sierra, *Colloids and Surfaces A: Physicochemical and Engineering Aspects*, 2019, **583**, 123960.
70. A. Dutta, B. Boruah, P. M. Saikia and R. K. Dutta, *Journal of Molecular Liquids*, 2013, **187**, 350-358.
71. A. Sánchez-Coronilla, J. Navas, T. Aguilar, E. I. Martín, J. J. Gallardo, M. R. Gómez-Villarejo, M. I. Carrillo-Berdugo, R. Alcántara, C. Fernández-Lorenzo and J. Martín-Calleja, *ChemPhysChem*, 2017, **18**, 346-356.
72. A. Dutta, B. Boruah, A. K. Manna, B. Gohain, P. M. Saikia and R. K. Dutta, *Spectrochimica Acta Part A: Molecular and Biomolecular Spectroscopy*, 2013, **104**, 150-157.
73. V. V. Kostjukov, *Chemical Physics Letters*, 2021, **785**, 139152.

CHAPTER IV

Spectroscopic and theoretical analysis of methylene blue with amphiphiles of identical charge: the impact of counterion binding.

Spectroscopic and theoretical analysis of methylene blue with amphiphiles of identical charge: the impact of counterion binding.

Abstract

This study investigates the interaction between Methylene Blue (MB) and two cationic surfactants, cetyl trimethyl ammonium tosylate (CTAT) and cetyl trimethyl ammonium bromide (CTAB), as well as a surface-active ionic liquid (SAIL) known as 1-butyl-3-methyl imidazolium octyl sulfate (BMImOS). The methods employed include conductometric titrations, UV absorption spectroscopy, steady-state fluorescence spectroscopy, zeta potential measurements, and density functional theory (DFT) calculations. The binding constant of MB with various amphiphiles was derived using both conductometric and steady-state fluorescence methods. As a cationic dye, MB preferentially binds to the negatively charged counterions of the cationic surfactants CTAT and CTAB. This binding causes MB to remain in the aqueous bulk phase, which consequently delays micellization. Notably, the tosylate counterion of CTAT exhibited a stronger binding affinity for MB than the bromide counterion of CTAB. Additionally, BMImOS, being a SAIL, can form micelles due to the octyl sulfate anion. This results in the encapsulation of MB in the Stern layer of the micelle, leading to a change in the polarity of the microenvironment surrounding MB and promoting earlier micellization of BMImOS, which shows the least binding affinity with MB. Furthermore, this study provides a new perspective using DFT to examine the possibility of charge transfer from the highest occupied molecular orbital (HOMO) of the counterions of various amphiphiles to the lowest unoccupied molecular orbital (LUMO) of MB, as evidenced by the TDDFT diagrams.

1. Introduction

Over the past few decades, there has been significant interest in the interaction between dyes and various amphiphilic molecules that possess different charge characteristics. This fascination stems from the wide range of applications these interactions have in several industries. In the textile industry, for example, amphiphilic compounds are used to enhance dye uptake and fixation[1, 2], resulting in more vibrant and durable colors on fabrics. Additionally, these interactions play a crucial role in the cosmetics industry[3], where they help stabilize colorants and enhance the overall performance of beauty products. In the food industry, amphiphiles are used to ensure the even distribution of dyes[4], thereby maintaining consistent color and appeal in products[5]. Furthermore, the combination of dyes and amphiphiles has proven to be effective in wastewater treatment processes[6, 7], where they aid in the removal of contaminants by facilitating the absorption and precipitation of dye pollutants. This diverse array of applications highlights the importance of understanding how dyes interact with amphiphiles in various contexts. In addition to its industrial applications, it is also beneficial in various medicinal and analytical branches of chemistry, including metal ion detection[8, 9], biological transport[10-12], drug delivery[13, 14], and photodynamic therapy[15]. Surfactants and surface-active ionic liquids (SAILs) have the ability to solubilize dyes by altering the polarity of the surrounding microenvironment[16]. Surfactants are unique amphiphiles characterized by a polar head group and a long hydrophobic tail. They exhibit self-association properties, forming micelles when their concentration reaches or exceeds the critical micellar concentration (CMC)[17]. In recent years, ionic liquids have proven to be more advantageous than surfactants, primarily due to their lower toxic environmental impact[18, 19], negligible vapor pressure[20], high viscosity[21], and thermal stability[22]. SAILs are increasingly recognized as green solvents[23] and find extensive applications across various fields of chemistry, including nanoparticle synthesis[24, 25], polymerization[26, 27], advanced material

fabrication[28], catalysis[29-31], drug delivery[32, 33], and separation and extraction processes[34]. Dyes are unsaturated organic compounds that contain chromophores and autochrome within their structure. Methylene blue (MB), a derivative of phenothiazine (PTZ), is widely utilized in medicine for treating methemoglobinemia[35, 36], various urinary tract infections[37], cytopathology[38], placebo effects[39], neurotoxicity from ifosfamide[40], and cases of cyanide poisoning[41]. Additionally, it serves as a dye or stain in endoscopic polypectomy and is employed in various biological applications, such as staining nerve fibers in the body[42]. MB is also used as bone cement in several orthopedic procedures[43]. Notably, previous studies have reported interactions between MB and various surfactants[44-48]. In this study, a comprehensive interaction investigation was conducted utilizing the dye methylene blue (MB) alongside two conventional cationic surfactants: cetyl trimethyl ammonium tosylate (CTAT) and cetyl trimethyl ammonium bromide (CTAB), as well as a surfactant ionic liquid (SAIL) known as 1-butyl-3-methyl imidazolium octyl sulfate (BMImOS). It is established that dyes and surfactants with opposing charges tend to interact more favorably, leading to enhanced solubilization of the dyes due to the formation of oppositely charged micelles[49, 50]. However, our investigation specifically targets the interactions between dyes and surfactants that share similar charges. CTAT is distinctive in that it carries a bulky counterion, the tosylate anion, while BMImOS possesses an octyl sulfate chain, which contributes to its unique properties. In contrast, CTAB features a smaller counterion, the bromide ion. The primary aim of this research is to investigate how the various characteristics of these counterions affect the solubilization of the dye. To analyze these interactions in detail, various spectroscopic techniques were employed, including UV-visible absorption spectroscopy, steady-state emission spectra, zeta potential measurements, and anisotropy assessments. Furthermore, we implemented constant conductometric titration to ascertain Gibbs free energy and binding affinities related to the dye-surfactant interactions. In order to delve deeper into the molecular

dynamics at play, density functional theory (DFT) calculations were performed. This allowed us to identify the optimized structures and frontier molecular orbitals (FMOs) associated with the surfactants and dye. Additionally, we examined the potential electrostatic forces of attraction between the dye molecules and the counterions present in the amphiphiles, providing insights into the underlying mechanisms of dye solubilization. This multifaceted approach aims to yield a comprehensive understanding of the factors influencing dye-surfactant interactions in the context of similar charge characteristics.

2. Experimental

2.1 Materials

Methylene blue (purity ≥99%), CTAT (purity ≥98%), CTAB (purity ≥96%), and BMImOS (purity ≥95%) served as the main chemicals for all the experiments. All materials were obtained from Sigma Aldrich (Table 1). No additional purification was performed on any of the chemicals. All experimental solutions were prepared using double-distilled water. The chemical structures for all substances are illustrated in Figure 1.

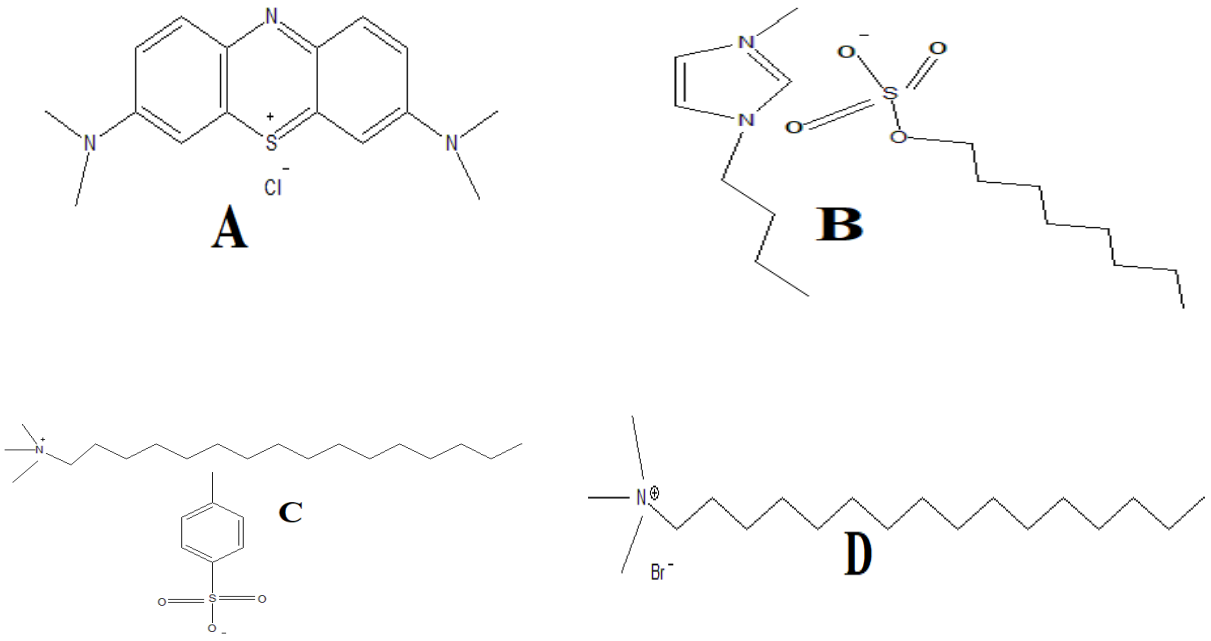

Figure 1: Chemical Structures of (A) MB, (B) BMImOS, (C) CTAT, (D) CTAB.

Table 1. Specifications of chemical compounds used in the Study

materials	chemical formula	CAS	supplier	purity
Methylene Blue	$C_{16}H_{18}ClN_3S$	61-73-4	Sigma Aldrich	≥ 99%
Cetyl trimethyl ammonium tosylate	$CH_3(CH_2)_{15}N(CH_3C_6H_4SO_3)(CH_3)_3$	138-32-9	Sigma Aldrich	≥ 98%
Cetyl trimethyl ammonium bromide	$CH_3(CH_2)_{15}N(Br)(CH_3)_3$	200-311-3	Sigma Aldrich	≥ 96%
1-butyl-3-methyl imidazolium octyl sulphate	$C_{16}H_{32}N_2O_4S$	445473-58-5	Sigma Aldrich	≥95%

2.2 Preparation of stock solution

A 1.0 mM stock solution of Methylene blue (MB) was created by dissolving a specific amount of the compound in water. The target experimental concentration of the dye was obtained by diluting the stock solution. The concentration of all amphiphiles in the aqueous solution was held at roughly 15 times higher than their respective CMCs. All solutions underwent proper sonication to ensure clarity.

2.3 Electrical conductivity measurements

In this study, measurements of electrical conductivity were taken using a conductivity meter from Eutech (Singapore), which was set with a cell constant of 1 cm^{-1}. To guarantee precise readings, the solution's temperature was kept constant at 298 K, using a water bath with an accuracy of ±0.1 K. A stock solution was created in an aqueous environment at roughly 15 times the critical micelle concentration (CMC) and was gradually added to a container with 6 mL of water, using a Hamilton microsyringe. After each addition of the stock solution, the mixture was thoroughly stirred to ensure consistency before recording the specific conductance (k). Each measurement was performed three times to guarantee dependability, and the average

value was computed along with an error assessment of the standard deviations. The CMC values were obtained by examining the breakpoints in the graphs of specific conductance (k) plotted against the surfactant concentration, yielding important insights into the surfactant's behavior in the solution.

2.4 UV visible spectral measurements

The absorbance was recorded using a UV-1601 Shimadzu spectrophotometer from Japan, utilizing a quartz cuvette with a path length of 10 mm. Spectra were collected across a wavelength range from 200 to 800 nm. To prepare the dye solution, 5 µL of the MB stock solution was mixed with 2 mL of water in the cuvette, giving a concentration of 0.0025 mM. This low concentration of MB was chosen to avoid self-aggregation of the dye molecules and to minimize the van der Waals attractive forces between adjacent hydrophobic regions of the molecules. Gradual additions of BMImOS, CTAT, and CTAB were introduced to the aqueous MB solution to investigate the premicellar and post-micellar characteristics of the microenvironment. The temperature was precisely maintained at a consistent 25 ± 0.1 °C using a water bath. Each experiment was conducted in duplicate to reduce any possible errors.

2.5 Steady-state fluorescence and steady-state anisotropy study

The Perkin Elmer LS 55 fluorescence spectrophotometer, featuring a Peltier system, was utilized to assess the fluorescence spectra, emission intensity, and anisotropy of different surfactant-dye mixtures at a stable temperature of 298.15 K, with an accuracy of ±0.02 K. All measurements were conducted using a quartz cuvette with a path length of 10 mm. For recording the fluorescence spectra, a 10 µL stock solution of MB was added to 2 mL of water within the cuvette, achieving an MB concentration of about 0.0025 mM. Fluorometric titrations were performed by incrementally adding BMImOS (ranging from 0 to 102 mM), CTAT (from 0 to 0.80 mM), and CTAB (from 0 to 3 mM) to each sample, while keeping the EY concentration constant. Emission spectra were collected within the wavelength range of 620

nm to 750 nm, with the excitation and emission slit widths fixed at 2.5 nm and 12 nm, respectively. The scan speed was set to 250 nm/min. Anisotropy measurements were conducted using an excitation wavelength of 610 nm and an emission wavelength of 687 nm for MB. The average anisotropy value was calculated from six consecutive readings. All anisotropy measurements were taken over an integration duration of 20 seconds. The temperature was reliably maintained at 298.15 K with the help of the Peltier system and circulating water, and the sample temperature was stabilized at 298 K prior to each measurement. Each experiment was repeated twice to reduce the likelihood of errors.

2.6 Zeta potential measurement

Zeta potential measurements were conducted using the Nano ZS Zetasizer from Malvern, UK, which was set to an observation angle of 90° and illuminated by a He-Ne laser for enhanced accuracy. Throughout the entire experimental procedure, the temperature was rigorously maintained at a stable 25°C to ensure consistent results. The experiments involved a series of different solution concentrations, allowing for a comprehensive evaluation of the zeta potential. A specific dye solution was meticulously prepared as a base, to which varying amounts of BMImOS, CTAT, and CTAB were introduced, both at premicellar and post-micellar concentrations. To guarantee the reliability and reproducibility of the findings, each measurement was repeated twice under identical conditions, and the resulting zeta potential values were recorded in millivolts (mV). This careful approach aimed to provide an accurate understanding of the interactions and stability within the solutions studied.

2.7 Density functional theory calculations

Recent developments in density functional theory calculations have greatly improved our comprehension of both covalent and non-covalent interactions at the molecular scale. This advancement is leading to fresh insights and applications across a variety of chemistry and materials science domains. The structures of MB, BMImOS, CTAT, and CTAB were created

using Avogadro software and then fine-tuned through an auto-optimization feature within the same program. The auto-optimization applied the MMFF94S force field, conducting four steps per update, and utilized the steepest descent algorithm to enhance accuracy. Additionally, to assess the interaction energy between MB and several amphiphiles at a 1:1 ratio on a molecular scale, energy optimization was carried out on these pre-optimized structures using Gaussian 09 software. All data were gathered using the B3LYP functional along with the 6-21G (d, p) basis set to provide a balance of accuracy and computational efficiency. In order to study the structures of the highest occupied molecular orbital (HOMO) and the lowest unoccupied molecular orbital (LUMO), time-dependent density functional theory (TDDFT) calculations were performed on those optimized structures, thereby clarifying the nature of the interactions between the dye and various surfactants.

3. Result and discussion

3.1 Conductivity measurement of MB surfactants

The measurement of specific conductance has been conducted to investigate the binding interaction between methylene blue (MB) and various surfactants, as well as to gain insights regarding changes in the critical micelle concentrations (CMCs) of these surfactants in the presence and absence of MB. The aggregation behavior of BMImOS, CTAC, and CTAB has been monitored with and without MB, and the results are illustrated in Figure 2.

From Figure 2, it is clear that the addition of surfactants to the aqueous medium significantly increases conductivity. Since all the surfactants are ionic, they readily dissociate into ions, which enhances conductivity. As the specific concentration of each surfactant is reached, the rate of conductivity increments decreases, leading to a reduction in the slope of the conductivity plot. This results in a breakpoint in the conductivity graphs, termed the CMC for each surfactant[51]. Figure 2B and 2C also indicate that both CTAC and CTAB exhibit delayed micellization in the presence of MB. For CTAT, the CMC value changes from 0.23 mM to 0.29

mM, and for CTAB, the CMC value changes from 0.92 mM to 0.97 mM in the presence of MB. This can be explained by the formation of ion pairs between MB and the surfactants' counterions. Typically, during micelle formation, the counterion of each surfactant helps reduce the electrostatic repulsion between the polar head groups of surfactant monomers, allowing them to group together and form a micelle. When MB is added to CTAC and CTAB solutions, the negatively charged tosylate and bromide ions readily form ion pairs with the positively charged MB. Consequently, the availability of the counterions in the stern layer of the micelle is diminished, which delays micellization. In contrast, for BMImOS, the association is primarily governed by the octyl sulfate counterion, which binds to MB, leading to earlier micellization. For BMImOS, the CMC value changes from 40.69 mM to 32.48 mM. This phenomenon stems from the ion pair formation between MB and octyl sulfate. The oppositely charged octyl sulfate and MB foster a favorable association, prompting octyl sulfate monomers to come together, thereby facilitating early micellization (Fig. 2A). From Figure 2, the degree of dissociation (β) can be calculated by using the following equation[52],

$$\beta = \frac{S_2}{S_1} \quad (1)$$

Where S_2 and S_1 are the post-micellar and pre-micellar slopes, respectively.

From equation (1), the Gibbs free energy (ΔG) can be determined by using the equation

$$\Delta G = (2 - \beta)\, RT \ln CMC \quad (2)$$

Where R and T are the universal gas constant and temperature in the Kelvin scale, from equation 2, the binding constant (K) has been determined by using the following formula.

$$\Delta G = - RT \ln K \quad (3)$$

The binding constant values are presented in Table 2. From this table, it is evident that the binding affinity of CTAC for MB is the highest, indicating a strong electrostatic attraction

between MB and the tosylate counterion of CTAC. Additionally, the binding constant for the MB-CTAB system is also significantly high; however, the bulky planar tosylate ion demonstrates greater binding affinity than the bromide ion of CTAB. For BMImOS, micelle formation occurs through the interaction between the octyl sulfate ion and MB, allowing MB to intercalate into the stern layer of the micelle. This results in a softer incorporation of MB within the BMImOS micelle, yielding the lowest binding affinity. The ΔG values presented in Table 2 reveal essential insights into the stability of the various systems studied. Notably, the MB-CTAT system demonstrates the highest level of stability among the tested configurations, indicating its robust performance in terms of electrostatic force of attraction. In contrast, the MB-BMImOS system exhibits the lowest stability, suggesting the soft incorporation of MB into the Stern layer of the octyl sulphate micellar environment. These findings highlight the significant differences in stability between the two systems.

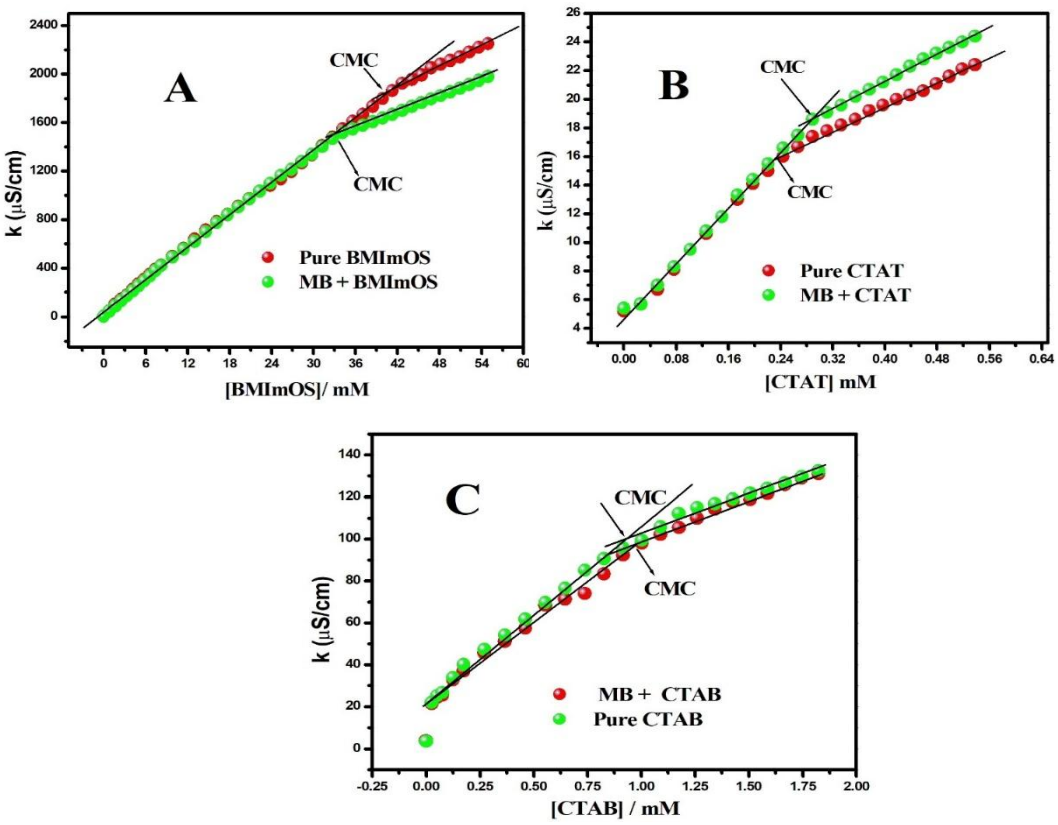

Figure 2: Plot of specific conductivity *vs.* concentration of (A) BMImOS, (B) CTAT, and (C) CTAB in the presence and absence of MB.

Table 2. CMC of surfactants, degree of dissociation, Gibbs free energy, and binding constant in the presence of MB obtained from conductometric titrations

CMC (mol/L)	Premicellar slope (S_1)	Post micellar slope (S_2)	Degree of dissociation (β)	Gibbs free energy(ΔG) KJ/mol	Binding constant (k) dm^3/mol
MB in BMImOS					
0.032	43.21	27.52	0.637	-11.623	108.9
MB in CTAT					
$2 \cdot 9 \times 10^{-4}$	46.04	20.15	0.438	-31.523	3.35×10^5
MB in CTAB					
0.97×10^{-3}	80.36	39.29	0.489	-25.973	3.57×10^4

3.2 UV visible spectral analysis

Absorption spectroscopy provides valuable insights into the interactions between a dye in aqueous solutions and organized surfactant media in their ground state. An aqueous solution of methylene blue (MB) exhibits a maximum absorption wavelength (λmax) at 665.69 nm, along with a shoulder peak at 617.33 nm. These observations are consistent with those reported in the literature[53]. The presence of the shoulder peak may result from the aggregation of MB in the aqueous solution, which induces π-π stacking of the dye's hydrophobic portions[54]. When various amphiphiles are added to the aqueous solution of MB, both before and after the critical micelle concentration, a decrease in absorbance is observed. The addition of cetyltrimethylammonium bromide (CTAB) and cetyltrimethylammonium tosylate (CTAT) leads to a slight reduction in absorption intensity (Fig. 3B and 3C). This decrease can be attributed to the significant electrostatic attraction between MB and the counterions of CTAT and CTAB[55]. As a result, MB preferentially remains in the aqueous bulk phase and shows reduced interaction with the Stern layer of the micelles formed by these surfactants. Although

the polar head groups of these micelles carry the same charge, the possibility of hydrophobic interactions has been ruled out, as there is no significant spectral shift. It can thus be concluded that the interaction leads to the formation of ion pairs between MB and the counterions of the respective surfactants in the aqueous phase. The addition of BMImOS to the aqueous solution of MB results in a significant decrease in absorbance (Fig. 3A). The octyl sulfate counterion, with its long hydrophobic chain of eight carbon atoms, possesses surfactant properties. Consequently, micelle formation occurs with the oppositely charged counterion, and the incorporation of MB into the Stern layer of the micelle likely results in a considerable decrease in absorbance. Moreover, since the imidazolium cation is known to act as a quencher[56], the observed change in absorbance suggests the formation of a ground-state complex between MB and the quencher, causing a steady decrease in absorbance.

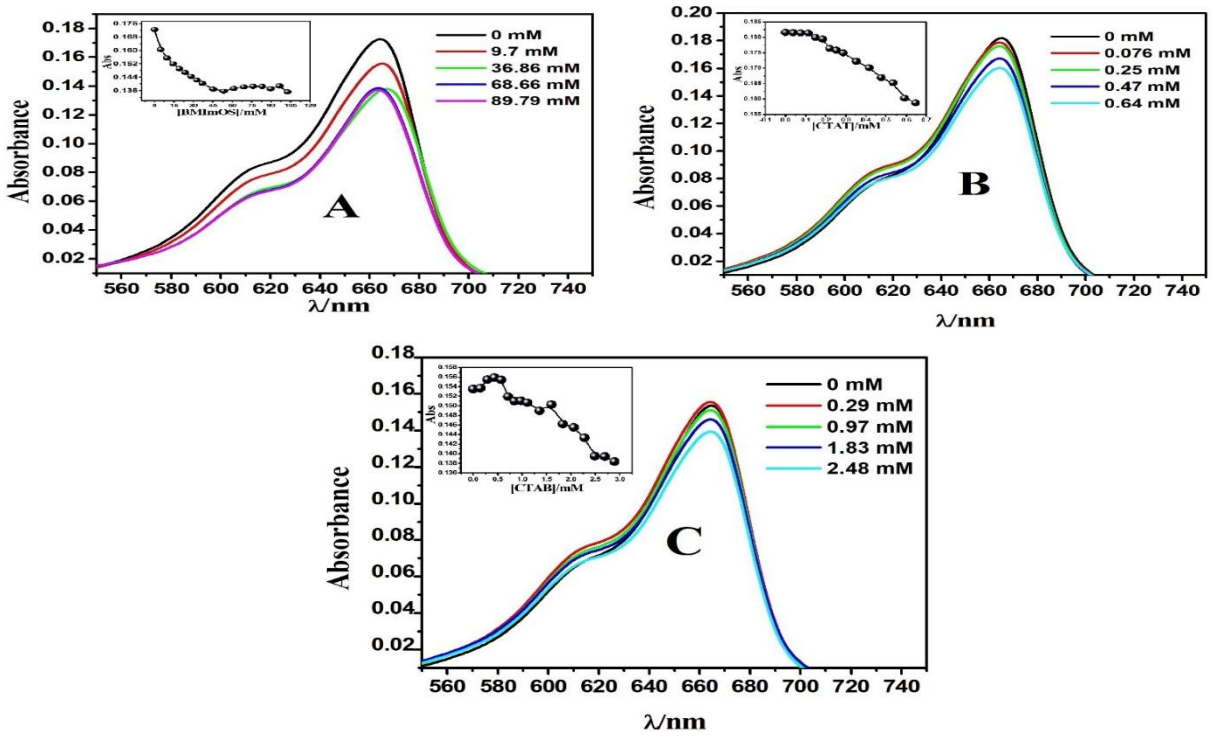

Figure 3. Absorbance of MB with varying concentration of (A) BMImOS, (B) CTAT, and (C) CTAB, (Inset shows Absorbance vs corresponding [Amphiphile]).

3.3 Emission spectral analysis

Emission spectra provide valuable information about the interaction between dyes and amphiphiles, as well as the nature of the microenvironment in which the probe is located. An aqueous solution of MB exhibits an emission wavelength ($\lambda_{emission}$) of 687.37 nm, which aligns with published literature[57]. However, the addition of various amphiphiles to this aqueous solution at both pre- and post-micellar concentrations affects fluorescence intensity. Notably, the changes in the emission spectra differ between ionic liquids and surfactants. When BMImOS is added to the aqueous solution of MB, an initial decrease in fluorescence intensity is observed (Fig. 4A) when the concentration of BMImOS is less than or equal to the critical micelle concentration (CMC). This phenomenon can be attributed to the quenching effect of the imidazolium ring, as the imidazolium cation acts as a quencher[58, 59], thereby reducing the fluorescence intensity. Conversely, when the concentration of BMImOS exceeds the CMC, a sharp increase in emission intensity occurs. This increase can be explained by the intercalation of MB into the micellar region formed by the octyl sulfate anion. As the dye incorporates into the stern layer of the micellar environment, the polarity of the surrounding microenvironment shifts from more polar to less polar. Since the dye possesses a predominantly hydrophobic structure, this reduction in polarity allows it to reorganize into a more stable form and minimizes the energy gap between its highest occupied molecular orbitals (HOMOs) and lowest unoccupied molecular orbitals (LUMOs)[60]. As a result, the emission intensity increases. In the case of cationic surfactants, fluorescence intensity rises initially (Fig. 4B and 4C). However, when the concentration of the surfactant increases, fluorescence intensity decreases rapidly. This decrease can be explained by the fact that when the surfactant concentration is below the CMC, micelles do not form, allowing for expected hydrophobic interactions between the hydrophobic parts of the surfactant monomers and the dye. This type of hydrophobic stacking creates a less polar microenvironment for MB in water/surfactant binary systems, leading to an increase in emission intensity. Yet, when the surfactant

concentration exceeds the CMC, the intercalation of MB into the micellar environment becomes unfavorable due to the like charges of the surfactant monomer's polar head groups. As a result, when the surfactant concentration falls below the critical micelle concentration, the MB molecule becomes more accessible to the surrounding water. In this aqueous environment, MB can interact with the counterions present in the surfactant, creating a more polar microenvironment around it. This interaction between MB and the counterions has the potential to facilitate the formation of exciplexes, i.e., excited-state complexes formed between the dye and the counterions. This process can lead to a gradual reduction in emission intensity, as dynamic shifts in the local environment influence the photophysical behavior of the dye.

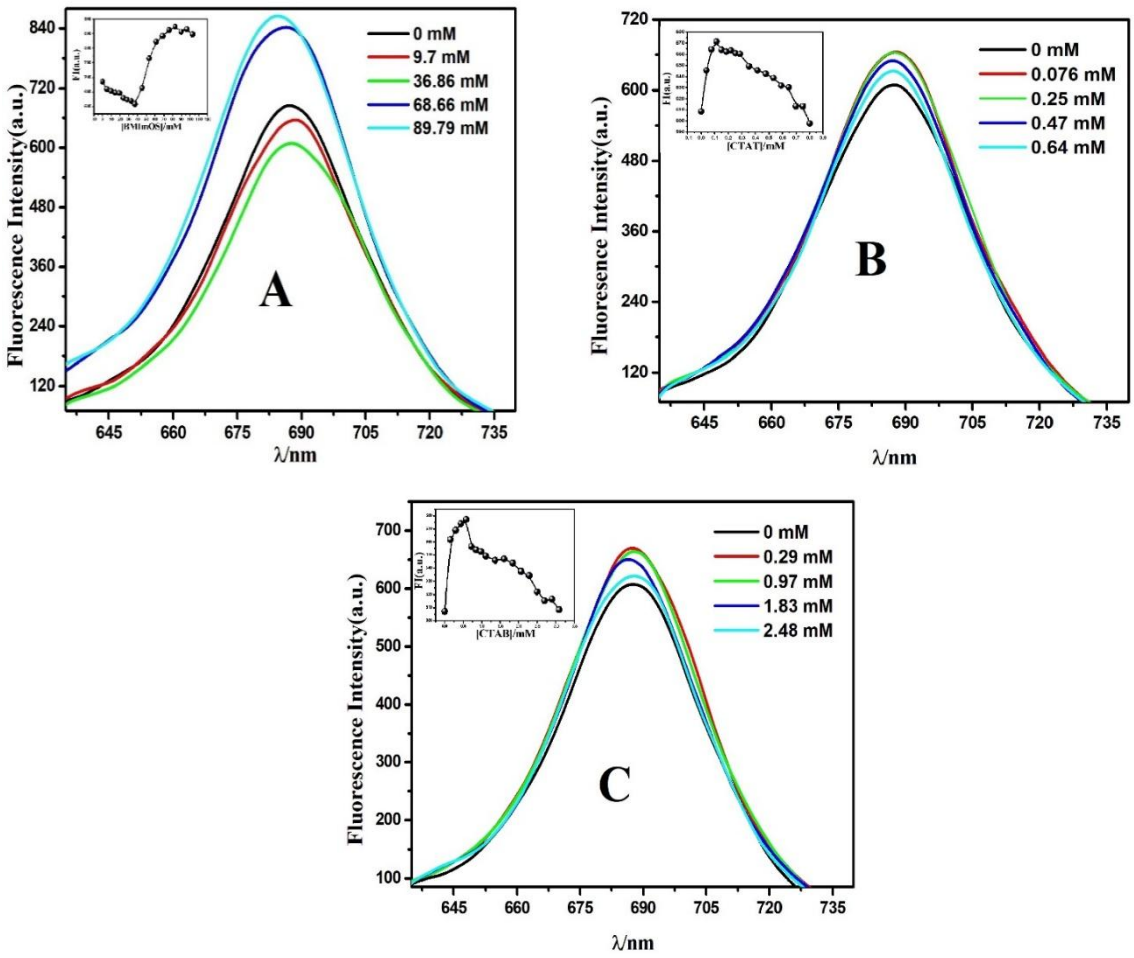

Figure 4. Variation of Fluorescence intensity of MB with varying concentration of (A) BMImOS, (B) CTAT, and (C) CTAB, (Inset shows Fluorescence Intensity vs corresponding [Amphiphile]).

3.3.1 Determination of the binding constant of the various MB-amphiphile systems

The study examines the intricate relationship between the fluorescence intensity of methylene blue (MB) and varying concentrations of different surfactants, ultimately determining a crucial parameter known as the binding constant. This constant helps to elucidate the mechanistic pathways and interaction patterns between MB and the surfactants.

In the systems involving MB with CTAT and CTAB, fluorescence intensity exhibited notable enhancements when the surfactant concentration remained below the critical micelle concentration (CMC). Specifically, for the MB-CTAT system, an increase in fluorescence was observed up to a concentration of 0.11 mM CTAT. For the MB-CTAB system, a similar increase was evident at 0.57 mM CTAB. To quantify these interactions, Beneshi-Hindelbrand's equation [61] was employed to derive the binding constant, and the equation is as follows,

$$\frac{1}{F-F_0} = \frac{1}{(F_\infty - F_0)\, K_b\, [\text{Surfactant}]^n} + \frac{1}{(F_\infty - F_0)} \qquad (4)$$

Where F_0, F and F_∞ are the fluorescence intensities in the absence of surfactant, the intermediate surfactant concentration, and the final surfactant concentration, respectively. K_b is the binding constant, and can be determined by plotting $\frac{1}{F-F_0}$ *Vs.* $\frac{1}{[\text{Surfactant}]^n}$.

The calculated binding constant values are summarized in Table 3, where a 1:1 molar ratio of surfactant to MB was maintained to facilitate the generation of a linear relationship (Fig. 5B and 5C). The binding constant data aligns well with the values obtained from conductometric plots, reinforcing the reliability of the findings. In contrast, the dynamics of the MB-BMImOS system revealed a consistent decline in fluorescence intensity as the concentration of BMImOS increased from 0 mM to 36.86 mM. This trend prompted the application of the Stern-Volmer equation[62] to evaluate the binding or association constant, represented by $K_{SV,}$ and the equation is as follows,

$$\frac{F_0}{F} = 1 + K_{sv}[Q] \quad (5)$$

Here, F_0 and F are the fluorescence intensities of the probe in the presence and absence of quencher molecules. K_{sv} is the binding constant, also known as the Stern-Volmer constant, and [Q] denotes the concentration of the quencher.

A direct plot of F_0/F against [Q] yielded a linear relationship, indicating the occurrence of either static or dynamic quenching phenomena (Fig. 5A). The imidazolium cation's role as a quencher likely contributes to the steady decrease in fluorescence intensity observed in this system. However, once the concentration of BMImOS reached or exceeded the CMC, a marked increase in fluorescence intensity was observed. This phenomenon can be attributed to the formation of micelles, which facilitate the incorporation of MB into the Stern layer of the micellar environment. The resulting alteration in the microenvironment's polarity leads to an enhanced fluorescence intensity. Furthermore, the binding constant for the MB-BMImOS system is notably low, which is consistent with the findings from conductometric measurements. This lower binding constant value indicates a weaker association of MB within the Stern layer of the BMImOS system, suggesting that the interaction between MB and BMImOS is less robust compared to the interactions observed with the other surfactants.

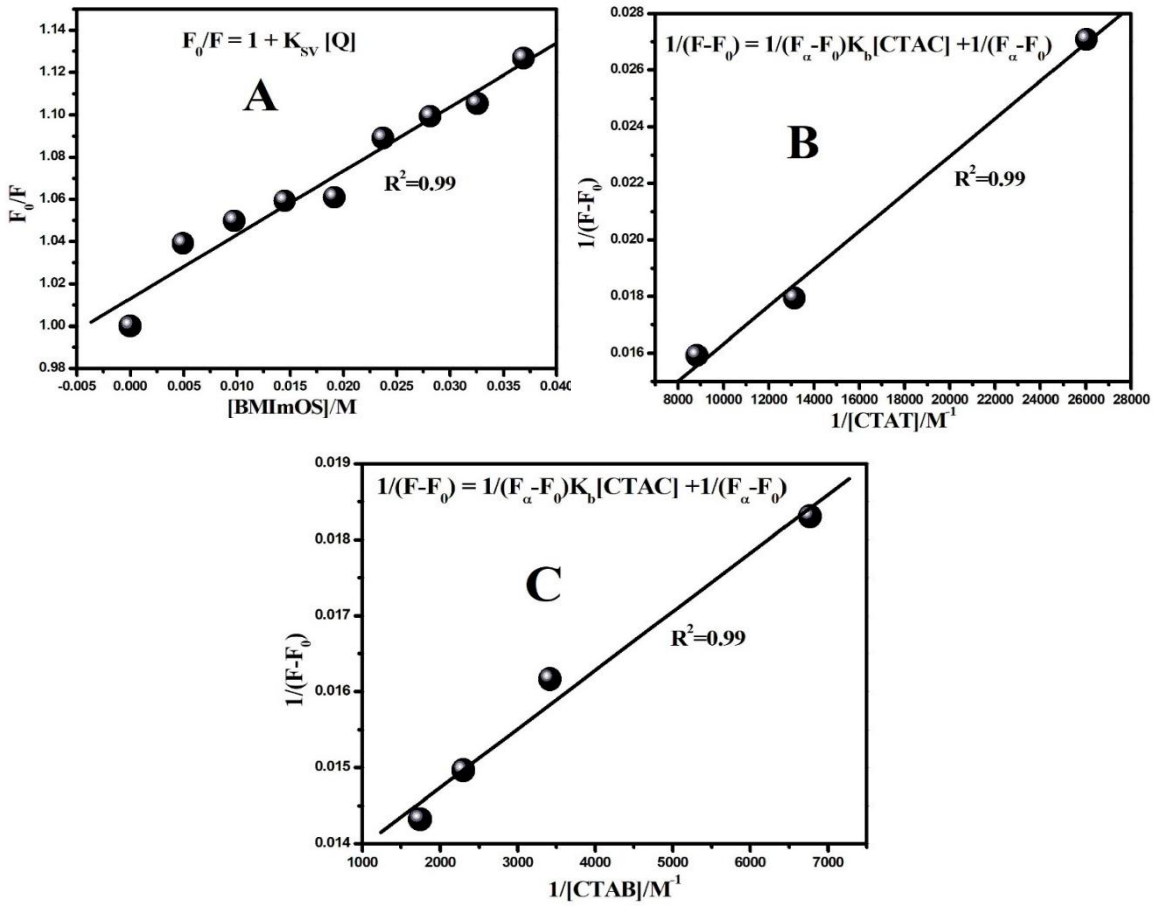

Figure 5: (A) Stern Volmer plot of MB BMImOS system, (B) and (C) are the Beneshi Hildebrand plot of MB-CTAT and MB-CTAB systems respectively.

Table 3. The binding constants of different systems obtain from steady state fluorescence spectra

System	Binding constant (M^{-1})	Number of binding sites (n)
MB-BMImOS	30.21	---
MB-CTAT	1.5×10^5	1
MB-CTAB	1.6×10^4	1

3.3.2 Stokes shift

The Stokes shift is a fundamental characteristic of a fluorophore, arising from the energy loss associated with the relaxation of excited-state electrons[63]. This phenomenon can be quantitatively assessed using the appropriate equation that relates the emission and absorption spectra of the fluorophore.

$$\text{Stokes' shift} = 10^7 \left[\frac{1}{\lambda ex} - \frac{1}{\lambda em}\right] \quad (6)$$

Where λ_{ex} and λ_{em} indicate the peaks of excitation and emission, respectively, measured in nanometers. The absorbance, fluorescence intensity, and Stokes shift are summarized in Table 4. For the MB-CTAT and MB-CTAB systems, the values of the Stokes shift do not vary significantly, as the microenvironment for methylene blue (MB) remains consistent in these systems. Being a cationic dye, MB does not enter the micelles formed by the cationic surfactants; instead, it tends to stay in the aqueous bulk phase, forming an ion pair with the counterions of CTAT and CTAB. In contrast, in the case of the MB-BMImOS system, the Stokes shift varies due to the solubilization of MB in the Stern layer of the micelles formed by the octylsulfate counterion of BMImOS. This change results in a different polarity of the microenvironment.

Table 4. Various spectroscopic parameters along with the calculation of Stokes' shift of MB and MB-Amphiphiles in their pre- and post-micellar concentration.

Concentration (mM)	λ_{max}^{abs}(nm)	Absorbance	λ_{max}^{flu}(nm)	Fluorescence Intensity (F.I.)	Stokes shift (Δν, cm^{-1})
MB in water					
10^{-5}	664.44	0.173	687.37	686.71	502.06
MB in BMImOS					
9.7	665.40	0.156	688.54	656.23	505.06
36.86	667.24	0.138	687.70	606.89	445.88
68.66	663.81	0.139	686.72	842.70	502.57
89.79	663.81	0.137	684.28	863.17	450.65
MB in CTAT					
0.076	664.81	0.178	688.37	664.39	514.82
0.25	664.81	0.175	687.84	663.31	503.62
0.47	664.75	0.167	687.86	649.30	506.04
0.64	664.69	0.160	687.62	632.11	501.69
MB in CTAB					
0.29	664.24	0.155	687.35	670.16	506.34
0.97	664.39	0.151	687.74	664.03	511.02
1.83	664.39	0.146	687.43	650.15	504.12
2.48	664.39	0.139	687.89	621.69	514.19

3.4 Measurement of Anisotropy

The measurement of anisotropy provides valuable insights into the rigidity of the microenvironment surrounding a probe within an amphiphile/water binary system.

Anisotropy can be measured by using the following equation[64],

$$r = \frac{I_V - GI_H}{I_V + 2GI_H} \quad (7)$$

Here, I_V and I_H are the intensities of excitation light towards parallel and perpendicular directions, respectively, arising from the probe's vertically polarised excitation.

Factor G defines

$$G = \frac{I_V}{I_H} \quad (8)$$

In this context, the aqueous solution of methylene blue (MB) demonstrates a nonzero anisotropy value. This can be attributed to its asymmetric molecular structure and its ability to form hydrogen bonds with the surrounding water molecules, which influences its rotational dynamics. Upon the introduction of the ionic liquid BMImOS, an increase in the measured anisotropy is observed. This enhancement is corroborated by the spectral behavior of MB when situated within the micellar system formed by BMImOS. The underlying mechanism can be explained by the encapsulation of MB within the stern layer of the micelle, which is primarily shaped by the octyl sulfate chain of BMImOS. Such intercalation effectively restricts the rotational freedom of the MB molecules, resulting in a higher anisotropy value[64]. Conversely, when cationic surfactants such as cetyltrimethylammonium bromide (CTAB) or cetyltrimethylammonium tosylate (CTAT) are added to the aqueous solution of MB, there are no significant alterations in the anisotropy values. This finding suggests that MB does not penetrate into the stern layer of the micelles formed by these cationic surfactants. Instead, MB appears to preferentially associate with the counterions of the amphiphiles present in the bulk aqueous phase. As a consequence of residing in the aqueous phase associated with the cationic micelles, MB is not subjected to additional constraints on its rotational movement. Therefore, the absence of substantial changes in the anisotropy value can be attributed to this unrestricted rotational freedom, which highlights the interaction dynamics between MB and the cationic surfactants, in contrast to the behavior observed with BMImOS. This detailed understanding of the anisotropic behavior in these systems is crucial for elucidating the microenvironmental properties and the interactions influencing the rigidities within amphiphile and water systems[65].

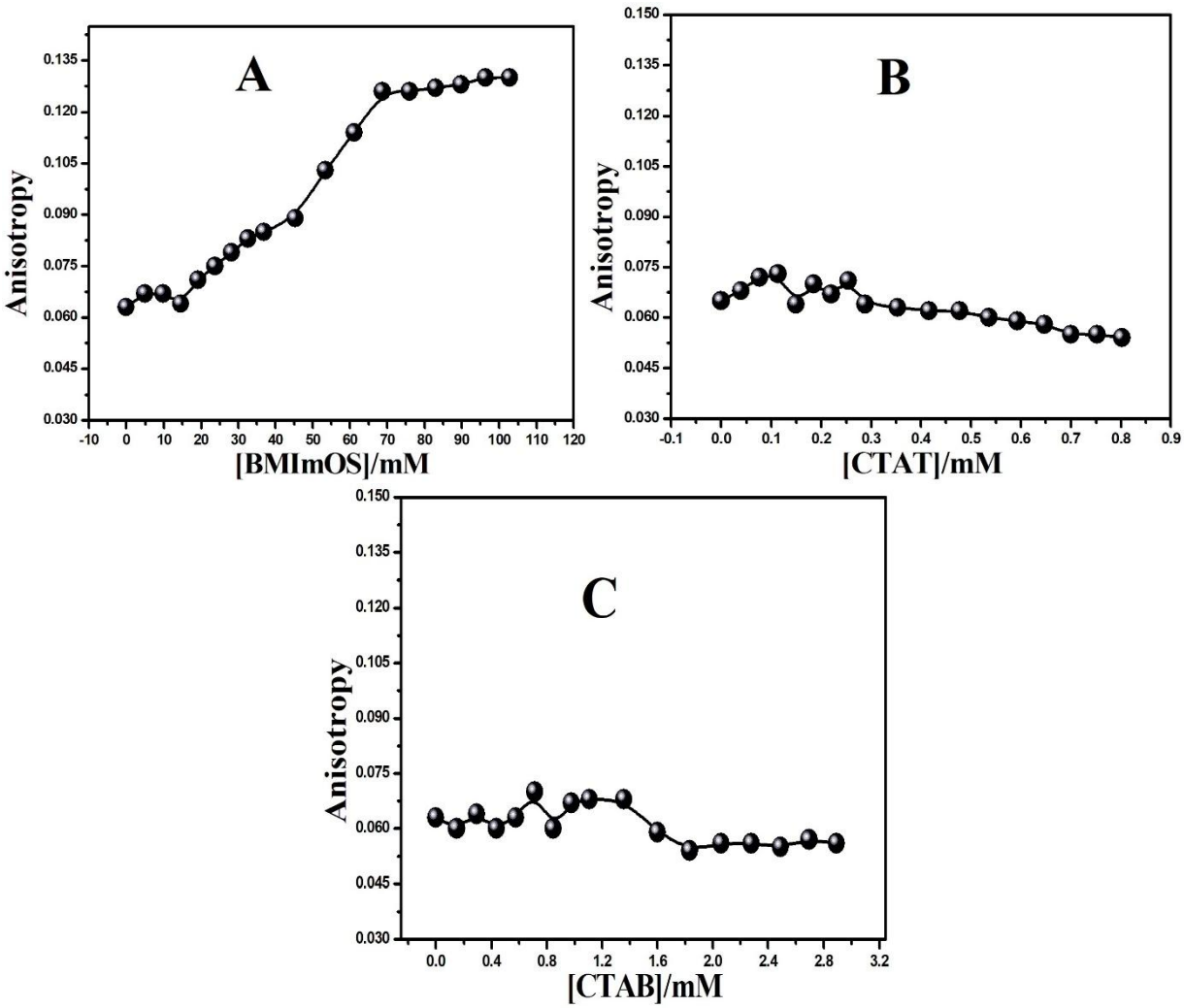

Figure 6: Variation of Anisotropy of MB with varying concentration of (A) BMImOS, (B) CTAT, and (C) CTAB,

3.5 Measurement of Zeta potential

The measurement of zeta potential is crucial as it provides vital insights into the stability of colloidal systems. A higher zeta potential typically indicates greater stability within these systems[66]. For instance, an aqueous solution of methylene blue (MB) exhibits a zeta potential of -13.3 mV. This negative value can be attributed to the hydrogen bonding that occurs between the methylene blue molecules and the water, creating a stable colloidal environment. When cationic surfactants are introduced into the aqueous MB solution, there is a noteworthy shift in the zeta potential, with values becoming increasingly positive. This change suggests an enhancement in colloidal stability, which can be explained by the electrostatic repulsion

generated between the positively charged micelles formed by the cationic surfactants and the methylene blue molecules that remain dispersed in the aqueous phase. On the other hand, the addition of BMImOS to the aqueous MB solution presents a more complex scenario. As the concentration of BMImOS surpasses the critical micelle concentration (CMC), the zeta potential begins to decrease and shift back toward a more negative value. Interestingly, when the concentration of BMImOS exceeds the CMC, there is a significant drop in zeta potential, which suggests the onset of colloidal flocculation or instability[67]. This phenomenon occurs because the methylene blue molecules become incorporated into the stern layer of the micellar structure formed by the octyl sulfate chains of BMImOS. Consequently, as methylene blue molecules penetrate the micellar surface due to electrostatic attractions, a dramatic reduction in surface potential is observed, signifying a destabilization of the colloidal system. The Zeta potential values and the anisotropy values of MB-amphiphiles are presented in Table 5.

Table 5. Zeta potential, and anisotropy values of aqueous MB and MB- MB-amphiphiles in their respective premicellar and post-micellar concentrations.

Concentration(mM)	**Zeta potential (mV)**	**Anisotropy**
	MB in water	
10^{-5}	-13.3	0.065
	MB in CTAT	
0.11	22.3	0.063
0.18	30.2	0.064
0.54	23.4	0.062
	MB in BMImOS	
14.49	-30.5	0.064
23.69	-32.2	0.075
68.67	-6.12	0.126
	MB in CTAB	
0.43	14.5	0.060
0.71	38.3	0.070
2.06	27.3	0.056

3.6 Density functional theory calculations

Density function theory (DFT) is a theoretical framework used to predict the stability of a system and the nature of the interactions between its components. In this study, DFT calculations were conducted using a 1:1 molecular ratio to assess the stability of methyl blue (MB) when interacting with various amphiphiles, as well as to identify the type of interaction occurring between MB and the amphiphiles[68]. All the optimised structures of MB-amphiphiles have been depicted in Figure 7. The energy optimization data (E_{opt}) for the MB-CTAT system indicates that it is the most stable configuration, as it has the lowest E_{opt} value. The planar structure of the bulky tosylate anion facilitates effective binding with MB, resulting in the highest binding ability among the systems studied. In contrast, since CTAB has a much smaller counterion, it can be concluded that the binding efficiency of the tosylate anion is greater than that of the bromide ion. This is evidenced by the less negative E_{opt} for the MB-CTAB system compared to the MB-CTAT system, suggesting that the MB-CTAT system is more stable. On the other hand, in the case of BMImOS, the octyl sulfate anion is not planar, leading to lower binding ability. Consequently, the E_{opt} for the MB-BMImOS system is higher than that of the other MB-surfactant systems. All the optimised energy values of MB-amphiphiles have been presented in Table 6. Furthermore, the analysis of frontier molecular orbitals (FMOs) provides additional insights into the types of interactions present[69]. For MB alone, both the highest occupied molecular orbital (HOMO) and the lowest unoccupied molecular orbital (LUMO) are localized on the MB molecule (Fig. 8). However, in the MB-amphiphile systems, all HOMOs are found in the counterion of the amphiphiles, while all LUMOs are located on MB. This indicates the formation of exciplexes between MB and the counterions of CTAT, CTAB, and the octyl sulfate anion of BMImOS, along with a potential charge transfer from the HOMOs to the LUMOs in these systems[70]. Notably, the energy gaps between HOMOs and LUMOs for MB-CTAT and MB-BMImOS are quite similar, suggesting

that binding with bulky counterions may enhance the stability of MB. This conclusion is further supported by conductometric experiments, which indicate the highest binding ability for the MB-CTAT system. In this theoretical examination, since only one molecule of BMImOS is present, the Stern layer of the micellar system cannot be effectively determined. Nevertheless, BMImOS demonstrates the least binding ability in conductometric experiments due to micelle formation and the intercalation of MB into the stern layer of the micellar interface. Additionally, the MB-CTAB system reveals a greater energy gap between its FMOs, with the small counterion Br- exhibiting lower binding ability compared to the larger counterions in the other MB-amphiphile systems.

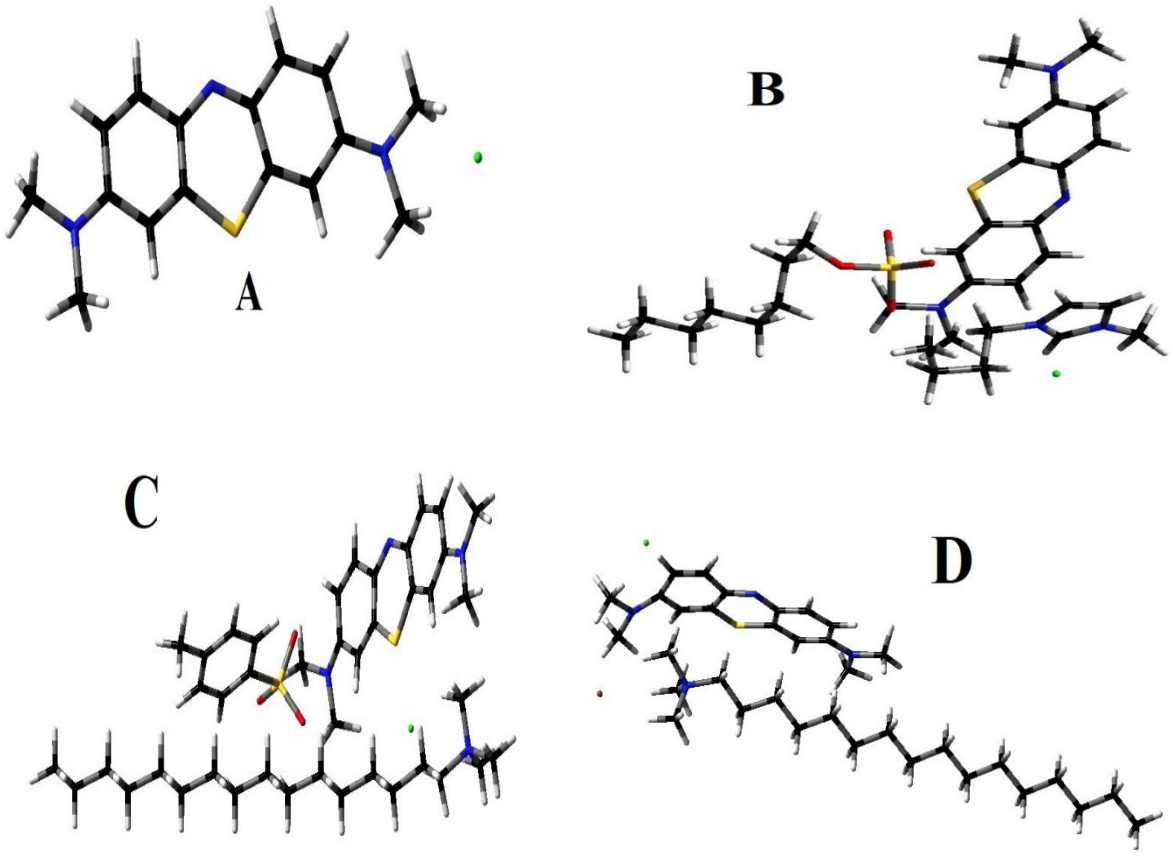

Figure 7. B3LYP/6-21G (d, p) - optimised structure of (a) MB, (b) MB-BMImOS, (c) MB-CTAT, (d) MB-CTAB. Colour code for atoms: red, oxygen; dark grey, carbon; light grey, hydrogen; yellow, sulphur; blue, nitrogen; green, chlorine; brown, bromine.

Table 6. Optimized energy, energy of HOMO and LUMO, band gap, and dipole moments of (a) MB, (b) MB-BMImOS, (c) MB-CTAT, and (d) MB- CTAB systems.

System	E_{OPT} (a.u)	Energy of HOMO (E_1) (ev)	Energy of LUMO (E_2) (ev)	ΔE (E_2-E_1) (eV)	Dipole moment (Debye)
MB	-1634.68	-0.22291	-0.12756	0.09535	20.13
MB-BMImOS	-3064.51	-0.187	-0.10297	0.08403	15.45
MB-CTAT	-3324.42	-0.187	-0.10297	0.0843	19.32
MB-CTAB	-3196.26	0.19260	0.09920	0.0934	18.993

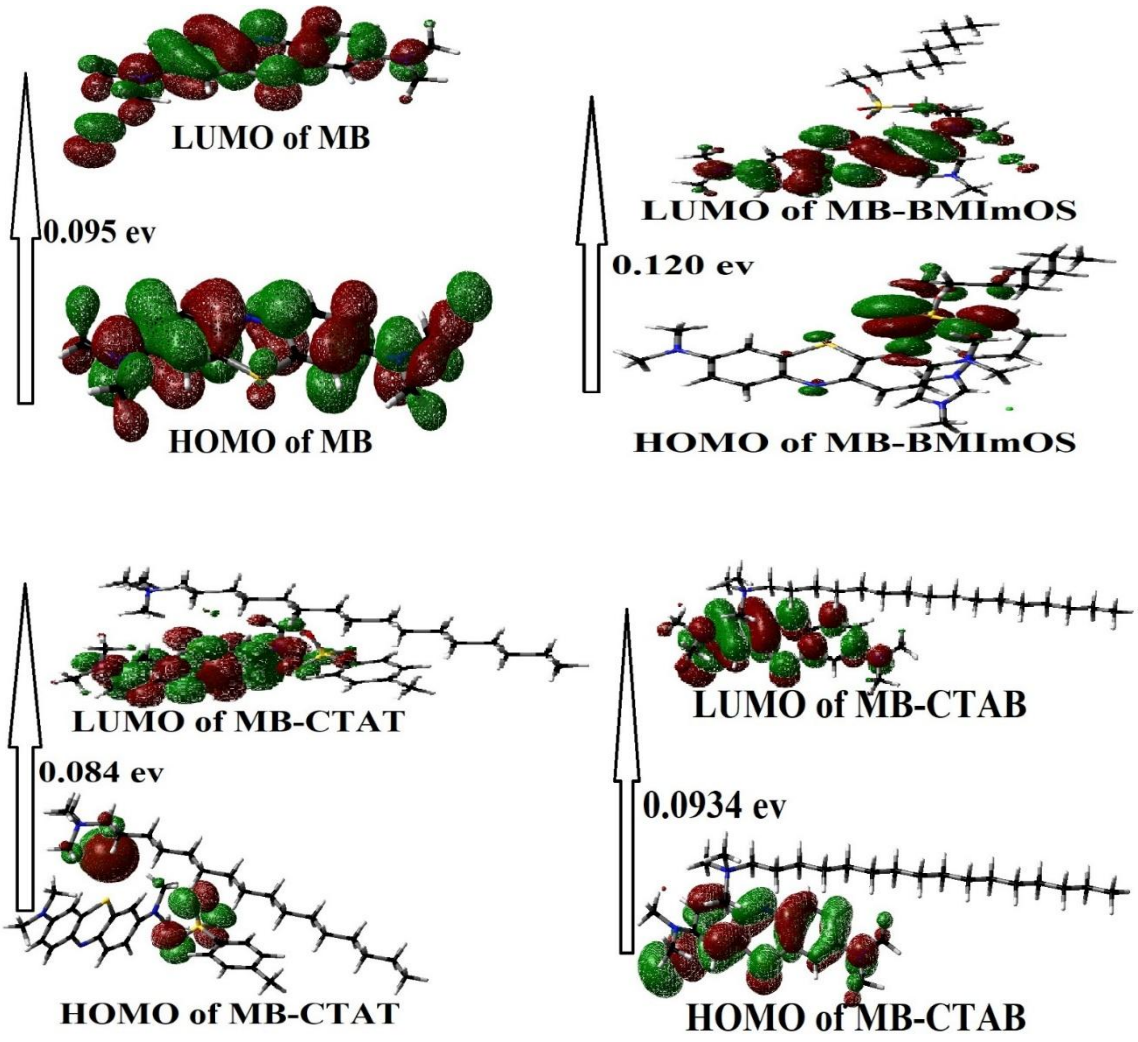

Figure 8. HOMO-LUMO diagrams of MB with various amphiphiles

4. Conclusion

This work examines the interaction of a cationic dye known as methylene blue (MB) with two cationic surfactants: cetyl trimethyl ammonium tosylate (CTAT) and cetyl trimethyl ammonium bromide (CTAB), along with a surface-active ionic liquid (SAIL) called 1-butyl-3-methyl imidazolium octyl sulfate (BMImOS). The study primarily focuses on how the counterions of the various surfactants affect the properties of the microenvironments. As a cationic dye, MB does not enter the Stern layer of the micelles formed by CTAT and CTAB. Instead, MB prefers to remain in the aqueous bulk phase, where it can electrostatically bind with the anionic counterions of CTAT and CTAB. This binding results in delayed micellization for both surfactants, and the critical micelle concentration (CMC) values were determined using conductometric methods. There is no significant spectral shift observed in the UV-visible and steady-state fluorescence spectra for these systems. In the case of the MB-BMImOS system, the anionic counterion (octyl sulfate) can form micelles. Being oppositely charged, MB can encapsulate within the stern layer of BMImOS, causing early micellization. Binding constants were determined both conductometrically and through steady-state fluorescence spectra, and the results from these different methods align very well. CTAT exhibits the highest binding affinity for MB, which can be attributed to the planar structure of the tosylate anion. Conversely, BMImOS shows the lowest binding ability with MB, likely due to the encapsulation of MB in the stern layer of the octyl sulfate micelle. In the MB-CTAT and MB-CTAB systems, ion pairs form between MB and the anionic counterions in the aqueous bulk phase, resulting in a positive zeta potential for both pre- and post-micellar concentrations of CTAT and CTAB. In the MB-BMImOS system, MB tends to reside in the stern layer of the octyl sulfate micelle. This incorporation leads to a decrease in negative zeta potential values and an increase in anisotropy. However, no significant changes in anisotropy are observed in the MB-CTAT or MB-CTAB systems. Additionally, the energies of all systems were optimized

using DFT calculations. The MB-CTAT system emerged as the most stable, exhibiting the lowest energy optimization value. The TDDFT diagrams for MB-CTAT and MB-BMImOS clearly show that the counterions of the surfactants and the SAIL occupy the highest occupied molecular orbital (HOMO) position, while the lowest unoccupied molecular orbital (LUMO) is positioned on MB. This observation suggests a possible charge transfer phenomenon from the counterions of the surfactants and the SAIL to MB. Ultimately, this work serves as an investigative initiative into the effects of counterions in aqueous/micelle binary systems and may significantly contribute to various fields, including analytical chemistry, material fabrication, medicinal photosensitization, drug delivery, wastewater treatment, and other related areas.

REFERENCES:

[1] M.Y. Hossain, T. Jiang, W. Zhu, S. Sarker, M.N. Pervez, M.I.U. Hoque, Y. Cai, V. Naddeo, Journal of Natural Fibers 19 (2022) 11283.

[2] A.R. Tehrani Bagha, H. Bahrami, B. Movassagh, M. Arami, F.M. Menger, Dyes and Pigments 72 (2007) 331.

[3] N. Kumar, R. Tyagi, Journal of Dispersion Science and Technology 35 (2014) 205.

[4] I. Kralova, J. Sjöblom, Journal of Dispersion Science and Technology 30 (2009) 1363.

[5] P. Bogdanova, C. Vakh, A. Bulatov, Food Chemistry 380 (2022) 131812.

[6] T.U. Rashid, S.M.F. Kabir, M.C. Biswas, M.A.R. Bhuiyan, Industrial & Engineering Chemistry Research 59 (2020) 9719.

[7] B. Han, D. Shu, S. Cao, Z. Lian, F. An, W. Li, S. Bai, Journal of Molecular Liquids 410 (2024) 125657.

[8] H.A. Gazzaz, B.H. Robinson, Langmuir 16 (2000) 8685.

[9] P. Bandyopadhyay, A.K. Ghosh, S. Bandyopadhyay, Chemical Physics Letters 476 (2009) 244.

[10] K. Bogman, F. Erne-Brand, J. Alsenz, J. Drewe, Journal of Pharmaceutical Sciences 92 (2003) 1250.

[11] H. You, H. Spaeth, V.N.L. Linhard, A.J. Steckl, Langmuir 25 (2009) 11698.

[12] K. Liu, L. Zheng, C. Ma, R. Göstl, A. Herrmann, Chemical Society Reviews 46 (2017) 5147.

[13] B.K. Paul, N. Guchhait, The Journal of Physical Chemistry B 115 (2011) 11938.

[14] L.-T. Huang, T.-F. Yeh, Y.-L. Kuo, P.-C. Chen, C.-M. Chen, Pediatrics & Neonatology 56 (2015) 19.

[15] H. Wang, W. Zhao, X. Liu, S. Wang, Y. Wang, ACS Applied Bio Materials 3 (2020) 593.

[16] V.S. Farafonov, A.V. Lebed, N.O. McHedlov-Petrossyan, Langmuir 33 (2017) 8342.

[17] A.R. Tehrani-Bagha, K. Holmberg, Materials 6 (2013) 580.

[18] P. Wei, X. Pan, C.-Y. Chen, H.-Y. Li, X. Yan, C. Li, Y.-H. Chu, B. Yan, Chemical Society Reviews 50 (2021) 13609.

[19] M. Petkovic, K.R. Seddon, L.P.N. Rebelo, C. Silva Pereira, Chemical Society Reviews 40 (2011) 1383.

[20] M. Amde, J.-F. Liu, L. Pang, Environmental Science & Technology 49 (2015) 12611.

[21] C.-Z. Liu, F. Wang, A.R. Stiles, C. Guo, Applied Energy 92 (2012) 406.

[22] Q. Zhang, J.n.M. Shreeve, Chemical Reviews 114 (2014) 10527.

[23] S.L. Piper, M. Kar, D.R. MacFarlane, K. Matuszek, J.M. Pringle, Green Chemistry 24 (2022) 102.

[24] Z. He, P. Alexandridis, Physical Chemistry Chemical Physics 17 (2015) 18238.

[25] K.J. Mohammed, S.K. Hadrawi, E. Kianfar, BioNanoScience 13 (2023) 760.

[26] J. Yuan, M. Antonietti, Polymer 52 (2011) 1469.

[27] I. Osada, H. de Vries, B. Scrosati, S. Passerini, Angewandte Chemie International Edition 55 (2016) 500.

[28] H. Mahmood, M. Moniruzzaman, S. Yusup, T. Welton, Green Chemistry 19 (2017) 2051.

[29] R. Sheldon, Chemical Communications (2001) 2399.

[30] H. Olivier-Bourbigou, L. Magna, Journal of Molecular Catalysis A: Chemical 182 (2002) 419.

[31] V.I. Pârvulescu, C. Hardacre, Chemical Reviews 107 (2007) 2615.

[32] N. Adawiyah, M. Moniruzzaman, S. Hawatulaila, M. Goto, MedChemComm 7 (2016) 1881.

[33] J.L. Shamshina, P.S. Barber, R.D. Rogers, Expert opinion on drug delivery 10 (2013) 1367.

[34] S.P. Ventura, F.A. e Silva, M.V. Quental, D. Mondal, M.G. Freire, J.A. Coutinho, Chemical Reviews 117 (2017) 6984.

[35] S. Curry, Annals of emergency medicine 11 (1982) 214.

[36] S.R. David, N.S. Sawal, M.N.S.B. Hamzah, R. Rajabalaya, Journal of Pharmacology and Pharmacotherapeutics 9 (2018) 1.

[37] Y.-Y. Huang, A. Wintner, P.C. Seed, T. Brauns, J.A. Gelfand, M.R. Hamblin, Scientific reports 8 (2018) 7257.

[38] P. Varghese, A.T. Abdel-Rahman, S. Akberali, A. Mostafa, J.M. Gattuso, R. Carpenter, The breast journal 14 (2008) 61.

[39] C.A. Paciullo, D.M. Horner, K.W. Hatton, J.D. Flynn, Pharmacotherapy: The Journal of Human Pharmacology and Drug Therapy 30 (2010) 702.

[40] A. Richards, H. Marshall, A. McQuary, Journal of Oncology Pharmacy Practice 17 (2011) 372.

[41] R. Gracia, G. Shepherd, Pharmacotherapy: The Journal of Human Pharmacology and Drug Therapy 24 (2004) 1358.

[42] M. Oz, D.E. Lorke, M. Hasan, G.A. Petroianu, Medicinal research reviews 31 (2011) 93.

[43] F. Ghasemi, A. Jahani, A. Moradi, M.H. Ebrahimzadeh, N. Jirofti, Archives of Bone and Joint Surgery 11 (2023) 485.

[44] P. Karunanithi, R. Vigneshwari, E.P. Raj, P. Rajesh, S. Krishnamoorthy, S. Dash, Chemical Physics Impact 5 (2022) 100092.

[45] O. Yazdani, M. Irandoust, J.B. Ghasemi, S. Hooshmand, Dyes and Pigments 92 (2012) 1031.

[46] M.T. Muhammad, M.N. Khan, Journal of Molecular Liquids 234 (2017) 309.

[47] A. Pedraza, M.D. Sicilia, S. Rubio, D. Pérez-Bendito, Analytica chimica acta 588 (2007) 252.

[48] P. Shah, S.K. Jha, A. Bhattarai, Journal of Molecular Liquids 340 (2021) 117200.

[49] M.D. Garcia, A. Sanz-Medel, Talanta 33 (1986) 255.

[50] B. Simončič, M. Kert, Dyes and Pigments 54 (2002) 221.

[51] N. Scholz, T. Behnke, U. Resch-Genger, Journal of fluorescence 28 (2018) 465.

[52] M. Taj Muhammad, M.N. Khan, Journal of Molecular Liquids 234 (2017) 309.

[53] J. Kalmár, G. Lente, I. Fábián, Dyes and Pigments 127 (2016) 170.

[54] Y.-J. Hu, Y. Liu, R.-M. Zhao, J.-X. Dong, S.-S. Qu, Journal of Photochemistry and Photobiology A: Chemistry 179 (2006) 324.

[55] P. Garg, G. Kaur, G.R. Chaudhary, S. Kaur, S.L. Gawali, P. Hassan, Colloids and Surfaces B: Biointerfaces 164 (2018) 116.

[56] S. Bandyopadhyay, R. Banik, R. Sardar, S. Ghosh, Journal of Molecular Liquids 411 (2024) 125684.

[57] T. Cwalinski, W. Polom, L. Marano, G. Roviello, A. D'Angelo, N. Cwalina, M. Matuszewski, F. Roviello, J. Jaskiewicz, K. Polom, Journal of clinical medicine 9 (2020) 3538.

[58] Y. Shu, M. Liu, S. Chen, X. Chen, J. Wang, The Journal of Physical Chemistry B 115 (2011) 12306.

[59] V. Kumar, S. Pandey, The Journal of Physical Chemistry B 116 (2012) 12030.

[60] S. Bandyopadhyay, R. Banik, R. Sardar, S. Ghosh, Journal of Molecular Liquids (2025) 127953.

[61] S. Yefimova, Functional materials (2009).

[62] A.M. Khan, S. Bashir, A. Shah, M.F. Nazar, H.M.A. Rahman, S.S. Shah, A.Y. Khan, A.R. Khan, F. Shah, Colloids and Surfaces A: Physicochemical and Engineering Aspects 539 (2018) 407.

[63] N. Pandey, N. Tewari, S. Pant, M.S. Mehata, Spectrochimica Acta Part A: Molecular and Biomolecular Spectroscopy 267 (2022) 120498.

[64] P. Quagliotto, N. Barbero, C. Barolo, K. Costabello, L. Marchese, S. Coluccia, K. Kalyanasundaram, G. Viscardi, Dyes and Pigments 82 (2009) 124.

[65] S. Mondal, S. Ghosh, Journal of Photochemistry and Photobiology B: Biology 115 (2012) 9.

[66] S. Fazeli, B. Sohrabi, A.R. Tehrani-Bagha, Dyes and Pigments 95 (2012) 768.

[67] A.M. Khan, F. Shafiq, S.A. Khan, S. Ali, B. Ismail, A.S. Hakeem, A. Rahdar, M.F. Nazar, M. Sayed, A.R. Khan, Journal of Molecular Liquids 274 (2019) 673.

[68] A. Dutta, B. Boruah, P.M. Saikia, R.K. Dutta, Journal of Molecular Liquids 187 (2013) 350.

[69] D. Karataş, D. Senol-Arslan, O. Ozdemir, Clays and Clay Minerals 66 (2018) 426.

[70] A. Dutta, B. Boruah, A.K. Manna, B. Gohain, P.M. Saikia, R.K. Dutta, Spectrochimica acta part A: molecular and biomolecular spectroscopy 104 (2013) 150.

SUMMARY & CONCLUSION

SUMMARY AND CONCLUSION

The collective research examines the intricate interplay between diverse dyes and amphiphilic systems—encompassing both conventional surfactants and surface-active ionic liquids (SAILs)—in aqueous environments. Across four systematically designed investigations, the studies probe how variations in head group charge, hydrophobic tail architecture, counterion size, and micellar polarity govern dye solubilization, aggregation dynamics, and spectroscopic responses. The methodological framework is rooted in a multi-technique experimental approach, including UV–visible absorption, steady-state and time-resolved fluorescence spectroscopy, time-correlated single photon counting (TCSPC), dynamic light scattering (DLS), zeta potential analysis, and conductometric titration, supplemented with Density Functional Theory (DFT) and Time-Dependent DFT (TDDFT) calculations to yield molecular-level insights. In the first chapter, Acridine Red (AR), a cationic azo dye, was studied with anionic SDS, hydrophobic-tailed BMImOS, and hydrophobic-chain-free BMImBr. BMImOS displayed superior solubilization efficiency even below the critical micelle concentration, an effect attributed to reduced head-group repulsion and enhanced dye encapsulation through its hydrophobic tail. In contrast, BMImBr, lacking a tail, formed only salt-like ion pairs with negligible micellar solubilization. Spectral shifts, fluorescence lifetime enhancement, and anisotropy measurements confirmed AR incorporation into BMImOS micelles, while DFT/TDDTF analysis supported favorable HOMO–LUMO overlap and electrostatic charge transfer, emphasizing the role of hydrophobic tailoring in SAIL design. In the second chapter, Eosin Y (EY), an anionic xanthene dye, interacted with cationic CTAC, anionic SLAS and NaDC, and the zwitterionic C_{12}DmCB. The interaction efficiency followed the order C_{12}DmCB > CTAC >> SLAS ≈ NaDC. C_{12}DmCB induced the most pronounced bathochromic shifts, lifetime enhancement, and anisotropy increases, reflecting efficient EY stabilization without the toxicity concerns typical of cationics. CTAC facilitated moderate binding through

electrostatic attraction, while anionic systems showed poor solubilization due to repulsion. DFT results confirmed superior thermodynamic stability for the EY–C_{12}DmCB complex, demonstrating the zwitterionic advantage in reducing repulsion while promoting strong micelle–dye interactions. The third investigation with Phloxine B (PhB), an anionic xanthene dye, further illuminated this advantage. C_{12}DmCB yielded the most significant solubilization and stabilization, evidenced by marked spectral shifts, longer fluorescence lifetimes, increased micellar size, and reduced zeta potential. SDS showed negligible binding due to like-charge repulsion, while CTAC exhibited moderate affinity via electrostatic attraction. DFT analysis revealed the lowest HOMO–LUMO gap for the PhB–C12DmCB system, indicating the highest stability and confirming that balanced charge distribution in zwitterionic surfactants enhances micellization and encapsulation efficiency. The fourth study explored Methylene Blue (MB) with cationic CTAB, CTAT, and BMImOS, where counterion effects dominated interaction behavior. CTAT, with bulky tosylate counterions, formed strong ion-pair interactions with MB, delaying micellization but improving binding affinity and stability. CTAB, with smaller bromide ions, showed weaker incorporation, while BMImOS permitted partial MB embedding into its Stern layer via electrostatic interaction with the octyl sulfate tail. DFT revealed the MB–CTAT complex as the most stable, with HOMO–LUMO localization patterns suggesting charge transfer. Across all systems, zwitterionic surfactants and hydrophobically tailored SAILs consistently outperformed conventional anionic or cationic surfactants when electrostatic repulsion would otherwise hinder dye incorporation. The integrated findings present a coherent framework for understanding and engineering dye-amphiphile interactions at the molecular level. Opposite-charge dye–surfactant pairs benefit from strong electrostatic attraction, but optimal solubilization often requires additional hydrophobic or steric stabilization, while same-charge systems can still achieve effective binding via counterion-mediated complexation or hydrophobic partitioning. Hydrophobic chains, as in BMImOS,

reduce electrostatic repulsion, lower the CMC, and increase dye loading capacity, whereas their absence, as in BMImBr, limits solubilization. Zwitterionic surfactants like C12DmCB balance positive and negative charges within the same molecule, minimizing electrostatic barriers, enhancing dye packing efficiency, and surpassing cationic systems in binding performance without associated toxicity. Counterion engineering offers another powerful design lever, as bulky, charge-delocalized counterions can form stabilizing ion pairs with like-charged dyes, influencing micellization behavior and stability. The strong correlation between experimental observables—such as spectral shifts, fluorescence lifetimes, anisotropy changes, and micellar size—and DFT-predicted parameters like HOMO–LUMO gaps and charge distribution validates mechanistic interpretations and enables predictive system design. These insights have direct applications in drug delivery, photosensitization for photodynamic therapy and solar energy harvesting, wastewater treatment, and bioimaging, with environmentally benign and tunable systems like SAILs and zwitterionics offering sustainable solutions. Ultimately, this body of work advances from isolated case studies toward a generalizable design philosophy for micellar systems, advocating optimization of head group charge, strategic hydrophobic integration, and counterion selection to control interaction strength and micellization thermodynamics. The integration of high-resolution experimental data with first-principles computational modeling not only confirms mechanistic pathways but also provides predictive capacity for developing next-generation amphiphilic assemblies tailored for industrial, biomedical, and environmental applications while minimizing ecological impact.

BASIC DATA

Basic Data

Chapter I

1.1 Absorbance vs [SDS]/mM obtained from UV absorption spectra at 298K

[SDS]/mM	Absorbance
0	0.188
0.474	0.197
0.944	0.201
1.41	0.208
1.87	0.208
2.33	0.207
2.79	0.207
3.69	0.204
4.58	0.203
5.45	0.201
6.31	0.1999
7.16	0.194
8	0.19
8.82	0.184
9.63	0.182
10.83	0.18
12	0.179
13.14	0.177
14.26	0.176
15.72	0.175

1.2 Absorbance vs [BMImOS]/mM obtained from UV absorption spectra at 298K

[BMImOS]/mM	Absorbance
0	0.18486
2.95	0.1817
6.85	0.18012
10.85	0.17854
16.31	0.17696
23.63	0.17696
30.72	0.17696
37.61	0.17696
44.3	0.17222
50.8	0.15484
57.11	0.14852
63.26	0.14536
69.23	0.14536
75.04	0.1422

1.3 Absorbance vs [BMImBr]/mM obtained from UV absorption spectraat 298K

[BMImBr]/mM	Absorbance
0	0.18576
0.98912	0.26961
1.95886	0.27219
2.9098	0.27735
3.84246	0.26445
4.75737	0.25155
5.65504	0.24381
6.53595	0.24252
7.40056	0.22833
8.24931	0.21543
9.08265	0.19866
9.90099	0.18576
10.70473	0.17415
11.49425	0.16512
13.03215	0.14835
14.51751	0.129
15.95298	0.11094
17.34104	0.09417

1.4 Variation of Fluorescence Intensity with varying concentrations of SDS at 298K

[SDS]/mM	F.I.
0	159.04
0.47714	148.35
0.9505	139.89
1.42012	135.89
1.88605	132.42
2.34834	128.34
2.80702	123.49
3.26214	119.38
3.71373	114.44
4.16185	110.87
4.60653	109.88
5.0478	123.47
5.48571	133.12
5.9203	137.29
6.35161	138.87
7.2045	139.1
8.04469	138.52
8.87246	138.27

1.5 Variation of Fluorescence Intensity with varying concentrations of BMImOS at 298K

[BMImOS]/mM	F.I.
0	61.38
2.95	55.55
6.85	51.34
10.68	48.33
16.31	45.87
23.63	42.84
30.72	40.64
37.61	39.01
44.3	37.23
50.8	33.8
57.11	31.09
63.26	29.75
69.23	28.86
75.04	28.44
80.7	27.87
86.2	27.43
92.9	26.99
99.36	26.44
111.71	25.72

1.6 Variation of Fluorescence Intensity with varying concentrations of BMImBr at 298K

[BMImBr]/mM	F.I.
0.98	27.23
1.94	26.78
2.88	26.47
3.8	26.26
4.72	25.9
5.6	25.63
6.5	25.29
7.33	25
8.2	24.6
9	24.33
9.8	24.12
10.6	23.85
12.17	23.65
13.7	23.09

1.7 Steady state anisotropy measurement of the AR/SDS system with varying concentrations of SDS at 298K

[SDS]/mM	Anisotropy
0	0.0225
0.47809	0.022
0.95238	0.0196
1.42292	0.0218
1.88976	0.0228
2.35294	0.02067
2.8125	0.02367
3.26848	0.0265
4.16988	0.02567
5.05747	0.03367
5.93156	0.04083
6.79245	0.04967
7.64045	0.0655
8.47584	0.06867
9.29889	0.0716
10.10989	0.0692
10.90909	0.068
11.69675	0.07017
12.47312	0.0704

1.8 Steady state anisotropy measurement of AR/BMImOS system with varying concentrations of BMImOS at 298K

[BMImOS]/mM	Anisotropy
0	0.022
2.95858	0.01954
6.84932	0.02387
10.67961	0.02317
16.31478	0.02574
23.62949	0.02691
30.72626	0.02785
37.61468	0.02796
44.3038	0.03065
50.80214	0.04657
57.11775	0.06365
63.25823	0.0688
69.23077	0.07137
75.04216	0.07254
80.69884	0.0743
86.2069	0.07605
91.57212	0.08073
96.8	0.07722
101.8957	0.07617
106.8643	0.07769
111.7103	0.07675
116.4384	0.07886

Steady state anisotropy measurement of the AR/BMImBr system with varying concentrations of BMImBr at 298K

[BMImBr]/mM	Anisotropy
0	0.022
0.98	0.024
1.94	0.022
2.88	0.024
3.8	0.022
4.72	0.022
5.6	0.022
6.5	0.02
7.33	0.022
8.2	0.022
9	0.022
9.8	0.022
10.6	0.022
12.17	0.022
13.7	0.024

1.10 Hydrodynamic diameter data vs. Mean Intensity of AR/SDS system when [SDS] = 5.98 mM at 298K

Size d (nm)	Mean Intensity %	Size d (nm)	Mean Intensity %	Size d (nm)	Mean Intensity %	Size d (nm)	Mean Intensity %
0.4	0	5.615	0	78.82	0	1106	0
0.4632	0	6.503	0	91.28	0	1281	0
0.5365	0	7.531	0	105.7	0	1484	0
0.6213	0	8.721	0	122.4	0	1718	0
0.7195	0	10.1	0	141.8	0	1990	0
0.8332	0	11.7	0	164.2	0	2305	0
0.9649	0	13.54	0	190.1	0	2669	0
1.117	0	15.69	0	220.2	0	3091	0
1.294	0	18.17	0	255	0	3580	0
1.499	0	21.04	0	295.3	0	4145	0
1.736	0	24.36	0	342	0	4801	0
2.01	0	28.21	0	396.1	0	5560	0
2.328	0	32.67	0	458.7	0	6439	0
2.696	0	37.84	0	531.2	0	7456	0
3.122	0	43.82	15.9	615.1	0	8635	0
3.615	0	50.75	84.1	712.4	0	1.00E+04	0
4.187	0	58.77	0	825	0		
4.849	0	68.06	0	955.4	0		

1.11 Hydrodynamic diameter data vs. Mean Intensity of AR/SDS system when [SDS] = 10.17 mM at 298K

Size d (nm)	Mean Intensity %	Size d (nm)	Mean Intensity %	Size d (nm)	Mean Intensity %	Size d (nm)	Mean Intensity %
0.4	0	5.615	0	78.82	0	1106	0
0.4632	0	6.503	0	91.28	1.9	1281	0
0.5365	0	7.531	0	105.7	7.7	1484	0
0.6213	0	8.721	0	122.4	15.4	1718	0
0.7195	0	10.1	0	141.8	21.1	1990	0
0.8332	0	11.7	0	164.2	21.6	2305	0
0.9649	0	13.54	0	190.1	16.1	2669	0
1.117	0	15.69	0	220.2	7.3	3091	0
1.294	0	18.17	0	255	0.5	3580	0
1.499	0	21.04	0.5	295.3	0	4145	0
1.736	0	24.36	2.8	342	0	4801	0
2.01	0	28.21	3.4	396.1	0	5560	0
2.328	0	32.67	1.6	458.7	0	6439	0
2.696	0	37.84	0	531.2	0	7456	0
3.122	0	43.82	0	615.1	0	8635	0
3.615	0	50.75	0	712.4	0	1.00E+04	0
4.187	0	58.77	0	825	0		
4.849	0	68.06	0	955.4	0		

1.12 Hydrodynamic diameter data vs. Mean Intensity of AR/BMImOS system when [BMImOS] = 24.93 mM at 298 K

Size d (nm)	Mean Intensity %	Size d (nm)	Mean Intensity %	Size d (nm)	Mean Intensity %	Size d (nm)	Mean Intensity %
0.4	0	0.4	0	78.82	0	1106	0
0.4632	0	0.4632	0	91.28	0	1281	0
0.5365	0	0.5365	0	105.7	6.5	1484	0
0.6213	0	0.6213	0	122.4	19.4	1718	0
0.7195	0	0.7195	0	141.8	28.9	1990	0
0.8332	0	0.8332	0	164.2	27.2	2305	0
0.9649	0	0.9649	0	190.1	15.3	2669	0
1.117	0	1.117	0	220.2	2.8	3091	0
1.294	0	1.294	0	255	0	3580	0
1.499	0	1.499	0	295.3	0	4145	0
1.736	0	1.736	0	342	0	4801	0
2.01	0	2.01	0	396.1	0	5560	0
2.328	0	2.328	0	458.7	0	6439	0
2.696	0	2.696	0	531.2	0	7456	0
3.122	0	3.122	0	615.1	0	8635	0
3.615	0	3.615	0	712.4	0	1.00E+04	0
4.187	0	4.187	0	825	0		
4.849	0	4.849	0	955.4	0		

1.13 Hydrodynamic diameter data vs. Mean Intensity of AR/BMImOS system when [BMImOS] = 54.86 mM at 298K

Size d (nm)	Mean Intensity %	Size d (nm)	Mean Intensity %	Size d (nm)	Mean Intensity %	Size d (nm)	Mean Intensity %
0.4	0	5.615	0	78.82	0	1106	0
0.4632	0	6.503	0	91.28	0	1281	0
0.5365	0	7.531	0	105.7	0	1484	0
0.6213	0	8.721	0	122.4	0	1718	0
0.7195	0	10.1	0	141.8	0	1990	0
0.8332	0	11.7	0	164.2	0	2305	0
0.9649	0	13.54	0	190.1	0	2669	0
1.117	0	15.69	0	220.2	18	3091	0
1.294	0	18.17	0	255	38.9	3580	0
1.499	0	21.04	0	295.3	33.6	4145	0
1.736	0	24.36	0	342	9.5	4801	0
2.01	0	28.21	0	396.1	0	5560	0
2.328	0	32.67	0	458.7	0	6439	0
2.696	0	37.84	0	531.2	0	7456	0
3.122	0	43.82	0	615.1	0	8635	0
3.615	0	50.75	0	712.4	0	1.00E+04	0
4.187	0	58.77	0	825	0		
4.849	0	68.06	0	955.4	0		

1.14 Hydrodynamic diameter data vs. Mean Intensity of AR/BMImBr system when [BMImBr] = 4.98 mM at 298 K

Size d (nm)	Mean Intensity %	Size d (nm)	Mean Intensity %	Size d (nm)	Mean Intensity %	Size d (nm)	Mean Intensity %
0.4	0	5.615	0	78.82	0	1106	0
0.4632	0	6.503	0	91.28	0	1281	0
0.5365	0	7.531	0	105.7	0	1484	0
0.6213	0	8.721	0	122.4	0	1718	0
0.7195	0	10.1	0	141.8	0	1990	0
0.8332	0	11.7	0	164.2	0	2305	0
0.9649	0	13.54	0	190.1	0	2669	0
1.117	0	15.69	0	220.2	0	3091	0
1.294	0	18.17	0	255	0	3580	0
1.499	0	21.04	0	295.3	0	4145	0
1.736	0	24.36	0	342	0	4801	0
2.01	0	28.21	0	396.1	0	5560	0
2.328	0	32.67	100	458.7	0	6439	0
2.696	0	37.84	0	531.2	0	7456	0
3.122	0	43.82	0	615.1	0	8635	0
3.615	0	50.75	0	712.4	0	1.00E+04	0
4.187	0	58.77	0	825	0		
4.849	0	68.06	0	955.4	0		

1.15 Hydrodynamic diameter data vs. Mean Intensity of AR/BMImBr system when [BMImBr] = 10.97 mM at 298K

Size d (nm)	Mean Intensity %	Size d (nm)	Mean Intensity %	Size d (nm)	Mean Intensity %	Size d (nm)	Mean Intensity %
0.4	0	5.615	0	78.82	0	1106	0
0.4632	0	6.503	0	91.28	0	1281	0
0.5365	0	7.531	0	105.7	0	1484	0
0.6213	0	8.721	0	122.4	0	1718	0
0.7195	0	10.1	0	141.8	0	1990	0
0.8332	0	11.7	0	164.2	0	2305	0
0.9649	0	13.54	0	190.1	0	2669	0
1.117	0	15.69	0	220.2	0	3091	0
1.294	0	18.17	0	255	0	3580	0
1.499	0	21.04	0	295.3	0	4145	0
1.736	0	24.36	0	342	0	4801	0
2.01	0	28.21	0	396.1	0	5560	0
2.328	0	32.67	0	458.7	0	6439	0
2.696	0	37.84	0	531.2	0	7456	0
3.122	0	43.82	0	615.1	0	8635	0
3.615	0	50.75	0	712.4	0	1.00E+04	0
4.187	0	58.77	100	825	0		
4.849	0	68.06	0	955.4	0		

Aggregation number data of AR/SDS, AR/BMImOS, AR/BMImBr systems at 298K

[CPC] /mM	ln (I_0/I) AR/SDS System	ln (I_0/I) AR/BMImOS System	ln (I_0/I) AR/BMImBr System
0	0	0	0
0.04902	0.01511	0.01574	0.01569
0.09709	0.02191	0.02548	0.01409
0.14423	0.03483	0.03604	0.02641
0.19048	0.04181	0.04369	0.03331
0.23585	0.05271	0.05014	0.03546
0.28037	0.05806	0.05735	0.04226
0.32407	0.0713	0.06267	0.04884
0.36697	0.07857	0.07247	0.0557
0.40909	0.08578	0.07976	0.06438
0.45045	0.08908	0.0837 0.09311	0.0673 0.07391

Chapter II

2.1 Specific conductivity (k) data of C_{12}DmCB and EY/C_{12}DmCB at different concentrations of C_{12}DmCB at 298K

[C_{12}DmCB] /mM	k of C_{12}DmCB without EY	k of C_{12}DmCB with EY
0	2.5	4.9
0.0892	9.9	12.2
0.17781	18.3	20.2
0.26584	26.5	28.7
0.35329	35.1	36.4
0.44016	43	45.1
0.52647	52.1	53.2
0.61221	60.2	61.6
0.6974	68.2	70
0.78204	76.6	77
0.86613	85.1	85.2
0.94968	92.7	92.8
1.03269	101	101
1.11518	109.4	108.5
1.19713	116.7	114.1
1.27857	124.1	121
1.35949	131.5	126.5
1.43991	138.1	132.9
1.51981	145.4	138.3
1.59922	150.8	142.7
1.67813	156.6	146.3
1.75654	163.7	150
1.83447	167.6	153.8
1.91192	171.3	157.2
1.98889	175.2	160.8
2.06538	179.4	164.3
2.14141	182.4	167.1
2.21697	185	171.1
2.29207	188	175.2
2.36672	191	179
2.44091	194	182.9
2.58795	197	184.1
2.73323	207	192
2.87679	210	199
3.01864	217	208
3.15882	223	213
3.29737	230	222

2.2 Specific conductivity (k) of CTAC and EY/CTAC at different concentrations of CTAC at 298K

[CTAC] /mM	k of CTAC without EY	k of CTAC with EY
0	2	3.5
0.04983	6.5	7.1
0.09934	10.5	11.7
0.14851	15	16.2
0.19737	19.3	21
0.2459	23.6	25.8
0.29412	28.1	30.7
0.34202	32.6	35.6
0.38961	37.1	40.3
0.43689	41.4	44.9
0.48387	45.8	49.7
0.53055	50.3	54.7
0.57692	54.7	59.1
0.623	58.7	63.9
0.66879	63.2	68.5
0.71429	67.6	72.2
0.75949	71.8	76.2
0.80442	75.8	80.4
0.84906	80.1	84
0.89342	82.9	87.7
0.9375	86.2	92.6
0.98131	89.1	96.1
1.02484	92.7	99.8
1.06811	95.7	103.2
1.11111	99.6	105.5
1.15385	102.9	108
1.19632	105.7	110
1.23853	107.6	112.5
1.28049	109.9	115.1
1.32219	112.3	117.8
1.36364	115.7	119.6
1.44578	120.7	124.5
1.52695	125.1	129.1
1.60714	130.1	132.8
1.68639	134	135.5
1.76471	134.8	140.2

2.3 Specific conductivity (k) of SLAS and EY/SLAS at different concentrations of SLAS at 298K

[SLAS]/ mM	k of SLAS without EY	k of SLAS with EY
0	3	4.6
0.49834	32.4	32.7
0.99338	62.2	64.2
1.48515	91	90
1.97368	119.8	120.8
2.45902	147.8	150.5
2.94118	173.7	180.2
3.4202	201	207
3.8961	227	236
4.36893	252	261
4.83871	280	288
5.30547	306	315
5.76923	330	341
6.23003	357	368
6.6879	379	397
7.14286	405	422
7.59494	431	447
8.04416	457	472
8.49057	479	497
8.93417	500	524
9.375	526	546
9.81308	546	571
10.24845	564	596
10.68111	583	618
11.11111	602	638
11.53846	618	662
11.96319	636	679
12.38532	658	700
12.80488	678	721
13.22188	697	738
13.63636	716	756
14.45783	750	792
15.26946	783	822
16.07143	812	853
16.86391	840	875
17.64706	870	904

2.4 Specific conductivity (k) of NaDC and EY/NaDC at different concentrations of NaDC at 298K

[NaDC]/ mM	k of NaDC without EY	k of NaDC with EY
0	2.5	3.5
0.19934	13.4	14.8
0.39735	23.7	25.9
0.59406	34.7	37.2
0.78947	45.5	49
0.98361	57.6	59.8
1.17647	68.3	70.5
1.36808	79.5	81
1.55844	90.5	91
1.74757	100.8	102.2
1.93548	111.9	113.2
2.12219	121.6	123.7
2.30769	132.8	133.5
2.49201	144.1	143.9
2.67516	152.3	153.4
2.85714	162.9	164
3.03797	174.5	174
3.21767	183.2	185.2
3.39623	192.2	196.1
3.57367	198	207
3.75	205	218
3.92523	213	226
4.09938	220	233
4.27245	228	240
4.44444	235	247
4.61538	243	254
4.78528	250	260
4.95413	254	267
5.12195	260	274
5.28875	270	280
5.45455	274	288
5.78313	294	301
6.10778	304	314
6.42857	320	330
6.74556	333	346
7.05882	350	360

2.5 Absorbance vs [C_{12}DmCB]/mM Obtained from the UV absorption spectra of EY/C_{12}DmCB system at 298K

[C_{12}DmCB]/mM	Absorbance
0	0.202
0.264	0.211
0.523	0.207
0.78	0.183
1.03	0.14
1.27	0.116
1.51	0.101
1.75	0.097
1.98	0.101
2.43	0.112
2.86	0.121
3.28	0.132
3.68	0.135
4.08	0.133

2.6 Absorbance vs [CTAC]/mM Obtained from the UV absorption spectra of EY/CTAC system at 298K

[CTAC]/mM	Absorbance
0	0.044
0.15	0.159
0.29	0.182
0.43	0.191
0.57	0.204
0.71	0.215
0.85	0.223
0.98	0.232
1.1	0.239
1.35	0.254
1.6	0.269
1.83	0.283
2.06	0.29
2.28	0.297
2.49	0.299
2.69	0.296
2.89	0.289

2.7 Absorbance vs [SLAS]/mM Obtained from the UV absorption spectra of EY/SLAS system at 298K

[SLAS]/mM	Absorbance
0	0.025
1.48	0.162
2.93	0.198
4.34	0.234
5.74	0.279
7.1	0.347
8.45	0.365
9.76	0.381
11.05	0.39
13.57	0.404
16	0.418
18.34	0.431
20.6	0.435
22.78	0.437

2.8 Absorbance vs [NaDC]/mM Obtained from the UV absorption spectra of EY/NaDC system at 298K

[NaDC]/mM	Absorbance
0	0.11
0.59	0.156
1.17	0.164
1.74	0.171
2.3	0.174
2.84	0.177
3.38	0.179
3.9	0.182
4.42	0.189
5.43	0.189
6.4	0.197
7.33	0.207
8.24	0.215
9.11	0.221
9.96	0.231

2.9 Variation of Fluorescence Intensity with varying concentrations of $C_{12}DmCB$ of the EY/$C_{12}DmCB$ system at 298K

[$C_{12}DmCB$]/mM	F.I.
0	686.62
0.26	689.3
0.523	622.19
0.78	521.44
1.03	338.72
1.27	173.47
1.51	86.16
1.75	47.93
1.98	31.8
2.43	25.31
2.86	28.9
3.28	54.94
3.68	140.5
4.08	174.34
4.45	193.52
4.82	203.79
5.18	209.4
5.52	211.45

2.10 Variation of Fluorescence Intensity with varying concentrations of CTAC of the EY/CTAC system at 298K

[CTAC]/mM	F.I.
0	424.39
0.15	15.29
0.29	24.11
0.43	34.07
0.57	49.06
0.71	65.26
0.85	84.33
0.98	107.82
1.1	141.14
1.35	264.67
1.6	518.2
1.83	611.22
2.06	670.77
2.28	724.63
2.49	739.53
2.69	749.53
2.89	753.49

2.11Variation of Fluorescence Intensity with varying concentrations of SLAS of the EY/SLAS system at 298K

[SLAS]/mM	F.I.
0	391.925
1.48	601.275
2.93	728.225
4.34	774.1
5.74	813.35
7.1	834.125
8.45	856.1
9.76	865.25
11.05	869.825
13.57	864.9
16	862.2
18.34	851.75
20.6	842.9
22.78	833.6

2.12 Variation of Fluorescence Intensity with varying concentrations of NaDC of the EY/NaDC system at 298K

[NaDC]/mM	F.I.
0	609.09
0.59	667.03
1.17	670.8
1.74	670.77
2.3	666.16
2.84	666.39
3.38	663.26
3.9	661.07
4.42	660.18
5.43	654.6
6.4	647.58
7.33	642.08
8.24	637.1
9.11	633.52
9.96	630.06
10.78	630.3

2.13 Steady state anisotropy measurement of the EY/C_{12}DmCB system with varying concentrations of C_{12}DmCB at 298K

[C_{12}DmCB]/mM	Anisotropy
0	0.035
0.26	0.037
0.52	0.05
0.78	0.038
1.03	0.037
1.27	0.036
1.51	0.034
1.75	0.033
1.98	0.032
2.43	0.025
2.86	0.027
3.28	0.045
3.68	0.076
4.08	0.095
4.45	0.105
4.82	0.112
5.18	0.115
5.52	0.12

2.14 Steady state anisotropy measurement of the EY/CTAC system with varying concentrations of CTAC at 298K

[CTAC]/mM	Anisotropy
0	0.035
0.14778	0.017
0.29268	0.012
0.43478	0.008
0.57416	0.005
0.7109	0.01
0.84507	0.012
0.97674	0.012
1.10599	0.011
1.35747	0.033
1.6	0.053
1.83406	0.073
2.06009	0.082
2.27848	0.091
2.48963	0.095
2.69388	0.102
2.89157	0.103
3.083	0.104

2.15 Steady state anisotropy measurement of the EY/SLAS system with varying concentrations of SLAS at 298K

[SLAS]/mM	Anisotropy
0	0.026
1.47783	0.026
2.92683	0.027
4.34783	0.027
5.74163	0.028
7.109	0.028
8.4507	0.028
9.76744	0.028
11.05991	0.029
13.57466	0.029
16	0.03
18.34061	0.03
20.60086	0.03
22.78481	0.03
24.89627	0.03
26.93878	0.03
28.91566	0.031
30.83004	0.03

2.16 Steady state anisotropy measurement of the EY/NaDC system with varying concentrations of NaDC

[NaDC]/mM	Anisotropy
0	0.035
0.59113	0.036
1.17073	0.039
1.73913	0.04
2.29665	0.04
2.8436	0.039
3.38028	0.039
3.90698	0.039
4.42396	0.04
5.42986	0.041
6.4	0.042
7.33624	0.043
8.24034	0.044
9.11392	0.044
9.95851	0.045
10.77551	0.046
11.56627	0.046
12.33202	0.047

2.17 Hydrodynamic diameter data vs. Mean Intensity of EY/H_2O system

Size d.nm	Mean Intensity %	Size d.nm	Mean Intensity %	Size d.nm	Mean Intensity %	Size d.nm	Mean Intensity %
0.4	0	5.615	0	78.82	0	1106	0
0.4632	0	6.503	0	91.28	0.8	1281	0
0.5365	0	7.531	0.9	105.7	14.5	1484	0
0.6213	0	8.721	4.4	122.4	28.3	1718	0
0.7195	0	10.1	5.9	141.8	28.2	1990	0
0.8332	0	11.7	3.3	164.2	13.8	2305	0
0.9649	0	13.54	0	190.1	0	2669	0
1.117	0	15.69	0	220.2	0	3091	0
1.294	0	18.17	0	255	0	3580	0
1.499	0	21.04	0	295.3	0	4145	0
1.736	0	24.36	0	342	0	4801	0
2.01	0	28.21	0	396.1	0	5560	0
2.328	0	32.67	0	458.7	0	6439	0
2.696	0	37.84	0	531.2	0	7456	0
3.122	0	43.82	0	615.1	0	8635	0
3.615	0	50.75	0	712.4	0	1.00E+04	0
4.187	0	58.77	0	825	0		
4.849	0	68.06	0	955.4	0		

2.18 Hydrodynamic diameter data vs. Mean Intensity of EY/C_{12}DmCB system when [C_{12}DmCB] = 0.78 mM

Size d.nm	Mean Intensity %	Size d.nm	Mean Intensity %	Size d.nm	Mean Intensity %	Size d.nm	Mean Intensity %
0.4	0	5.615	4.5	78.82	0	1106	0
0.4632	0	6.503	0.9	91.28	0	1281	0
0.5365	0	7.531	0	105.7	0	1484	0
0.6213	0	8.721	0	122.4	0	1718	0
0.7195	0	10.1	0	141.8	0	1990	0
0.8332	0	11.7	0	164.2	0	2305	0
0.9649	0	13.54	0	190.1	0	2669	0
1.117	0	15.69	0	220.2	0	3091	0
1.294	0	18.17	0	255	0	3580	0
1.499	0	21.04	0	295.3	0	4145	0
1.736	0	24.36	0	342	12.4	4801	0
2.01	0	28.21	0	396.1	33.9	5560	0
2.328	0	32.67	0	458.7	35	6439	0
2.696	0	37.84	0	531.2	13.4	7456	0
3.122	0	43.82	0	615.1	0	8635	0
3.615	0	50.75	0	712.4	0	1.00E+04	0
4.187	0	58.77	0	825	0		
4.849	0	68.06	0	955.4	0		

2.19 Hydrodynamic diameter data vs. Mean Intensity of EY/C_{12}DmCB system when [C_{12}DmCB] = 3.68 mM

Size d.nm	Mean Intensity %	Size d.nm	Mean Intensity %	Size d.nm	Mean Intensity %	Size d.nm	Mean Intensity %
0.4	0	5.615	0	78.82	0	1106	0
0.4632	0	6.503	4.7	91.28	0	1281	0
0.5365	0	7.531	24.6	105.7	0	1484	0
0.6213	0	8.721	0.9	122.4	0	1718	0
0.7195	0	10.1	0	141.8	0	1990	0
0.8332	0	11.7	0	164.2	0	2305	0
0.9649	0	13.54	0	190.1	0	2669	0
1.117	0	15.69	0	220.2	0	3091	0
1.294	0	18.17	0	255	0	3580	0
1.499	0	21.04	0	295.3	7.7	4145	0
1.736	0	24.36	0	342	35.7	4801	0
2.01	0	28.21	0	396.1	26.4	5560	0
2.328	0	32.67	0	458.7	0	6439	0
2.696	0	37.84	0	531.2	0	7456	0
3.122	0	43.82	0	615.1	0	8635	0
3.615	0	50.75	0	712.4	0	1.00E+04	0
4.187	0	58.77	0	825	0		
4.849	0	68.06	0	955.4	0		

2.20 Hydrodynamic diameter data vs. Mean Intensity of EY/CTAC system when [CTAC] = 0.43 mM

Size d.nm	Mean Intensity %	Size d.nm	Mean Intensity %	Size d.nm	Mean Intensity %	Size d.nm	Mean Intensity %
0.4	0	5.615	0	78.82	0	1106	0
0.4632	0	6.503	0	91.28	0	1281	0
0.5365	0	7.531	0	105.7	0	1484	0
0.6213	0	8.721	0	122.4	0	1718	0
0.7195	0	10.1	0	141.8	0	1990	0
0.8332	0	11.7	0	164.2	0	2305	0
0.9649	0	13.54	0	190.1	0	2669	0
1.117	0	15.69	0	220.2	0	3091	0
1.294	0	18.17	0	255	13.9	3580	0
1.499	0	21.04	0	295.3	32.1	4145	0
1.736	0	24.36	0	342	35	4801	0
2.01	0	28.21	0	396.1	18.7	5560	0
2.328	0	32.67	0	458.7	0.3	6439	0
2.696	0	37.84	0	531.2	0	7456	0
3.122	0	43.82	0	615.1	0	8635	0
3.615	0	50.75	0	712.4	0	1.00E+04	0
4.187	0	58.77	0	825	0		
4.849	0	68.06	0	955.4	0		

2.21 Hydrodynamic diameter data vs. Mean Intensity of EY/CTAC system when [CTAC] = 2.06 mM

Size d.nm	Mean Intensity %	Size d.nm	Mean Intensity %	Size d.nm	Mean Intensity %	Size d.nm	Mean Intensity %
0.4	0	5.615	0	78.82	0	1106	0
0.4632	0	6.503	0	91.28	0	1281	0
0.5365	0	7.531	0	105.7	0	1484	0
0.6213	0	8.721	0	122.4	0	1718	0
0.7195	0	10.1	0	141.8	10.9	1990	0
0.8332	0	11.7	0	164.2	26.6	2305	0
0.9649	0	13.54	0	190.1	29.9	2669	0
1.117	0	15.69	0	220.2	16	3091	0
1.294	0	18.17	0	255	0	3580	0
1.499	0	21.04	0	295.3	0	4145	0
1.736	0	24.36	1.2	342	0	4801	0
2.01	0	28.21	8	396.1	0	5560	0
2.328	0	32.67	7.1	458.7	0	6439	0
2.696	0	37.84	0.3	531.2	0	7456	0
3.122	0	43.82	0	615.1	0	8635	0
3.615	0	50.75	0	712.4	0	1.00E+04	0
4.187	0	58.77	0	825	0		
4.849	0	68.06	0	955.4	0		

2.22 Hydrodynamic diameter data vs. Mean Intensity of EY/SLAS system when [SLAS] =4.34 mM

Size d.nm	Mean Intensity %	Size d.nm	Mean Intensity %	Size d.nm	Mean Intensity %	Size d.nm	Mean Intensity %
0.4	0	5.615	0	78.82	0	1106	0
0.4632	0	6.503	0	91.28	0	1281	0
0.5365	0	7.531	0	105.7	0	1484	0
0.6213	0	8.721	0	122.4	0	1718	0
0.7195	0	10.1	0	141.8	0	1990	0
0.8332	0	11.7	0	164.2	0	2305	0
0.9649	0	13.54	0	190.1	0	2669	0
1.117	0	15.69	0	220.2	0	3091	0
1.294	0	18.17	0	255	6.8	3580	0
1.499	0	21.04	0	295.3	23.6	4145	0
1.736	0	24.36	0	342	33.1	4801	0
2.01	0	28.21	0	396.1	26.3	5560	0
2.328	0	32.67	0	458.7	10.3	6439	0
2.696	0	37.84	0	531.2	0	7456	0
3.122	0	43.82	0	615.1	0	8635	0
3.615	0	50.75	0	712.4	0	1.00E+04	0
4.187	0	58.77	0	825	0		
4.849	0	68.06	0	955.4	0		

2.23 Hydrodynamic diameter data vs. Mean Intensity of EY/SLAS system when [SLAS] = 20.6 mM

Size d.nm	Mean Intensity %	Size d.nm	Mean Intensity %	Size d.nm	Mean Intensity %	Size d.nm	Mean Intensity %
0.4	0	5.615	0	78.82	0	1106	5.5
0.4632	0	6.503	0	91.28	0	1281	0
0.5365	0	7.531	0	105.7	0	1484	0
0.6213	0	8.721	0	122.4	0	1718	0
0.7195	0	10.1	0	141.8	0	1990	0
0.8332	0	11.7	0	164.2	0	2305	0
0.9649	0	13.54	0	190.1	0	2669	0
1.117	0	15.69	0	220.2	0	3091	0
1.294	0	18.17	0	255	0	3580	0
1.499	0	21.04	0	295.3	0	4145	0
1.736	0	24.36	0	342	0	4801	0
2.01	0	28.21	0	396.1	0	5560	0
2.328	0	32.67	0	458.7	1.3	6439	0
2.696	0	37.84	0	531.2	9.6	7456	0
3.122	0	43.82	0	615.1	19.9	8635	0
3.615	0	50.75	0	712.4	25.4	1.00E+04	0
4.187	0	58.77	0	825	23.3		
4.849	0	68.06	0	955.4	15		

2.24 Hydrodynamic diameter data vs. Mean Intensity of EY/NaDC system when [NaDC] = 1.74mM

Size d.nm	Mean Intensity %	Size d.nm	Mean Intensity %	Size d.nm	Mean Intensity %	Size d.nm	Mean Intensity %
0.4	0	5.615	0	78.82	0	1106	0
0.4632	0	6.503	0	91.28	0	1281	0
0.5365	0	7.531	0	105.7	0	1484	0
0.6213	0	8.721	0	122.4	0	1718	0
0.7195	0	10.1	0	141.8	0	1990	0
0.8332	0	11.7	0	164.2	0	2305	0
0.9649	0	13.54	0	190.1	0	2669	0
1.117	0	15.69	0	220.2	0	3091	0
1.294	0	18.17	0	255	0	3580	0
1.499	0	21.04	0	295.3	0	4145	0
1.736	0	24.36	0	342	0	4801	0
2.01	0	28.21	0	396.1	0	5560	0
2.328	0	32.67	0	458.7	0	6439	0
2.696	0	37.84	0	531.2	0	7456	0
3.122	0	43.82	0	615.1	66.1	8635	0
3.615	0	50.75	0	712.4	33.9	1.00E+04	0
4.187	0	58.77	0	825	0		
4.849	0	68.06	0	955.4	0		

2.25 Hydrodynamic diameter data vs. Mean Intensity of EY/NaDC system when [NaDC] = 8.24 mM

Size d.nm	Mean Intensity %	Size d.nm	Mean Intensity %	Size d.nm	Mean Intensity %	Size d.nm	Mean Intensity %
0.4	0	5.615	0	78.82	0	1106	1.5
0.4632	0	6.503	0	91.28	0	1281	2.1
0.5365	0	7.531	0	105.7	0	1484	3.4
0.6213	0	8.721	0	122.4	0	1718	4.8
0.7195	0	10.1	0	141.8	0	1990	5.7
0.8332	0	11.7	0	164.2	0	2305	5.7
0.9649	0	13.54	0	190.1	0	2669	5
1.117	0	15.69	0	220.2	0	3091	3.9
1.294	0	18.17	0	255	0	3580	2.7
1.499	0	21.04	0	295.3	0	4145	1.9
1.736	0	24.36	0	342	2.9	4801	1.7
2.01	0	28.21	0	396.1	7.7	5560	2.1
2.328	0	32.67	0	458.7	11.4	6439	0
2.696	0	37.84	0	531.2	12.4	7456	0
3.122	0	43.82	0	615.1	10.8	8635	0
3.615	0	50.75	0	712.4	7.6	1.00E+04	0
4.187	0	58.77	0	825	4.4		
4.849	0	68.06	0	955.4	2.2		

Chapter III

3.1 Absorbance vs [C_{12}DmCB]/mM obtained from UV absorption spectra of PhB/C_{12}DmCB system at 298K

[C12DmCB]/mM	Absorbance
0	0.175
0.265	0.164
0.525	0.09
0.78	0.076
1.03	0.072
1.27	0.071
1.51	0.07
1.75	0.0688
1.98	0.0685
2.43	0.071
2.87	0.073
3.29	0.074
3.69	0.077
4.08	0.078
4.46	0.078
4.83	0.078
5.18	0.079

3.2 Absorbance vs [CTAB]/mM obtained from the UV absorption spectra of PhB/CTAB system at 298K

[CTAB]/mM	Absorbance
0	0.1788
0.15	0.09297
0.29	0.0912
0.43	0.08972
0.57	0.08852
0.71	0.08774
0.85	0.08595
0.98	0.08499
1.1	0.08478
1.36	0.08417
1.6	0.08298
1.83	0.08247
2.06	0.08163
2.28	0.08234
2.49	0.08174

Absorbance vs [SDS]/mM obtained from the UV absorption spectra of PhB/SDS system at 298K

[SDS]/mM	Absorbance
0	0.20085
1.22	0.23778
2.43	0.24704
3.61	0.24669
4.77	0.24535
5.91	0.24527
7.03	0.24358
8.12	0.23991
9.2	0.23518
11.29	0.22881
13.3	0.22418
15.25	0.2198
17.13	0.21674
18.95	0.2155

3.4 Variation of Fluorescence Intensity with varying concentrations of C_{12}DmCB of PhB/ C_{12}DmCB system at 298K

[C_{12}DmCB]/mM	F.I.
0	265.96
0.265	231.72
0.525	160.55
0.78	64.56
1.03	27.03
1.27	21.08
1.51	25.4
1.75	33.69
1.98	41.72
2.43	62.01
2.87	115.33
3.29	147.49
3.69	156.71
4.08	166.68
4.46	169.98
4.83	172.14

3.5 Variation of Fluorescence Intensity with varying concentrations of CTAC of the PhB/ CTAC system at 298K

[CTAC]/mM	F.I.
0	295.91
0.15	6.9
0.29	16.57
0.43	23.85
0.57	32.43
0.71	39.35
0.85	46.72
0.98	55.44
1.1	62.56
1.36	69.92
1.6	81.26
1.83	95.17
2.06	101.04
2.28	102.06
2.49	103.59
2.7	104.81

3.6 Variation of Fluorescence Intensity with varying concentrations of SDS of the PhB/ SDS system at 298K

[SDS]/mM	F.I.
0	348.83
1.22	284.18
2.43	288.45
3.61	289.62
4.77	288.69
5.91	286.48
7.03	285.48
8.12	284.17
9.2	282.87
11.29	279.71
13.3	276.7
15.25	273.96
17.13	270.63
18.95	268.79
20.7	265.23

3.7 Steady state anisotropy measurement of the PhB/C_{12}DmCB system with varying concentrations of C_{12}DmCB

at 298K

[C_{12}DmCB]/mM	Anisotropy
0	0.04
0.265	0.053
0.525	0.061
0.78	0.049
1.03	0.039
1.27	0.032
1.51	0.026
1.75	0.025
1.98	0.023
2.43	0.028
2.87	0.08
3.29	0.112
3.69	0.129
4.08	0.134
4.46	0.137
4.83	0.139
5.18	0.14

3.8 Steady state anisotropy measurement of the PhB/CTAB system with varying concentrations of CTAB

at 298K

[CTAC]/mM	Anisotropy
0	0.035
0.15	0.005
0.29	0.012
0.43	0.017
0.57	0.017
0.71	0.018
0.85	0.019
0.98	0.023
1.1	0.025
1.36	0.032
1.6	0.04
1.83	0.047
2.06	0.053
2.28	0.054
2.49	0.057
2.7	0.067
2.9	0.07

3.9 Steady state anisotropy measurement of the PhB/SDS system with varying concentrations of SDS

at 298K

[SDS]/mM	Anisotropy
0	0.038
1.22	0.039
2.43	0.039
3.61	0.04
4.77	0.043
5.91	0.04
7.03	0.04
8.12	0.042
9.2	0.042
11.29	0.042
13.3	0.045
15.25	0.049
17.13	0.05
18.95	0.05
20.7	0.052
22.4	0.053

3.10 Hydrodynamic diameter data vs. Mean Intensity of PhB/H_2O system at 298K

Size d.nm	Mean Intensity %	Size d.nm	Mean Intensity %	Size d.nm	Mean Intensity %	Size d.nm	Mean Intensity %
0.4	0	5.615	0	78.82	0	1106	0
0.4632	0	6.503	0	91.28	0	1281	0
0.5365	0	7.531	0	105.7	0	1484	0
0.6213	0	8.721	0	122.4	0	1718	0
0.7195	0	10.1	0	141.8	0	1990	0
0.8332	0	11.7	0	164.2	0	2305	0
0.9649	0	13.54	0	190.1	0	2669	0
1.117	0	15.69	0	220.2	0	3091	0
1.294	0	18.17	0	255	0	3580	0
1.499	0	21.04	0	295.3	0	4145	0
1.736	0	24.36	0	342	1.6	4801	0
2.01	0	28.21	0	396.1	10.9	5560	0
2.328	0	32.67	0	458.7	21.9	6439	0
2.696	0	37.84	0	531.2	26.5	7456	0
3.122	0	43.82	0.8	615.1	21.2	8635	0
3.615	0	50.75	2.4	712.4	9.8	1.00E+04	0
4.187	0	58.77	2.7	825	0.8		
4.849	0	68.06	1.3	955.4	0		

3.11Hydrodynamic diameter data vs. Mean Intensity of PhB/C_{12}DmCB system when [C_{12}DmCB] = 0.78mM at 298K

Size d.nm	Mean Intensity %	Size d.nm	Mean Intensity %	Size d.nm	Mean Intensity %	Size d.nm	Mean Intensity %
0.4	0	5.615	0	78.82	0	1106	0
0.4632	0	6.503	0	91.28	0	1281	0
0.5365	0	7.531	0	105.7	0	1484	0
0.6213	0	8.721	0	122.4	0	1718	0
0.7195	0	10.1	0	141.8	0	1990	0
0.8332	0	11.7	0	164.2	3.7	2305	0
0.9649	0	13.54	0	190.1	6.4	2669	0
1.117	0	15.69	0	220.2	3.7	3091	0
1.294	0	18.17	0	255	0	3580	0
1.499	0	21.04	0	295.3	0	4145	0
1.736	0	24.36	0	342	0	4801	0
2.01	0	28.21	0	396.1	1.2	5560	0
2.328	0	32.67	0	458.7	14.7	6439	0
2.696	0	37.84	0	531.2	28.9	7456	0
3.122	0	43.82	0	615.1	28.6	8635	0
3.615	0	50.75	0	712.4	12.9	1.00E+04	0
4.187	0	58.77	0	825	0		
4.849	0	68.06	0	955.4	0		

3.12 Hydrodynamic diameter data vs. Mean Intensity of PhB/C_{12}DmCB system when [C_{12}DmCB] = 3.69 mM at 298K

Size d.nm	Mean Intensity %	Size d.nm	Mean Intensity %	Size d.nm	Mean Intensity %	Size d.nm	Mean Intensity %
0.4	0	5.615	0	78.82	0	1106	0
0.4632	0	6.503	0	91.28	0	1281	0
0.5365	0	7.531	0	105.7	0	1484	0
0.6213	0	8.721	0	122.4	0	1718	0
0.7195	0	10.1	0	141.8	0	1990	0
0.8332	0	11.7	0	164.2	0	2305	0
0.9649	0	13.54	0	190.1	14.8	2669	0
1.117	0	15.69	0	220.2	53.8	3091	0
1.294	0	18.17	0	255	31.4	3580	0
1.499	0	21.04	0	295.3	0	4145	0
1.736	0	24.36	0	342	0	4801	0
2.01	0	28.21	0	396.1	0	5560	0
2.328	0	32.67	0	458.7	0	6439	0
2.696	0	37.84	0	531.2	0	7456	0
3.122	0	43.82	0	615.1	0	8635	0
3.615	0	50.75	0	712.4	0	1.00E+04	0
4.187	0	58.77	0	825	0		
4.849	0	68.06	0	955.4	0		

3.13 Hydrodynamic diameter data vs. Mean Intensity of PhB/CTAC system when [CTAC] =0.43 mM at 298K

Size d.nm	Mean Intensity %	Size d.nm	Mean Intensity %	Size d.nm	Mean Intensity %	Size d.nm	Mean Intensity %
0.4	0	5.615	0	78.82	0	1106	0
0.4632	0	6.503	0	91.28	0	1281	0
0.5365	0	7.531	0	105.7	0	1484	0
0.6213	0	8.721	0	122.4	0	1718	0
0.7195	0	10.1	0	141.8	0	1990	0
0.8332	0	11.7	0	164.2	35.3	2305	0
0.9649	0	13.54	0	190.1	64.7	2669	0
1.117	0	15.69	0	220.2	0	3091	0
1.294	0	18.17	0	255	0	3580	0
1.499	0	21.04	0	295.3	0	4145	0
1.736	0	24.36	0	342	0	4801	0
2.01	0	28.21	0	396.1	0	5560	0
2.328	0	32.67	0	458.7	0	6439	0
2.696	0	37.84	0	531.2	0	7456	0
3.122	0	43.82	0	615.1	0	8635	0
3.615	0	50.75	0	712.4	0	1.00E+04	0
4.187	0	58.77	0	825	0		
4.849	0	68.06	0	955.4	0		

3.14 Hydrodynamic diameter data vs. Mean Intensity of PhB/CTAC system when [CTAC] =2.06 mM at 298K

Size d.nm	Mean Intensity %	Size d.nm	Mean Intensity %	Size d.nm	Mean Intensity %	Size d.nm	Mean Intensity %
0.4	0	5.615	0	78.82	0	1106	0
0.4632	0	6.503	0	91.28	0	1281	0
0.5365	0	7.531	0	105.7	0	1484	0
0.6213	0	8.721	0	122.4	0	1718	0
0.7195	0	10.1	0	141.8	0	1990	0
0.8332	0	11.7	0	164.2	0	2305	0
0.9649	0	13.54	0	190.1	100	2669	0
1.117	0	15.69	0	220.2	0	3091	0
1.294	0	18.17	0	255	0	3580	0
1.499	0	21.04	0	295.3	0	4145	0
1.736	0	24.36	0	342	0	4801	0
2.01	0	28.21	0	396.1	0	5560	0
2.328	0	32.67	0	458.7	0	6439	0
2.696	0	37.84	0	531.2	0	7456	0
3.122	0	43.82	0	615.1	0	8635	0
3.615	0	50.75	0	712.4	0	1.00E+04	0
4.187	0	58.77	0	825	0		
4.849	0	68.06	0	955.4	0		

3.15 Hydrodynamic diameter data vs. Mean Intensity of PhB/SDS system when [SDS] =3.61 mM at 298K

Size d.nm	Mean Intensity %	Size d.nm	Mean Intensity %	Size d.nm	Mean Intensity %	Size d.nm	Mean Intensity %
0.4	0	5.615	0	78.82	0	1106	0
0.4632	0	6.503	0	91.28	0	1281	0
0.5365	0	7.531	0	105.7	0	1484	0
0.6213	0	8.721	0	122.4	0	1718	0
0.7195	0	10.1	0	141.8	0	1990	0
0.8332	0	11.7	0	164.2	0	2305	0
0.9649	0	13.54	0	190.1	0	2669	0
1.117	0	15.69	0	220.2	26.2	3091	0
1.294	0	18.17	0	255	45.9	3580	0
1.499	0	21.04	0	295.3	27.9	4145	0
1.736	0	24.36	0	342	0	4801	0
2.01	0	28.21	0	396.1	0	5560	0
2.328	0	32.67	0	458.7	0	6439	0
2.696	0	37.84	0	531.2	0	7456	0
3.122	0	43.82	0	615.1	0	8635	0
3.615	0	50.75	0	712.4	0	1.00E+04	0
4.187	0	58.77	0	825	0		
4.849	0	68.06	0	955.4	0		

3.16 Hydrodynamic diameter data vs. Mean Intensity of PhB/SDS system when [SDS] =17.13 mM at 298K

Size d.nm	Mean Intensity %	Size d.nm	Mean Intensity %	Size d.nm	Mean Intensity %	Size d.nm	Mean Intensity %
0.4	0	5.615	0	78.82	0	1106	0
0.4632	0	6.503	0	91.28	0	1281	0
0.5365	0	7.531	0	105.7	0	1484	0
0.6213	0	8.721	0	122.4	0	1718	0
0.7195	0	10.1	0	141.8	0	1990	0
0.8332	0	11.7	0	164.2	0	2305	0
0.9649	0	13.54	0	190.1	0	2669	0
1.117	0	15.69	0	220.2	0.5	3091	0
1.294	0	18.17	0	255	6.3	3580	0
1.499	0	21.04	0	295.3	14.8	4145	0
1.736	0	24.36	0	342	21.5	4801	0
2.01	0	28.21	0	396.1	23	5560	0
2.328	0	32.67	0	458.7	18.8	6439	0
2.696	0	37.84	0	531.2	11.2	7456	0
3.122	0	43.82	0	615.1	3.8	8635	0
3.615	0	50.75	0	712.4	0	1.00E+04	0
4.187	0	58.77	0	825	0		
4.849	0	68.06	0	955.4	0		

Chapter IV

4.1 Specific conductivity (k) of BMImOS and MB/BMImOS at different concentrations of BMImOS at 298K

[BMImOS]/mM	K of pure BMImOS	K of MB/BMImOS
0	4	4.2
0.83195	48.1	46.8
1.66113	102.1	88.6
2.48756	143.2	130.2
3.31126	177	170.9
4.13223	225	212
4.9505	269	254
5.76606	306	294
6.57895	348	335
7.38916	388	380
8.19672	423	421
9.80392	495	490
11.40065	560	555
12.98701	638	620
14.56311	715	700
16.12903	783	775
17.68489	843	840
19.23077	910	905
20.76677	973	970
22.29299	1033	1035
23.80952	1083	1100
25.31646	1137	1165
26.81388	1195	1215
28.30189	1267	1280
29.78056	1335	1340
31.25	1410	1403
32.71028	1480	1468
34.16149	1550	1518
35.60372	1612	1548
37.03704	1669	1578
38.46154	1734	1608
39.8773	1799	1638
41.2844	1865	1668
42.68293	1926	1701
44.07295	1955	1734
45.45455	1993	1765
46.82779	2050	1795
48.19277	2080	1823

Specific conductivity (k) of BMImOS and MB/BMImOS at different concentrations of BMImOS at 298K

4.2

[BMImOS]/mM	K of pure BMImOS	K of MB/BMImOS
0	4	4.2
0.83195	48.1	46.8
1.66113	102.1	88.6
2.48756	143.2	130.2
3.31126	177	170.9
4.13223	225	212
4.9505	269	254
5.76606	306	294
6.57895	348	335
7.38916	388	380
8.19672	423	421
9.80392	495	490
11.40065	560	555
12.98701	638	620
14.56311	715	700
16.12903	783	775
17.68489	843	840
19.23077	910	905
20.76677	973	970
22.29299	1033	1035
23.80952	1083	1100
25.31646	1137	1165
26.81388	1195	1215
28.30189	1267	1280
29.78056	1335	1340
31.25	1410	1403
32.71028	1480	1468
34.16149	1550	1518
35.60372	1612	1548
37.03704	1669	1578
38.46154	1734	1608
39.8773	1799	1638
41.2844	1865	1668
42.68293	1926	1701
44.07295	1955	1734
45.45455	1993	1765
46.82779	2050	1795
48.19277	2080	1823

Specific conductivity (k) of CTAB and MB/CTAB at different concentrations of CTAB at 298K

4.3

[CTAB]/mM	K of pure CTAB	K of MB/CTAT
0	3.7	3.9
0.02496	22	21.5
0.04983	25.2	24.4
0.07463	26.8	25.4
0.12397	33.9	32.9
0.17298	40.1	37
0.27005	47.3	45.8
0.36585	54.2	51.1
0.46042	61.8	57.4
0.55377	69.7	68.5
0.64593	76.5	71.3
0.73693	85.1	74
0.82677	90.6	83.3
0.91549	95.7	92.4
1.00311	99.4	98
1.08964	105.8	102.1
1.17512	112.2	105.4
1.25954	115	109.9
1.34294	116.8	114.2
1.42534	119	117.8
1.50675	121.7	118.7
1.58718	124	121.8
1.66667	126.7	125.8
1.74521	129.6	129
1.82284	132.4	130.9

4.4 Absorbance vs [BMImOS]/mM obtained from the UV absorption spectra of MB/BMImOS system at 298K

[BMImOS]/mM	Absorbance
0	0.1725
4.92611	0.16057
9.7561	0.15552
14.49275	0.15196
19.13876	0.14912
23.69668	0.14682
28.16901	0.14455
32.55814	0.14233
36.86636	0.14026
45.24887	0.13684
53.33333	0.13568
61.13537	0.13725
68.66953	0.13818
75.94937	0.13855
82.98755	0.13849
89.79592	0.13713
96.38554	0.13876
102.7668	0.13524

4.5 Absorbance vs [CTAT]/mM obtained from the UV absorption spectra of MB/CTAT system at 298K

[CTAT]/mM	Absorbance
0	0.18158
0.03842	0.1815
0.0761	0.18145
0.11304	0.18138
0.14928	0.17996
0.18483	0.17947
0.21972	0.17642
0.25395	0.17583
0.28756	0.17496
0.35294	0.17221
0.416	0.17014
0.47686	0.16693
0.53562	0.16524
0.59241	0.16025
0.6473	0.15875

4.6 Absorbance vs [CTAB]/mM obtained from the UV absorption spectra of MB/CTAB system at 298K

[CTAB]/mM	Absorbance
0	0.1535
0.14778	0.15367
0.29268	0.15549
0.43478	0.15588
0.57416	0.15543
0.7109	0.15195
0.84507	0.15099
0.97674	0.15106
1.10599	0.15067
1.35747	0.14897
1.6	0.15025
1.83406	0.14621
2.06009	0.14549
2.27848	0.14331
2.48963	0.13948
2.69388	0.1394
2.89157	0.13835

4.7 Variation of Fluorescence Intensity with varying concentrations of BMImOS of MB/BMImOS system at 298K

[BMImOS]/mM	F.I.
0	685.32
4.92611	659.56
9.7561	652.81
14.49275	646.99
19.13876	645.96
23.69668	629.29
28.16901	623.41
32.55814	620
36.86636	608.28
45.24887	663.4
53.33333	765.29
61.13537	822.19
68.66953	841.72
75.94937	861.89
82.98755	873.73
89.79592	855.71
96.38554	864.63
102.7668	847.25

4.8 Variation of Fluorescence Intensity with varying concentrations of CTAT of MB/CTAT system at 298K

[CTAT]/mM	F.I.
0	608.61
0.03842	645.54
0.0761	664.37
0.11304	671.43
0.14928	663.9
0.18483	662.23
0.21972	663.42
0.25395	660.99
0.28756	660.4
0.35294	649.36
0.416	645.67
0.47686	642.38
0.53562	638.67
0.59241	631.79
0.6473	630.44
0.70041	613.34
0.75181	613.25
0.80158	597.79

4.9 Variation of Fluorescence Intensity with varying concentrations of CTAB of MB/CTAB system at 298K

[CTAB]/mM	F.I.
0	607.17
0.14778	661.8
0.29268	669.04
0.43478	674.01
0.57416	677.2
0.7109	656.61
0.84507	654.03
0.97674	652.72
1.10599	649.28
1.35747	646.04
1.6	647.11
1.83406	643.95
2.06009	637.51
2.27848	634.44
2.48963	621.98
2.69388	615.19
2.89157	616.41
3.083	608.4

4.10 Steady state anisotropy measurement of the MB/BMImOS system with varying concentrations of BMImOS at 298K

[BMImOS]/mM	Anisotropy
0	0.063
4.92611	0.067
9.7561	0.067
14.49275	0.064
19.13876	0.071
23.69668	0.075
28.16901	0.079
32.55814	0.083
36.86636	0.085
45.24887	0.089
53.33333	0.103
61.13537	0.114
68.66953	0.126
75.94937	0.126
82.98755	0.127
89.79592	0.128
96.38554	0.13
102.7668	0.13

4.11 Steady state anisotropy measurement of the MB/CTAT system with varying concentrations of CTAT at 298K

[CTAT]mM	Anisotropy
0	0.065
0.03842	0.068
0.0761	0.072
0.11304	0.073
0.14928	0.064
0.18483	0.07
0.21972	0.067
0.25395	0.071
0.28756	0.064
0.35294	0.063
0.416	0.062
0.47686	0.062
0.53562	0.06
0.59241	0.059
0.6473	0.058
0.70041	0.055
0.75181	0.055
0.80158	0.054

4.12 Steady state anisotropy measurement of the MB/CTAB system with varying concentrations of CTAB at 298K

[CTAB]mM	Anisotropy
0	0.063
0.14778	0.06
0.29268	0.064
0.43478	0.06
0.57416	0.063
0.7109	0.07
0.84507	0.06
0.97674	0.067
1.10599	0.068
1.35747	0.068
1.6	0.059
1.83406	0.054
2.06009	0.056
2.27848	0.056
2.48963	0.055
2.69388	0.057
2.89157	0.056

LIST OF PUBLICATIONS

& REPRINTS

For the Thesis

- Bandyopadhyay, Sumanta, Rajesh Banik, Raju Sardar, and Soumen Ghosh. "An inclusive comparison regarding aggregation of surface active ionic liquid and conventional surfactant with a cationic dye Acridine Red exposed in view of spectroscopic and theoretical study." *Journal of Molecular Liquids* 411 (2024): 125684.
- Bandyopadhyay, Sumanta, Rajesh Banik, Raju Sardar, and Soumen Ghosh. "Aggregation and characterization of the microenvironment of solvatochromic eosin yellow dye in the presence of zwitterionic, cationic, and anionic surfactants: A spectroscopic and theoretical approach." *Journal of Molecular Liquids* (2025): 127953.

Poster presentation

- Presented a poster at the 21st National Conference on Surfactants, Emulsions & Biocolloids (NATCOSEB- XXI) on 23-25th November, 2023.
- Presented a poster at the International Conference on Emerging Materials (ICEM) on 20-21st April, 2017.